ANALYSIS AND DEVELOPMENT OF RECONFIGURABLE ANTENNAS FOR 5G APPLICATIONS

THESIS SUBMITTED BY

JOYDEEP PAL

DOCTOR OF PHILOSOPHY (ENGINEERING)

DEPARTMENT OF ELECTRONICS AND TELECOMMUNICATION ENGINEERING

FACULTY COUNCIL OF ENGINEERING AND TECHNOLOGY

JADAVPUR UNIVERSITY

KOLKATA, INDIA

2022

JADAVPUR UNIVERSITY

KOKATA – 700032, INDIA

INDEX NO. 122/19/E

1. **Name of the Thesis**: ANALYSIS AND DEVELOPMENT OF RECONFIGURABLE ANTENNAS FOR 5G APPLICATIONS

2. **Name, Designation & Institution of the Supervisor**:

   Dr. Bhaskar Gupta, Professor, Dept. of Electronics and Telecommunication Engineering, Jadavpur University, Kolkata – 700032, West Bengal, India

3. **List of Publications**: Kindly refer to **Appendix I**

4. **List of Patents**: NIL

5. **List of Presentations in National/International/Conferences/Workshops**:

[1] **J. Pal**, K. Patra and B. Gupta, "Indoor Channel Characterisation and Modelling for 5G Applications at 22GHz," *2019 IEEE 19th Mediterranean Microwave Symposium (MMS)*, 2019, pp. 1-4, doi: 10.1109/MMS48040.2019.9157298.

STATEMENT OF ORIGINALITY

I, **Joydeep Pal**, registered on **11.06.2019** do hereby declare that this thesis entitled "**Analysis and Development of Reconfigurable Antennas for 5G Applications**" contains literature survey and original research work done by the undersigned candidate as part of Doctoral studies.

All information in this thesis have been obtained and presented in accordance with existing academic rules and ethical conduct. I declare that, as required by these rules and conduct, I have fully cited and referred all materials and results that are not original to this work.

I also declare that I have checked this thesis as per the "Policy on Anti Plagiarism, Jadavpur University, 2019", and the level of similarity as checked by iThenticate software is 1%.

Joydeep Pal

Signature of Candidate

Date: 22/12/22

Certified by Supervisor: Gupta

Prof. Bhaskar Gupta
Professor
Dept. of E. & T.C. Engg.
Jadavpur University
Kolkata

Dr. Bhaskar Gupta
Professor, Dept. of ETCE
Jadavpur University, Kolkata – 700032

CERTIFICATE FROM THE SUPERVISORS

This is to certify that the thesis entitled "**Analysis and Development of Reconfigurable Antennas for 5G Applications**" submitted by **Shri Joydeep Pal**, who got his name registered on **11.06.2019** for the award of Ph. D. (Engg.) degree of Jadavpur University is absolutely based upon his own work under the supervision of **Prof. Bhaskar Gupta**, Dept. of Electronics and Telecommunication Engineering, Jadavpur University, Kolkata – 700032, West Bengal, India, and that neither his thesis nor any part of the thesis has been submitted for any degree/diploma or any other academic award anywhere before.

B gupta 22/12/22

Dr. Bhaskar Gupta
Professor, Dept. of ETCE
Jadavpur University, Kolkata – 700032

Prof. Bhaskar Gupta
Professor
Dept. of E. & T.C. Engg.
Jadavpur University
Kolkata

ACKNOWLEDGEMENT

Well, it is always difficult to find appropriate words for all the work, time and memories wrapped around it. It is even more difficult to acknowledge all the people who have contributed in some way or the other to this thesis and in the way they deserve it. So, if you do not find yourself in the following pages in the way you were expecting it, I am sorry for that. If this should really be the case, feel free to drop by, to complain to me about that and help me remember the good times we had together. The entire list of people who were a part of this process can broadly be clustered into three groups: Teachers (who constantly and incessantly guided and corrected me throughout), friends (who helped me and more importantly accepted my insanity) and family (whose constant complaining actually got me through to the end)

Firstly, I would like to take the opportunity to express my deepest and sincere gratitude to my supervisor Prof. Bhaskar Gupta. I am grateful to Prof. Gupta for his constant support and encouragement over the years. His continuous involvement and originality have both triggered and nourished my intellectual maturity that I will benefit from, for a long time to come. Inhuman levels of patience coupled with his uncanny ability to have an answer for almost all problems make him an ideal to strive towards.

I am grateful to all the faculty members of the Department of Electronics and Telecommunication Engineering, Jadavpur University, who have given me valuable suggestions throughout my work. I enjoyed discussing and receiving advice from Prof. Manotosh Biswas, Prof. Sayan Chatterjee and Prof. Sudhabindo Roy to name a few.

Dr. Kaushik Patra, who always stood by my side like my own shadow. I have the privilege to reach him any time and with any problem. He showed us the actual meaning of scientific research. His constant encouragement, support and unconditional love made me a different person altogether.

My entire research work was carried out at the Microstrip Laboratory of the ETCE Department of Jadavpur University. Hence, I take the opportunity to acknowledge the fellowship of antenna engineers present in the lab. Proceeding chronologically from the time I started my Ph.D I would like to acknowledge Dr. Sayantan Dhar, Dr. Arindam Deb, Dr. Rajendra Prosad Ghosh, Dr. Sudipta Maity, Dr. Amrita Chakraborty, Mr. Sumit Mitra, Dr. Buddhadev Pradhan, Dr. Ayona Chakraborty, Dr. Rinki Ghoshal, Mr. Sharanbasappa B. Belamgi, Mr. Mishor Biswas and Dr. Sourav Banik. There were a few people who probably deserve special mention. I thank Mr. Ardhendu Kundu, Dr. Amartya Banerjee, Dr. Suman Pradhan, Dr. Arka Bhattacharya, Mr. Sayan Sarkar and Ms. Baisakhi Bandyopadhyay who instilled in me a sense of camaraderie and workmanship which will stay with me forever. A special appreciation for Mr. Ardhendu Kundu who was my partner in crime since masters. Our craziness is what kept us going on, I

shall cherish these memories for a long time. Mere thanks will not be enough to quantify the help I have received from Dr. Amartya Banerjee, Mr. Sayan Sarkar and Dr. Suman Pradhan. We have been accused of being too academic to outright pranksters. Special gratitude is due to them for their valuable time and suggestions.

I would like to thank for helping me in many aspects of my research. Mr. Soham Ghosh and Mr. Sourav Ray especially helped me out in fabrication and measurements present in this thesis. They were my patterners in all aspects whether it was an in-depth technical discussion or crime in disguise.

During my tenure at this department where I worked, I had the privilege to have three Heads of the Department namely, Dr. P. Venkateswaran, Dr. Sheli Sinha Chaudhuri and Dr. Ananda Shakar Chowdhury – each of whom personally assisted me in every problem I came across during their times in office. I would like to thank personally each of them and additionally, each of the staff members of this department whose assistance made my journey comfortable, easier to take and indeed an experience to cherish for the years to come. I would also like to thank all the administrative staff members, officers of the University, at the Research Section or at the Faculty office, on in any other department – whose active assistance I received at all the times.

Finally, this acknowledgement will not be complete without recognizing the support I have received from my family. The constant nagging from my wife about how long it would take to finish my Ph.D along with the most potent question of "what exactly are you doing?" actually motivated me to keep things simple. So, the biggest thanks is reserved for my wife Sucheta for her consistent support, patience, impatience, care and lots of perseverance. My elder and younger brothers always supported me in my research work by taking additional family responsibilities. Finally, I would like to dedicate this thesis to my beloved father who is no more with me now. His struggle, courage and self-belief always motivated me to aim heigh. He would be even happier than me today. My mother always concerned about my health during my tenure of staying away from her. Without the blessings of my parents, I could not have been what I am now.

Dated: 22/12/2022

Joydeep Pal

Joydeep Pal

Contents

List of Figures

Chapter 3

Chapter 4

Chapter 5

Chapter 6

Chapter 7

Chapter 8

Chapter 9

List of Tables

Chapter 8

Chapter 9

To My Patents,

Late Shri Sukumar Pal & Smt. Ashalata Pal

"Thy infinite gifts come to me only on these very small hands of mine.
Ages pass, and still thou pourest, and still there is room to fill."

- Rabindranath Tagore

Chapter 1
Introduction

1.1 Preface

We have witnessed evolutionary change in every aspect around us especially in the domain of technology. It is the ever-growing desire and demand of human race to avail better facilities for the ease of life and that drives the technology to grow fast [1]. Information Technology along with the allied fields especially communication domain has been evolved remarkably in the last few decades [2]. In the 1st Generation cellular system only audio transmission was introduced. But with time the domain has matured extensively and become ready to serve much more than simple audio. The requirement of advanced services such as data and video or other multimedia applications demand larger bandwidth and higher data rate that propel the telecom-Generation to evolve from 1G to 4G [3]. So far, the cellular network is serving the voice, data, or VoLTE services with larger bandwidth. In the last decade the research community has come up with diverse ideas of which automation, Internet of Things, Remote Sensing are few to mention [4]. Subsequently researchers of multiple communities belonging to specially RF, Communication, Network and Signal Processing domains are jointly contributing to make the network backbone ready for these advanced services and hence a new generation of cellular technology has begun its chapter, i.e., 5G [5]. This is not simply the predecessor of the previous generations but a heterogenous network architecture where most of the Information services are integrated in the same platform.

1.2 5G: What and Why?

5G stands for the 5th Generation of cellular network. In simple terms it will provide faster data speed, larger bandwidth with very low latency between network nodes to transform the overall experience of communication that will develop a sustainable, safer, and faster future [6]. It is all about connecting every node reliably without delay - so that things can be measured and managed in real time. The technology opens new possibilities, which allows us to deliver

solutions that are profoundly impactful across society by increasing tele-density and broadband penetration in rural and urban areas [7].

The 2G cellular domain primarily focused on consumer needs, offering voice and messaging services whereas 3G provided web browsing. In present 4G technology high speed data and video stream are being delivered [3]. Two most important emerging technologies i.e., cloud and edge computing will have significant impact on the latency to reduce it to near zero (>1ms). It will revolutionize our societies and industries by connecting billions of network nodes accruing and sharing information in real time. Advance RF systems including mmWave technologies along with massive MIMO and other advanced antenna systems will support the enhanced Mobile Broadband (eMBB) technology which will provide exceedingly larger data bandwidth demand. To describe 5G in terms of numbers is quite straightforward. It will provide 20Gbps peak data rate with less than 1ms latency. Along with that it will support 99.999% network uptime with more than 99.999% reliability and network security. This architecture will also provide minimum 10Gbps peak data rate at around 350 mph vehicular mobility with 3ft positioning accuracy [8]. The projected device density will be 2.5Mn/mil^2 with respect to 250 per mil^2 in 4G. It has also been forecasted by few top-notch organizations involved in 5G deployment worldwide that by 2026 the mobile subscription (8.8Bn subscribers) will be more than the global population (7.8Bn) within which 3.5Bn will be 5G subscribers. Along with that 60% of the global population will have 5G coverage and 77% of the mobile data traffic will be video [9].

In recent time 5G becomes a focused area of discussion. At the same time many controversies are raised regarding the actual requirement of 5G deployment in multiple demography in present socioeconomic scenarios. The benefits of global 5G rollout are well discussed in numerous literatures [10-12] and a general belief across research communities is that the impact on the society will be incredible in the positive sense. In author's perspective, 5G is exceedingly crucial to deploy from environmental standpoint. Government of different countries and other responsible global autonomous bodies has taken initiative for Green Telecom in coming future [13-14]. Power consumption and CO_2 emission have significantly increased because of ongoing rise in data traffic demand. The goal of green telecommunication is to create systems that will improve energy efficiency and reduce Operational Expenditure (OPEX) without sacrificing perceived Quality of Services (QoS) by the end user. Due to low cost, ease of

deployment and low power consumption micro, pico and femto cells are appealing to achieve green telecommunication goals. Thus, it is predicted that 5G technology will reduce the global carbon emission by 15% by 2030 and subsequently will combat the global climate change to great extend [5-7].

1.3 Motivation

Communication technologies are advancing at an extremely rapid pace, particularly on the wireless front. Wireless domain has emerged as one of the possible frontends in existing and upcoming 5G ecosystems to cater diverse advanced applications [15]. Service Providers need to deploy large number of communication nodes (wireless or wireline nodes) within limited area to cater to multiple integrated services. Hence many wireless nodes will be operated within constrained operating spectrum in coming times. Several P2P/P2MP (Point to Point/Multipoint) radio links operated in licensed and unlicensed bands are being employed. Also, many upcoming complex wireless nodes are being planned to be deployed in near future to make IoT or industrial automation a reality. As a result, RF spectrum is gradually getting congested due to the constraint of usable spectrum [16]. Few works on MIMO technology or Cognitive Radios have already been introduced to increase spectrum efficiency [20-21]. In contrast, the deployment of a significant number of wireless nodes in the impending heterogeneous cellular networks [22-23] will make the RF front ultra-dense in nature and will create an Ultra-Dense-Network (UDN) environment. The existence of such nodes in proximity in a dense RF network will create issues of Inter-Symbol (ISI) and co-channel interference resulting in low SINR and randomly fluctuating throughput [19]. The occurrence of these issues limits the peak data rate, distorts the received signal and changes the overall channel properties [17]. In 5G ecosystems, the deployment of RF nodes will be increased by manifold which would increase multipath, shadowing and fading in the communication channel and worsen the scenarios even further [18]. Wireless Channel State Information (CSI) will also be altered, which is one of the prerequisites to determine the transmission power and modulation techniques in specific environment for efficient data transmission.

Significant research has already been done and implemented in signal processing and wireless system design front to mitigate these issues. A comprehensive review of the existing research publications is done to find the relevant works from antenna and propagation

community that will address the issues of signal interference, multipath and spectrum insufficiency in the upcoming 5G ecosystem. Though a limited contribution has been noted so far. Thus, advanced techniques need to devise to exploit the existing spectrum to integrate multiple services and an antenna perspective approach is highly desirable in this regard.

Concurrently, enhancement in wireless connectivity is important to update the existing cellular network coverage specially to cater to massive sensor connectivity for IoT services in coming 5G ecosystem [24]. Recently Reconfigurable Intelligent Surfaces (RIS) are being studied largely to alter the propagation environment to enhance signal coverage in indoor and outdoor environments [25]. The deployment of wireless nodes in proximity with RISs will make the existing network ultra-dense and random in nature, causing unavoidable concerns in the propagation channel [26]. Thus, characterization and modeling of wireless channels is highly desirable in present scenarios to devise accurate Channel State Information (CSI) prior to design efficient communication systems [27]. UWB communications, on the other hand, have gained a lot of interest because of its large bandwidth, resistance to deep fading and low power consumption [28]. As a result, UWB technology is more suited for sophisticated applications such as RF imaging, location detection and ranging of wireless nodes with centimeter-level of positioning accuracy [29]. Researchers in recent time are paying significant attention to Body Area Networks (BAN) and Personal Communication Systems (PCS) from a healthcare and security standpoint [20] using this technology. Simultaneously, it is vital to gain advance knowledge about the channel behavior with the varying nature of environment and signal bandwidth. This prior requirement eventually necessitates the characterization and modeling of these UWB channels to develop robust access points/modems containing suitable antenna systems that will serve high-speed, short-range communication in the future UDN environments [31].

Researchers have used different calibration techniques to calibrate the channel measurement equipment before conducting the measurement campaign without nullifying the impact of terminal antennas. Thus, the wireless channel characteristics and models are terminal antenna and environment dependent eventually limiting the universal use of these models to predict small and large scale channel characteristics.

Thus, brief investigation on the wireless channel characterization and modeling, and subsequently designing sophisticated multifunctional antennas to overcome challenges mentioned earlier is the primary motivation behind this dissertation entitled '*Analysis and Development of Reconfigurable Antennas for 5G Applications'*.

1.4 Solution Approach – A Very Brief Overview

We believe the solution of every problem lays behind the degree of understanding of the problem. It is well established that Receive Signal Strength (RSS) or Signal to Interference and Noise Ratio (SINR) or multipath effect can be improved significantly by changing the operational polarization or frequency to other available reconfigurable states on the basis of SINR or Bit Error Rate (BER) feedback of an interfered RF link [32-34]. The incorporation of multifunction antennas in the system minimizes the received signal distortion in the communication channels caused by multipath, fading and shadowing. Hence the wireless systems can be made further interference immune with polarization or frequency reconfigurability. Concurrently, a high gain antenna can increase the SINR of a RF link by firmly directing the radiated beam towards the receiver antenna with increased gain. This also reduces the interference largely and desirable for outdoor P2P applications to cater to a larger coverage area with reasonably less input power. Thus, implementation of a high gain frequency and polarization agile antenna in the present 5G UDN environment is highly appreciable.

So far multifunctional antennas are predominantly used to integrate multiple services. Extensive research has already done in recent times showing advantages of using such antennas in 5G domain in terms of catering diverse services. In this dissertation a detail discussion on designing prototype planar compact reconfigurable antennas is presented. Realized antenna gain is enhanced largely by using Higher Order broadside Modes (HOM). Antenna array is also designed with antenna elements operate in HOM to increase the gain even further. The proposed designs are enabled with large number of reconfigurable states that would eventually provide the system designers higher degree of flexibilities from system design aspect. These agile antennas can also be incorporated in the system to increase spectrum efficiency and also mitigate the channel multipath and fading effect. To understand the nature of wireless channel prior to design such antennas, a brief investigation on the channel characteristic is presented for indoor static environment using frequency domain measurement approach. An investigation on the effects of

terminal antennas in the channel measurement systems is done and closed form expressions are derived analytically to calibrate the channel measurement system using a two port network model approach.

1.5 Novel Aspects

Author has focused to propose apposite reconfigurable antennas to cope up with the issues discussed in the previous section. Wireless channel characterization and modeling also have similar importance as the prior knowledge of the channel is highly desirable before to design antenna systems. The following novel aspects are discussed in the dissertation.

i. Closed form analytical expressions for terminal independent wireless channel is proposed using frequency domain channel measurement and two port network model approach.
ii. UWB wireless channel modeling and characterization is discussed for indoor static environment for 5G application using frequency domain measurement technique.
iii. Penta-Polarization agile compact planar antenna operates in TM_{03} mode is investigated for the first time in the open literature.
iv. Two frequency and polarization agile compact single-layered planar antennas operate in fundamental mode are investigated. The dual and tri band reconfigurable antennas are designed to operate in five distinct polarization states which is not available in the literature so far. Thus, the antennas can be operated with ten and fifteen reconfigurable states respectively for interference and multipath fading mitigation in UDN environment.
v. Highly compact pattern and frequency agile 2D planar array operates in higher order TM_{03} mode for improved signal coverage, high SINR and low multipath fading is investigated. The array is designed to scan both the principle planes with consistent realized gain in broadside direction.
vi. A 2D antenna array with antenna elements that operates at TM_{03} mode to enhance the realized antenna gain is proposed in K band. It is suitable for overall coverage and SINR improvement in mmWave technology in 5G outdoor applications.

1.6 Organization of the Thesis

The organization of the dissertation is presented below

Chapter 2A represents the initial research works on wireless channel characterization and modeling. The constant progress in characterizing and modeling the channel is discussed in the subsequent sections. The literature survey in the context of 5G ecosystem is also taken care. Survey on different channel measurement techniques, specially frequency domain channel measurement approach is included.

Chapter 2B presents the early research activities on antenna reconfigurability in general. It starts from the very beginning of the application of multifunction antennas specially in case of microstrip planar antennas. In the subsequent sections the gradual evolution of the antenna reconfigurability is discussed emphasizing 5G standpoint. The evolution is also categorized based on application, technology, material and so on.

In **Chapter 3**, closed form expressions for terminal independent wireless channel measurement using frequency domain approach are discussed using two port network model approach. The transfer functions of the Tx and Rx antenna and overall trans-receiver system is derived from the frequency domain measurement. FFT and IFFT techniques are used to obtain time and frequency domain derivations. In the subsequent section different antennas are used in the laboratory measurement setup to check the antenna independency of the wireless channel.

Chapter 4 presents a frequency domain UWB channel measurement campaign in university indoor static environment. The detail measurement setup and environment are discussed in the subsequent sections. A large-scale statistical path loss model is proposed. In later sections a 5^{th} order autoregressive model for small scale fading channel is proposed.

Chapter 5 deals with the proposal of a compact dual band penta-polarization agile planar antenna. The theory of frequency and polarization reconfigurability is discussed thereafter. The design of the feed network and ten attainable reconfigurable states are analyzed further. In the subsequent sections measurement of all important antenna parameters and a logical comparison with recently published works are depicted.

Chapter 6 gives the proposal of a compact frequency and polarization agile antenna with fifteen reconfigurable states. The technique proposed in chapter 3 is extended further for tri-band Penta polarization reconfigurability. The detail working principle of Penta polarization reconfigurability at three distinct operating bands is discussed in the next section. Detailed discussion about the design of feed network and fabrication process is shown in the following sections. Measurement of the fabricated antenna is discussed with a fair comparison with latest research works. The chapter is concluded in a note of its novelty with respect to the existing works.

Chapter 7 focuses on multifunctional antennas operating at higher order modes to attain larger gain with reconfigurability. A Penta polarized planar antenna operating at TM_{03} mode is proposed for the first time in the literature. The technique discussed in chapters 3 and 4 is further extended for planar antennas operated at TM_{03} mode. The design and operating principal are presented in subsequent sections. Measurement results of the fabricated prototype is depicted next.

In **Chapter 8**, 2D antenna array operated in TM_{03} mode is presented for achieving higher realized gain. It is shown in the theory that the antenna gain is increased significantly by designing array with antenna elements operated at higher order modes radiate at broadside direction. A detailed comparison of the gain improvement between fundamental and TM_{03} mode antenna and array is discussed.

Chapter 9 deals with the frequency and pattern reconfigurable planar antennas. The theory of the frequency tuning ability is presented. In the subsequent section a detailed overview of 360º beam scanning in phi plane and ±40º beam scanning in theta plane is discussed. Detailed measurements and a brief comparison with recent works in the open literature is depicted subsequently.

Chapter 10 presents the concluding comments and the future possibility of this dissertation.

References

[1] M. Vaezi et al., "Cellular, Wide-Area, and Non-Terrestrial IoT: A Survey on 5G Advances and the Road Toward 6G," in IEEE Communications Surveys & Tutorials, vol. 24, no. 2, pp. 1117-1174, Second quarter 2022, doi: 10.1109/COMST.2022.3151028.

[2]The Evolution of Industry 1.0 to 4.0, 2019, [online] Available: https://www.seekmomentum.com/blog/manufacturing/the-evolution-of-industry-from-1-to-4."Minimum requirements related to technical performance for IMT-2020 radio interfaces", 2017, [online] Available: https://www.itu.int/pub/R-REP-M.2410-2017.

[3] J. A. del Peral-Rosado, R. Raulefs, J. A. López-Salcedo and G. Seco-Granados, "Survey of Cellular Mobile Radio Localization Methods: From 1G to 5G," in IEEE Communications Surveys & Tutorials, vol. 20, no. 2, pp. 1124-1148, Second quarter 2018, doi: 10.1109/COMST.2017.2785181.

[4] H. Lasi, P. Fettke, H.-G. Kemper, T. Feld and M. Hoffmann, "Industry 4.0", Bus. Inf. Syst. Eng., vol. 6, no. 4, pp. 239-242, 2014.

[5]5G: The Future of IoT, 2019, [online] Available: https://www.5gamericas.org/wp-content/uploads/2019/07/5G_Americas_White_Paper_on_5G_IOT_FINAL_7.16.pdf. X. Lin and N. Lee, 5G and Beyond: Fundamentals and Standards, cham, Switzerland: Springer Nat, 2021.

[6]https://www.fortunebusinessinsights.com/industry-reports/internetof-things-iot-market 100307.

[7] https://www.ericsson.com/en/mobilityreport/reports.

[8] I. Rahman et al., "5G Evolution Toward 5G Advanced: An overview of 3GPP releases 17 and 18," in Ericsson Technology Review, vol. 2021, no. 14, pp. 2-12, October 2021, doi: 10.23919/ETR.2021.9904665.

[9] 3GPP, TS 22.263, "Service Requirements for Video, Imaging and Audio for Professional Applications (VIAPA)", Dec. 2020.

[10] A. Tudzarov and S. Gelev, "Requirements for next generation business transformation and their implementation in 5G architecture", International Journal of Computer Applications, vol. 162, no. 2, pp. 31-35, 2017.

[11] D. Jiang and G. Liu, "An Overview of 5G Requirements" in 5G Mobile Communications, Springer, pp. 3-26, 2017.

[12] A. Kumar, K. Singh and D. Bhattacharya, "Green communication and wireless networking," 2013 International Conference on Green Computing, Communication and Conservation of Energy (ICGCE), 2013, pp. 49-52, doi: 10.1109/ICGCE.2013.6823398.

[13] H. Chater and H. Chafnaji, "Green telecommunication with Heterogonous Networks: A survey," 2014 International Conference on Multimedia Computing and Systems (ICMCS), 2014, pp. 1490-1494, doi: 10.1109/ICMCS.2014.6911141.

[14] X. Wen, J. Chen, Z. Hu and Z. Lu, "A p-Opportunistic Channel Access Scheme for Interference Mitigation Between V2V and V2I Communications," in IEEE Internet of Things Journal, vol. 7, no. 5, pp. 3706-3718, May 2020, doi: 10.1109/JIOT.2020.2967647.

[15] Cui, Q. et al., "Preserving Reliability of Heterogeneous Ultra-Dense Distributed Networks in Unlicensed Spectrum," in IEEE Communications Magazine, vol. 56, no. 6, pp. 72-78, June 2018, doi: 10.1109/MCOM.2018.1700474.

[16] Fan, C., Huang, D., Wang, P. and Hsu, C.:" Interference-aware video streaming overcrowded unlicensed spectrum," 2016 18th Asia-Pacific Network Operations and Management Symposium, 2016, pp. 1-6, doi: 10.1109/APNOMS.2016.7737216.

[17] V. Kumar, H. Li, J. -M. J. Park and K. Bian, "Crowd-Sourced Authentication for Enforcement in Dynamic Spectrum Sharing," in IEEE Transactions on Cognitive Communications and Networking, vol. 5, no. 3, pp. 625-636, Sept. 2019, doi: 10.1109/TCCN.2019.2909028.

[18] W. Feng, Y. Wang, D. Lin, N. Ge, J. Lu and S. Li, "When mmWave Communications Meet Network Densification: A Scalable Interference Coordination Perspective," in IEEE Journal on Selected Areas in Communications, vol. 35, no. 7, pp. 1459-1471, July 2017, doi: 10.1109/JSAC.2017.2698898.

[19] S. Haykin, "Cognitive radio: Brain-empowered wireless communications", IEEE Journal on Selected Areas in Communications, vol. 23, no. 2, pp. 201-220, 2005.

[20] S. Sridharan and S. Vishwanath, "On the capacity of a class of MIMO cognitive radios", IEEE Journal of Selected Topics in Signal Processing, vol. 2, no. 1, pp. 103-117, 2008.

[21] M. Kamel, W. Hamouda and A. Youssef, "Ultra-Dense Networks: A Survey", IEEE Communications Surveys & Tutorials, vol. 18, no. 4, pp. 2522-2545, May. 2016.

[22] Y. Teng, M. Liu, F. R. Yu, V.C. M. Leung, M. Song and Y. Zhang, "Resource Allocation for Ultra-Dense Networks: A Survey Some Research Issues and Challenges", IEEE Communications Surveys & Tutorials, Aug. 2018.

[23] M. Alsabah et al., "6G Wireless Communications Networks: A Comprehensive Survey," in IEEE Access, vol. 9, pp. 148191-148243, 2021, doi: 10.1109/ACCESS.2021.3124812.

[24] Y. Cao, T. Lv and W. Ni, "Intelligent Reflecting Surface Aided Multi-User mmWave Communications for Coverage Enhancement," 2020 IEEE 31st Annual International Symposium on Personal, Indoor and Mobile Radio Communications, 2020, pp. 1-6, doi: 10.1109/PIMRC48278.2020.9217160.

[25] J. Liu, M. Sheng, L. Liu and J. Li, "Interference Management in Ultra-Dense Networks: Challenges and Approaches," in IEEE Network, vol. 31, no. 6, pp. 70-77, November/December 2017, doi: 10.1109/MNET.2017.1700052.

[26] Y. Rahayu, T. A. Rahman, R. Ngah and P. S. Hall, "Ultra-wideband technology and its applications," 2008 5th IFIP International Conference on Wireless and Optical Communications Networks (WOCN '08), 2008, pp. 1-5, doi: 10.1109/WOCN.2008.4542537.

[27] D. Minoli and B. Occhiogrosso, "Ultrawideband (UWB) Technology for Smart Cities IoT Applications," 2018 IEEE International Smart Cities Conference (ISC2), 2018, pp. 1-8, doi: 10.1109/ISC2.2018.8656958.

[28] S. van Roy, C. Oestges, F. Horlin and P. De Doncker, "A Comprehensive Channel Model for UWB Multisensor Multiantenna Body Area Networks," in IEEE Transactions on Antennas and Propagation, vol. 58, no. 1, pp. 163-170, Jan. 2010, doi: 10.1109/TAP.2009.2036280.

[29] C. Briso, C. Calvo and Y. Xu, "UWB Propagation Measurements and Modelling in Large Indoor Environments," in IEEE Access, vol. 7, pp. 41913-41920, 2019, doi: 10.1109/ACCESS.2019.2905142.

[30] S. Sharma, A. Gupta and V. Bhatia, "A Simple Modified Peak Detection Based UWB Receiver for WSN and IoT Applications," 2017 IEEE 85th Vehicular Technology Conference (VTC Spring), 2017, pp. 1-6, doi: 10.1109/VTCSpring.2017.8108192.

[31] C. L. Guo and H. Y. Li, "A review on polarization-based spectrum sensing", Transactions on Emerging Telecommunications Technologies, vol. 27, no. 10, pp. 1345-1364, 2016.

[32] K. Salehian, Y. Wu, D. Prendergast and G. Gagnon, "Evaluating the Use of Cross-Polarization Discrimination in Mitigating Interference from Unlicensed Devices onto DTV," in IEEE Transactions on Broadcasting, vol. 54, no. 4, pp. 779-783, Dec. 2008, doi: 10.1109/TBC.2008.2007026.

[33] O. Mosiane, N. Oozeer and B. A. Bassett, "Machine learning for radio frequency interference mitigation using polarization," 2017 IEEE Radio and Antenna Days of the Indian Ocean (RADIO), 2017, pp. 1-2, doi: 10.23919/RADIO.2017.8242211.

Chapter 2A
Literature Review- Wireless Channel Characterization and Modeling

2.1.1 Introduction

Characterizing the wireless channel in different static and dynamic environments is always an essential domain of research. Prior information of the wireless media before design and deployment of wireless nodes is an important aspect. The vital channel matrices vary significantly due to the variation of environmental behavior. While propagating through the wireless media the transmitted signal encounters reflection, refraction, diffraction or scattering phenomena depending on the nature of the surrounding environment before being received at the receiving terminal. Thus, the received signal properties i.e., amplitude, frequency and phase are altered randomly. The nature of signal degradation in a multipath fading environment also significantly depends on frequency and bandwidth of the operating band [1].

2.1.2 Importance of Channel Characterization and Modeling

The requirement of characterizing wireless channel matrices and subsequent modeling is presented as follows.

1. Effective deployment of wireless network requires channel characterization and modeling of Received Signal Strength (RSS) that is termed as large scale pathloss model. The models are required for coverage prediction and Interference analysis [2].
2. Effective design of Physical and Media Access Control (MAC) layers in communication systems requires comprehensive investigations on the multipath effects also termed as small-scale fading effects. These models are exclusively used in calculating the channel data rate limitations, error rate calculation and delay-throughput analysis [3].

2.1.3 Parameters Effecting Signal Propagation

There are many aspects that has direct or indirect impact on the signal propagation in free space in different environmental scenarios [4]. In indoor situations, reflection and scattering phenomena usually take the lead, whereas in outdoor environments, reflection and diffraction predominate. In indoor location the effect is comparatively stronger due to the existence of large number of reflectors and scatterers. Along with operating frequency and bandwidth, the nature of surrounding environment plays a significant role in creating multipath and subsequent signal degradation. Environmental disturbances due to the random dynamic nature of the surrounding objects such as moving vehicles or movement of living bodies introduce the time dependency in the channel behavior. It is also observed in few studies that channel behavior largely depends on the terminal antennas [5-7] (Omnidirectional, Sectored or Multi Input Multi Output Antenna, MIMO) that are used for channel measurement campaign in different locations.

2.1.4 Channel Modeling Aspects and Techniques

Wireless channels are characterized and modelled in three different approaches as defined below.

1. Frequency Domain [8]
2. Time Domain [9]
3. Space Domain [10]

While propagating across wireless media, frequency components experience varying attenuation or gain. Thus, the received signal shows an amplitude fluctuation in the frequency domain. In time domain the transmitted impulse arrives at the receive end with different delays due to multipath effect as transmitted signal propagates in different paths with distinct lengths. Lastly, in space domain the vector sum of the receive signals from different direction with different angles are taken. In a nutshell the overall channel modeling aspects are shown below.

1. RSS Modeling: Empirical formulas are derived from the channel measurement data of the received signal strength at multiple environment and models are devised based on the measured data to predicts the signal coverage in other environments [11-13].

2. Impulse Response Modeling: The power delay profile is devised from the vectorially added replica of the received pulses that mainly captures the small-scale fading parameters and predicts the data rate and error probability of the channel [14-16].
3. Frequency Response Modeling: Frequency domain measured dada are converted to time domain using FFT (Fast Fourier Technique) and IR modeling techniques are applied to devise the model. Also, in few cases the frequency domain measured data are processed to attain frequency domain matrices such as coherence bandwidth or Doppler spectrum [17-20].
4. Time and angle of arrival of transmitted signal to devise space domain models.

Researchers in the literature largely follow two channel modeling techniques, for instance empirical and deterministic channel models. All channel models are classified briefly in the following ways.

1. Distance-power relation for coverage prediction [21].
2. Multipath delay spread for data rate limitation and time diversity [22].
3. Doppler spread for receiver adaptation speed and frequency diversity [23].
4. Angle of arrival of the signal for multiple antenna system and positioning [24].
5. Time of arrival of received signal for positioning [25].

In the following sections author tries to incorporate most of the relevant channel models for different scenarios.

I. Large-Scale Pathloss Models

Path loss models [26-30] explain the signal attenuation as a function of the propagation distance and other factors between a broadcast and a receive antenna. Several models use various elements of the terrain profile to determine signal attenuation, while others solely use operating frequency and distance.

A. Empirical or Statistical Model in Outdoor Environment

Rural and urban locations have various effects on wireless signal propagation. In a rural environment, the signal is affected by huge vegetation, hills, trees and water, whereas in an urban location, the signal is changed by large buildings. In-depth study has been done on the wireless

channel characteristics in those open spaces and numerous significant models have been put forth [31-33].

i. Okumura Model

This model [34] presented in Eq. 2.1, is widely used in urban environment. It is simple and accurate in terms of predicting pathloss for outdoor coverage in early cellular systems, though this model responses slowly to the rapid changes in terrain profile.

$$pl(dB) = PL_f + a_{mu}(f,d) + g(h_{te}) + g(h_{re}) + g(area) \quad (2.1)$$

PL_f is the free space pathloss values, a_{mu} is the median attenuation in free space at frequency f and distance d. $g(h_{te})$ and $g(h_{re})$ are the gain factor of the Tx and Rx antenna at h_{te} and h_{re} height (meter). $g(area)$ is the environmental gain.

ii. Okumura-Hata Model

This model is an extension of the Okumura model [35]. The closed form expression of the model for Urban environment is as follows.

$$pl(Urban)(dB) = 69.55 + 29.16\log(f_c) + 13.82\log(h_{te}) - a(h_{re}) + (44.9 - 6.55\log(h_{te}))logd \quad (2.2)$$

where f is in MHz and $a(h_{re})$ is the correction factors of the antenna height. Nevertheless, the antenna height correction factor changes depending on the surroundings. Large metropolitan outdoor environments are best suited for this type.

iii. COST 231 Model (Waltisch Model)

This model is basically the theoretical representation of model proposed by Waltisch et al. and presented as follows [36].

$$PL_d = \begin{cases} PL_0 + PL_s + PL_d, & for\ \ PL_s + PL_d > 0 \\ PL_0, & for\ PL_s + PL_d \leq 0 \end{cases} \quad (2.3)$$

where $PL_0, PL_s\ and\ PL_d$ are the free space, scattering and diffraction losses respectively where the individual losses are represented separately for different environments. This model was recommended for IMT-200 by the ITU.

iv. Dual-Slope Ray Model

This model is based on Two-ray model and applicable for specific Line of Sight (LoS) cases where the Tx and Rx antennas are kept at the height of several operating wavelengths [37-39]. The empirical representation of the model as follows.

$$PL_d(d) = PL_b + \begin{cases} 10n_1 logd + PL_0, & for\ 1 < d < d_{brk} \\ 10(n_1 - n_2) logd_{brk} + 10n_2 logd + PL_0 & for\ d > d_{brk} \end{cases} \quad (2.4)$$

where d_0 and d_{brk} are the reference and break point distances. N1 and n1 are the exponent of the slope before and after the break point.

B. Empirical Model in indoor Environment

Signal propagation in the indoor environment largely depends on the layout of the building, materials used for the construction and the indoor scatterers. Signal travels in multiple paths due several reflections, refraction, diffraction and scattering within the building. In the power-distance relation the decay of the signal power or the pathloss exponent lies between 1.5 to 1.8 in those confined environments. It also depends upon the operating frequencies and the signal bandwidth. The following deterministic models are proposed in the literature for efficient indoor channel characterization.

i. Ray-Tracing Method

Ray-Tracing methods [43-48] are combined with the Universal Theory of Diffraction and evolved to efficiently characterize indoor channel in Ultra-Heigh-Frequencies. This is basically

an amalgamation of two-dimensional ray tracing results with the computational technique and forms a three-dimensional ray tracing model that reduces the computational time remarkably.

ii. Finite Difference Time Domain (FDTD) – Indoor Propagation Model

So far, the reflection from the indoor walls is modelled with some specific attenuation or losses without considering the actual reflection or transmission loss. This issue has been treated by a numerical approach using FDTD [43-44] method. The measured results from ray tracing and FDTD are compared, and it is observed that losses through the walls varied significantly from different indoor cases, even the variation is severe at the higher operating frequencies.

C. Site Dependent Large- Scale pathloss Model

Site specific models [42] are derived from analytical approach rather than extensive measurement data as statistical models. Maxwell's wave equations are analytically solved for different environments to predict the coverage of different environments. Thus, detailed understanding of the target location is required to accurately predict the propagation metrices. It provides very accurate results but requires large computation time in order to dealing with extensive complex equations.

i. Ray-Tracing Method (RTM)

Ray-tracing method [43-45] is based on Geometrical theory of Optics where the high frequency electromagnetic waves are assumed to propagate in a straight line as rays and deviate after encountering medium interfaces with different media properties such as refractive index. The method is very accurate when the distance between the transmitter and receiver is much larger compared to the operating wavelength and hence used extensively. Image and Brute-force ray-tracing methods are two widely used ray-tracing methods.

1. Image-based RTM

In this method [46] the images of a source at different planes are captured and used as secondary source of subsequent reflections. This method is quite simple and efficiently used for

simple environments, though the method faces difficulties in predicting the receive power in complex environments.

2. Brute-Force RTM

A large number of transmitted rays are considered in this ray-tracing method [49], but a certain number is reached at the receiver location depending on the environmental attenuations or blockages. The number of received rays and distance between transmitter and receiver determines the spatial resolution and accuracy of the model. This model consumes more power than the image method.

2D and 3D RTM

Depending upon the generation of rays from the sources, two-dimensional and three-dimensional ray tracing method is proposed in the literature. Generally, 2D model [41] is more accurate where the Tx and Rx antenna heights are comparatively lower than the surrounding buildings of the environment and close to the ground. In 3D RTM [42] the transmitter and the receiver are considered as point source and rays are transmitted at all directions in all possible ways to cover the 3D space. Launching of large number of rays makes the model significantly accurate despite the large computational time. Researchers in the literature also propose many advanced versions of the above model.

ii. Numerical Model (FDTD)

In few complex environmental scenarios, the antennas inevitably deployed in location close to a structure having complex material properties does not provide any asymptotic solution of the propagating waves. The solution comes from the numerical approach of the Maxwell's equations specially using FDTD method [43-44]. The method solves the equations for entire target area and provides highly accurate coverage prediction in exceedingly complex environments. This 3D method requires high computational resources, memory, and time. Researchers also proposed 2D and 2.5D FDTD [50-51] model to analyze indoor propagation. This model is also combined with ray-tracing model to propose more advanced, simple and accurate model.

iii. Method of moment Model (MoM)

Method of Moment based numerical approach [52-54] for pathloss prediction is appropriate in comparatively small buildings having large obstacles. Considering the computational constraints, this model is generally used to analyze objects that are as large as around ten times of the operating wavelength. Researchers in the open literature also presented combined model of ray tracing and MoM model. Also, another hybrid model that is an amalgamation of ray-tracing and Periodic Moment Method which is generally used to predict building penetration losses and scattering losses in indoor buildings with periodic structures.

iv. Artificial Neural Network (ANN) Based Model

The main limitations of statistical models, particularly those based on numerical techniques, are that they use a lot of memory, computation time and resources, which results in decreased computational efficiency. The propagation models that were inspired by ANNs are extremely effective and precise. This model is effective at reliably generating statistical channel matrices from a large set of noisy indoor measurement data. In general, the model creates a geometrical database of every indoor space and trains the neural network using common channel matrix formulas. The accuracy of the database affects the model. The researchers have also suggested upgraded versions of this model to get around problems like sluggish convergence of uncertain solution during ANN model training [55-57].

v. Unconventional Models

Many unconventional propagation models [56-60] are observed in the open literature that are based on different propagating field approximation in different scenarios. These models are also found to be extremely efficient in predicting wave propagation in multiple scenarios.

1. Vector-Parabolic Equation Model

To encounter the three-dimensional electromagnetic scattering problem a vector-parabolic model [58] is devised primarily based on the parabolic version of the Maxwell's wave equations. This model is largely applied in outdoor cases in microwave frequencies where scattering phenomenon is largely generated by the sharp edges of a particular building or by a cluster of buildings.

2. Waveguide Structure Mode

The architecture and position of large buildings in metropolitan areas forms guided structure and thus wave propagating in such environment resembles propagation in a waveguide. Thus, researchers developed algorithm and subsequent models [60-61] that can compute fields in those environments. The emulated data is compared with the empirical data of those locations and found to be in good agreement.

3. Far-Field Approximation Model

This is also a numerical technique-based model [59] applied in outdoor scenarios, specifically in high altitude terrain with scattered large buildings. The model requires low computation time with respect to the other numerical techniques specially the models based on Integral techniques. This model is further improved by incorporating the Green's Function perturbation method.

II. Small-scale Fading Models

In a multipath environment signal propagates in different paths and are captured in the receiver end after encountering multiple reflection, diffraction and scattering phenomenon [62]. The prime features of the signal i.e., amplitude, frequency and phase are varied eventually. At the receiver the vector addition of the delayed replicas of the transmitted signals represents the power delay profile of the channel. These changes in received power profile in static and dynamic environment follow specific stochastic distribution process.

A. Rician Distribution

The probability distribution function of the power delay profile in presence of a static dominant receive signal component is represented by the Rician distribution [1, 63]. The closed form representation of the density function is as follows.

$$p(d) = \begin{cases} \frac{d}{\sigma} e^{\left[-\frac{d^2+X^2}{2\sigma^2}\right]} I_0\left(\frac{Xd}{\sigma^2}\right) & X \geq 0, \quad d \geq 0 \\ 0 \quad r < 0 \end{cases} \tag{2.5}$$

where d is the received signal envelope, σ is the mean variance and X is the peak of the dominant signal

B. Rayleigh Distribution

If in the power envelope no dominant path exists, then the statistical distribution is Rayleigh distribution [64]. This is dominant in case of non-line-of-sight propagation. Generally, for cellular communication the power distribution follow Rayleigh distribution. The PDF of the distribution is shown below.

$$p(d) = \begin{cases} \frac{d}{\sigma} e^{\left[-\frac{d^2}{2\sigma^2}\right]} & 0 \le d \le \infty \\ 0 & r < 0 \end{cases} \tag{2.6}$$

C. Log-Normal Fading Model

This is an efficient statistical model that predicts the power profile in specific environments where the transmitted signal encounters several reflections and diffractions. The PDF is shown below [65-66].

$$p(d) = \frac{1}{d\sqrt{2\pi\sigma^2}} e^{\left[-\frac{\ln(d)-p}{2\sigma^2}\right]} \tag{2.7}$$

D. Suzuki Model

It is a hybrid model of Rayleigh and log-normal model that provides much more accurate approximation of the power delay profile of the small-scale fading nature of the channel. This model is suitable for those locations where wide range of environmental variation is observed. This model is invariably used to derive delay profile in very small mobile cells and it is efficient in non LoS scenarios also. The probability density function (PDF) is given below [67].

$$p(d) = \int_0^\infty \frac{d^2}{\sigma^2} e^{\left[-\frac{d^2}{2\sigma^2}\right]} \frac{1}{d\sqrt{2\pi}\sigma s} e^{\left[-\frac{\ln(\sigma)-p}{2\sigma^2}\right]} \tag{2.8}$$

E. Weibull Model

This is a widely accepted indoor small scale fading model [68]. This model is basically a modified envelop plot of the measured receive power profile with respect to Rayleigh plot in a scale where the Rayleigh plot turns out to be a straight line. The PDF is written as below.

$$p(d) = \frac{\alpha b}{d_0}\left(\frac{db}{d_0}\right)^2 e^{\left[-\frac{bd}{d}\right]^2} \tag{2.9}$$

where α is the shape parameter and d_0 is the RMS value of d.

F. Nakagami Model

This statistical model was devised by Nakagami [65] and is the most general representation of all statistical distribution models. The PDF of this model is presented as below.

$$p(d) = \frac{2m^m d^{2m-1} e^{\left[-\frac{m}{\Omega}d^2\right]}}{\Gamma(m)\Omega^m} \tag{2.10}$$

G. Other Fading Models

Researchers found to combine multiple models or distribution and proposed many new hybrid models [69-72] that are much more efficient from many aspects. Rayleigh-Nakagami model, Nakagami-log-normal model and Distributed-K model are few examples.

III. Impulse Response Model

The impulse response approach [73-77] is one of the most sophisticated methods to characterization and model small scale multipath fading channel. This model is suitable for both time and frequency domain approach. The time varying nature of the channel is easily taken care of by this model. In general, the propagation channel can be modeled by linear time variant filter. The time variant nature is due to the receiver motion or due to the relative motion of the environment. The addition of multiple reflected or diffracted waves varies the overall amplitude,

hence causing the filtering effect. The output of the model is attained by convoluting the input signal with the channel impulse response.

In literature researchers conducted extensive measurement campaign in indoor and outdoor environment in both time and frequency domain approach to propose impulse response-based models for different environments.

A. Models Based on Measurements

The key motivation of the channel measurements is to characterize the wireless channels by deriving different frequency and time domain channel matrices and subsequently relate the matrices to devise algorithm or models that can emulate the channel properties in different locations without conducting measurements. Thus, channel measurement is an important and crucial part. In the open literature a significant number of empirical models are discussed. Those models are broadly categorized as follows.

1. Direct Pulse Measurements [78]
2. Spread Spectrum Slide Correlator Measurement [79]
3. Swept Frequency Measurement [80]

The mentioned techniques are discussed in detail in [81].

i. Statistical models of Time-Delay Spread

In a multipath environment signal propagates in diverse paths and reaches at receiver end in varying time instance due to different path lengths. Hence the received power profile envelope is generated where the signal power is plotted against different time instant. This time delay is largely dependent on the recipient of the last delectable, received signal. Important time domain channel matrices are devised from the delay profile such as Excess Delay, RMS delay or time delay spread. In [82] researchers propose channel parameter based on time delay spread.

1. Saleh-Valenzuela Model

Selah and Valenzuela have proposed a deterministic model that essentially predicts and represent the existence of cluster of reflectors in the propagation environment. The model [83]

also shows that statistical behavior of the channel that is independent of the polarization of the terminal antennas in a non-LoS.

2. Delta-K Model

This is an advanced model of Saleh-Valenzuela Model where the group of the scatterers in the propagation path forming multiple clusters in the envelop of the received power profile. The model [84, 85] precisely deals with the statistical variations in different cluster.

3. Log-Normal-Distance

This model [86] is dealt with the relation between RMS Delay Spread and other statistical parameters in urban, rural, and hilly scenarios. Firstly, τ_{rms} is log-normally distributed over distance and increases with shadow fading. Secondly, the mean of τ_{rms} increases with distance.

4. Simulation of Indoor Radio Channel Impulse Response Model (SIRCIM)

It is a measurement based statistical channel model. Mostly in indoor scenarios the small-scale fading nature is captured using the SIRCIM model for the early development of WiFi. This model also supports development of simulation software useful in emulating the indoor scenarios using CIR in a very wide frequency range (10KHz-60GHz). In recent time a similar simulation software i.e., Simulation of Mobile Radio Channel Impulse Response (SMRCIM) is developed by the research group [87] of Rappaport *et. al* for measuring the outdoor channel.

5. Discrete Time Model

In this model the time scale of the PDP is sub-divided into several time blocks. In each bin there may be single multipath component, or the bin remains empty and the possibility of more than one component is excluded in the model [88]. This model efficiently characterizes the time domain statistics of indoor fading channel.

ii. Deterministic Model of time-delay spread

The measurement-based time domain small scale fading models that are discussed so far are only suitable to characterize channels of that environment because the models are majorly site specific. Two such widely accepted models are discussed.

1. Ray tracing Time delay Model

As previously discussed, a 3D ray tracing technique is very efficient to capture all the multipath components in any environment provided that minute details of the environmental structure are available. But the model [89, 90] can't predict the actual delay profile as it varies with distance for different environments. It is also important to mention that this model is capable to incorporate actual antenna parameters and radiation patterns which provide very close approximate results. Researchers also proposed 7-ray or 25-ray [91] models and the predicted delay spread for those models agreed well with the measured ones.

2. Virtual Reflection Point (VRP) Model

This is an extension of the seven-ray model that can be precisely applied in outdoor environment. This is a simple model where several virtual points are assumed at the intersection between different propagating media such as streets or buildings. This model [89] is only suitable for static environment.

IV. Joint Angle-Delay Estimation (JADE)

Most of the models [92] discussed so far primarily consider the time delay effect of the propagating signal to characterize the channel. It is observed that these models are not optimum without incorporating the spatial behavior. Thus, researchers focused on investigating the space and time variation jointly by considering the direction of arrival and angle of arrival of the transmitted signal at the receiver end. Subsequently researchers proposed many advanced variations of the model which are well discussed in the open literature. The variations are i. JADE Maximum- Likelihood Model [93], ii. JADE Music Model [94], iii. SI-JADE Model [95, 96] and iv. JADE-ESPRIT Model [97].

2.1.5 Recent progress in Ultra-Wide Band Channel Characterization

Wireless domain is playing a vital role in the impending heterogeneous network by integrating versatile, multifaceted and critical applications. In indoor scenarios also, wireless connectivity is becoming very crucial now a days. Network coverage enhancement is becoming very important for massive sensor connectivity for IoT services in recent 5G system [98] which necessitates the deployment of large numbers of wireless nodes. Such deployment of many RF devices will make the RF frontend ultra-dense and extremely random in nature, causing unavoidable concerns in the propagation channel [99]. Thus, characterization and modeling of the indoor propagation is highly desirable. Consequently, research on UWB communication has gained a lot of interest in recent time due to large bandwidth, resistance to deep fading, and low power consumption [100]. Thus, it is found that UWB technology is more suited for sophisticated applications like Internet of Things (IoT), sensors, automation, imaging and location detection and ranging of wireless nodes with centimeter-level accuracy [101].

Wide range of UWB channel measurement campaign is carried out to characterize indoor environment and subsequent models are devised in literature [102-110]. It is observed that authors have primarily focused on measurement based deterministic and statistical models. In the recent past, many heuristic approaches have also been proposed for UWB channel modeling [108, 110, 111]. IEEE 802.15.3a is the standardized channel model for indoor UWB communication [112-113] aimed at short-range applications. Contrarily IEEE 802.15.4a is proposed further for channel models for both indoor and outdoor environments with increased coverage. A frequency domain measurement approach is opted in [113] to investigate the path loss and amplitude statistics for LOS and nLOS environments in UWB (1-11GHz). Few significant works on indoor channel modeling based on frequency domain measurement are reported in the literature [114]. Cassoli et al. also presented large- and small-scale indoor channel characterization and modeling in time domain measurement approach [115, 116]. In recent times researchers have largely focused on on-body and off-body channel modeling [117, 118] for body centric communication for defense and medical purposes. Authors also characterize and model wireless channel within Vehicular and aircraft cabin in recent past [119, 120] for high-speed short-range communication. Chia et al. suggest measurement based statistical model in UWB

for high rise residential apartments following the cluster and Multi Path Component (MPC) based approach. Frequency domain autoregressive channel model for indoor environments was first proposed by Kaven et al. [111] and further extended by Ghassemzadeh et al [121]. Authors in those works analyze and model the indoor environments using 2^{nd} and 5^{th} order AR process.

In most of the UWB channel measurement campaigns authors primarily model indoor static channel in prescribed UWB (3.1 to 10.6GHz band) using frequency or time domain approach. It is noted that authors predominantly model the radio channel (propagation channel including terminal equipment effect) instead of propagation channel, where the models are terminal dependent and valid for specific measurement setup [144]. Subsequently, the frequency and time dispersive channel parameters derived from the measured Channel Transfer Functions (CTFs) are found to be erroneous and formulate inaccurate channel models. In few cases authors calibrate the measurement setup in an anechoic chamber to deconvolute the effect of terminal antennas and other active devices [121-124].

2.1.6 Conclusion

The prior information about the impact of the environment on the statistical behavior of the propagating wave is a crucial aspect before designing any trans-receiver system. The study of wireless channels is essential in terms of coverage, SINR and overall data rate prediction in any environment. In this section important large-scale pathloss models along with small scale fading channel models are discussed for indoor and outdoor environment. The evolution of advanced models is also depicted. UWB channel modeling aspects are presented. With the advancement of 5G the operating frequency and bandwidth of the transmitted signals are also increasing. Thus, the propagation of high frequency wideband signals in present ultra-dense network environment needs a comprehensive study prior to devise modems for 5G applications.

It is very important to note that all the models discussed in the literature treat the terminal antenna as isotropic radiator while deriving the channel matrices. But it is known that isotropic radiator does not exist, and the smallest practically realizable antenna has a specific directional property. Thus, terminal antenna used for channel measurement has certain impact on the measured results. Hence an antenna independent channel model is necessary to study to come up with some meaningful physical interpretation of the wireless channel.

References:

[1] T. S. Rappaport, Wireless Communications: Principles & Practice, Upper Saddle River, NJ, Prentice Hall PTR, 1996.

[2] S. D. Chitte, S. Dasgupta and Z. Ding, "Distance Estimation From Received Signal Strength Under Log-Normal Shadowing: Bias and Variance," in IEEE Signal Processing Letters, vol. 16, no. 3, pp. 216-218, March 2009, doi: 10.1109/LSP.2008.2012229.

[3] Kaveh Pahlavan; Prashant Krishnamurthy, "Fundamentals of Physical Layer Transmission," in Networking Fundamentals: Wide, Local and Personal Area Communications , Wiley, 2009, pp.83-124, doi: 10.1002/9780470779422.ch3.

[4] E. R. Magsino, I. W. -H. Ho and Z. Situ, "The effects of dynamic environment on channel frequency response-based indoor positioning," 2017 IEEE 28th Annual International Symposium on Personal, Indoor, and Mobile Radio Communications (PIMRC), 2017, pp. 1-6, doi: 10.1109/PIMRC.2017.8292442.

[5] M. Andersson, C. Orlenius and M. Franzen, "Measuring the Impact of Multiple Terminal Antennas on the Bit Rate of Mobile Broadband Systems Using Reverberation Chambers," 2007 International workshop on Antenna Technology: Small and Smart Antennas Metamaterials and Applications, 2007, pp. 368-371, doi: 10.1109/IWAT.2007.370151.

[6] Andersson, Mats & Orlenius, Charlie & Franzen, Magnus. (2007). Measuring the Impact of Multiple Terminal Antennas on the Bit Rate of Mobile Broadband Systems Using Reverberation Chambers. 368 - 371. 10.1109/IWAT.2007.370151.

[7] B. Yanakiev, J. Ø. Ødum Nielsen, M. Christensen and G. F. Pedersen, "On Small Terminal Antenna Correlation and Impact on MIMO Channel Capacity," in IEEE Transactions on Antennas and Propagation, vol. 60, no. 2, pp. 689-699, Feb. 2012, doi: 10.1109/TAP.2011.2173442.

[8] S. J. Howard and K. Pahlavan, "Measurement and analysis of the indoor radio channel in the frequency domain," in IEEE Transactions on Instrumentation and Measurement, vol. 39, no. 5, pp. 751-755, Oct. 1990, doi: 10.1109/19.58620.

[9] G. R. MacCartney and T. S. Rappaport, "A Flexible Millimeter-Wave Channel Sounder With Absolute Timing," in IEEE Journal on Selected Areas in Communications, vol. 35, no. 6, pp. 1402-1418, June 2017, doi: 10.1109/JSAC.2017.2687838.

[10] G. J. Foshini, "Layered space-time architecture for wireless communication in a fading environment when using multiple antennas", Bell Laboratories Technical Journal 1996, vol. 1, no. 2, pp. 41-59, 1996.

[11] G. Wang, H. Chen, Y. Li and M. Jin, "On received-signal-strength based localization with unknown transmit power and path loss exponent", IEEE Wireless Commun. Lett., vol. 1, no. 5, pp. 536-539, Oct. 2012.

[12] Juan Manuel Castro-Arvizu et al., "Received Signal Strength-Based Indoor Localization Using a Robust Interacting Multiple Model-Extended Kalman Filter Algorithm", International Journal of Distributed Sensor Networks, Aug. 2017.

[13] J. Ying and K. Pahlavan, "Precision of RSS-Based Localization in the IoT", Int J Wireless Inf Networks, vol. 26, pp. 10-23, 2019.

[14] M. Sablatash, R. Tiedemann and K. Moreland, "A Multipath RF Propagation Model for Computer Simulation of Complex Impulse Responses of Broadcast Teletext Channels," in IEEE Journal on Selected Areas in Communications, vol. 5, no. 2, pp. 286-298, February 1987, doi: 10.1109/JSAC.1987.1146538.

[15] R. Jain, "Channel Models A Tutorial" Feb. 2007, available as http://www1.cse.wustl.edu/~jain/cse574-08/ftp/channel-model-tutorial.pdf

[16] H. Hashemi, "Impulse response modeling of indoor radio propagation channels," Selected Areas in Communications, IEEE Journal on , vol.11, no.7, pp.967-978, Sep 1993.

[17] S. J. Howard and K. Pahlavan, "Measurement and analysis of the indoor radio channel in the frequency domain," in IEEE Transactions on Instrumentation and Measurement, vol. 39, no. 5, pp. 751-755, Oct. 1990, doi: 10.1109/19.58620.

[18] G. W. Snedecor and W. G. Cochran, Statistical Methods, IA, Ames:Iowa State University Press, 1976.

[19] A. A. M. Saleh, A. J. Rustako and R. S. Roman, "Distributed antennas for indoor radio communications", IEEE Trans. Communications, vol. COM-35, pp. 1245-1251, Dec. 1987.

[20] D M. J Devasirvatham, "Time delay spread measurements of wideband radio systems within a building", Electron. Lett., pp. 949-950, Nov. 1984.

[21] B. Alavi and K. Pahlavan, "Modeling of the TOA-based distance measurement error using UWB indoor radio measurements," in IEEE Communications Letters, vol. 10, no. 4, pp. 275-277, April 2006, doi: 10.1109/LCOMM.2006.1613745.

[22] R. Ganesh and K. Pahlavan, "On the modeling of fading multipath indoor radio channels," 1989 IEEE Global Telecommunications Conference and Exhibition 'Communications Technology for the 1990s and Beyond', 1989, pp. 1346-1350 vol.3, doi: 10.1109/GLOCOM.1989.64171.

[23] S.L. Cotton and W.G. Scanlon, "Characterization and modeling of on-body spatial diversity within indoor environments at 868 MHz", IEEE Transactions on Wireless Communications, vol. 8, no. l, pp. 14-18, Feb. 2009.

[24] S.L. Cotton, G.A. Conway and W.G. Scanlon, "A Time-Domain Approach to the Analysis and Modeling of On-Body Propagation Characteristics Using Synchronized Measurements at 2.45 GHz", IEEE Transactions on Antennas and Protragation, vol. 57, no. 4, pp. 943, Apr. 2009.

[25] Xinrong Li, K. Pahlavan and J. Beneat, "Performance of TOA estimation techniques in indoor multipath channels," The 13th IEEE International Symposium on Personal, Indoor and Mobile Radio Communications, 2002, pp. 911-915 vol.2, doi: 10.1109/PIMRC.2002.1047354.

[26] K. Haneda, N. Omaki, T. Imai, L. Raschkowski, M. Peter and A. Roivainen, "Frequency-Agile Pathloss Models for Urban Street Canyons," in IEEE Transactions on Antennas and Propagation, vol. 64, no. 5, pp. 1941-1951, May 2016, doi: 10.1109/TAP.2016.2536170.

[27] H. Masui, T. Kobayashi and M. Akaike, "Microwave path-loss modeling in urban line-of-sight environments", IEEE J. Sel. Areas Commun., vol. 20, no. 6, pp. 1151-1155, Aug. 2002.

[28] T.-S. Rappaport, E. Ben-Dor, J.-N. Murdock and Q. Yijun, "38 GHz and 60 GHz angle-dependent propagation for cellular & peer-to-peer wireless communications", Proc. IEEE Int. Conf. Commun. (ICC'12), pp. 4568-4573, Jun. 2012.

[29] A. Sulyman, A. Nassar, M. Samimi, G. MacCartney, T. Rappaport and A. Alsanie, "Radio propagation path loss models for 5G cellular networks in the 28 GHz and 38 GHz millimeter-wave bands", IEEE Commun. Mag., vol. 52, no. 9, pp. 78-86, Sep. 2014.

[30] S. Sun et al., "Investigation of Prediction Accuracy, Sensitivity, and Parameter Stability of Large-Scale Propagation Path Loss Models for 5G Wireless Communications," in IEEE Transactions on Vehicular Technology, vol. 65, no. 5, pp. 2843-2860, May 2016, doi: 10.1109/TVT.2016.2543139.

[31] A. Neskovic, N. Neskovic and G. Paunovic, "Modern approaches in modeling of mobile radio systems propagation environment," in IEEE Communications Surveys & Tutorials, vol. 3, no. 3, pp. 2-12, Third Quarter 2000, doi: 10.1109/COMST.2000.5340727.

[32] R. Bonneau, M. Salazar-Palma, M. Wicks and T. Sarkar, "A Survey of Various Propagation Models for Mobile Communication", Smart Antennas, pp. 239-307, 2005.

[33] K. T. Herring, J. W. Holloway, D. H. Staelin and D. W. Bliss, "Path-Loss characteristics of urban wireless channels", IEEE Transactions on Antennas and Propagation, vol. 58, no. 1, pp. 171-177, 2010.

[34] T. Okumura, E. Ohmori, and K. Fukuda, “Field Strength and its Variability in VHF and UHF Land Mobile Service,” Review Electrical Communication Laboratory, 16, 9-10, 1968, pp. 825-873.

[35] M. Hata, “Empirical Formula for Propagation Loss in Land Mobile Radio Service,” IEEE Transactions on Vehicular Technology, VT-29,3, 1980, pp. 317-325.

[36] J. Waltisch and H. L. Bertoni, “A Theoretical Model of UHF Propagation in Urban Environments,” IEEE Transactions on Antennas and Propagation, AP-36, 12, 1988, pp. 1788-1796.

[37] T. S. Rappaport and L. B. Milstein, “Effect of Radio PropagationPath Loss on DS-CDMA Cellular Frequency Reuse Efficiencyfor the Reverse Channel,’’ IEEE Transactions on Vehicular Technologv, VT41, 3, August 1992, pp. 231-242.

[38] H. Xia, H. L. Bertoni, L. R Maciel, A. Lindsay-Stewart, and R.Rowe, “Radio Propagation Characteristics for Line-of-sight Microcellular and Personal Communications,” IEEE Transactionson Antennas and Propagation, AP-41, 10, October 1993, pp. 1439-1447.

[39] M. J. Feuerstein, K. L Blackard, T. S. Rappaport, S. Y. Seidel; and H. H. Xia, “Path Loss, Delay Spread, and Outage Models as Functions of Antenna Height for Macrocellular System Design,” IEEE Transactions on Vehicular Technology, VT-43, 3, August 1994, pp. 487-498.

[40] S. Ohayashi and J. Zander, “A Body-Shadowing Model for Indoor Radio Communication Environments,” IEEE Transactions on Antennas and Propagation, AP-46,6, 1998, pp. 920-927.

[41] W. Honcbarenko, H. L. Bertoni, and J. Dailing, “Mechanisms Goveming UHF Propagation on Single Floors in Modem Office Buildings,” IEEE Transactions on Antennas and Propagation, AP- 41, 4, 1992, pp. 496-504.

[42] S. Y. Seidel and T. S. Rappaport, “Site-Specific Propagation Prediction for Wireless In-Building Personal Communication System Design,” IEEE Transactions on Vehicular Technology, VT-43, 4, 1994, pp. 879-891.

[43] A. Lauer, 1. Woff, A. Bahr, J. Pamp, J. Kunisch, “Multi-Mode FDTD Simulations of Indoor Propagation Including Antenna Properties,” in Proceedings of the I995 IEEE 45th Vehicular Technology Conference, Chicago, IL, pp. 454-458.

[44] W. Ying, S. Safavi-Naeini, and S. K. Chaudhuri, :’A Hybrid Technique Based on Combining Ray Tracing and FDTD Methods for Site-Specific Modeling of Indoor Radio Wave Propagation,” IEEE Transacrions on Antennas and Propagation, VT-48, 5, May 2000, pp. 743-754.

[45] G. M. Whitman, K. S. Kim, and E. Niver, “A Theoretical Model for Radio Signal Attenuation Inside Buildings,” IEEE Transactions on Vehicular Technology, VT-44, 3, August 1995, pp. 621-629.

[46] J. W. Mckown and R. L. Hamilton, Jr., “Ray Tracing as a Design Tool for Radio Networks,” IEEE Network Magazine, 5, Nov. 1991, pp. 27-30.

[47] F. Villanese, W. G. Scanlon, N. E. Evans, and E. Gamhi, “Hybrid ImageRay-Shooting UHF Radio Propagation Predictorfor Populated Indoor Environments,” Electronics Leffers 35, 21, October 1999, pp. 1804-1805.

[48] K. Rizk, J. F. Wagen, and F. Gardiol, “Two-Dimensional Raytracing Modeling for Propagation Prediction in Microcellular Environments,” IEEE Transactions on Vehicular Technology, VT-46, 2, May 1997,pp. 508-518.

[49] G. M. Whitman, K. S. Kim, and E. A. Niver, “Theoretical Model for Radio Signal Attenuation Inside Buildings,” IEEETransactions on Vehicular Technology, VT-44, 3, August 1995, pp. 621-629.

[50] A. Lauer, 1. Woff, A. Bahr, J. Pamp, J. Kunisch, "Multi-Mode FDTD Simulations of Indoor Propagation Including AntennaProperties," in Proceedings of the I995 IEEE 45th Vehicular Technology Conference, Chicago, IL, pp. 454-458.

[51] W. Ying, S. Safavi-Naeini, and S. K. Chaudhuri, :'A Hybrid Technique Based on Combining Ray Tracing and FDTD Methods for Site-Specific Modeling of Indoor Radio Wave Propagation," IEEE Transacrions on Antennas and Propagation, VT-48, 5, May 2000, pp. 743-754.

[52] C. Yang, B. Wu, and C. KO, "A Ray-Tracing Method for Modeling Indoor Wave Propagation and Penetration," IEEE Transactions on Antennas andPropagation, VT-46,6, June 1998, pp. 907-919.

[53] B. De Backer, H. Bojeson, F. Olyslager, and D. De Zutter, "The Study of Wave-Propagation through a Windowed Wall at 1.8 GHz," IEEE 46th Vehicular Technology Conference, 1, 1996, pp. 165-1 69.

[54] Z. Sandor, L. Nagy, 2. Szabo, and T. Csaba, "3D Ray Launching and Moment Method for Indoor Propagation Purposes,"The 8th IEEE International Symposium on Personal, Indoor and Mobile Radio Communicafions, 1997, PIMRC '97, 1, pp. 130 134.

[55] A. Neskovic and D. Paumovic, "Indoor Electric Field Level Prediction Model Based on the Artificial Neural Networks," ZEEE Communicalions Letters, 4, 6,2000, pp. 190-192.

[56] K. E. Stocker, B. E. Gschwendtner, and F. M. Landstorfer, ''Neural Network Approach to Prediction of Terrestrial WavePropagation for Mobile Radio," ZEE Proceedings H Microwaves, Antennas andt'ropagation, 140,4, August 1993, pp. 315-320.

[57] P. Chang and W. Yang, "Environment-Adaptation Mobile Radio Propagation Prediction Using Radial Basis Function NeuralNetworks," IEEE Transactions on Vehicular Technologv, VT-46, I, February 1997, pp, 155-160.

[58] A. A. Zaporozhets, "Application of Vector Parabolic Equation Method to Urban Radiowave Propagation Problems," ZEE Proceedings - Microwaves, Antennas and Propagation, 146,4, August 1999, pp. 253-256.

[59] C. Brennan and P. J. Cullen, "Application of the Fast Far-field Approximation to the Computation of UHF Path Loss Over Irregular Terrain," IEEE Transactions on Antennas and Propagation, AP-46,6, June 1998, pp. 881-890.

[60] R. Mazar and A. Bronshtein, “Propagation Model of a City Slreet for Personal and Microcellular Communications,” Electronics Letters, 33; 1, January 1991, pp. 91-92.

[61] N. Blaunstein, “Average Field Attenuation in the Street Waveguide,” IEEE Transactions on Antennas and Propagation, AP-46,12, December 1998, pp. 1782-1789.

[62] T. K. Sarkar et. al., Smart Antennas, New York, John Wiley and Sons, March 2003.

[63] L. J. Greenstein, D. G. Michelson, and V. Erceg, “Moment- Method Estimation of the Ricean K-factor,” IEEE Communications Letters, 3,6, June 1999, pp. 175-176.

[64] V. Fung, T. S. Rappaport, and B. Thomas, “Bit Error Simulation for pi 14 DQPSK Mobile Radio Communications Using Tworay and Measurement-based Impulse Response Models,” IEEE Journal on Selected Areas in Communications, 11, 3, April 1993, pp. 393-405.

[65] C. C. Hess, Handbook of Land-Mobile Radio System Coverage, Norwood, MA, Anech House, Inc.

[66] A. Safak, “Statistical Analysis of the Power Sum of Multiple Correlated Lognormal Components,” ZEEE Transactions onVehicular Technology, VT-42, 1, February 1993, pp. 58-61.

[67] H. Suzuki, “A Statistical Model for Urban Radio Propagation,” IEEE Transactions on Communications, COM-25, 1977, pp. 673- 680.

[68] IEEE Vehicular Technology Society Committee on Radio Propagation, “Coverage Prediction for Mobile Radio Systems Operating in the 8001900 MHz Frequency Range,” IEEE Transactions on Vehicular Technology, VT-37, 1, February 1988, pp. 3-72.

[69] A. Abdi and M. Kaveh, “K Distribution: An Appropriate Substitute for Rayleigb-lognormal Distribution in Fading-Shadowing Wireless Channels,” Electronics Letters, 34, 9, April 1998, pp. 851-852.

[70] G. E. Corazza and F. Vatalaro, “A Statistical Model for Land Mobile, Satellite Channels and its Application to Nongeostationary Orbit Systems,” IEEE Transactions on Vehicular Technology, VT- 43, August 1994, pp. 738-741.

[71] P. G. Babalis and C. N. Capsalis, “Impact of the Combined Slow and Fast Fading Channel Characteristics on the Symbol Error Probability for Multipath Dispersionless Channel Characterized by a Small Number of Dominant Paths,” IEEE Transactions on Communications, COM-47, 5, May 1999, pp. 653-657.

[72] D. S. Polydorou and C. N. Capsalis, “A New Theoretical Model for the Prediction of Rapid Fading Variations in Indoor Environment,” IEEE Transactions on Vehicular Technology, VT- 46, August 1997, pp. 748-755.

[73] S. Kozono and A. Taguchi, “Mobile Propagation Loss and Delay Spread Characteristics with a Low Base Station Antenna on an Urban Road,” IEEE Transactions on Vehicular Technology, VT-42, 1, 1993,pp. 103-109.

[74] J. A. Wepman, J. R. Hoffman, and L. H. Loew, “Analysis of Impulse Response Measurements for PCS Channel Modeling Applications,” IEEE Transactions on Vehicular Technology, VT- 44,3,1995, pp. 613-620.

[75] C. L. Holloway, M. G. Cotton, and P. McKenna, “A Model for Predicting the Power Delay Profile Characteristics Inside a Room,” IEEE Transactions on Vehicular Technology, VT-48, 4, 1999, pp. 1110-1120.

[76] P.E. Driessen, “Prediction of Multipath Delay Profiles in Mountainous Terrain,” IEEE Joumal on Selected Areas in Communications, 18,3,2000, pp. 336-346.

[77] Y. Li, “A Theoretical Formulation for the Distribution Density of Multipath Delay Spread in a Land Mobile Radio Environment,” IEEE Transactions on Vehicular Technology, VT-43, 2, 1994, pp. 379-388.

[78] T. S. Rappaport, "Characterization of UHF multipath radio channels in factory buildings," in IEEE Transactions on Antennas and Propagation, vol. 37, no. 8, pp. 1058-1069, Aug. 1989, doi: 10.1109/8.34144.

[79] Dixon, R. C., Spread Spectrum Systems, 2nd Edition, John Wiley and Sons, New York, 1984.

[80] H. Zaghloul, G. Morrison, M. Fattouche, “Frequency response and path loss measurements in indoor channel, Electronics Litters, Vol. 27, No. 12, pp. 1021-1022, June 1991.

[81] V. Erceg, L. Greenstein, S. Tjandra, S. Parkoff, A. Gupta, B. Kulic, et al., "An empirically based path loss model for wireless channels in suburban environments", IEEE J. Select. Areas Commun., vol. 17, pp. 1205-1211, July 1999.

[82] https://www.itu.int/dms_pubrec/itu-r/rec/p/R-REC-P.1407-6-201706-I!!PDF-E.pdf

[83] A. A. M. Saleh and R. L. Valenzuela, “A Statistical Model for Indoor Multipath Propagation,” IEEE Journal on Selected Areas in Communications, 5,2, 1987, pp. 128-137.

[84] G. L. Turin, "A Statistical Model for Urban Multipath Propagation," IEEE Transactions on Vehicular Technology, VT-21, 1, 1972, pp. 1-9.

[85] H. Hashemi, "Impulse Response Modeling of Indoor Radio Propagation Channels," IEEE Journal on Selected Areas in Communications, 11, 7, September 1993, pp. 967-978.

[86] L. J. Greenstein, V. Erceg, Y. S. Yeh, and M. V. Clark, "A New Path-Gain/Delay-Spread Propagation Model for Digital Cellular Channels," IEEE Transactions on Vehicular Technology, VT-46,2, May 1997, pp. 477-485.

[87] T. S. Rappaport, S. Y. Seidel, and K. Takamizawa, "Statistical Channel Impulse Response Models for Factory and Open Plan IEEE Antennas and Propagation Magazine. Vol. 45, No. 3, June 2003 Building Radio Communicate System Design," IEEE Transactions on Communications, COM-39,5, May 1991, pp. 794-807.

[89] T. Taga, T. Furuno, and K. Suwa, "Channel Modeling for 2- GHz-band Urban Line-of-sight Street Microcells," IEEE Transactions on Vehicular Technology, VT-48, 1, January 1999, pp. 262- 272.

[88] R. Ganesb and K. Pahlavan, "Statistical Modelling and Computer Simulation of Indoor Radio Channel," IEE Proceedings I Communications, Speech and Vision, 138, 3, June 1991, pp. 153- 161.

[90] G. E. Athanasiadou, A. R. Nix, and J. P. McGeehan, "A Microcellular Ray-tracing Propagation Model and Evaluation of its Narrow-Band and Wide-Band predictions," IEEE Journal on Selected Areas in Communications, 18, 3, March 2000 pp. 322-335.

[91] R. J. C. Bultitude, P. Melancon, H. Zaghloul, G. Morrison, and M. Prokki, "The Dependence of Indoor Radio Channel Multipath Characteristics of Transmimeceiver Ranges," IEEE Journal on Selected Areas in Communications. 11. 7. SeDtember1993 pp. 979-990.

[92] M. C. Vanderveen, C. B. Papadias, and A. Paulraj, "Joint Angle and Delay Estimation (JADE) for Multipath Signals Aniving at an Antenna Array," IEEE Communicatiow Letters, 1, 1, January 1997, pp. 12 -14.

[93] M. Wax and A. Leshem, "Joint Estimation of Time Delays and Directions of Anival of Multiple Reflections of a Known Signal," IEEE Transactions on Signal Processing, SP-45, IO, October 1997, pp. 2477-2484.

[94] M. C. Vanderveen, C. B. Papadias, and A. Paulraj, “Joint Angle and Delay Estimation (JADE) for Multipath Signals Arriving at an Antenna Array,” IEEE Communicatiow Letters, 1, 1, January 1997, pp. 12 -14.

[95] A. J. van der Veen, M. C. Vanderveen, and A. J. Paulraj, “Joint Angle and Delay Estimation Using Shift-invariance Properties,” IEEE Signal Processing Letters, 4, 5, May 1997, pp. 142- 145.

[96] A. J. van der Veen, M. C. Vanderveen, and A. J. Paulraj, “Joint Angle and Delay Estimation Using Shift-Invariance Techniques,” IEEE Transactions on Signal Processing, SP-46, 2, February 1998, pp. 405-418.

[97] M. C. Vanderveen, A. J. Van der Veen, and A. Paulraj, “Estimation of Multipath Parameters in Wireless Communications,”IEEE Transactions on Signal Processing, SP-46, 3, March 1998, pp. 682-690.

[98] M. Alsabah et al., "6G Wireless Communications Networks: A Comprehensive Survey," in IEEE Access, vol. 9, pp. 148191-148243, 2021, doi: 10.1109/ACCESS.2021.3124812.

[99] J. Liu, M. Sheng, L. Liu and J. Li, "Interference Management in Ultra-Dense Networks: Challenges and Approaches," in IEEE Network, vol. 31, no. 6, pp. 70-77, November/December 2017, doi: 10.1109/MNET.2017.1700052.

[100] Y. Rahayu, T. A. Rahman, R. Ngah and P. S. Hall, "Ultra wideband technology and its applications," 2008 5th IFIP International Conference on Wireless and Optical Communications Networks (WOCN '08), 2008, pp. 1-5, doi: 10.1109/WOCN.2008.4542537.

[101] S. van Roy, C. Oestges, F. Horlin and P. De Doncker, "A Comprehensive Channel Model for UWB Multisensor Multiantenna Body Area Networks," in IEEE Transactions on Antennas and Propagation, vol. 58, no. 1, pp. 163-170, Jan. 2010, doi: 10.1109/TAP.2009.2036280.

[102] F. Zhu, Z. Wu, and C. Nassar, “Generalized fading channel model with application to UWB,” in Proc. IEEE Conference on Ultra WidebandSystems and Technologies, pp. 13-17, May 2002.

[103] D. Cassioli, M. Win, and A. Molisch, “A statistical model for the UWB indoorchannel,” in Proc. IEEE Vehicular Technologies Conf., vol. 2, pp.1159-1163, May 2001.

[104] D. Cassioli, M. Win, and A. Molisch, “The ultra-wide bandwidth indoor channel: From statistical model to simulations,” IEEE J. Select. Areas Commun., vol. 20, no. 6, pp. 1247-1257, Aug. 2002.

[105] S. Chalillou, D. Helal, and C. Cattaneo,” Timed simulator for UWB communication systems,” in Proc. IEEE Conference on Ultra Wide band Systems and Technologies, pp. 6-11, May 2002.

[106] R. Cramer, R. A. Scholtz, and M. Z. Win, “Evaluation of an ultra-wideband propagation channel,” IEEE Trans. Antennas Propagat., vol.50, no. 5, pp. 561-570, May 2002.

[107] Taylor, J. D. (1995), Introduction to Ultra-Wideband Rada Systems, CRC Press, Boca Raton, Fla.

[108] S. S. Ghassemzadeh, R. Jana, C. W. Rice, W. Turin and V. Tarokh, "Measurement and modeling of an ultra-wide bandwidth indoor channel," in IEEE Transactions on Communications, vol. 52, no. 10, pp. 1786-1796, Oct. 2004, doi: 10.1109/TCOMM.2003.820755.

[109] A. Dezfooliyan and A. M. Weiner, "Evaluation of Time Domain Propagation Measurements of UWB Systems Using Spread Spectrum Channel Sounding," in IEEE Transactions on Antennas and Propagation, vol. 60, no. 10, pp. 4855-4865, Oct. 2012, doi:10.1109/TAP.2012.2207358.

[110] B. M. Donlan, D. R. McKinstry and R. M. Buehrer, "The UWB indoor channel: large and small scale modeling," in IEEE Transactions on Wireless Communications, vol. 5, no. 10, pp. 2863-2873, Oct. 2006, doi: 10.1109/TWC.2006.04482.

[111] S. J. Howard and K. Pahlavan, "Autoregressive modeling of wide-band indoor radio propagation," in IEEE Transactions on Communications, vol. 40, no. 9, pp. 1540-1552, Sept. 1992, doi: 10.1109/26.163575.

[112] Federal Communication Commission, "Revision of Part 15 of the Commission'2 rules Regarding Ultra-Wideband Transmission System: First order and report" Technical Report FCC 02-48, (April 2002).

[113] R. Cardinali, L. De Nardis, P. Lombardo and M.. -G. Di Benedetto, "UWB ranging accuracy for applications within IEEE 802.15.3a," 2nd International Workshop Networking with Ultra Wide Band and Workshop on Ultra Wide Band for Sensor

Networks, 2005. Networking with UWB 2005., 2005, pp. 65-69, doi: 10.1109/NETUWB.2005.1470004.

[114] H. Hashemi, “The indoor propagation channel,” Proc. IEEE, vol. 81, pp. 943–968, July 1993.

[115] D. Cassioli, M. Win, and A. Molisch, “The ultra-wide bandwidth indoor channel: From statistical model to simulations,” IEEE J. Select. Areas Commun., vol. 20, no. 6, pp. 1247-1257, Aug. 2002.

[116] S. Chalillou, D. Helal, and C. Cattaneo, ”Timed simulator for UWB communication systems,” in Proc. IEEE Conference on Ultra Wide band Systems and Technologies, pp. 6-11, May 2002.

[117] T. S. P. See and Z. N. Chen, "Experimental Characterization of UWB Antennas for On-Body Communications," in IEEE Transactions on Antennas and Propagation, vol. 57, no. 4, pp. 866-874, April 2009, doi: 10.1109/TAP.2009.2014595.

[118] A. Sani et al., "Experimental Characterization of UWB On-Body Radio Channel in Indoor Environment Considering Different Antennas," in IEEE Transactions on Antennas and Propagation, vol. 58, no. 1, pp. 238-241, Jan. 2010, doi: 10.1109/TAP.2009.2024969.

[119] S. Chiu, J. Chuang and D. G. Michelson, "Characterization of UWB Channel Impulse Responses Within the Passenger Cabin of a Boeing 737-200 Aircraft," in IEEE Transactions on Antennas and Propagation, vol. 58, no. 3, pp. 935-945, March 2010, doi: 10.1109/TAP.2009.2037707.

[120] O. P. Pasquero and R. D’Errico, "A Spatial Model of the UWB Off-Body Channel in Indoor Environments," in IEEE Transactions on Antennas and Propagation, vol. 64, no. 9, pp. 3981-3989, Sept. 2016, doi: 10.1109/TAP.2016.2588582.

[121] S. S. Ghassemzadeh, R. Jana, C. W. Rice, W. Turin and V. Tarokh, "Measurement and modeling of an ultra-wide bandwidth indoor channel," in IEEE Transactions on Communications, vol. 52, no. 10, pp. 1786-1796, Oct. 2004, doi: 10.1109/TCOMM.2003.820755.

[122] A. Alvarez, G. Valera, M. Lobeira, R. P. Torres and J. L. Garcia, "Ultra wideband channel model for indoor environments," in Journal of Communications and Networks, vol. 5, no. 4, pp. 309-318, Dec. 2003, doi: 10.1109/JCN.2003.6596613.

[123] C. Briso, C. Calvo and Y. Xu, "UWB Propagation Measurements and Modelling in Large Indoor Environments," in IEEE Access, vol. 7, pp. 41913-41920, 2019, doi: 10.1109/ACCESS.2019.2905142.

[124] A. Chandra et al., "Frequency-Domain In-Vehicle UWB Channel Modeling," in IEEE Transactions on Vehicular Technology, vol. 65, no. 6, pp. 3929-3940, June 2016, doi: 10.1109/TVT.2016.2550626.

Chapter 2B
Literature Review- Reconfigurable Antennas

2.2.1 Introduction

With the increasing user requirements and massive proliferation of wireless devices to cater to advanced applications, researchers had to think beyond the conventional antennas and opt for multifunctional antennas as relevant alternative. However, researchers have to deal with various constraints such as antenna impedance bandwidth, radiation pattern, polarization, antenna footprint, operating band, etc. for practical realization of such unorthodox antennas. Those limitations drive the researchers to consider multifunctional antennas which can change available reconfigurable states as per system requirement. Thus, antenna agility provides additional degrees of freedom to the system designers along with signal processing and communication domain. Antenna reconfigurability is achieved by incorporating electronic switches (Varactor diodes, PIN diodes, Field Effect Transistor (FET), etc.), mechanical means (changing antenna parameters physically), or electromechanical switches (Micro-Electrico-Mechanical-System, MEMS). Chronological development of reconfigurable antenna till date has been studied in this chapter. An emphasis on the applicability and requirement of 5G reconfigurable antennas is also presented.

2.2.2 Reconfigurable Antennas and its importance

Antenna reconfigurability is termed as the capacity to change the operating features by using electrical, mechanical, and other means [1-2]. The reconfigurable antenna matrices are as mentioned.

1. Frequency of Operation
2. Polarization of the propagating wave
3. Radiation pattern of the far-filed wave

Those parameters are tuned alone, or in any combination in accordance with the system requirement, the process being termed as hybrid reconfigurability.

Electromagnetic spectrum is getting congested due to the rapid deployment of wireless nodes in impending heterogenous network environment. Cognitive radio and antenna reconfigurability have been investigated largely to counter these challenges. Cognitive radio scans the available spectrum and allocates the unused frequency bands to the trans-receiver system. This imposes critical limitations as the antenna system doesn't have any prior information about the spectrum availability and hence it is not possible to design agile antennas in the live RF links. On the other hand, a reconfigurable antenna with multiple reconfigurable states can be employed to counter those challenges by suitably changing the available states as per requirement. Also multiband, or wideband antennas are not suitable replacement of the frequency reconfigurable antennas as the co-channel noise automatically gets cancelled due to specific operating frequency and hence the filter requirement in the trans-receiver circuit is nullified largely.

2.2.3 Development of Reconfigurable Antenna

Ab initio, the idea of antenna reconfigurability arose from the requirement to integrate multiple services in different reconfigurable state. An antenna can simply be reconfigured by altering either the physical geometry or by changing the electrical properties. R. E Webster investigated [3] one of the earliest reconfigurable antennae where the impedance bandwidth of an electrically small antenna was improved by tuning the impedance bandwidth using a tunable reactive element. Wanselow et al. [4] explored a wide frequency tunable antenna at around 50MHz. Seth and Chow studied [5] and suggested the first antenna pattern reconfigurability using varactor diodes in a Yagi-Uda antenna. Itoh and Herbert [6] examine pattern reconfigurability of a leaky wave antenna applying mechanically tuned switches. The application of antenna reconfigurability in satellite communication was also investigated [7]. The initial frequency tunability for microstrip patch antennas is studied by Schaubert [8] where the author used tunable screws and tuned the operating frequency. In this work authors also reported the variation in polarization. Bhartia et al [9] was the first to change the resonant frequency in microstrip patch antenna using varactor diode. The applied reverse bias voltage across the diode was varied to change the varactor capacitance which in turn altered the reactance of the path

eventually changing the resonant frequency of the antenna. In a stacked patch the frequency tunability was first introduced by Lee at al [10]. They varied the stack profile mechanically that changes the overall effective permittivity which in turn shifted the resonant frequency.

In initial research, mechanical switching was used largely for multi-functional antennas. With the gradual development in communication scenarios the antennas needed to work in a very fast switching scenarios where the existing techniques fell short to meet the stringent requirement. Thus, researchers introduced electronic or MEMS switches in the design of reconfigurable antennas.

I. Electro-Mechanical Switch

Micros-electro-Mechanical system (MEMS) in parallel with VLSI has evolved and are used to design complex integrated circuits with significantly reduced size, low loss which consume comparatively less power [11]. Despite high switching time this device is being used extensively in designing reconfigurable antennas. A detailed survey on frequency and pattern reconfigurable antennas based on MEMS switch is presented in the following sections. The MEMS RF switches have low insertion loss and high isolation which made it an obvious choice for researchers while designing low loss antennas. It also requires very less operating power. It exhibits large switching time and very high actuation voltage nearly 260V which limits its use in high frequency switching and low power scenarios.

A. Frequency Reconfigurability

In [12] the frequency reconfigurability of a microstrip dipole antenna was obtained by manipulating the length of the antenna sides using cantilever MEMS switch. Interconnected MEMS switches are used in a 3×3 patch array for dual band frequency reconfigurability in [13]. MEMS actuators were used in [14] to shift the resonant frequency between two switchable operating bands by changing the capacitance value (by turning ON/OFF the MEMS actuator). MEMS switches are also incorporated in the antenna design to achieve pattern reconfigurability along with frequency tuning. Jefre et al. [15] has proposed a MEMS based frequency and pattern agile antenna. By controlling the slot length using MEMS switches in the planar antenna the frequency of operation is altered in many research articles. In fractal antenna geometries the

lengths are varied using the switches and thereby the operating frequency is also varied. Gotei et al. has studied [16] a MEMS based Co-Planar Waveguide (CPW) fed frequency reconfigurable planar antenna. The resonant frequency was varied by applied voltage in the MEMS switches that changes the effective permittivity and hence shifted the resonances. Boyel et al [17] proposed a Penta-band reconfigurable antenna by incorporating an external matching circuitry. A continuous frequency tuning operating is discussed in [18] where MEMS switches with CPW stub are arranged in periodic fashion.

B. Pattern Reconfigurability

Chiao et all. was the first to investigate MEMS based pattern reconfigurable antennas where the antenna arms are shifted to realize beam steerability. Pattern reconfigurability in CPW fed and square patch antennas are also discussed in [19]. A planar spiral antenna was proposed in [20] to steer the radiated beam from broadside to endfire direction using a RF MEMS switch. The internal electric field distributions are manipulated to attain the pattern reconfigurability. Parasitic loaded slotted Yagi-Uda array was proposed in [21] for beam reconfigurability. Concentric annular ring based planar antenna connected using MEMS switch was proposed to generate broadside radiation and broadside null subsequently by keeping the switches in ON and OFF modes respectively.

II. Electronically switchable Antennas

Despite several advantages, low switching speed, high operating voltage and complex packaging restrict the real time application of MEMS switches [30-34]. These challenges are largely alleviated by electronics switches such as FETs, varactor, or PIN diodes. The application of these switches in designing of reconfigurable antennas are discussed in the subsequent sections [22].

A. PIN Diodes

PIN diodes are advantageous in terms of fast-switching speed along with low insertion loss and high isolation. The diode closely behaves like actual switches simply by using forward

and reverse bias states. Thus, these diodes are incorporated in the reconfigurable antennas to activate or disconnect any specific part of the antenna and thereby alter the antenna properties.

i. Frequency Reconfigurability

The prime idea to change the resonant frequency of an antenna is to change the length of the resonant path. Researchers used PIN diodes extensively in this purpose. Lin et al. proposed ring radiator loaded frequency [23] reconfigurable antenna. A Yagi-Uda dipole array was investigated by Cia et al. [24] for frequency reconfigurable application simply by changing the electrical length of the director and driven elements. In [25] a hepta-band folded dipole antenna was discussed. The same group of researchers has worked on increasing the operating bandwidth by precisely overlapping the shifted resonances. In [26] Hamid et al. investigated a bandwidth reconfigurable Vivaldi Antenna. Later, the same group extended their work and used PIN switches precisely to operate the antenna in narrow and wide bands [27-28]. In [29] a quad-band reconfigurable planar antenna was proposed where the PIN switches alternately excited the inverted L and patch antenna to attain four different resonant frequencies. Zhang et al. has studied [30] a planar monopole structure where three PIN switches were used to excite multiple armed branches that generated six resonances. Frequency agile antennas generating frequency bands for Personal Communication Systems (PCS) and WiBro were also explored in [31] where the ground slits were switched using PINs to excite those frequencies. A continuous frequency tunable rectangular patch antenna with 1.85 tuning ratio is investigated in [32]. The antenna is loaded using shorting posts using PIN diode thereby altering the reactive load and subsequently the resonance frequencies. Frequency and pattern reconfigurable annular ring antenna were proposed in [33] where the radial stubs were switched to change the input impedance and subsequently shifts the resonances of the antenna.

ii. Pattern Reconfigurability

The idea of pattern reconfigurability is to excite multiple radiators having different radiation pattern using PIN switching. On the other way the radiation pattern can be altered by reconfiguring the antenna by suitable coupling or decoupling parasitic elements using PIN diodes. For example, Kang et al. [34] demonstrated pattern reconfigurability by alternately

exciting dipole and loop antenna modes. Also, Luis et al. [35] proposed a novel dual band reconfigurable antenna where a U-shaped patch was attached to a rectangular patch antenna. Subsequently, each radiator was excited as per requirement using connected PIN switches to attain different patterns. A square patch antenna with switchable broadside and directed conical radiation pattern was investigated by Liu et al. [36] where four plates around the patch were coupled or decoupled as per requirement by PIN diodes to attain two distinct radiation patterns. A simple pattern reconfigurability was achieved in [37] where a Yagi-Uda antenna with two-sided directors was investigated. PIN diodes were connected at each director and alternately turned ON to switch the beam direction. An interesting study of pattern reconfigurability is investigated in [38] where a metallic cavity with radiating slots in each side was used to alter the beam at different directions using PIN diodes. The diode connected at each slot was shorted by tuning it ON thereby restricting the radiation from that slot.

The initial requirement of high-speed RF PIN diode as switching element was sensed to attain fast beam switching in phased array antennas. The phase of the radiating elements (incorporating the self-reactance of diode) was respectively changed to switch the main beam. A microcontroller based hexagonal patch for pattern diversity was studied in [39]. The patch was loaded with six parasitic elements shorted with the ground using vias and PIN diodes. The vias were shorted as per requirement to change the surface current distribution on the antenna that altered the radiation pattern.

iii. Polarization Reconfigurability

By suitably changing the orientation of surface current distribution on the radiating element the polarization of the far-field radiated wave can be altered. Researchers in the literature has opted different techniques for this purpose using PIN diodes. A corner-cut rectangular patch with two center cross slots was designed by Nishamol et al. [40] to excite both LP states with RHCP state using PIN switches. Orthogonal modes of the path antenna were generated by suitably biasing the PIN diodes to realize these three distinct polarization states [41]. A quadra-polarization reconfigurable aperture coupled planar antenna is investigated in [42] where dual circular and linear polarization states were realized using reconfigurable microstrip feed lines connected with branch line couplers using PIN diodes. The authors of the previous work have extended the work further and proposed an efficient polarization

reconfigurable antenna [43] where they incorporated external phase shifter to get $\pi/2$ phase difference. Scott et al. [44] proposed a polarization agile loop antenna where a PIN switch were turned ON and OFF respectively to generate standing and travelling waves that initiated Vertical and Circular polarization states. In a different study [45] the authors proposed an annular slot antenna with quad-polarization agility. Using PIN switch, the perturbation along 45° and 45°+π were added to generate CP states, whereas the perturbations are shorted using PIN diodes to initiate LP states. The sense of rotation of the CP states were realized by properly switching the perturbation angles at 45°, 45°+$\pi/2$, 45°+π and 45°+$3\pi/2$ respectively. A corner-truncated patch antenna for polarization diversity was studied [63] where the truncated corners were coupled and decoupled using PIN diodes to generate LP and CP states respectively.

B. Varactor Diode

In few recent applications, continuous tuning of operating frequency or beam scanning in both the principal planes are desirable. The capacitance of a varactor diode is varied in accordance with the reverse DC bias voltage which in turn varies the reactive load and corresponding phase. Researchers have started the usage of this diode to design continuous frequency and pattern tunable antennas for versatile indoor and outdoor applications. Despite its high tuning ability, the prerequisite of large bias voltage limits its use in low power systems. Reconfigurable antennas based on varactor diode are discussed below.

i. Frequency Reconfigurability

A frequency tunable CPW fed planar monopole was discussed in [46] where authors used varactor and PIN diodes simultaneously. A 5GHz tuning range was attained by the varactor diode whereas the PIN was used to get UWB and notched band response. A reconfigurable slot loaded elliptical shaped monopole antenna was investigated in [47] where the varactor was placed across the slot to get wide tuning range between 5-6GHz frequency. In [48] a dual slot loaded planar antenna was studied where varactor and PIN diodes are incorporated. PIN diode was used to switch between the two slots whereas the varactor was placed to tune the operating frequency. Xiong et al. [49] proposed a differentially fed microstrip antenna with frequency reconfigurable capability. A precise feeding scheme was used to tackle the coupling issues of the

patch antenna for a wide range of frequency band. Formal et al. studied a cross slot patch antenna having 10% tuning range [50]. A probe fed patch was presented in [51] where varactor diode was placed at the center of the patch to attain 16% tuning range.

ii. Pattern Reconfigurability

A reconfigurable reflecting surface was investigated in [64] where numerous square patches were periodically arranged. The varactor diodes are placed in-between to realize phase gradient by the variable reactive load of the diodes to scan the beam within ±40° in the elevation plane. A reflector array having 30 patch elements was designed in [65] to attain continuous scanning along 2π azimuth and ±40º elevation plane. Varactor diodes were placed along the aperture coupled feed lines. The bias voltage was varied to alter the feed line impedance and eventually the phase of the reflector antenna. Thus, the phase gradient of the array elements allows the radiated beam to scan in both the principal planes. A Frequency Selective Surface based Artificial Magnetic Conductor was placed in conjunction with bow-tie antenna to realize frequency and pattern diversity [66]. The AMC structure was fabricated on a grounded dielectric slab and the varactor diodes were placed within the metal structures. The diode bias voltage was changed to attain frequency tuning whereas the polarity of the bias voltage was reversed to alter the beam direction.

iii. Polarization Reconfigurability

A dual fed square ring antenna was proposed by Tsai et al. [52] for frequency and polarization reconfigurable antenna where two varactor diodes were place in the feeding system. By varying the bias voltages, the reactive load was varied that changed the polarization states between one LP to dual CP states. A quasi-lumped coupler fed microstrip patch antenna for polarization diversity application was devised in [53].

C. Field Effect Transistor (FET)

Field Effect Transistors also have attractive discrete switching features at RF range. It is a voltage-controlled device and operated with low bias voltage. It has also fast switching speed which make this component very useful in designing reconfigurable antennas, though large

insertion loss and complex biasing limits its application in antenna domain. Kawasaki et al. [54] has suggested a frequency tunable planar slot antenna using FET switch for the first time. Two FETs were placed under the slots and biased alternately to attain 10% frequency tuning. In [55] a capacitively loaded and electrically small Planar Inverted F antenna (PIFA) is investigated for frequency tuning application using GaAs FET switch. Multiple shorting plates/plate-straps were used to connect the radiator with the ground via the FETs. The FET switches were biased accordingly to make the straps either shorted or in floating state that in turn varied the operating frequency. A quad band reconfigurable circular monopole antenna was studies in [56]. Four stubs are used in the design that were coupled or decoupled using two Single Pole Double Throw (SPDT) switch. FETs were biased accordingly to attain four discreate operating bands by the proposed antenna. Shinoda et al. [57] studied and proposed a beam scanning planar antenna using FET switch.

2.2.4 Reconfigurability using Liquid Crystal Device (LCD), Ferro-Electric and Ferrite Material

It is widely observed that reconfigurability of antenna parameters can be attained by altering the antenna dimensions, reactive loads and electrical parameters such as surface current/internal electric fields. Additionally, by changing the material properties permittivity or permeability, the antenna parameters can be manipulated as per requirement. Few materials such as Liquid Crystal substrate, Ferrite and Ferro-electric materials change its material properties in the proximity of electric or magnetic field. Few works on antenna reconfigurability based on those materials are presented below.

The first proposal of frequency reconfigurable antenna based on Ferrite substrate was investigated in [58] where a patch antenna was biased using magnetic fields aligned in three axial directions along the ferrite substrate of the prototype antenna. A two element microstrip array was analyzed in [59] for pattern reconfigurable application using Ferrite substrate. The relative phase between the two elements was altered using the applied DC magnetic field along the ferrite substrate that eventually steered the mean in a specific direction. Das et al. proposed a ten-element phased array antenna using ferrite substrate [60]. The phase difference between the elements was realized by using a non-linear transmission line that provide different time delay in

the input signal and thus varying phase. An interesting observation was found in the study by Pourush et al. [61] where a six-by-six patch array was fabricated using a ferrite substrate for frequency agile application. It was noted that antennas based on ferrite substrate can operate within specific frequency range having certain cut off and resonant limitation. Ferro-Electric substrates were used in few cases in the literature to design antennas for beam scanning application. By applying proper bias, the permittivity of the material was altered which changed the phase constant and subsequently the phase different between the antenna elements. This method eventually steered the beam to certain direction to mitigate co-channel and Inter symbol interference. In [61], ferro-electric materials were used to create phase difference between two patch array elements by suitably biasing the ferroelectric substrate to scan the radiated beam in the broadside direction. Material properties of Liquid Crystal was also changed by applying electric field across it. In [62] the radiation pattern of a reflect array mono-pulse antenna is constructively and destructively added in the far-filed for pattern reconfigurable application. An inverted microstrip line-based polarization reconfigurable antenna was investigated in [63] where the applied bias voltage varied the relative permittivity of the liquid crystal substrate which eventually altered the phase between the two different feed networks of the antenna. Thus, the differential phase ultimately defined the required polarization.

2.2.5 Reconfigurable Antennas – Recent Trends and Shortcomings

A paradigm shift in the communication domain has been noticed in the last few years. Frequency, polarization and patterns are reconfigured to make antennas more compact and suitable for diverse applications. To cater those diverse application the cellular domain has evolved in 5G. Researchers from all communities specially from RF, Signal processing, Communication and Data Networking are contributing significantly to make the network architecture capable to withstand the upcoming challenges. In antenna community also researchers are primarily working in the same direction. A brief literature review of recent published works on muti functional antennas are discussed below.

I. Frequency and Polarization Reconfigurability

Z. Nei *et al*., proposed a frequency-polarization agile AMC based monopole MSA [64] with multilayer structure using dual coax feed. A compact tri-polarized continuous frequency tuning at dual frequency band MSA was studied in [65]. In [66], a multilayer, complex feed, high profile liquid metal based reshapable aperture antenna was proposed. Dual band quad-polarized and dual polarized large MSA with low gain was presented in [67-68]. Meta-surface inspired planar multilayer large slot antennas were proposed in [69] for frequency-polarization agile application. Capacitively Loaded Loops (CLL) was used in the proximity of a planar monopole antenna as the near-field resonant parasitic elements to attain frequency and polarization reconfigurable antenna in [72]. Probably a single article on penta-polarization agile antenna operating in a single frequency band was proposed so far in the literature [70]. It was a multilayer, meta-surface inspired cross slot MSA excited with a complex feed structure. Authors also propose prototypes having different polarizations in different bands for cognitive radio and career aggregation (CA) in Long Term Evolution (LTE) systems [71].

A switchable polarizer was used in [73] for dual CP generation. Hu et al., [74] proposed stacked multilayer complex SIW cavity structure for quad-polarization applications. A complex feed, large profile multilayer slot antenna for tri-polarization agility was studied in [75]. Differentially fed single layered patch operating at dual compressed higher-order modes was proposed for wideband, high gain applications with dual reconfigurable CP [76]. Multilayer and complex orthogonal SIW fed MSA for adjustable polarization was proposed in [77]. The higher-order mode antenna array was proposed for high gain applications with very complex feed networks and multi-layer structures [78-80]. H. Tran et al., presented a complex multilayer high gain quad linear polarization diversity MSA [82]. S.K Koul et al., [81] prescribed a design with different polarization states operating at different frequencies which can be useful in Career Aggregations (CA) in LTE or 5G but would not be suitable for mitigating channel interference. The most recent techniques that are studied for designing multifunctional antennas such as meta-surface [84], liquid conductor antennas [85], surface plasmonic [83] are with noticeable inadequacies for practical and industrial applications.

II. Frequency and Pattern Reconfigurability

Mostly, Phased Array Antenna (PAA) was proposed for beam steering applications. Though multiple antenna elements, phase shifters (with inherent losses) and composite signal processing units makes the PAA's bulky, lossy and expensive [86]. Microstrip Yagi antennas were also suggested in the literature but limited to discrete and 1-D scanning with significantly large footprint area [87-88]. Multiple Input and Multiple Output (MIMO) technique was also studied extensively in the last few years for beamforming applications in fixed or multiple frequency bands. However, these bulky multiport structures exhibit low antenna efficiency due to strong inter-elemental cross coupling hence confines its performance and applications [89]. Dielectric resonator antenna (DRAs) and Quasi-planar dielectric stacked patch array (DP) were also proposed for wide frequency tuning and beam scanning application [90-91]. These 3D antennas also exhibit exceedingly low gain and limited to discrete or 1-D beam scanning. In general, Leaky Wave antennas (LWA) attain beam scanning capability with varying frequency. In few recent proposals LWAs with coplanar waveguide (CPW) or Fabry–Perot structure are proposed for fixed frequency and continuous beam scanning applications [92]. Digitally coded or reconfigurable metasurfaces are also introduced to achieve dynamic beam scanning and frequency tunibility [93-94] Most recently, periodic structures or high impedance surfaces such as SRR (Split Ring Resonator), EBG (Electromagnetic Band Gap), FSS (Frequency Selective Surfaces) and AMCs (Artificial Magnetic Conductor) are also fused in the design to achieve frequency and pattern agility in antenna systems [95-100]. The Gain enhancement in planar antennas on the other hand is always a desirable feature. Many interesting methods are already discussed in the open literature regarding this. In several cases researchers prescribed antennas operating in higher order modes to increase the gain [101-103]. Most of the works reported so far have dealt with 1-D and 2-D beam scanning in fixed, multi and continuous tunable frequency bands with certain inherent flaws such as structural complexities, multilayer high-profile designs along with complex feeding and large footprint area. Also, these antennas exhibit severe gain instability in the beam-scanning and frequency tuning range. The complex multilayered structure and critical biasing network [104] placed additional constraints on the practical realization of those proposed antennas.

The important observation is that all the recently proposed antennas with advanced techniques suffer from several unavoidable complications. Firstly, most of the antennas are

having multilayer high profile bulky structures which impose significant difficulties in antenna fabrication. Secondly, most of the antennas are having multiple feed ports which trouble system integration or interfacing the antenna with other devices in the trans-receiver system. Thirdly, the electro-mechanical mechanism to control the liquid metal in reconfigurable liquid antennas is extremely cumbersome. Finally, the asymmetric structure with a complex feed network and large footprint area imposes difficulties for practical realization.

III. High gain planar antennas (Special focus on planar antennas operating at higher order modes)

Array configurations can be used to increase antenna gain [105] at the cost of complex feed network. Superstrate loaded patch antennas [106, 107] choose substrate-superstrate resonance gain condition for the gain enhancement. The availability and cost of high permittivity substrates is an issue in this case. Low permittivity multilayer structure [108, 109] can be used as directive antennas with an expense of increased antenna profile and loss of conformity. Zero index material slabs were also used to concentrate the radiated energy from the source antenna [110, 111] and thus increase gain with fabrication complexities and low bandwidth. The application of partially refractive surfaces (PRS) as antenna superstrate [112] results in Fabry-Perot cavity (FPC) antennas are having high gain applications with increased antenna profile and narrow bandwidth. Using an artificial magnetic conductor (AMC) as a ground plane, the antenna profile can also be reduced [113, 114]. AMC and PRS together used for further profile reduction [115-118] and gain enhancement. Patch stacking is a widely used technique to enhance impedance bandwidth. In some cases, it was used for gain enhancement too [119, 120] at the cost of increasing the antenna profile. Fractal boundaries behave like an array by accumulating local current elements and exhibit high directivity when localized modes are in phase [121, 122]. However, these structures have complex geometries producing high Side Lobe Level (SLL). Leaky wave antennas (LWAs) based on modulated meta-surfaces can provide higher gain but [123-124] suffers from low-aperture efficiency, higher edge losses, and design complexities. Patches operating in Higher-Order Modes (HOMs) are another technique to enhance antenna gain because of larger electrical size than that of its fundamental mode counterpart [125]. This approach can efficiently mitigate both fabrication tolerance and low gain issues. But high SLL

that is primarily caused by enlarged spacing between two radiating slots of patch operating in HOM makes this approach less attractive. SLL can be reduced by decreasing the overall size of the patch at resonance that can be attained by increasing the permittivity of substrate [126]. Though this technique suffers due to increased Q factor, hence narrow impedance bandwidth. The SLL of a rectangular patch operating in TM_{30} mode [127] is improved by incorporating two slots near the two radiating edges at the cost of low gain (6.8 dB) due to miniaturized radiating area at resonance. In Reference [128], an annular concentric ring working in TM_{11} is used with a circular patch working on TM_{13} mode, while in [129] and [130], a narrow radiating slot is introduced in the middle of the TM_{12} mode patch. Thus, radiation pattern of these structures is modified by superposing far-field patterns of the modes responsible for SLL reduction. The techniques are useful for the E-plane pattern only [131]. A square patch operating in TM_{03} mode was proposed in Reference [132] for gain enhancement, side-lobe reduction, and beamwidth adjustment by reshaping the surface current distribution on the patch resonator using rectangular slots. An orthogonally placed cross slot patch operating in TM_{50} was reported in [133] for dual polarized application. A compressed HOM patch antenna was proposed for enhanced gain-bandwidth and dual polarized application at the cost of multiple coaxial feed. Partially notch loaded patch antennas with E-plane reduced SLL and enhanced gain, operated in TM_{30} and TM_{70} modes respectively [134] have been proposed by removing the out of phase surface current patch sections. Similar approach has been chosen in [135] to reduce SLL for TM_{30} and TM_{50} mode antennas using single and multiple slots respectively. A low grating lobe 1 × 8 array antenna was proposed in [136] based on TM_{50} mode square patch antenna elements using transverse slots at the cost of complex Substrate Integrated Coaxial Line (SICL) feed producing only E-plane pattern variation and large aperture area. A high gain and low grating lobe electrically large 2 × 2 array antenna were proposed using FPC [137] having large profile and multilayer structure. In [138], equivalent amplitude distribution of input power to the antenna elements of a 9 × 9 array has been proposed to attain low SLL with an expanse of complex feed and array synthesis.

The important observation is that all the recently proposed antennas with advanced techniques suffer from several unavoidable complications. Firstly, most of the antennas are having multilayer high profile bulky structures which impose significant difficulties in antenna fabrication. Secondly, most of the antennas are having multiple feed ports which trouble system integration or interfacing the antenna with other devices in the trans-receiver system. Thirdly, the

electro-mechanical mechanism to control the liquid metal in reconfigurable liquid antennas is extremely cumbersome. Finally, the asymmetric structure with a complex feed network and large footprint area imposes difficulties for practical realization.

2.2.6 Conclusion

A detail review of the research works on multifunctional antennas is presented in this chapter. Reconfigurable antenna concepts have been investigated for a number of years but still it is an emerging area to incubate advance applications. Multiple switching techniques are discussed to generate antenna reconfigurability. The challenges of those switches are also discussed. A brief discussion on the recent trend in antenna reconfigurability is also presented. The drawbacks and limitations of recently proposed antennas are also discussed but at the same time antennas agility stands out to be lucrative technique to overcome numerous upcoming issues in 5G UDN environment. It should also be observed that the precise design of such prototype antennas requires appropriate skill to get desired performances despite of complex biasing, high insertion loss of the switches and so on. It is also noticed in the literature that the requirement of reconfigurable antennas in recent is very crucial and subsequent research in this domain is highly appreciable.

References:

[1] J.T. Bernhard, Reconfigurable Antennas, Morgan and Claypool, 2007.

[2] Sima Noghanian; Satish K. Sharma, "Compact Reconfigurable Antennas," in Multifunctional Antennas and Arrays for Wireless Communication Systems , IEEE, 2021, pp.198-231, doi: 10.1002/9781119535096.ch6.

[3] R.E. Webster, “A Single-Control Tuning Circuit for Electrically Small Antennas,” IEEE Transactions on Antennas and Propagation, vol. 3, no. 1, pp. 12 – 15, 1955.

[4] R.D. Wanselow and D. Milligan, “A Compact, Low Profile, Transmission Line Antenna – Tunable over Greater than Octave Bandwidth,” IEEE Transactions on Antennas and Propagation, vol. 14, no. 6, pp. 701 – 707, 1966.

[5] D. Seth and Y. L. Chow, "An Electrically Tunable Yagi Array," International Symposium on Antennas and Propagation Society, vol. 10, pp. 85 – 88, 1972.

[6] T. Itoh and A.S. Herbert, "Simulation Study of Electronically Scannable Antennas and Tunable Filters Integrated in a Quasi – Planar Dielectric Waveguide," IEEE Transactions on Microwave Theory and Techniques, vol. 26, no. 12, pp. 987 – 991, 1978.

[7] P.J.B. Clarricoats. "Reconfigurable Mesh Reflector Antennas – A Review," IEE Colloquium for Reflector Antennas, pp. 1 – 8, 1992.

[8] D.H. Schaubert, F.G. Farrar, A. Sindoris and S.T. Hayes, "Microstrip Antennas with Frequency Agility and Polarization Diversity," IEEE Transactions on Antennas and Propagation, vol. 29, no. 1, pp. 118 – 123, 1981.

[9] P. Bhartia and I. Bahl, "A Frequency Agile Microstrip Antenna," International Symposium on Antennas and Propagation Society, vol. 20 , pp. 304 – 307, 1982.

[10] J.S. Dahele and K.F. Lee, "A Tunable Dual-Frequency Stacked Microstrip Antenna," International Symposium on Antennas and Propagation Society, vol. 20, pp. 308 – 311, 1982

[11] E.R. Brown, "RF-MEMS Switches for Reconfigurable Integrated Circuits," IEEE Transactions on Microwave Theory and Techniques, vol. 56, no. 11, pp. 1868 – 1880, 1998.

[12] J.H. Schaffner, R.Y. Loo, D.F. Sievenpiper, F.A. Dolezal, G.L. Tangonan, J.S. Colburn and J.J. Lynch, "Reconfigurable aperture antennas using RF MEMS switches for multi-octave tunability and beam steering," IEEE International Symposium on Antennas and Propagation Society, vol. 1, pp. 321 – 324, 2000.

[13] W.H. Weedon, W.J. Payne and G.M. Rebeiz, "MEMS-Switched Reconfigurable Antennas," IEEE International Symposium on Antennas and Propagation Society, vol. 3, pp. 654 – 657, 2001.

[14] R.N. Simons, D. Chun and L.D. Katehi, "Microelectromechanical systems (MEMS) actuators for antenna reconfigurability," IEEE MTTS International Microwave Symposium Digest, vol. 1, pp. 215 – 218, 2001.

[15] L. Jofre, B.A. Cetiner and F.D. Flaviis, "Miniature Multi-Element Antenna for Wireless Communications," IEEE Transactions on Antennas and Propagation, vol. 50, no. 5, pp. 658 – 669, 2002.

[16] R.V. Goteti, R.E. Jackson Jr., R. Ramadoss, "MEMS-Based Frequency Switchable Microstrip Patch Antenna Fabricated Using Printed Circuit Processing Techniques," IEEE Antennas and Wireless Propagation Letters, vol. 5, pp. 228 – 230, 2006.

[17] K.R. Boyle and P.G. Steeneken, "A Five-Band Reconfigurable PIFA for Mobile Phones," IEEE Transactions on Antennas and Propagation, vol. 55, no. 11, pp. 3300 – 3309, 2007.

[18] E. Erdil, K. Topalli, M. Unlu, O.A. Civi and T. Akin, "Frequency Tunable Microstrip Patch Antenna Using RF MEMS Technology," IEEE Transactions on Antennas and Propagation, vol. 55, no. 4, pp. 1193 – 1196, 2007.

[19] B.A. Cetiner, J.Y. Qian, H.P. Chang, M. Bachman, G.P. Li and F. De Flaviis, "Monolithic Integration of RF MEMS Switches With a Diversity Antenna on a PCB Substrate," IEEE Transactions on Microwave Theory and Techniques, vol. 51, no. 1, pp. 332 – 335, 2003.

[20] G. Huff and J.T. Bernhard, "Integration of Packaged RF MEMS Switches With Radiation Pattern Reconfigurable Square Spiral Microstrip Antennas," IEEE Transactions on Antennas and Propagation, vol. 54, no. 2, pp. 464 – 469, 2006.

[21] L. Petit, L. Dussopt and J-M. Laheurte, "MEMS-Switched Parasitic-Antenna Array For Radiation Pattern Diversity," IEEE Transactions on Antennas and Propagation, vol. 54, no. 9, pp. 2624 – 2631, 2006.

[22] G.M. Rebeiz, RF MEMS Theory, Design and Technology, Wiley Interscience, John Wiley and Sons, New Jersey, 2003.

[23] Y.-Y. Lin and T.-G. Ma, "Frequency-Reconfigurable Self-Oscillating Active Antenna With Gap-loaded Ring Radiator," IEEE Antennas and Wireless Propagation Letters, vol. 12, pp. 337– 340, 2013

[24] Y. Cai, Y. J. Guo, and P.-Y. Qin, "Frequency Switchable Printed Yagi-Uda Dipole Sub-Array for Base Station Antennas," IEEE Transactions on Antennas and Propagation, vol. 60, no. 3, pp. 1639 – 1643, 2012.

[25] Y. Li, Z. Zhang, J. Zheng and Z. Fang, "Compact Hepta band Reconfigurable Loop Antenna for Mobile Handset," IEEE Antennas and Wireless Propagation Letters, vol. 10, pp. 1162 – 1165, 2011.

[26] M.R. Hamid, P.S. Hall, P. Gardner and F. Ghanem, "Switchable Filtering in Vivaldi Antenna," Electronics Letters, vol. 46, no.7, pp. 477 – 478, 2010.

[27] M.R. Hamid, P. Gardner, P.S. Hall and F. Ghanem, “Switched-Band Vivaldi Antenna,” IEEE Transactions on Antennas and Propagation, vol. 59, no. 5, pp. 1472 – 1480, 2011.

[28] M.R. Hamid, P. Gardner, P.S. Hall and F. Ghanem, “Vivaldi Antenna With Integrated Switchable Band Pass Resonator,” IEEE Transactions on Antennas and Propagation, vol. 59, no. 5, pp. 1472 – 1480, 2011.

[29] Y. Li, Z. Zhang, W. Chen, Z. Feng and M.F. Iskander, “A Quadband Antenna With Reconfigurable Feedings,” IEEE Antennas and Wireless Propagation Letters, vol. 8, pp. 1069 – 1071, 2009.

[30] C. Zhang, S. Yang, S. El-Ghazaly, A.E. Fathy and V.K. Nair, “A Low-Profile Branched Monopole Laptop Reconfigurable Multiband Antenna for Wireless Applications,” IEEE Antennas and Wireless Propagation Letters, vol. 8, pp. 216 – 219, 2009.

[31] S.-B. Byun, J.-A. Lee, J.-H. Lim, and T.-Y. Yun, “Reconfigurable Ground –Slotted Patch Antenna Using Pin Diode Switching,” ETRI Journal, vol. 29, no. 6, pp. 832 – 834, 2007.

[32] A.-F. Sheta and S.F. Mahmoud, “A Widely Tunable Compact Patch Antenna,” IEEE Antennas and Wireless Propagation Letters, vol. 7, pp. 40 – 42, 2008.

[33] C. -Y. -D. Sim, T. -Y. Han and Y. -J. Liao, "A Frequency Reconfigurable Half Annular Ring Slot Antenna Design," in IEEE Transactions on Antennas and Propagation, vol. 62, no. 6, pp. 3428-3431, June 2014, doi: 10.1109/TAP.2014.2314314.

[34] W. Kang, S. Lee and K. Kim, “A Pattern Reconfigurable Antenna Using PIN Diodes,” Microwave and Optical Technology Letters, vol. 53, no. 8, pp. 1883 – 1887, 2011.

[35] J.R. De Luis and F. De Flaviis, “Frequency Agile Switched Beam Antenna Array System,” IEEE Transactions on Antennas and Propagation, vol. 58, no. 10, pp. 3196 – 3204, 2010.

[36] W.-L. Liu, T.-R. Chen, S.-H. Chen and J.-S. Row, “Reconfigurable Microstrip Antenna with Pattern and Polarization Diversities,” Electronics Letters, vol. 43, no.2, pp. 77 – 78, 2007.

[37] S. Lim and H. Ling, “Design of Electrically Small, Pattern Reconfigurable Antenna,” Electronics Letters, vol. 43, no.24, pp. 1326 – 1327, 2007.

[38] J. Sarrazin, Y. Mahe, S. Avrillon and S. Toutain, “Pattern Reconfigurable Cubic Antenna,” IEEE Transactions on Antennas and Propagation, vol. 57, no. 2, pp. 310 – 317, 2009.

[39] W. H. Chen, J. W. Sun, X. Wang, Z. H. Feng, F. L. Chen, Y. Furuya, and A. Kuramoto, “A Novel Planar Switched Parasitic Array Antenna With Steered Conical Pattern,” IEEE Transactions on Antennas and Propagation, vol. 55, no. 6, pp. 1883 – 1887, 2007.

[40] M. S. Nishamol, V. P. Sarin, D. Tony, C. K. Aanandan, P. Mohanan, and K. Vasudevan, "An Electronically Reconfigurable Microstrip Antenna With Switchable Slots for Polarization Diversity," IEEE Transactions on Antennas and Propagation, vol. 59, no. 9, pp. 3424– 3427, 2011.

[41] P.-Y. Qin, A. R. Weily, Y. J. Guo, and C.-H. Liang, "Polarization Reconfigurable U-Slot Patch Antenna," IEEE Transactions on Antennas and Propagation, vol. 58, no. 10, pp. 3383–3388, 2010.

[42] Y.-F. Wu, C.-H. Wu, D.-Y Lai, and F.-C. Chen, "A Reconfigurable Quadri-Polarization Diversity Aperture-Coupled Patch Antenna," IEEE Transactions on Antennas and Propagation, vol. 55, no. 3, pp. 1009– 1012, 2007.

[43] S.-Y. Wang, D.-Y Lai, and F.-C. Chen, "A Low-Profile Switchable Quadripolarization Diversity Aperture-Coupled Patch Antenna," IEEE Antennas and Wireless Propagation Letters, vol. 8, pp. 522 – 524, 2009.

[44] H.Scott and V.F. Fusco, "Polarization Agile Circular Wire Loop Antenna," IEEE Antennas and Wireless Propagation Letters, vol. 1, pp. 64 – 66, 2002.

[45] M.K. Fries, M. Grani and R. Vahldieck, "A Reconfigurable Slot Antenna with Switchable Polarization," IEEE Microwave and Wireless Components Letters, vol. 13, no. 11, pp. 490 – 492, 2003.

[46] S. A. Aghdam, "Reconfigurable Antenna With a Diversity Filtering Band Feature Utilizing Active Devices for Communication Systems," IEEE Transactions on Antennas and Propagation, vol. 61, no. 10, pp. 5223– 5228, 2013.

[47] E. Erfani, J. Nourinia, C. Ghobadi, M. N.-Jazi and T.A. Denidni, "Design and Implementation of an Integrated UWB/Reconfigurable-Slot Antenna for Cognitive Radio Applications," IEEE Antennas and Wireless Propagation Letters, vol. 11, pp. 77– 80, 2012.

[48] N. Behdad and K. Sarabandi, "A varactor-tuned dual-band slot antenna," in IEEE Transactions on Antennas and Propagation, vol. 54, no. 2, pp. 401-408, Feb. 2006, doi: 10.1109/TAP.2005.863373.

[49] S.V. Hum and H.Y. Xiong, "Analysis and Design of a Differentially-Fed Frequency Agile Microstrip Patch Antenna," IEEE Transactions on Antennas and Propagation, vol. 58, no. 10, pp. 3122– 3130, 2010.

[50] M.A. Forman and Z. B. Popovic, "A Tunable Second Resonance Cross Slot Antenna," International Symposium on Antennas and Propagation, vol. 1, pp. 18 – 21, 1997.

[51] S.H. Al-Charchafchi and M. Frances, "Electronically Tunable Microstrip Patch Antennas," International Symposium on Antennas and Propagation, vol. 1, pp. 304 – 307, 1998.

[52] J.-F. Tsai and J.-S. Row, "Reconfigurable Square-Ring Microstrip Antenna," IEEE Transactions on Antennas and Propagation, vol. 61, no. 5, pp. 2857– 2860, 2013.

[53] F. Ferrero, C. Luxey, R. Staraj, G, Jacquemod, M. Yedlin, and V. Fusco, "A Novel Quad-Polarization Agile Patch Antenna," IEEE Transactions on Antennas and Propagation, vol. 57, no. 5, pp. 1562– 1566, 2009.

[54] S. Kawasaki and T. Itoh, "A Slot Antenna with Electronically Tunable Length," IEEE Antennas and Propagation Society International Symposium, vol. 1, pp. 130 - 133, 1991.

[55] L.M. Feldner, C.T. Rodenbeck, C.G. Christodoulou and N. Kinzie, "Electrically Small Frequency-Agile PIFA-as-a- Package for Portable Wireless Devices," IEEE Transactions on Antennas and Propagation, vol. 55, no. 11, pp. 3310– 3319, 2007.

[56] T. Aboufoul, A. Alomainy and C. Parini, "Reconfiguring UWB Monopole Antenna for Cognitive Radio Applications Using GaAs FET Switches," IEEE Antennas and Wireless Propagation Letters, vol. 11, pp. 392– 394, 2012.

[57] Y. Monnai and H. Shinoda, "Focus-Scanning Leaky-Wave Antenna With Electronically Pattern-Tunable Scatterers," IEEE Transactions on Antennas and Propagation, vol. 59, no. 6, pp. 2070–2077, 2011.

[58] D.M. Pozar and V. Sanchez, "Magnetic Tuning of a Microstrip Antenna on a Ferrite Substrate," Electronics Letters, vol. 24, no. 12, pp. 729 -731, 1988.

[59] J.C. Batchelor and R.J. Langley, "Beam Scanning Using Microstrip Lne on Biased Ferrite," Electronics Letters, vol. 33, no. 8, pp. 645- 646, 1997.

[60] N. Das and A.K. Ray, "Magneto Optical Technique for Beam Steering by Ferrite Based Patch Arrays," IEEE Transactions on Antennas and Propagation, vol. 49, no. 8, pp. 1239– 1242, 2001.

[61] R. Pourush, G.S. Tyagi, G.P. Srivastava and P.K.S. Pourush, "Radiation Performance of Switchable Ferrite Microstrip Array Antenna," IEEE Antennas and Wireless Propagation Letters, vol. 5, pp. 195– 198, 2006.

[62] W. Hu, M.Y. Ismail, R. Cahill, J.A. Encinar, V.F. Fusco, H.S. Gamble, D. Linton, R. Dickie, N. Grant and S.P. Rea, “Liquid-Crystal-Based Reflectarray Antenna with Electronically Switchable Monopulse Patterns,” Electronics Letters, vol. 43, no. 14, pp. 744-745, 2007.

[63] O.H. Karabey, S. Bildik, S. Bausch, S. Strunck, A. Gaebler and R. Jakoby, “Continuously Polarization Agile Antenna by Using Liquid Crystal-Based Tunable Variable Delay Lines,” IEEE Transactions on Antennas and Propagation, vol. 61, no. 1, pp. 70–76, 2013.

[64] Z. Nie, H. Zhai, L. Liu, J. Li, D. Hu and J. Shi, "A Dual-Polarized Frequency-Reconfigurable Low-Profile Antenna with Harmonic Suppression for 5G Application," in IEEE Antennas and Wireless Propagation Letters, vol. 18, no. 6, pp. 1228-1232, June 2019, doi: 10.1109/LAWP.2019.2913170.

[65] M. Ikram, N. Nguyen-Trong and A. Abbosh, "A Simple Single-Layered Continuous Frequency and Polarization-Reconfigurable Patch Antenna Array," in IEEE Transactions on Antennas and Propagation, vol. 68, no. 6, pp. 4991-4996, June 2020, doi: 10.1109/TAP.2019.2952461.

[66] V. T. Bharambe, J. Ma, M. D. Dickey and J. J. Adams, "RESHAPE: A Liquid Metal-Based Reshapable Aperture for Compound Frequency, Pattern, and Polarization Reconfiguration," in IEEE Transactions on Antennas and Propagation, vol. 69, no. 5, pp. 2581-2594, May 2021, doi: 10.1109/TAP.2020.3037803. [67] Selvam, Y. P., Elumalai, L., Alsath, M. G. N., Kanagasabai, M., Subbaraj, S. and Kingsly, S.: "Novel Frequency- and Pattern-Reconfigurable Rhombic Patch Antenna With Switchable Polarization," in IEEE Antennas and Wireless Propagation Letters, vol. 16, pp. 1639-1642, 2017, doi: 10.1109/LAWP.2017.2660069.

[68] P. Kumar, S. Dwari, R. K. Saini and M. K. Mandal, "Dual-Band Dual-Sense Polarization Reconfigurable Circularly Polarized Antenna," in IEEE Antennas and Wireless Propagation Letters, vol. 18, no. 1, pp. 64-68, Jan. 2019, doi: 10.1109/LAWP.2018.2880799.

[69] C. Ni, M. S. Chen, Z. X. Zhang and X. L. Wu, "Design of Frequency-and Polarization-Reconfigurable Antenna Based on the Polarization Conversion Metasurface," in IEEE Antennas and Wireless Propagation Letters, vol. 17, no. 1, pp. 78-81, Jan. 2018, doi: 10.1109/LAWP.2017.2775444.

[70] P. Liu, W. Jiang, S. Sun, Y. Xi and S. Gong, "Broadband and Low-Profile Penta-Polarization Reconfigurable Metamaterial Antenna," in IEEE Access, vol. 8, pp. 21823-21831, 2020, doi: 10.1109/ACCESS.2020.2969488.

[71] R. K. Singh, A. Basu and S. K. Koul, "A Novel Reconfigurable Microstrip Patch Antenna With Polarization Agility in Two Switchable Frequency Bands," in IEEE Transactions on Antennas and Propagation, vol. 66, no. 10, pp. 5608-5613, Oct. 2018, doi: 10.1109/TAP.2018.2860118.

[72] M. Fakharian, Mohammad, Rezaei Pejman,. and Ali A Orouji,.: "A Multi-Reconfigurable CLL-Loaded Planar Monopole Antenna." Radioengineering 29, no. 2 (2020).

[73] P. Jacob, A. S. Madhukumar and A. Alphones, "Interference Mitigation through Cross Polarized Transmission inFemto-Macro Network," IEEE Communications Letters, vol. 17, no. 10, pp. 1940-1943, October 2013, doi: 10.1109/LCOMM.2013.090213.131482..

[74] J. Hu, Z.Haoand W. Hong, "Design of a Wideband Quad-Polarization Reconfigurable Patch Antenna Array Using a Stacked Structure," IEEE Transactions on Antennas and Propagation, vol. 65, no. 6, pp. 3014-3023, June 2017,doi: 10.1109/TAP.2017.2695529.

[75] N. Zhu, X. Yang, T. Lou, Q. Cao and S.Gao, "Broadband Polarization-Reconfigurable Slot Antenna and Array With Compact Feed Network," IEEE Antennas and Wireless Propagation Letters, vol. 18, no. 6, pp. 1293-1297, June 2019,doi: 10.1109/LAWP.2019.2915650.

[76] Y.Luo, Z. N. Chen and K. Ma, "A Single-Layer Dual-Polarized Differentially Fed Patch Antenna With Enhanced Gain and Bandwidth Operating at Dual Compressed High-Order Modes Using Characteristic Mode Analysis," IEEE Transactions on Antennas and Propagation, vol. 68, no. 5, pp. 4082-4087, May 2020,doi: 10.1109/TAP.2019.2951536.

[77] F. Ren, W. Hong, K. Wu, D. Yu and Y. Wan, "Polarization-Adjustable Planar Array Antenna With SIW-Fed High-Order-Mode Microstrip Patch," IEEE Transactions on Antennas and Propagation, vol. 65, no. 11, pp. 6167-6172, Nov. 2017, doi: 10.1109/TAP.2017.2756686.

[78] Y. Zhang et al., "High-Gain Circularly Polarized Array Antenna With Low Grating Lobe Property Based on TM30/TM03 Mode," IEEE Antennas and Wireless Propagation Letters, vol. 20, no. 3, pp. 401-405, March 2021, doi: 10.1109/LAWP.2021.3052915.

[81] R. K. Singh, A. Basu and S. K. Koul, "A Novel Reconfigurable Microstrip Patch Antenna with Polarization Agility in Two Switchable Frequency Bands," IEEE Transactions on

Antennas and Propagation, vol. 66, no. 10, pp. 5608-5613, Oct. 2018, doi: 10.1109/TAP.2018.2860118.

[82] H. H. Tran, N. Nguyen-Trong, T. T. Le, A. M. Abbosh and H. C. Park, "Low-Profile Wideband High-Gain Reconfigurable Antenna With Quad-Polarization Diversity," IEEE Transactions on Antennas and Propagation, vol. 66, no. 7, pp. 3741-3746, July 2018, doi: 10.1109/TAP.2018.2826657.

[83] M. Wang, H. C. Wang, S. C.Tian, H. F. Ma and T. J. Cui, "Spatial Multi-Polarized Leaky-Wave Antenna Based on Spoof Surface Plasmon Polaritons," IEEE Transactions on Antennas and Propagation, vol. 68, no. 12, pp. 8168-8173, Dec. 2020,doi: 10.1109/TAP.2020.2997471.

[84] A. Pitilakis et al., "A Multi-Functional Reconfigurable Metasurface: Electromagnetic Design Accounting for Fabrication Aspects," in IEEE Transactions on Antennas and Propagation, vol. 69, no. 3, pp. 1440-1454, March 2021, doi: 10.1109/TAP.2020.3016479.

[85] J. Ren et al., "Radiation Pattern and Polarization Reconfigurable Antenna Using Dielectric Liquid," in IEEE Transactions on Antennas and Propagation, vol. 68, no. 12, pp. 8174-8179, Dec. 2020, doi: 10.1109/TAP.2020.2996811.

[86] A. Ludvig-Osipov, J. -M. Hannula, P. Naccachian and B. L. G. Jonsson, "Physical Limitations of Phased Array Antennas," in IEEE Transactions on Antennas and Propagation, vol. 69, no. 9, pp. 5512-5523, Sept. 2021, doi: 10.1109/TAP.2021.3069485.

[87] J. Shi, L. Zhu, N. -W. Liu and W. Wu, "A Microstrip Yagi Antenna With an Enlarged Beam Tilt Angle via a Slot-Loaded Patch Reflector and Pin-Loaded Patch Directors," in IEEE Antennas and Wireless Propagation Letters, vol. 18, no. 4, pp. 679-683, April 2019, doi: 10.1109/LAWP.2019.2901033.

[88] J. Shi, L. Zhu, N. -W. Liu and W. Wu, "Design Approach for a Microstrip Yagi Antenna With a Switched Beam Using Resonant TM10 and TM20 Modes," in IEEE Access, vol. 8, pp. 224365-224371, 2020, doi: 10.1109/ACCESS.2020.3043596.

[89] X. Chen, S. Zhang and Q. Li, "A Review of Mutual Coupling in MIMO Systems," in IEEE Access, vol. 6, pp. 24706-24719, 2018, doi: 10.1109/ACCESS.2018.2830653.

[90] I. Gharbi, R. Barrak, M. Menif, J. M. Ribero, A. Diallo and H. Ragad, "High gain patch antenna array using dielectric superstrate for the 5G applications," 2019 IEEE 19th

Mediterranean Microwave Symposium (MMS), 2019, pp. 1-4, doi: 10.1109/MMS48040.2019.9157289.

[91] S. -C. Tang, X. -Y. Wang and J. -X. Chen, "Low-Profile Frequency-Reconfigurable Dielectric Patch Antenna and Array Based on New Varactor-Loading Scheme," in IEEE Transactions on Antennas and Propagation, vol. 69, no. 9, pp. 5469-5478, Sept. 2021, doi: 10.1109/TAP.2021.3060053.

[92] K. Chen, Y. H. Zhang, S. Y. He, H. T. Chen and G. Q. Zhu, "An Electronically Controlled Leaky-Wave Antenna Based on Corrugated SIW Structure With Fixed-Frequency Beam Scanning," in IEEE Antennas and Wireless Propagation Letters, vol. 18, no. 3, pp. 551-555, March 2019, doi: 10.1109/LAWP.2019.2896354.

[93] He-Xiu Xu, Guang-Ming Wang, Tong Cai, Jun Xiao, and Ya-Qiang Zhuang, "Tunable Pancharatnam–Berry metasurface for dynamical and high-efficiency anomalous reflection," Opt. Express 24, 27836-27848 (2016)

[94] Xu, HX., Sun, S., Tang, S. et al. Dynamical control on helicity of electromagnetic waves by tunable metasurfaces. Sci Rep 6, 27503 (2016). https://doi.org/10.1038/srep27503

[95] H. -X. Xu et al., "Analysis and Design of Two-Dimensional Resonant-Type Composite Right/Left-Handed Transmission Lines With Compact Gain-Enhanced Resonant Antennas," in IEEE Transactions on Antennas and Propagation, vol. 61, no. 2, pp. 735-747, Feb. 2013, doi: 10.1109/TAP.2012.2215298.

[96] H. -X. Xu, G. -M. Wang, M. Q. Qi and T. Cai, "Compact Fractal Left-Handed Structures for Improved Cross-Polarization Radiation Pattern," in IEEE Transactions on Antennas and Propagation, vol. 62, no. 2, pp. 546-554, Feb. 2014, doi: 10.1109/TAP.2013.2290308.

[97] B. Liang, B. Sanz-Izquierdo, E. A. Parker and J. C. Batchelor, "A Frequency and Polarization Reconfigurable Circularly Polarized Antenna Using Active EBG Structure for Satellite Navigation," in IEEE Transactions on Antennas and Propagation, vol. 63, no. 1, pp. 33-40, Jan. 2015, doi: 10.1109/TAP.2014.2367537.

[98] Z. Xue, S. Zhong and Y. Ma, "Graphene-FSS Hybrid Absorptive Structure With Amplitude/Frequency Dual-Modulated Passband," in IEEE Antennas and Wireless Propagation Letters, vol. 20, no. 9, pp. 1711-1715, Sept. 2021, doi: 10.1109/LAWP.2021.3094835.

[99] R. W. Ziolkowski, P. Jin and C. -C. Lin, "Metamaterial-Inspired Engineering of Antennas," in Proceedings of the IEEE, vol. 99, no. 10, pp. 1720-1731, Oct. 2011, doi: 10.1109/JPROC.2010.2091610.

[100] Y. Xi, T. Wang, Y. Wang, H. Zhai and C. Liu, "A Low-Profile Wideband and Dual-Polarized Antenna With AMC Reflector," 2021 International Conference on Microwave and Millimeter Wave Technology (ICMMT), 2021, pp. 1-3, doi: 10.1109/ICMMT52847.2021.9617969.

[101] P. Juyal and L. Shafai, "A Novel High-Gain Printed Antenna Configuration Based on T12 Mode of Circular Disc," in IEEE Transactions on Antennas and Propagation, vol. 64, no. 2, pp. 790-796, Feb. 2016, doi: 10.1109/TAP.2015.2506724.

[102] P. Juyal and L. Shafai, "Gain Enhancement in Circular Microstrip Antenna via Linear Superposition of Higher Zeros," in IEEE Antennas and Wireless Propagation Letters, vol. 16, pp. 896-899, 2017, doi: 10.1109/LAWP.2016.2613996.

[103] X. Zhang, L. Zhu and Q. -S. Wu, "Sidelobe-Reduced and Gain-Enhanced Square Patch Antennas With Adjustable Beamwidth Under TM03 Mode Operation," in IEEE Transactions on Antennas and Propagation, vol. 66, no. 4, pp. 1704-1713, April 2018, doi: 10.1109/TAP.2018.2806220.

[104] P. Liu, Y. Li and Z. Zhang, "Circularly Polarized 2 Bit Reconfigurable Beam-Steering Antenna Array," in IEEE Transactions on Antennas and Propagation, vol. 68, no. 3, pp. 2416-2421, March 2020, doi: 10.1109/TAP.2019.2939669.

[105] Pozar DM. Microstrip antennas. Proc IEEE. 1992;80(1):79-91.

[106] D. Jackson and N. Alexopoulos, "Gain enhancement methods for printed circuit antennas," in IEEE Transactions on Antennas and Propagation, vol. 33, no. 9, pp. 976-987, September 1985, doi: 10.1109/TAP.1985.1143709.

[107] N. Alexopoulos and D. Jackson, "Fundamental superstrate (cover) effects on printed circuit antennas," in IEEE Transactions on Antennas and Propagation, vol. 32, no. 8, pp. 807-816, August 1984, doi: 10.1109/TAP.1984.1143433.

[108] H. Yang and N. Alexopoulos, "Gain enhancement methods for printed circuit antennas through multiple superstrates," in IEEE Transactions on Antennas and Propagation, vol. 35, no. 7, pp. 860-863, July 1987, doi: 10.1109/TAP.1987.1144186.

[109] Xiao-Hai Shen, G. A. E. Vandenbosch and A. Van de Capelle, "Study of gain enhancement method for microstrip antennas using moment method," in IEEE Transactions on Antennas and Propagation, vol. 43, no. 3, pp. 227-231, March 1995, doi: 10.1109/8.371990.

[110] Enoch S, Tayeb G, Sabouroux P, Guérin N, Vincent P. A metamaterial for directive emission. Phys Rev Lett. 2002;89(21):213902.

[111] H. Zhou et al., "A Novel High-Directivity Microstrip Patch Antenna Based on Zero-Index Metamaterial," in IEEE Antennas and Wireless Propagation Letters, vol. 8, pp. 538-541, 2009, doi: 10.1109/LAWP.2009.2018710.

[112] Feresidis AP, Vardaxoglou JC. High gain planar antenna using optimized partially reflective surfaces. IEE Proc Microw Antennas Propag. 2001;148(6):345-350.

[113] Feresidis AP, Goussetis G, Shenhong W, Vardax JC. To low profile high-gain planar antennas. IEEE Trans Antennas Propag. 2005;53(1):209-215.

[114] C. Mateo-Segura, G. Goussetis and A. P. Feresidis, "Sub-Wavelength Profile 2-D Leaky-Wave Antennas With Two Periodic Layers," in IEEE Transactions on Antennas and Propagation, vol. 59, no. 2, pp. 416-424, Feb. 2011, doi: 10.1109/TAP.2010.2096384.

[115] Zhou L, Li H, Qin Y, Wei Z, Chan CT. Directive emissions from subwavelength metamaterial-based cavities. Appl Phys Lett.2005;86(10):101101.

[116] Wang S, Feresidis AP, Goussetis G, Vardaxoglou JC. High- gain subwavelength resonant cavity antennas based on metamaterial ground planes. IEE Pro Microw Antennas Propag. 2006;153(1):1-6.

[117] Ourir A, de Lustrac A, Lourtioz J-M. All-metamaterial-based subwavelength cavities ($\lambda/60$) for ultrathin directive antennas.Appl Phys Lett. 2006;88:084103.

[118] J. R. Kelly, T. Kokkinos and A. P. Feresidis, "Analysis and Design of Sub-Wavelength Resonant Cavity Type 2-D Leaky-Wave Antennas," in IEEE Transactions on Antennas and Propagation, vol. 56, no. 9, pp. 2817-2825, Sept. 2008, doi: 10.1109/TAP.2008.928791.

[119] R. Q. Lee and K. . -F. Lee, "Experimental study of the two-layer electromagnetically coupled rectangular patch antenna," in IEEE Transactions on Antennas and Propagation, vol. 38, no. 8, pp. 1298-1302, Aug. 1990, doi: 10.1109/8.56971.

[120] S. Egashira and E. Nishiyama, "Stacked microstrip antenna with wide bandwidth and high gain," in IEEE Transactions on Antennas and Propagation, vol. 44, no. 11, pp. 1533-1534, Nov. 1996, doi: 10.1109/8.542079.

[121] Borja C, Font G, Blanch S, Romeu J. High directivity fractal boundary microstrip patch antenna. Electron Lett. 2000;36(9):778-779.

[122] James JR, Hall PS. Characteristics of microstrip patch antennas and some methods of improving frequency agility and bandwidth. Handbook of Microstrip Antennas. London, UK: Peregrinus; 1989 chap 3.

[123] B. H. Fong, J. S. Colburn, J. J. Ottusch, J. L. Visher and D. F. Sievenpiper, "Scalar and Tensor Holographic Artificial Impedance Surfaces," in IEEE Transactions on Antennas and Propagation, vol. 58, no. 10, pp. 3212-3221, Oct. 2010, doi: 10.1109/TAP.2010.2055812.

[124] G. Minatti, F. Caminita, M. Casaletti and S. Maci, "Spiral Leaky-Wave Antennas Based on Modulated Surface Impedance," in IEEE Transactions on Antennas and Propagation, vol. 59, no. 12, pp. 4436-4444, Dec. 2011, doi: 10.1109/TAP.2011.2165691.

[125] A. M. Patel and A. Grbic, "A Printed Leaky-Wave Antenna Based on a Sinusoidally-Modulated Reactance Surface," in IEEE Transactions on Antennas and Propagation, vol. 59, no. 6, pp. 2087-2096, June 2011, doi: 10.1109/TAP.2011.2143668.

[126] Zhong SS, Lo YT. Single-element rectangular microstrip antenna for dual-frequency operation. Electron Lett. 1983;19:298-300.

[127] P. Juyal and L. Shafai, "A Novel High-Gain Printed Antenna Configuration Based on T12 Mode of Circular Disc," in IEEE Transactions on Antennas and Propagation, vol. 64, no. 2, pp. 790-796, Feb. 2016, doi: 10.1109/TAP.2015.2506724.

[128] Maci S, Gentili GB, Piazzesi P, Salvador C. Dual-band slotloaded patch antenna. IEE Proc Microw Antennas Propag. 1995; 142(3):225-232.

[129] Kai-Ping Yang and Kin-Lu Wong, "Dual-band circularly-polarized square microstrip antenna," in IEEE Transactions on Antennas and Propagation, vol. 49, no. 3, pp. 377-382, March 2001, doi: 10.1109/8.918611.

[130] P. Juyal and L. Shafai, "A High-Gain Single-Feed Dual-Mode Microstrip Disc Radiator," in IEEE Transactions on Antennas and Propagation, vol. 64, no. 6, pp. 2115-2126, June 2016, doi: 10.1109/TAP.2016.2543804.

[131] P. Juyal and L. Shafai, "Sidelobe Reduction of TM12 Mode of Circular Patch via Nonresonant Narrow Slot," in IEEE Transactions on Antennas and Propagation, vol. 64, no. 8, pp. 3361-3369, Aug. 2016, doi: 10.1109/TAP.2016.2576503.

[132] X. Zhang, L. Zhu and Q. -S. Wu, "Sidelobe-Reduced and Gain-Enhanced Square Patch Antennas With Adjustable Beamwidth Under TM03 Mode Operation," in IEEE Transactions on Antennas and Propagation, vol. 66, no. 4, pp. 1704-1713, April 2018, doi: 10.1109/TAP.2018.2806220.

[133] Y. He, Y. Li, W. Sun, Z. Zhang and P. -Y. Chen, "Dual Linearly Polarized Microstrip Antenna Using a Slot-Loaded TM50 Mode," in IEEE Antennas and Wireless Propagation Letters, vol. 17, no. 12, pp. 2344-2348, Dec. 2018, doi: 10.1109/LAWP.2018.2874472.

[134] Ahmed Z, Ahmed MM. Sidelobe reduction and gain enhancement in higher order TM30 and TM70 mode rectangular patch antennas via partial notch loading. IET Microw Antennas Propag. 2019;13(12):1955-1962.

[135] J. Anguera, A. Andújar and J. Jayasinghe, "High-Directivity Microstrip Patch Antennas Based on TModd-0 Modes," in IEEE Antennas and Wireless Propagation Letters, vol. 19, no. 1, pp. 39-43, Jan. 2020, doi: 10.1109/LAWP.2019.2952260.

[136] Y. Zhang, W. Cao, Z. Qian, S. Shi and W. Peng, "Low Grating Lobe Array Antenna With Electrically Large Property Based on TM50 Mode," in IEEE Access, vol. 7, pp. 32897-32906, 2019, doi: 10.1109/ACCESS.2019.2903169.

[137] Y. Zhang, W. Cao, Z. Qian, S. Shi and W. Peng, "Low Grating Lobe Array Antenna With Electrically Large Property Based on TM50 Mode," in IEEE Access, vol. 7, pp. 32897-32906, 2019, doi: 10.1109/ACCESS.2019.2903169.

[138] H. Yang et al., "A New Strategy to Design Microstrip Antenna Array With Low Side-Lobe Level and High Gain," in IEEE Access, vol. 7, pp. 152715-152721, 2019, doi: 10.1109/ACCESS.2019.2948098.

Chapter 3
Antenna independent frequency and time domain representation of wireless channel

3.1 Introduction

Wireless channel behavior changes randomly due to multipath propagation, relative motion of Tx-Rx antennas and the environmental objects [1]. Hence, channel characterization is an important aspect to take care of prior to design any RF system. In the upcoming 5G cellular domain the challenges will become more critical because of the Ultra-Dense nature of the communication network [2-3]. Moreover, massive constructions using advanced materials and complex building structures make the wireless environment more prone to multipath fading [4-7]. In literature various empirical and statistical models have been proposed to capture long distance and small-scale fading channel responses [8-9]. For an outdoor environment, modified empirical methods and long-distance path loss models have been used for coverage prediction. Statistical methods have been considered in the case of an indoor multipath fading environments [10-12].

Several wideband channel sounding techniques based on direct pulse measurement, spread spectrum sliding correlator measurement and swept frequency measurements have been developed to determine small scale fading effects [13-18]. In all the frequency /time domain channel sounding techniques, channel impulse responses are calculated considering Tx and Rx antenna effects. Hence, the terminal effects inherently present in the measured results caused by ambiguous channel characterization and model. The results are antenna specific and unreliable for other antennas. In this chapter, a frequency domain approach is investigated to exclude the antenna transfer functions from the overall measurement data to obtain channel impulse response. In the proposed method, the wireless trans-receiver system is represented by a two-port network model to devise closed form analytical expressions to de-embed the terminal effects.

Identical horn antennas operating in the C band have been used to measure the channel transfer function and impulse response. A comparative investigation of the measured results with and without antenna effects is presented. It is observed that terminal antenna increases the propagation delay and reduces the coherence bandwidth of the channel.

3.2 Theory

Channel Impulse Response (CIR) is a wideband channel characterization that comprises all necessary information to analyze any radio transmission through a channel. Generally, wireless channels can be represented as linear filters with time varying Impulse Response (IR). Time variation occurs due to relative motions of the Tx and Rx nodes in the space, whereas the filtering behavior is caused by the superposition of multiple replicas of the transmitted signal at different time instants with varying amplitudes and delays [1]. Ideally any linear system comprising of linear subsystems can completely be characterized by its Transfer Function (TF) in the frequency domain or Impulse Response in the time domain (TF of cascaded stages in frequency domain or convolution of their IRs in time domain). Thus, antenna trans-receiver system behaves like a linear low pass filter and can be represented by cascading the transfer functions of the transmitting antenna (Tx), wireless channel, and the receiving antenna (Rx).

3.2.1 Transfer function of antenna trans-receiver system

Figure 3.1 shows antenna trans-receiver system in cascaded Transfer Function (TF) representation of the transmitting antenna TF (Tx-TF), receiving antenna TF (Rx-TF) and intermediate wireless channel (Channel TF or CTF). Transfer function of the Tx antenna [$Tx(\omega, \theta, \varphi)$], can be represented by the ratio of radiated electric far field, $E_{Tx}(\omega, \theta, \varphi, r)$ at a spatial point to the antenna input signal $V_{in}(\omega)$. Radiated electric far-field at a distance r is given below.

$$E_{Tx}(\omega, \theta, \varphi, r) = E_{Tx}(\omega, \theta, \varphi)\frac{e^{-jkr}}{r} \tag{3.1}$$

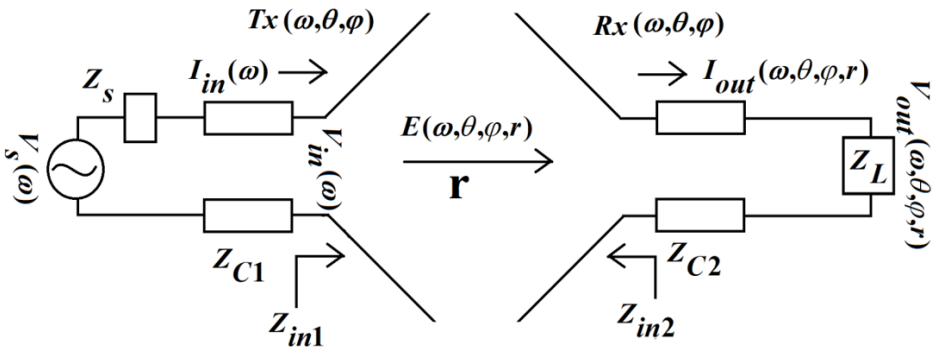

Fig. 3.1 Antenna trans-receiver system

Hence Tx-TF can be written as (3.2).

$$Tx(\omega,\theta,\varphi) = \widetilde{T_{Tx}}(\omega,\theta,\varphi)\sigma_{Tx} = \frac{E_{Tx}(\omega,\theta,\varphi,r)}{V_{in}(\omega)} re^{jkr} \tag{3.2}$$

Similarly, the TF of the Rx antenna, $Rx(\omega,\theta,\varphi)$ is the ratio of the output signal, $V_{out}(\omega,\theta,\varphi,r)$ of the receiving antenna to the incident field, $E_{Tx}(\omega,\theta,\varphi,r)$ as given by (3.3).

$$Rx(\omega,\theta,\varphi) = \widetilde{R_{Rx}}(\omega,\theta,\varphi)\sigma_{Rx} = \frac{V_{out}(\omega,\theta,\varphi,r)}{E_{Tx}(\omega,\theta,\varphi,r)} \tag{3.3}$$

where, $\omega = 2\pi f$, f is the operating frequency, ķ is the free space wave number, σ_{Rx} and σ_{Tx} are unit vectors that indicate the polarization direction of the Tx and Rx antennas respectively, (θ,φ) denotes the orientation of the antenna radiation, and r is the distance between Tx and Rx antennas.

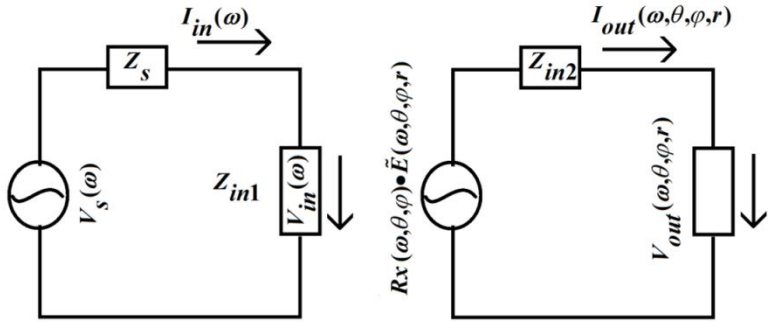

Fig. 3.2 Equivalent circuit representation

TF of the overall antenna trans-receiver system, $TF_{total}(\omega,\theta,\varphi,r)$ that includes all the terminal antenna TF and channel TF is derived by the ratio of the output signal $V_{out}(\omega,\theta,\varphi,r)$ to the exciting signal $V_s(\omega)$ as shown in Fig. 3.2 and presented in (3.4).

$$TF_{total}(\omega,\theta,\varphi,r) = \frac{V_{out}(\omega,\theta,\varphi,r)}{V_s(\omega)} \tag{3.4}$$

$Rx(\omega,\theta,\varphi)$ and $Tx(\omega,\theta,\varphi)$ depends on the operating frequency f and antenna orientation or pattern (θ,φ). Those parameters can be determined by an antenna's inherent properties, such as material, geometry, and operating modes. The system TF, $TF_{total}(\omega,\theta,\varphi,r)$ is also a function of distance r between the Tx-Rx antennas. It is noted that, $Rx(\omega,\theta,\varphi)$ is measured in meters in SI system, whereas $Tx(\omega,\theta,\varphi)$ and $TF_{total}(\omega,\theta,\varphi,r)$ are dimensionless. From the equivalent circuit representation in Fig. 3.2 and equations (3.1-3.4) $TF_{total}(\omega,\theta,\varphi,r)$ can be derived as follows.

$$V_{out}(\omega,\theta,\varphi,r) = \frac{Z_s(\omega)}{Z_s(\omega)+Z_{in2}(\omega)} Rx(\omega,\theta,\varphi)E_{Tx}(\omega,\theta,\varphi,r)$$

$$= \frac{Z_1(\omega)}{Z_1(\omega)+Z_{in2}(\omega)} Rx(\omega,\theta,\varphi)Tx(\omega,\theta,\varphi)\frac{e^{-jkr}}{r} \tag{3.5}$$

whereas, $$V_{in}(\omega) = \frac{Z_{in1}(\omega)}{Z_{in1}(\omega)+Z_s(\omega)}\ V_s(\omega) \tag{3.5a}$$

$Z_s(\omega)$, $Z_{in1}(\omega)$, $Z_{in2}(\omega)$ and $Z_L(\omega)$ denote the source, input terminal, output terminal and load end impedances respectively as depicted in the above figures. Also $Z_{c1}(\omega)$ and $Z_{c1}(\omega)$ are the characteristic impedances of the transmission lines connected at the input and the output ports or the terminal antennas.

Combining the above equations, we get.

$$TF_{total}(\omega,\theta,\varphi,r) = \frac{Z_1(\omega)}{Z_1(\omega)+Z_{in2}(\omega)} Rx(\omega,\theta,\varphi)Tx(\omega,\theta,\varphi)\frac{e^{-jkr}}{r}\frac{Z_{in1}(\omega)}{Z_{in1}(\omega)+Z_s(\omega)}$$

$$= \frac{Z_1(\omega)}{Z_1(\omega)+Z_{in2}(\omega)} Rx(\omega,\theta,\varphi)\sigma_{Rx} Tx(\omega,\theta,\varphi)\sigma_{Tx} \frac{e^{-jkr}}{r} \frac{Z_{in1}(\omega)}{Z_{in1}(\omega)+Z_s(\omega)} \quad (3.6)$$

Schmitt and Kanda [19,20] using the Rayleigh-Carson relation and plane wave–scattering theory, showed that an Ultra-Wide Band (UWB) antenna's transmitting transient response is proportional to the time derivative of the receiving transient response. In other work, Farr et al., [21] showed that the ratio of the TF's of a UWB transmitting and receiving antenna is proportional to operating frequency [21, 22]. Therefore, the Tx and Rx antennas are related in frequency and time domain as follows.

$$Tx(\omega,\theta,\varphi) = \frac{j\omega}{2\pi C_0} Rx(\omega,\theta,\varphi) \quad (3.7)$$

$$h_{Tx}(t,\theta,\varphi) = \frac{1}{2\pi C_0} \frac{d}{dt} h_{Rx}(t,\theta,\varphi) \quad (3.8)$$

where C_0 represents the velocity of electromagnetic wave in free space.

3.2.2 Practical Measurement Approach

An antenna trans-receiver system has been represented as a two-port network as shown in the Fig. 3.3. Two identical antennas are kept at far-field and aligned along boresight direction. The antennas are excited to operate in same frequency and polarisation. The system is represented by three subsystems viz. Tx, Rx antennas and the wireless propagation channel. Its overall transmission matrix can be replaced by the product of corresponding individual transmission matrices. Basically, transmission matrix [ABCD] relates the input and output voltages to the current ratios of a two-port network, which are difficult to measure and define in microwave frequencies. On the other hand, scattering [S] parameter relates incident, reflected and outgoing travelling waves. Hence, S-parameter can efficiently be measured using Vector Network Analyser (VNA) with sufficient accuracy [23].

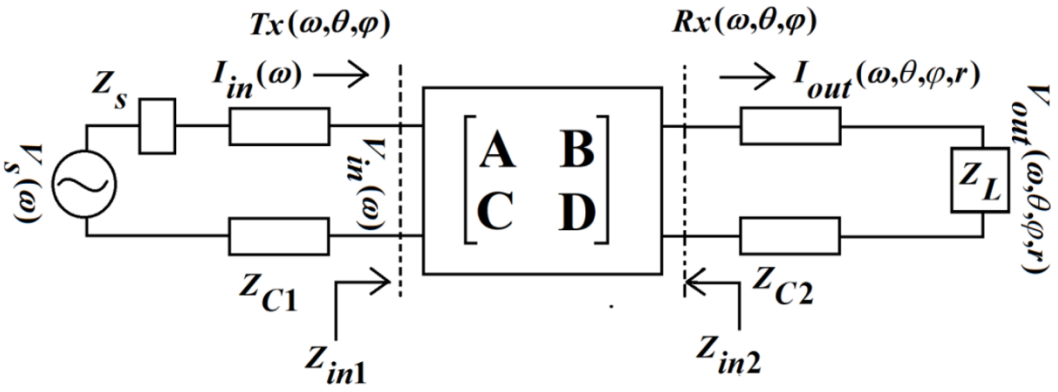

Fig. 3.3 Equivalent ABCD parameter representations

Therefore, the overall antenna system transfer functions are derived by ABCD parameters and subsequently convert them to S parameter expressions.

The Rx antenna is connected to a receiver, which is further connected with a load impedance Z_l; the relationship between the signal at the input of the Tx antenna and the voltage and current at the output end can be expressed as follows.

$$\begin{aligned} V_{in}(\omega) &= AV_{out}(\omega,\theta,\varphi,r) + BI_{out}(\omega,\theta,\varphi,r) \\ &= AV_{out}(\omega,\theta,\varphi,r) + BV_{out}(\omega,\theta,\varphi,r)\, Z_l \\ &= (A + B/Z_l)V_{out}(\omega,\theta,\varphi,r) \end{aligned}$$

Or, $$\frac{V_{out}(\omega,\theta,\varphi,r)}{V_{in}(\omega)} = \frac{1}{A+\frac{B}{Z_l}}$$

$$= \frac{1}{m\sqrt{\frac{Z_{c1}}{Z_{c1}}} + n\sqrt{Z_{c1}.Z_{c2}/Z_l}} \qquad (3.9)$$

where $m = A\sqrt{\frac{Z_{c1}}{Z_{c1}}}$, $n = B/\sqrt{Z_{c1}.Z_{c2}/Z_l}$ are the normalized ABCD parameters

Replacing 3.4 in (3.9), the Transfer functions can be represented as follows.

$$TF_{total}(\omega,\theta,\varphi,r) = \frac{V_{out}(\omega,\theta,\varphi,r)}{V_s(\omega)}$$

$$= \frac{1}{m\sqrt{\frac{Z_{c1}}{Z_{c1}}} + n\sqrt{\frac{Z_{c1}.Z_{c2}}{Z_l}}} \frac{Z_{in1}(\omega)}{Z_{in1}(\omega)+Z_s(\omega)} \qquad (3.10)$$

Considering $|\sigma_{Tx}.\sigma_{Rx}| = 1$ and combining (3.6), (3.7) and (3.10) following expression can be obtained,

$$Tx(\omega,\theta,\varphi) = \sqrt{\frac{1}{m\sqrt{\frac{Z_{c1}}{Z_{c1}}} + n\sqrt{\frac{Z_{c1}.Z_{c2}}{Z_l}}} \frac{Z_{in1}(\omega)+Z_s(\omega)}{Z_{in1}(\omega)} \frac{j\omega}{2\pi C_0} re^{jkr}} \quad (3.11)$$

$$Rx(\omega,\theta,\varphi) = \sqrt{\frac{1}{m\sqrt{\frac{Z_{c1}}{Z_{c1}}} + n\sqrt{\frac{Z_{c1}.Z_{c2}}{Z_l}}} \frac{Z_{in1}(\omega)+Z_s(\omega)}{Z_{in1}(\omega)} \frac{2\pi C_0}{j\omega} re^{jkr}} \quad (3.12)$$

ABCD parameters are derived from Fig. 3.3 and converted to S parameters considering the source and receiver impedances equal to the characteristic impedance, i.e., $Z_S = Z_{C1} = Z_{C2} = Z_l$. The transmission lines are connected with the input and out ports. Fig. 3.3 shows the equivalent two port transmission matrix representation of antenna trans-receiver system. Using the equivalent circuit model of the antenna system and considering input/output impedance relation, the transfer functions (TF) of all antenna subsystems can be represented by [S] matrix elements as below.

$$TF_{total}(\omega,\theta,\varphi,r) = \frac{S_{21}}{2} \quad (3.13)$$

$$Tx(\omega,\theta,\varphi) = \sqrt{\frac{2S_{21}}{(1-S_{11})(1+S_{22})} \frac{j\omega}{2\pi C_0} re^{jkr}} \quad (3.14)$$

$$Rx(\omega,\theta,\varphi) = \sqrt{\frac{2S_{21}}{(1-S_{11})(1+S_{22})} \frac{2\pi C_0}{j\omega} re^{jkr}} \quad (3.15)$$

As observed, overall antenna system transfer function, under the above impedance constraint, can be directly described by S21 or S12 of a transmitting-receiving antenna system with any impedance matching as impedance characteristic doesn't impact it. On the other hand, transmitting and receiving antenna transfer function is largely impacted by the impedance characteristic as shown in (3.14) and (3.15) respectively.

Hence, the overall TF can be represented by cascading the individual transfer function in frequency domain as presented below.

$$TF_{total}(\omega,\theta,\varphi,r) = TF_{Tx\_Antenna}(\omega,\theta,\varphi)TF_{Channel}(\omega,\theta,\varphi,r)TF_{Rx\_Antenna}(\omega,\theta,\varphi)$$

Thus, $$TF_{Channel}(\omega,\theta,\varphi,r) = \frac{H_{System}(\omega,\theta,\varphi,r)}{H_{Tx\_Antenna}(\omega,\theta,\varphi)H_{Rx\_Antenna}(\omega,\theta,\varphi)}$$

In time domain the relation can be presented using convolution property as shown below.

$$h(t,\tau) = h_{Tx}(t,\theta,\varphi) * h_{Channel}(t,\theta,\varphi) * h_{Rx}(t,\theta,\varphi),$$

Hence the channel TF can be evaluated using S parameters using (3.9-3.11) and presented in (3.16).

$$H_{Channel}(\omega,\theta,\varphi,r) = \frac{(1-S_{11})(1+S_{22})}{4r}e^{-jkr} \quad (3.16)$$

Equation (3.16) models the wireless channel transfer function in frequency domain excluding the antenna effects. Time domain channel impulse response can be evaluated by taking IFFT (Inverse Fast Fourier Transform) of (3.17) as shown below.

$$IR_{Channel}(t,\theta,\varphi) = IFFT(H_{Channel}(\omega,\theta,\varphi,r)) \quad (3.17)$$

3.3 Frequency and time domain measurement of channel response

Two identical C band horn antennas are kept in far-field at 100cm apart and radiates vertically polarization wave in boresight direction. To avoid multipath environment the experiment is conducted within anechoic chamber to ensure SISO (Single Input Single Output) environment. S parameters are evaluated using VNA (Agilent E5071B) with 1601-point sweep setup. Measured frequency domain data (S parameters) are used for post processing to estimate Tx-TF, Rx-TF, and $TF_{total}(\omega,\theta,\varphi,r)$ (overall system TF) using (3.13-3.15) respectively.

3.3.1 Frequency Domain Transfer Functions

I. Antenna System Transfer function ($TF_{total}(\omega, \theta, \varphi, r)$)

Fig. 3.4 shows measured antenna system transfer function plot. Linear amplitude and phase variation is observed in the C band spectrum. A slight fluctuation of amplitude at the higher frequencies in the C band is due to the improper impedance matching of the antenna, although antenna gain remains constant in boresight direction for the entire operating range of the band.

II. Transmitting and Receiving Antenna Transfer Functions ($Tx(\omega, \theta, \varphi), and\ Rx(\omega, \theta, \varphi)$)

Tx-TF and Rx-TF have been calculated using (3.14) and (3.15) respectively from the measured S parameters and plotted in Fig. 3.5(a & b) respectively. It has been observed that the amplitude and phase plot of the Tx and Rx antenna TFs is linear and identical in the C band. It is observed that the amplitude variation of the Tx and Rx antennas are different as the antennas of a particular trans-receiver system are proportional to the operating frequency in frequency domain and time derivative of the receiving transient response in time domain.

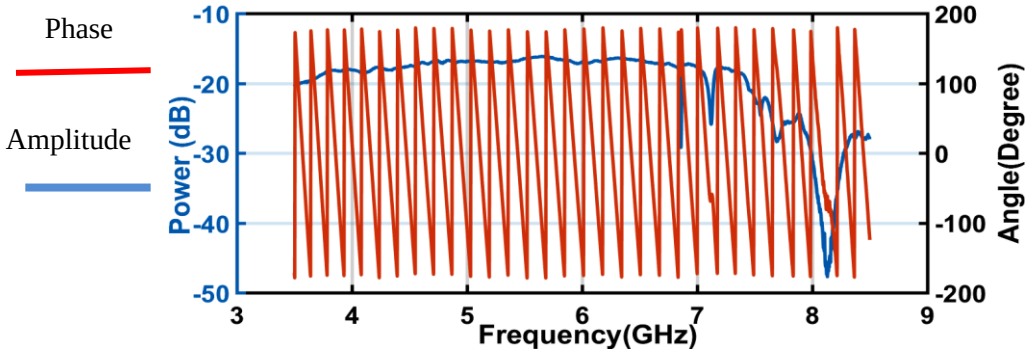

Fig. 3.4 Antenna system transfer function: amplitude and phase plot with respect to frequency

Non-linearity in amplitude has been observed in out of band spectra as horn antennas are designed to be operated in C band resulting in a slight mismatch in input impedance.

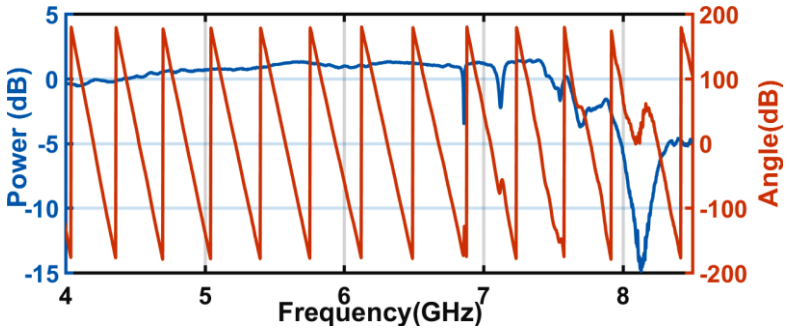

(a)

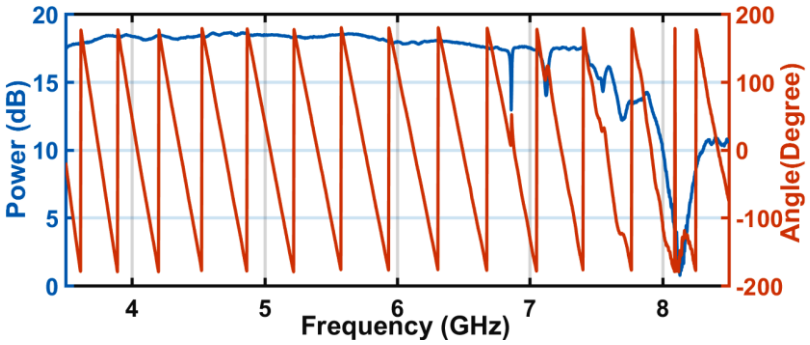

(b)

Fig. 3.5 (a) Transmitting and (b) Receiving antenna transfer function: amplitude and phase plot with respect to frequency

III. Channel Transfer Function

The Channel transfer function is calculated using (3.16) from the measured S parameters. Fig. 3.6 shows the amplitude and phase plot of the channel transfer function. It has been noted that the considered wireless channel is a Single Input Single Output (SISO) static channel. Hence the measured transfer function of the channel is also a linear time invariant system. Non-linearity in the higher frequencies is due to impedance mismatch of the antenna at those frequencies.

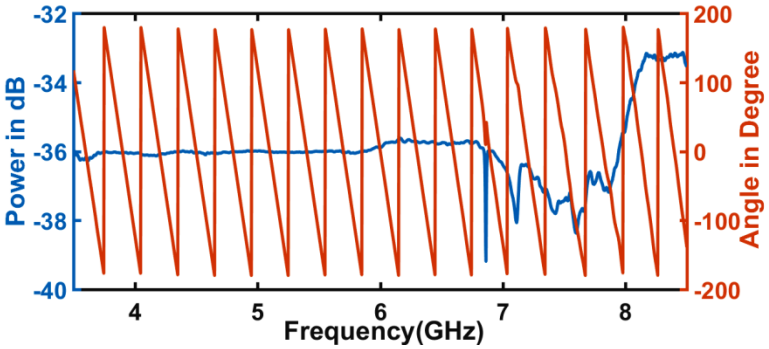

Fig. 3.6 Channel transfer function: amplitude and phase plot with respect to frequency

3.3.2 Time Domain Impulse Response

Time domain response of the antenna is evaluated using IFFT of (3.13-3.15). Fig. 3.7(a) shows the measured impulse responses of transmitting and receiving horn antennas. It is observed that the impulse response of both antennas is identical in nature which displays equal propagation delay and channel coherence bandwidth. It is also noted that despite of slight amplitude mismatch in frequency domain representation of Tx-TF and Rx-TF, the nature of the time domain Impulse Response (IR) of two identical horn antennas are similar, which is expected. The propagation delays of both the IRs are noted at 2.353ns. Channel Impulse Response (CIR) and Antenna System Impulse Response (ASIR) plots are shown in Fig. 3.7(b). It is observed that the propagation delays for CIR and ASIR are measured at 3.4ns and 6.2ns respectively as shown in Fig. 3.7(b).

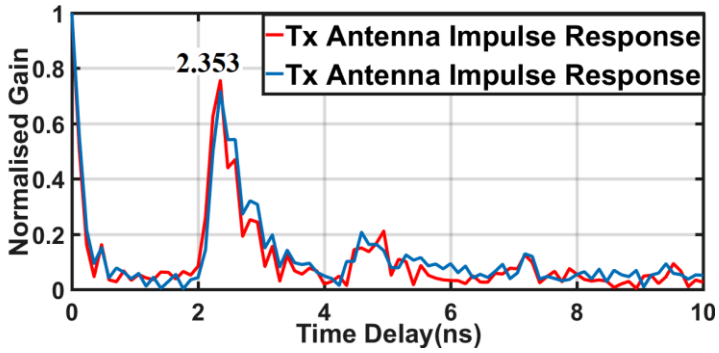

(a)

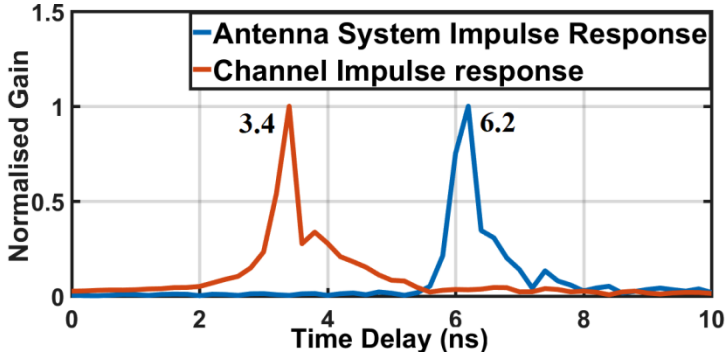

(b)

Fig. 3.7 (a) Transmit and receive antenna impulse response, (b) Antenna system (end to end) and channel impulse response

3.3.3 Channel responses with different antennas

In this section, the similar experiment is done with different antennas to verify the antenna independency of the derived expressions. Channel impulse response is measured using a pair of TEM horn antennas in the same frequency band. The antennas are kept in same distance and the measurements are taken in the similar environment. It is observed that the measured channel responses (time and frequency domain) are approximately similar to the results obtained for C band horn antennas and shown in Fig. 3.8. The delays of the measured channel using TEM horn and C band horn antennas appear at 3.3ns and 3.4ns respectively. This observation proves beyond doubt the necessity of measuring channel impulse response without antenna effects.

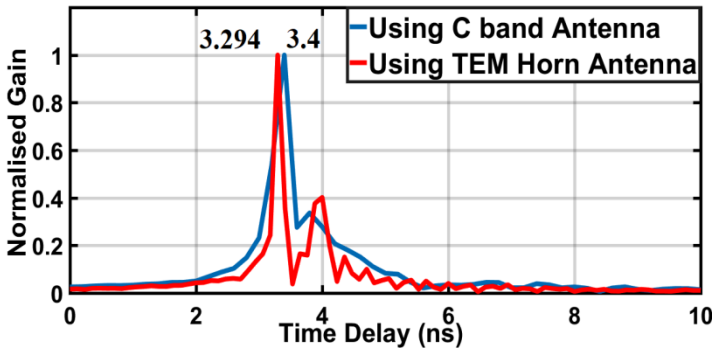

Fig. 3.8 Comparison of time domain channel impulse response using C band and TEM horn antennas

3.4 Discussion

The above-mentioned method shows the importance of exclusion of antenna effects prior to modeling and characterization of wireless channels. Characterization of an unknown multipath channel in any random environment to derive transfer function or impulse response of an unknown antenna can also be carried out using the above approach. Time and frequency domain channel sounders are used to measure the amplitude, phase and frequency variations of the transmitted signals. Subsequently the frequency and time domain statistical parameters are derived for channel characterize and modeling. No such work in literature has been proposed so far that explicitly de-embed the antenna effects (time or frequency domain) while measuring the multipath statistical parameters of a channel. ASTF and channel transfer function plots then exhibit dissimilar amplitude and phase variations because of antenna effects in measured antenna

system parameters. Amplitude and phase are two distinct important parameters in studying small scale fading in multipath environment as the spatial distribution of received power is the vector summation of the received signals with random phase and amplitudes coming from different directions. Thus, the variation of amplitude and phase in frequency domain due to antenna must not be neglected and is needed to be considered for modeling wireless channels. It has been noticed clearly from Fig. 3.7(b) that introduction of antennas increases propagation delay in a wireless channel. The peaks of the delay of ASIR and CIR show at 6.2ns and 3.4ns respectively in our experiment. It is noted that 3.4ns delay is equivalent to free space propagation delay that incurred for 90cm Tx and Rx antenna separation, which is expected as in this case as Tx-Rx antennas are kept at 100cm apart. It is also noticed that the half power pulse width of the respective time domain responses illustrates noticeable difference. Channel impulse response shows less width depicting wider coherence bandwidth in frequency domain.

The same approach can be carried out to measure transfer function of an unknown antenna operating in the same frequency band using the same measurement setup. If Tx antenna is replaced by the unknown antenna, the mentioned in (3.18) can be used to represent the transfer function of the antenna.

$$H_{Unkown}(\omega,\theta,\varphi,r) = \frac{H_{System}(\omega,\theta,\varphi,r)}{H_{Tx\_Antenna}(\omega,\theta,\varphi)H_{Rx\_Antenna}(\omega,\theta,\varphi)} \tag{3.18}$$

A multipath channel can be characterized using the same approach. Multipath CIR can be formulated using IFFT of (3.19) and measured CIR can be used further to derive other statistical parameters to characterize the channel.

$$H_{Multipath}(\omega,\theta,\varphi,r) = \frac{H_{measured\_System}(\omega,\theta,\varphi,r)}{H_{known\_Tx\_Antenna}(\omega,\theta,\varphi)H_{known\_Rx\_Antenna}(\omega,\theta,\varphi)} \tag{3.19}$$

3.5 Conclusion

In this chapter, a two-port network model approach is used for antenna trans-receiver systems to measure the time and frequency domain responses of Tx/Rx antenna, channel, and overall antenna system. Theory and corresponding measurements show the need to consider

antenna effects prior to characterize wireless channels. It is observed that antennas increase propagation delay and reduce the coherence bandwidth of the channel. Thus, an antenna independent channel measurements have been presented. Unknown antennas and multipath channel response have also been derived using the approach. Static channel which is characterized as a linear time invariant system has been considered in this approach. Observations for time variant channels where the Tx or Rx antennas or the surrounding objects are dynamic are subject to future research.

Channel characterization and modeling in different indoor environments are important aspect in recent communication scenarios. In the next chapter an indoor static environment is studied to characterize the terminal independent channel metrices using frequency domain measurement approach. The closed form expressions proposed in this chapter are applied to obtain antenna independent channel metrices. Subsequently, channel models are devised to emulate the channel behavior in laboratory setup to design RF systems for those specific propagation environments.

References

[1] T.S. Rappaport, (2002). Wireless Communications. Publisher: Prentice-Hall.

[2] M. Elkashlan, T. Q. Duong and H. -H. Chen, "Millimeter-wave communications for 5G: fundamentals: Part I [Guest Editorial]," in IEEE Communications Magazine, vol. 52, no. 9, pp. 52-54, September 2014, doi: 10.1109/MCOM.2014.6894452.

[3] T. S. Rappaport, G. R. MacCartney, M. K. Samimi and S. Sun, "Wideband Millimeter-Wave Propagation Measurements and Channel Models for Future Wireless Communication System Design," in IEEE Transactions on Communications, vol. 63, no. 9, pp. 3029-3056, Sept. 2015.

[4] J. W. Wallace, R. Mehmood and M. A. Jensen, "4–40 GHz Transmission Measurement of Indoor Building Materials at Normal Incidence," 2018 IEEE International Symposium on Antennas and Propagation & USNC/URSI National Radio Science Meeting, Boston, MA, 2018, pp. 2483-2484.

[5] F. Sagnard and G. E. Zein, "In situ characterization of building materials for propagation modeling: frequency and time responses," in IEEE Transactions on Antennas and Propagation, vol. 53, no. 10, pp. 3166-3173, Oct. 2005.

[6] S. S. Zhekov, O. Franek and G. F. Pedersen, "Dielectric Properties of Common Building Materials for Ultrawideband Propagation Studies [Measurements Corner]," in IEEE Antennas and Propagation Magazine, vol. 62, no. 1, pp. 72-81, Feb. 2020.

[7] S. S. Zhekov, Z. Nazneen, O. Franek and G. F. Pedersen, "Measurement of Attenuation by Building Structures in Cellular Network Bands," in IEEE Antennas and Wireless Propagation Letters, vol. 17, no. 12, pp. 2260-2263, Dec. 2018.

[8] T. K. Sarkar, M. N. Abdallah and M. Salazar-Palma, "Survey of Available Experimental Data of Radio Wave Propagation for Wireless Transmission," in IEEE Transactions on Antennas and Propagation, vol. 66, no. 12, pp. 6665-6672, Dec. 2018.

[9] C. Wang, J. Bian, J. Sun, W. Zhang and M. Zhang, "A Survey of 5G Channel Measurements and Models," in IEEE Communications Surveys & Tutorials, vol. 20, no. 4, pp. 3142-3168, Fourthquarter 2018.

[10] A. A. M. Saleh and R. Valenzuela, "A Statistical Model for Indoor Multipath Propagation," in IEEE Journal on Selected Areas in Communications, vol. 5, no. 2, pp. 128-137, February 1987.

[11] A. Sibille, "Statistical Modeling of the Radio-Electric Properties of Wireless Terminals in their Environment," in IEEE Antennas and Propagation Magazine, vol. 54, no. 6, pp. 117-129, December 2012.

[12] A. Sibille, "Statistical modeling of antennas in the context of radio channel modeling," 2014 XXXIth URSI General Assembly and Scientific Symposium (URSI GASS), Beijing, 2014, pp. 1-4.

[13] R. J. Pirkl and G. D. Durgin, "Optimal Sliding Correlator Channel Sounder Design," in IEEE Transactions on Wireless Communications, vol. 7, no. 9, pp. 3488-3497, September 2008.

[14] G. R. MacCartney and T. S. Rappaport, "A Flexible Millimeter-Wave Channel Sounder With Absolute Timing," in IEEE Journal on Selected Areas in Communications, vol. 35, no. 6, pp. 1402-1418, June 2017.

[15] D. Maas, M. H. Firooz, J. Zhang, N. Patwari and S. K. Kasera, "Channel Sounding for the Masses: Low Complexity GNU 802.11b Channel Impulse Response Estimation," in IEEE Transactions on Wireless Communications, vol. 11, no. 1, pp. 1-8, January 2012.

[16] H. Boeglen, A. Traore, M. M. Peinado, R. Lefort and R. Vauzelle, "An SDR based channel sounding technique for embedded systems," 2017 11th European Conference on Antennas and Propagation (EUCAP), Paris, 2017, pp. 3286-3290.

[17] J. O. Nielsen, W. Fan, P. C. F. Eggers and G. F. Pedersen, "A Channel Sounder for Massive MIMO and MmWave Channels," in IEEE Communications Magazine, vol. 56, no. 12, pp. 67-73, December 2018.

[18] P. F. M. Smulders and A. G. Wagemans, "Frequency domain sounding of MM-wave indoor radio channels," Proceedings of 2nd IEEE International Conference on Universal Personal Communications, Ottawa, Ontario, Canada, 1993, pp. 636-640 vol.2.

[19] M. Kanda, "Transients in a resistively loaded linear antenna compared with those in a conical antenna and a TEM horn," in IEEE Transactions on Antennas and Propagation, vol. 28, no. 1, pp. 132-136, January 1980, doi: 10.1109/TAP.1980.1142268.

[20] H.J. Schmitt, (1960), Transients in cylindrical antenna, IEEMonogr. Ser., 377E, Inst. of Electr. Eng., London.

[21] Taylor, J. D. (1995), Introduction to Ultra-Wideband Radar Systems, CRC Press, Boca Raton, Fla.

[22] E. G. Farr and C. E. Baum, “Extending the definitions of antenna gains radiation pattern into the time domain,” *Sens. Simul. Note*, vol. 350, Nov. 1992

[23] D.M. Pozar, (1990), Microwave Engineering, Addison-Wesley, Boston, Mass.

Chapter 4
Frequency Domain Ultra-Wide Band Channel Characterization and modeling in Indoor Static Environment

4.1 Introduction

Indoor propagation scenarios are changing rapidly due to the coexistence to larger number of electronic devices and diverse indoor construction using advanced building materials [1]. In static indoor scenarios, the presence of numerous scattering objects significantly increases the channel fading due to the vector addition of amplitude and phase varied multipath components (MPCs) at the receiving end. Because of the high dynamic range, frequency domain techniques based on a Vector Network Analyzer (VNA) efficiently assess an indoor static environment [2]. A distance and frequency-dependent indoor wireless channel characterization and modeling using the frequency domain approach is presented in this chapter for C, X, and Ku bands in both Line of Sight (LOS) and non-Line of Sight (nLOS) scenarios. The significance and advantages of this approach are listed below.

1. The closed form expressions of the antenna trans-receiver system derived in the previous chapter using a two-port network model approach are used to deconvolute terminal dependencies of the propagation channels. Subsequently, terminal independent Channel Transfer Functions (CTFs) and corresponding Channel Impulse Responses (CIRs) are derived. Furthermore, statistical behavior of large- and small-scale fading parameters for C, X, and Ku bands is presented for LOS and nLOS scenarios which are independent of the measurement setup.

2. A simple distance dependent large scale statistical path-loss model is proposed based on the terminal independent empirical data. Subsequently, a frequency dependent channel characterization and modeling of measured complex frequency responses are presented.

3. A frequency domain 5^{th} order Auto-Regressive (AR) model is presented for the small-scale statistical variations of the channel. The model provides important insights regarding the

presence of multiple clusters and the nature of amplitude & phase variation of the multipath components (MPCs) in the indoor propagation environment.

4. The proposed models are validated in frequency and time domain by comparing the model data with the measured results.

4.2 Experimental Setup and Measurement Environment

4.2.1 Measurement Setup

Frequency domain measurement approach is found to be more efficient for channel characterization in static environments where real time scenarios are not considered. It is due to the availability of VNA with large dynamic range, low loss shielded RF cables and low noise active devices such as LNA, power amplifier or attenuator. Scattering matrix [S] of the radio channel is derived by the two-port measurement approach using a VNA and terminal antennas as depicted in the schematic in Fig. 4.1(a). In Fig. 4.1(b), the actual measurement setup used in the field measurements is illustrated. The measured complex S_{21} (Transmission Coefficient) as shown in (4.1) represents the Channel Transfer Function (CTF) of the channel including the terminal antenna effects.

$$S_{21} \rightarrow H(n\Delta f) \; = \; Re[H(n\Delta f)] \; + \; img[H(n\Delta f)] \tag{4.1}$$

where n is the number of frequency samples taken within the specified band in the VNA

Three sets of conical shaped monopole antenna pairs operating at C, X and Ku bands are used in the measurement campaign. These omnidirectional antennas exhibit low Radar Cross Section (RCS) and Voltage Standing Wave Ratio (VSWR) with constant gain in the operating bandwidth. These antennas are efficient to detect multipath components arriving from different directions. Two antennas of same band are attached to the Tx and Rx ports of the VNA to conduct channel measurement at that specific frequency band. Double shielded low loss RF cables (Make: Radial, Model: SHF8 and 1.2 dBm/m loss at 10GHz) [3] and connectors are used to minimize the coupling of external noises. The measured data is stored in a storage device thru the USB interface of the VNA as shown in Fig. 4.1(b)

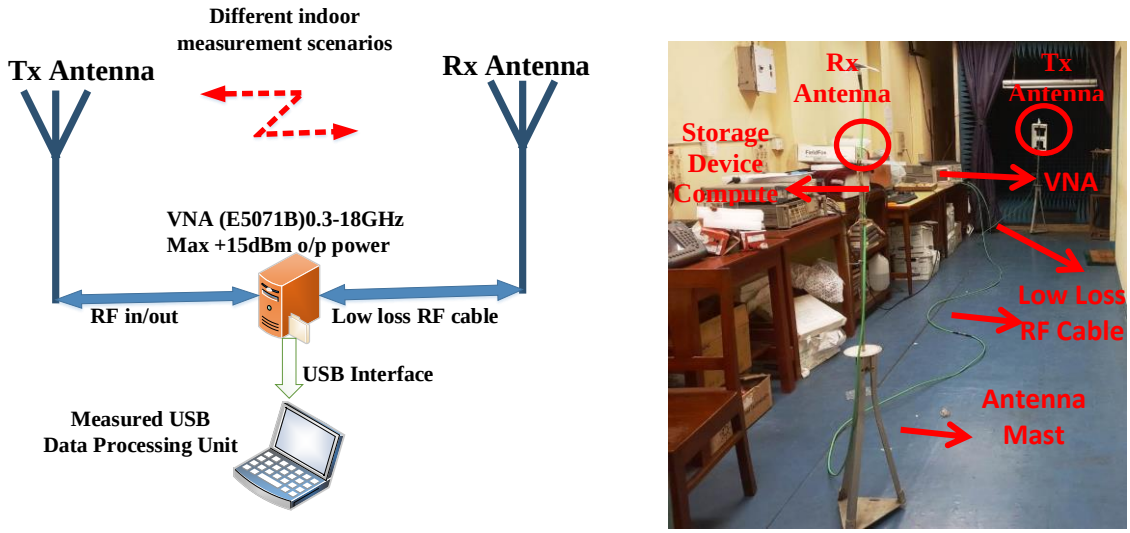

(a) (b)

Fig. 4.1 (a) Schematic diagram of the measurement setup, and (b) Actual Measurement Setup in Laboratory environment

The operating bandwidth (Bw) of the C, X and Ku bands are uniformly distributed in 1601 (N) sampling points in the VNA; hence the frequency resolution is given as $f_{res}=\frac{Bw}{N-1}=\frac{Bw}{1600}$. The time resolution ($t_{cir}$) is the required delay for each multipath component and given by $t_{res}=1/BW$. The time delay for each CIR is defined by the propagation delay by each frequency component and represented by $t_{cir}=1/f_{res}$. It is observed that t_{cir} is large enough to the bin size or t_{res} of all measurements. The maximum distance covered by the propagating signal within a single time delay of the channel impulse response is given as $L_{CIR}=3\times10^{8}\times\left(\frac{1}{fres}\right)\ m$. The sweep time in the VNA is an important aspect to analyze the static and dynamic nature of the environment and given by $t_{SW}=1.5\times N\times(1/IF\_BW)$ [4]. Bandwidth of the IF frequency (IF_BW) of the VNA is set in accordance with the sweep time. In general, IF_BW of the band pass filter in the VNA is varied between 1Hz to 40 KHz depending upon the VNA make and model [4]. Sweep time decreases with increasing IF_BW that supports fast data processing; but at the same time the noise floor in the VNA is elevated hence many Multipath Components (MPCs) are remained undetected. Author has fixed the VNA IF_BW to 3 KHz to get optimum results. t_{SW} is also equivalent to the coherence time (T_c) representing the time interval over which the frequencies of the CTFs remain invariant or within 3dB magnitude. The

corresponding Doppler spread, f_m $(= 1/T_c)$ is the inverse of the coherence time. In our measurement setup, f_m is measured at 1.25Hz which is significantly close to static environment. The parameters discussed above are listed in Table 4.1 for C, X and Ku bands.

TABLE 4.1: DETAILS OF THE DEVICES USED IN THE MEASUREMENT CAMPAIGN

Vector Network Analyzer (VNA)	Make and Model	Agilent E5071B VNA
	Operating Frequency Range	0.3-26.5 GHz
	Calibration Type	Manual
	Number of sample points	1601
	Power O/P	5dBm
	Noise Floor	-120dBm
RF Cables	Make and Model	Radial SHF8 model
	Power Loss in dB	1.2dBm/m loss at 10GHz
	Cable Length	2 m, 5 m
	RF Connector	N, L Type
Antennas	Antenna Type	Monopole
	Make and Model	EM6865 Wideband
	Operating Frequency Band	C, X, Ku band
	Input Impedance	50Ω
	Realized Gain	2.9dBi@ 1GHz 5.1dBi@ 18GHz
	Polarization Used	Vertical

TABLE 4.2: MEASUREMENT PARAMETERS IN C, X AND KU BAND

Parameters	Formulation	C-Band	X-Band	Ku-Band
Bandwidth	$f_U - f_L$	4-8 GHz	8-12 GHz	12-18 GHz
Centre Frequency	$\sqrt{f_L f_U}$	5.66 GHz	9.8 GHz	14.7 GHz
Sweep time	$t_{SW} = 1.5 \times N \times (1/IF\_BW)$	800ms	800ms	800ms
Frequency resolution	$f_{res} = \frac{Bw}{N-1} = \frac{Bw}{1600}$	2.5MHz	2.5MHz	3.75MHz
Time Resolution	$t_{res} = 1/BW$	250ps	250ps	167ps
Max. CIR length	$L_{CIR} = 3 \times 10^8 \times \left(\frac{1}{fres}\right)$	120m	120m	80m
Max. Path Delay	$t_{cir} = 1/f_{res}$	400µs	400µs	267µs
Doppler Spread	$f_m = 1/T_c = 1/t_{SW}$	1.25Hz	1.25Hz	1.25Hz

4.2.2 Measurement Scenarios and Data Acquisitions

The measurement campaign is performed in the indoor environment of Jadavpur University campus in India. The measurement campaign is conducted in multiple laboratories, departmental corridors and classes of different shapes, sizes, and clutters. For the ease of analysis and subsequent presentation, the environments are categorized as Site-A (laboratories), Site-B

(corridors) and Site-C (classes). The layout of the locations from each site (A, B, C) are shown in Fig. 4.2. Tx-Rx antenna position as well as the movement of the Rx antenna mast within few designated points on any specified room is depicted in the following images (Fig. 4.2).

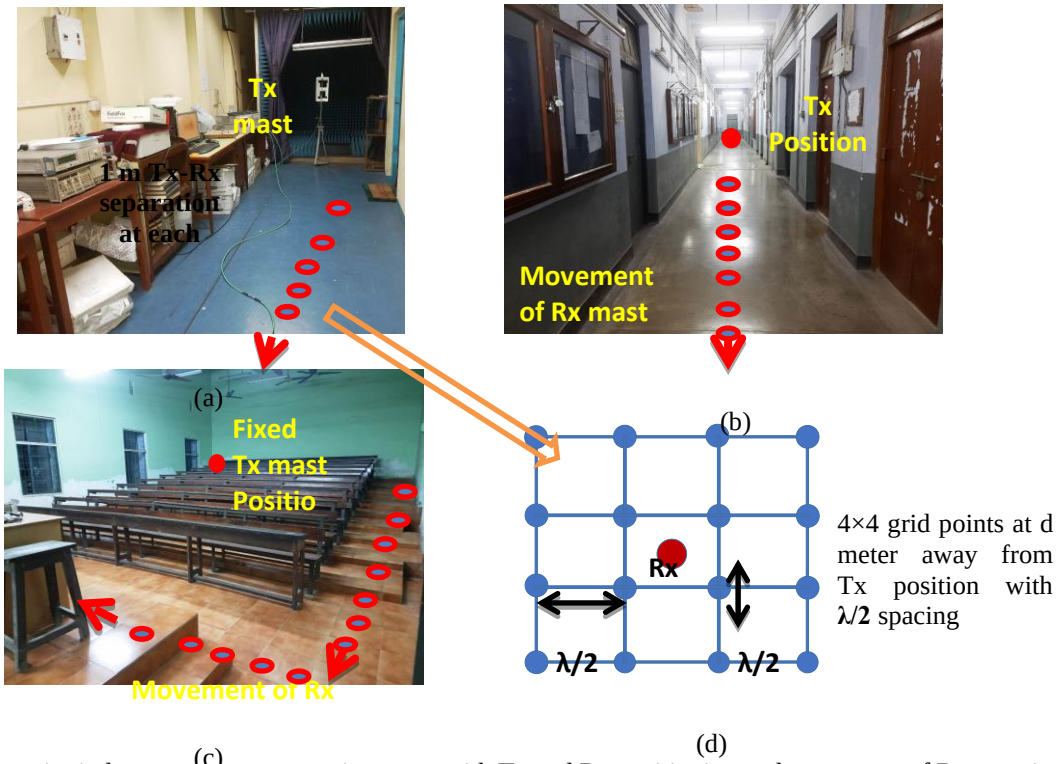

Fig. 4.2 University indoor measurement environment with Tx and Rx positioning and movement of Rx mast in (a) Laboratory- Site-A, (b) Corridor Site-B, and (c) Classroom Site-C, (d) Premeasured 4×4 grid points of any Rx location at d meter away from Tx position

The Tx antenna is placed at a fixed position (where the Internet Service Providers generally placed the access points or hotspots in an indoor environment) and the Rx node is moved within the site. The measurements are taken for Line of Sight (LoS) and non-Line of Site (n-LoS) antenna alignment scenarios. The Rx node is moved in 10 to15 different locations taking (0.5-1) meters gap (depending on room size) at each step as shown in Fig. 4.2(a). In order to minimize the local fluctuations while characterizing the small-scale fading, a large number of CTF data are captured within a small area around each Rx position. In this campaign the Rx mast is moved around a 4×4 premeasured square grid points (Fig. 4.2(d)) at each location where two adjacent points are separated by λ/2 distance (λ is the corresponding wavelength of $f_R = \sqrt{f_U f_L}$, which is the mean frequency value of C, X and Ku bands, and f_U & f_L are the upper / lower limit of any frequency band)

The measurement campaigns are conducted in the weekends to ensure optimum stationary environment (time-invariant). All entrance points, doors and windows are kept closed while taking the measurement. Minimum twists in the RF cables are ensured while moving the Tx or Rx must confirm negligible environmental variation in each measurement. We take 10 snapshots of the complex CTFs within a specific time interval at each spatial grid points to observe the time invariability of the environments. It is observed that there is no perceptible difference between the measured snapshots in time; hence the channel is assumed to be static in nature. In total, 14K CTF sample data is collected from Site-A, B and C respectively and stored in an external storage device for post processing and subsequent analysis.

4.3 Data Processing and Analysis

4.3.1 Terminal Independent Propagation Channel Response

The radiation pattern of an UWB antenna is frequency dependent [5] and at the same time the measured complex frequency responses are equipment setup and direction dependent. Consequently, the extracted measured data and subsequent analysis are antenna and measurement setup specific, thus unreliable for another setup. As a result, the derived models are also measurement setup specific. A limited number of authors in the open literature have conducted separate calibration of the measurement setup in anechoic chamber to deconvolute the terminal effects. In the previous chapter closed form analytical expressions are devised to derive standalone frequency and time domain channel response excluding the antenna and other terminal effects by a two-port network model approach of the antenna trans-receiver system. The schematic circuit representation is illustrated in Fig. 4.3.

As investigated in the previous chapter, the measured [S] matrix of the radio channel represents the transfer function of the Tx antenna, $TF_{tx}(f,\theta,\varphi)$, Rx antenna $TF_{rx}(f,\theta,\varphi)$ and the trans-receiver system $TF_{Antenna\ System}(f,\theta,\varphi)$ as follows.

$$TF_{tx}(f,\theta,\varphi) = \sqrt{\frac{2S_{21}}{(1-S_{11})(1+S_{22})}\frac{j\omega}{2\pi C_0} r e^{j\beta d}} \tag{4.2}$$

$$TF_{rx}(f,\theta,\varphi) = \sqrt{\frac{2S_{21}}{(1-S_{11})(1+S_{22})}\frac{2\pi C_0}{j\omega} r e^{j\beta d}} \tag{4.3}$$

$$TF_{Antenna\ System}(f,\theta,\varphi) = \frac{S_{21}}{2} \tag{4.4}$$

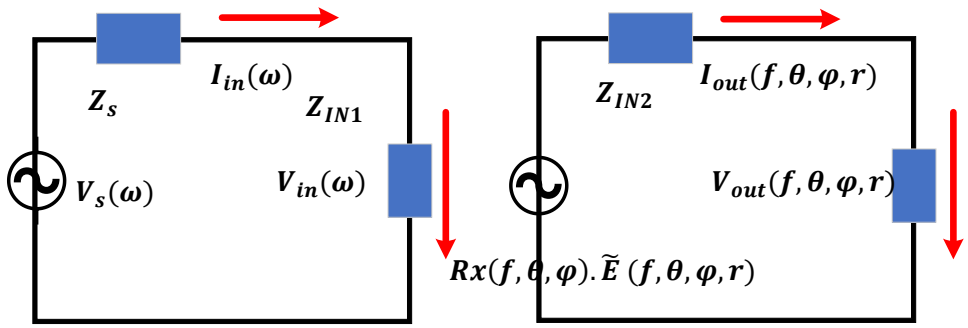

Fig. 4.3 Representation of the Antenna Trans-receiver system in two port network model approach (Cited from Chapter 3, Fig. 3.2)

where C_0, (θ,φ) and r denotes the velocity of light in free space, orientation of the main beam and Tx-Rx separation respectively. From the two-port model the overall system TF can be represented in frequency domain as shown in (4.4).

$$TF_{Antenna\ System} = TF_{tx} \times TF_{Channel} \times TF_{rx} \tag{4.4}$$

where $TF_{Channel}(f,\theta,\varphi)$ denotes the TF of the terminal independent propagation channel response and derived as,

$$TF_{Channel}(\omega,\theta,\varphi) = \frac{TF_{Antenna\ System}}{TF_{Tx}(\omega,\theta,\varphi)\ TF_{Tx}(\omega,\theta,\varphi)} \tag{4.5}$$

Subsequently, the terminal independent time domain CIR can be evaluated by taking Inverse Fast Fourier Transformation (IFFT) as sown below.

$$Impulse\ Response_{Channel}(t,\theta,\varphi) = IFFT[TF_{Channel}(\omega,\theta,\varphi)]$$

4.3.2 Data Processing

All possible measures are taken to ensure time-invariant propagation channel. Also 10 snapshots of the CTFs at different time span at 16 spatial grid points at all Rx position are taken to confirm any time-invariant and non-stationary nature of the channel. Thus, time and space averaged CTF data is considered to nullify any minute time fluctuation in the data with respect to time and space. Subsequently channel impulse responses are evaluated by using IFFT on the CTF's shown in (4.6). Hamming window is used in the IFFT process to ensure nearly 41dB side lobe suppression [6] in the output. Real passband technique is used instead of complex baseband process while performing IFFT. A complete analysis and subsequent advantages of this process for UWB communication is discussed in [7]. To be brief, UWB is principally a career pulse communication system; thus, real pass band is more suitable due to zero padding prior to IFT.

In general, CIR is represented by the ensemble average [2] of the received multipath with varying amplitude, phase and delay as shown in (4.7) which is well-studied in open literature.

$$h(\tau, t; d) = \sum_{i=1}^{L} a_i(t, d) e^{j\theta_i(t,d)} \delta(t - \tau_i) \tag{4.7}$$

a_i, θ_i and τ_i are the amplitude, phase and delay associated with each received multipath component (MPC) of total L number of MPCs. The power delay profile (PDP) is the squared representation of the corresponding CIRs [5] as shown in (4.8).

$$PDP = |h(\tau, t; d)|^2 \tag{4.8}$$

The propagation delay of the first arriving MPC causes an initial time delay in the measured PDPs. Also, the peak powers are varying for different sites and LoS/nLoS scenarios. For the convenience of further analysis, the PDPs are normalized in time and amplitude as discussed in [6]. The normalized PDPs at each spatial grid points are spatially averaged to obtain the averaged small-scale PDP to minimize the local spatial fluctuations. The noise threshold in the PDP is fixed at 40dB below the maximum peak power in the measured PDP to capture at-least 80% of the total MPCs. It is observed that the threshold values of the measured PDPs are always greater than the strongest noise signal present in any specific environment. PDPs measured at C band at Site-A for LoS and nLoS scenarios is displayed in Fig. 4.4. It shows the

existence of multiple clusters with direct, diffuse, and single dominant MPCs with respect to time delay.

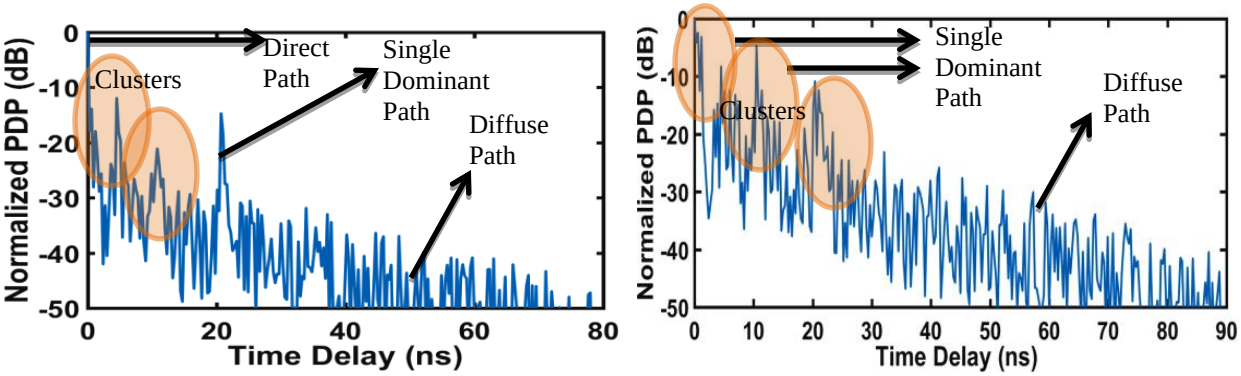

Fig. 4.4 Typical Normalized channel Power Delay Profile (PDP) of sample data measured in C band at Site-A for (a) LOS and (b) nLOS scenarios

4.4 Frequency and Distance dependent Large Scale Channel Model

4.4.1 Frequency Dependent CTF

The propagation channel is sounded by Continuous Wave (CW) for each frequency sample in the VNA (1601 samples at C, X, and Ku band), and the amplitude and phase varying replicas are received at the receiver end. The complex CTF of any specific operating band is thus the vector sum of all these CW replicas as represented in (4.9).

$$CTF = \sum_{i=1}^{N} H(f_i) \tag{4.9}$$

The CTFs for C, X and Ku bands at Site-A for LOS scenarios are shown in Fig. 4.5. The least square linear fit lines for each band are also shown. The frequency dependencies of the propagation channel are evidenced by the decaying exponent of the linear regression lines of the bands. The measured complex CTFs are simply represented by cascading the mean and the small-scale variations as presented in (4.10).

$$H(f) = \overline{H(f)}.|H(f)|_{mean\ Variation} \tag{4.10}$$

where $\overline{H(f)}$ is the small scale variation of the CTFs.

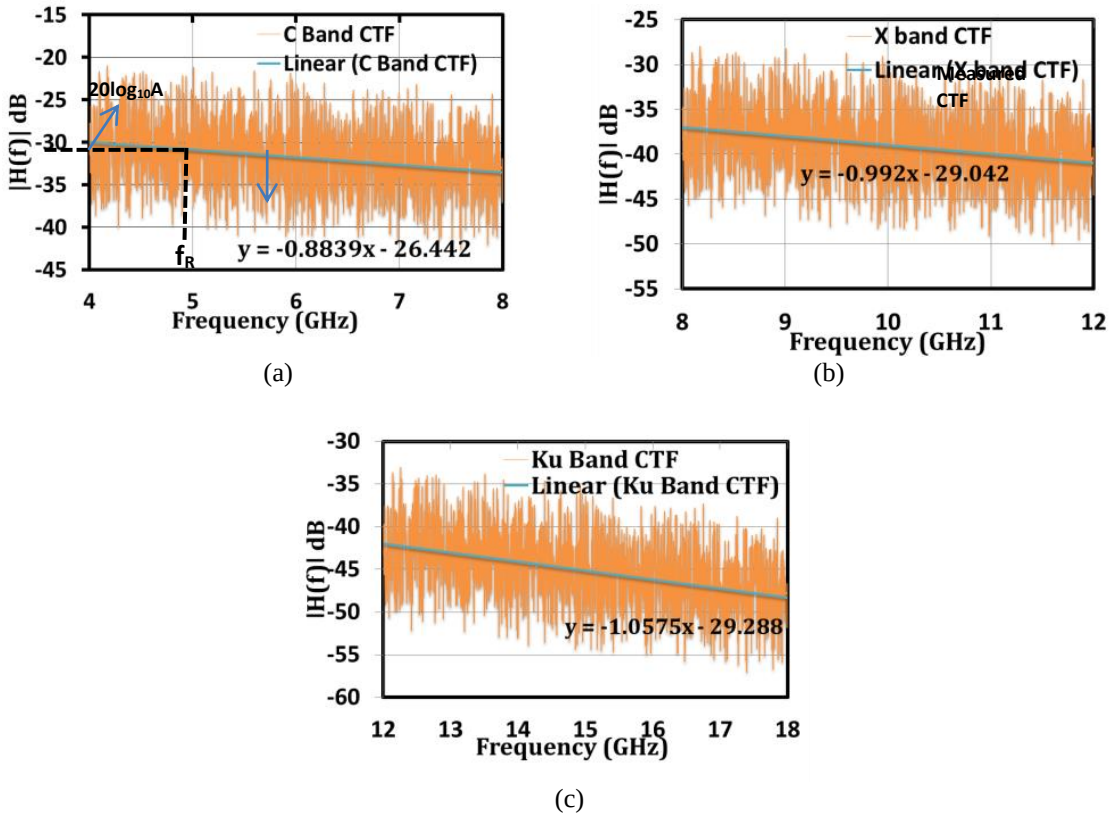

Fig. 4.5 Complex Channel Transfer Function (CTF) of indoor propagation channel at Site-A and corresponding least square linear fit lines of (a) C band, (b) X Band and (c) Ku Band at LOS scenarios.

Authors in the open literature have suggested two methods to represent the frequency dependency of the $|H(f)|$ [36]. In power law representation the complex frequency domain channel response is represented in (4.11).

$$|H(f)|_{mean\,Variation} = A.(f\ /\ f_R)^{-\gamma} \tag{4.11}$$

On the other hand, the exponential variation [37] is presented as below.

$$20log_{10}|H(f)|_{mean\,Variation} = \bar{A}.e^{-\bar{\gamma}f} \tag{4.12}$$

A and γ is the proportionality constant and power exponent respectively. Also f_R is the mean frequency value of each operating band as depicted in Table 4.2. In this work power law is

considered for its wide acceptability in the literature including IEEE 802.15.4a [19] standard for UWB indoor channel modelling.

In frequency domain CTFs are presented by the measured S_{21}; hence transmitted and receive power ratio is presented as below.

$$\frac{P_t}{P_r} = \frac{1}{|H(f)|^2} \tag{4.13}$$

Subsequently, the frequency dependent path loss is given as below.

$$Pl(f) = 10\log_{10}\left(\frac{P_t}{P_r}\right) = 10\log_{10}\frac{1}{|H(f)|^2} = -20\log_{10}|H(f)| = -20\log_{10}\{A.(f\ /\ f_R)^{-\gamma}\}$$

$$or \qquad Pl(f) = -20\log_{10} A + 20\gamma\log_{10}(f\ /\ f_R) \tag{4.14}$$

$$\text{at } f = f_R,\ Pl(f)_R = -20\log_{10} A$$

where $Pl(f)_R$ represents the interception point of the regression lines as shown in Fig. 4.5. The corresponding values at different sites and operating bands are listed in Table 4.3.

TABLE 4.3: EMPIRICAL FREQUENCY DEPENDENT PATH-LOSS PARAMETERS $-20\log_{10} A$ and γ

Locations	Statistical Parameters	C BAND		X BAND		Ku BAND		Antenna Alignment
		Mean	*SD*	*Mean*	*SD*	*Mean*	*SD*	
Site-A	$-20\log_{10} A$ (dB)	30.67	Na	37.11	Na	43.19	Na	LoS
	γ	0.89	0.11	1.1	0.12	1.26	0.12	LoS
	$-20\log_{10} A$ (dB)	33.82	Na	39.29	Na	49.07	Na	NLoS
	γ	0.92	0.13	1.19	0.15	1.31	0.16	NLoS
Site-B	$-20\log_{10} A$ (dB)	29.36	Na	33.31	Na	39.03	Na	LoS
	γ	0.75	0.03	0.89	0.04	1.01	0.06	LoS
	$-20\log_{10} A$ (dB)	27.55	Na	35.78	Na	44.67	Na	NLoS
	γ	0.82	0.5	0.85	0.05	1.13	0.07	NLoS
Site-C	$-20\log_{10} A$ (dB)	31.92	Na	34.82	Na	41.65	Na	LoS
	γ	0.63	0.06	0.99	0.07	0.96	0.08	LoS
	$-20\log_{10} A$ (dB)	32.21	Na	36.48	Na	43.98	Na	NLoS
	γ	0.86	0.09	1.03	0.1	0.99	0.7	NLoS

4.4.2 Distance dependent CTF

In (4.13), $Pl(f)_R$ is the path loss at a specific reference frequency f_R at a distance d. From the measured complex frequency response data $H(f_i, t_j : d)$ the path loss is measured as follows [2].

$$Pathloss(d) = \frac{1}{pq}\sum_{i=1}^{p}\sum_{j=1}^{q}\frac{1}{|H(f_i,t_j:d)|^2} \quad (4.15)$$

where p is the frequency range or samples and q is the snapshots of the frequency responses within specific measurement span at a distance d. Depending upon the environment the received signal power is varied by $1/d^{\alpha}$, where α is the path-loss exponent. Thus the distance dependent path loss expression in dB considering channel fading caused by different physical phenomenon [4.8-4.13] is define in (4.16).

$$Path_{Loss}(d)|_{dB} = PL_0 + 10\alpha \log\left(\frac{d}{d_0}\right) + \mathcal{X}_{\sigma}(d) d > d_0 \quad (4.16)$$

where PL_0(intercept point) is the path loss at $d_0 = 1m$, $10\alpha \log(d/d_0)$is the mean path loss with respect to d_0 and $\mathcal{X}_{\sigma}(d)$ is the log-normal shadow fading in dB.

I. Scattering Plot

Figures 4.6(a) and 4.6(b) show the scatter plot of (4.16) in the C, X, and Ku bands in Site-A for LOS and nLOS scenarios, respectively. The loss exponents and intersection locations are calculated using the least square linear fit lines. Shadow fading corresponds to deviation from the Least square linear fit line. The spatially varying shadow fading ($\mathcal{X}_{\sigma}$(d)) is also observed to be normally distributed.

It is apparent in the above plots that shadow fading increases for higher frequency bands and nLOS condition as a result of larger attenuation and increased MPCs. At higher frequency bands small objects become comparable with the operating wavelengths hence scattered the impinging signals which increases the loss. All distance dependent path-loss parameters such as PL_0, α and $\mathcal{X}_{\sigma}$ are measured at Site-A, Site-B and Site-C respectively in C, X and Ku bands and arranged in Table 4.3.

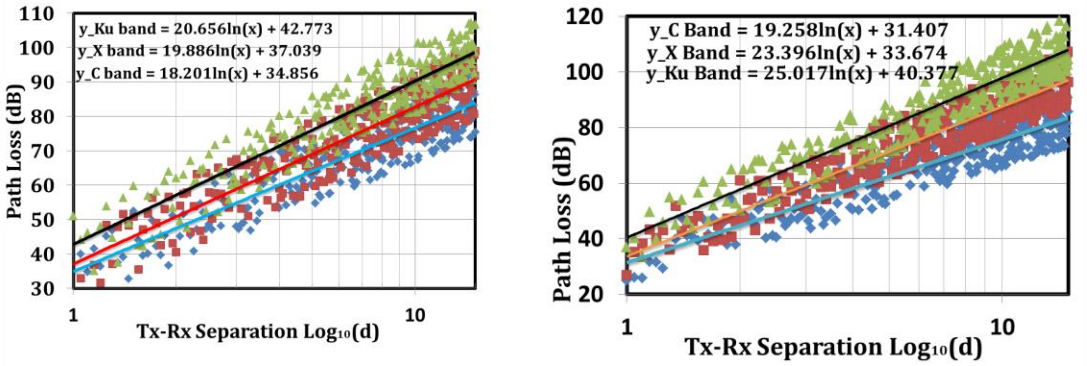

(a) (b)

Fig. 4.6 Scattering plot of spatially varied time averaged pathloss data of indoor propagation channel at Site-A in C, X, and Ku Bands with corresponding least square linear fit line in (a) LOS and (b) nLOS scenarios.

II. Findings from scattering plots

Few important conclusions are devised from the analysis of the statistical distributions of the measured large scale channel parameters as follows.

Intercept Point (PL_0): It is the signal strength at 1m distance from Tx antenna. The measured PL_0 for nLOS and LoS are very similar as shown in Table 4.3. This is attributed to the absence of any obstacle within 1m of T-R separation. Though intercept values reduce slightly with higher frequency bands due to higher losses.

TABLE 4.4: STATISTICAL DATA OF DISTANCE DEPENDENT PATHLOSS PARAMETERS PL_0, α, AND $\mathcal{X}_\sigma$

Locations		C BAND		X BAND		Ku BAND		Antenna Alignment
		Mean	*SD*	*Mean*	*SD*	*Mean*	*SD*	
SITE-A	PL_0(dB)	25	Na	31	Na	28	Na	LOS
	α	1.8	0.2	2.1	0.4	2.5	0.6	LOS
	$\mathcal{X}_\sigma$(dB)	2	0.3	2.5	0.5	3.1	0.7	LOS
	PL_0(dB)	37	Na	36	Na	38	Na	NLOS
	α	2.6	0.9	3.7	1.2	4.5	1.8	NLOS
	$\mathcal{X}_\sigma$(dB)	2.3	0.4	2.9	0.8	3.6	1.2	NLOS
SITE-B	PL_0(dB)	25	Na	31	Na	28	Na	LOS
	α	1.8	0.2	2.1	0.4	2.5	0.6	LOS
	$\mathcal{X}_\sigma$(dB)	2	0.3	2.5	0.5	3.1	0.7	LOS
	PL_0(dB)	37	Na	36	Na	38	Na	NLOS
	α	2.6	0.9	3.7	1.2	4.5	1.8	NLOS
	$\mathcal{X}_\sigma$(dB)	2.3	0.4	2.9	0.8	3.6	1.2	NLOS
SITE-C	PL_0(dB)	25	Na	31	Na	28	Na	LOS
	α	1.8	0.2	2.1	0.4	2.5	0.6	LOS
	$\mathcal{X}_\sigma$(dB)	2	0.3	2.5	0.5	3.1	0.7	LOS
	PL_0(dB)	37	Na	36	Na	38	Na	NLOS
	α	2.6	0.9	3.7	1.2	4.5	1.8	NLOS
	$\mathcal{X}_\sigma$(dB)	2.3	0.4	2.9	0.8	3.6	1.2	NLOS

Shadow fading ($\mathcal{X}_\sigma$): $\mathcal{X}_\sigma$ shows zero mean Gaussian distribution in any specific location. The Cumulative Distribution Functions (CDF) plot of $\mathcal{X}_\sigma$ at Site-B for C, X and Ku bands at LoS and nLoS alignments are shown in Fig. 4.7.

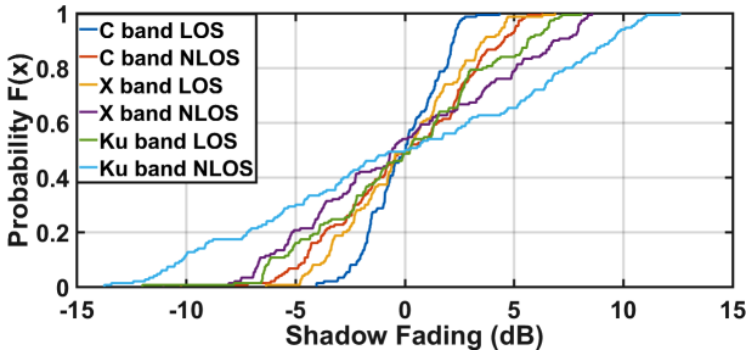

Fig. 4.7 CDF plot of shadow fading $\mathcal{X}_\sigma$ at three distinct operating bands and LOS/nLOS scenarios at Site-B.

It is interesting to note that at specific frequency band the standard deviation of the shadow fading is normally distributed over multiple sites with varying mean and alignment scenarios (LoS and nLoS). As an example, Fig. 4.8 illustrates the CDF plot of standard deviation σ_s of $\mathcal{X}_\sigma$ at C band at Site-A, Site-B and Site-C respectively for LoS and nLoS scenarios.

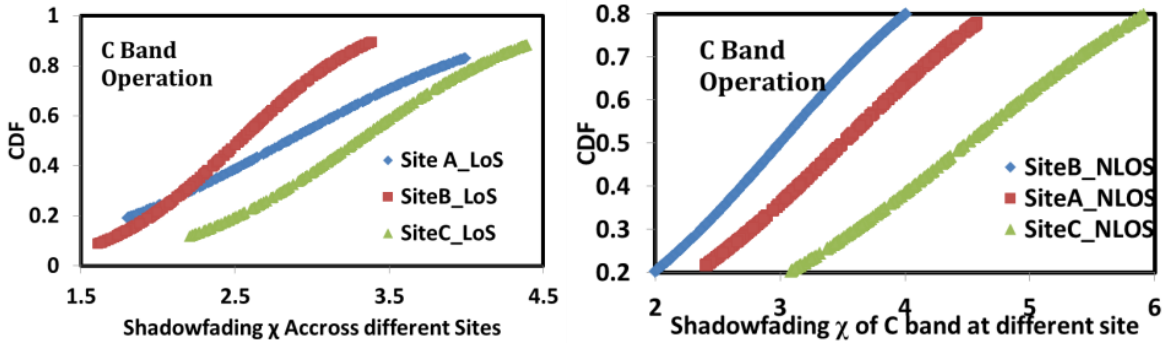

Fig. 4.8 CDF plot of standard deviation σ_s of shadow fading $\mathcal{X}_\sigma$ at C band for LoS and nLoS scenario at Site-A for (a) LoS and (b) nLoS scenario

It is also noted that at any specific location the σ_s also normally distributed for multiple frequency bands and alignment scenarios. As shown in Fig. 4.9, the CDF plot of standard deviation σ_s at C, X and Ku bands at Site-A for LoS and nLoS conditions are normally distributed.

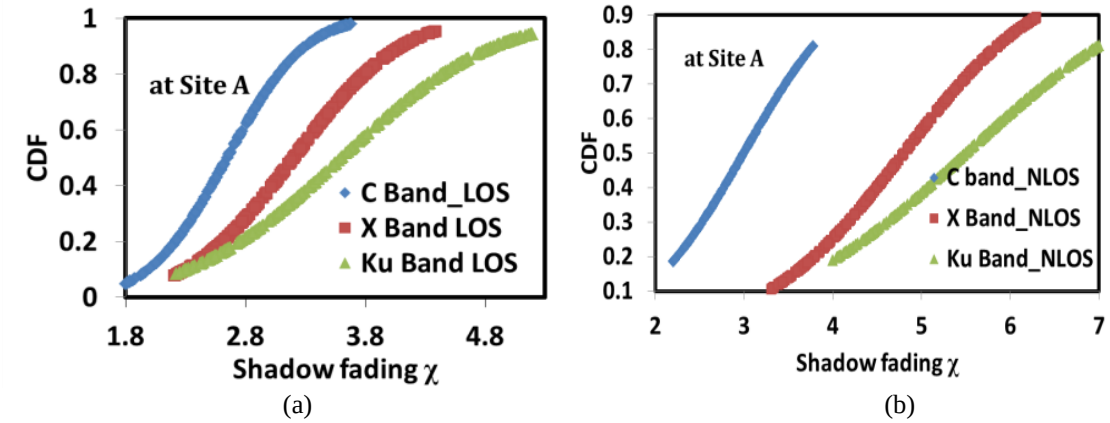

(a) (b)

Fig. 4.9 CDF plot of σ_s of $\mathcal{X}_\sigma$ for C, X and Ku band at Site-A for (a) LOS and (b) nLOS scenarios.

Site-A (Laboratories) shows larger variation due to the presence of large number of scatterers, while Site-B shows least variation as it represents the corridors with least scatterer. The corridors are constructed in the shape of a rectangular tunnel, which acts as a guided structure for RF transmission. It is observed that statistical means μ of σ_s is gradually shifted to higher values for higher frequency bands due to larger fluctuations in the received signal. It increases further in nLoS scenarios which are attributed to the presence of obstructions in direct path. Probability of the statistical mean μ of the standard deviation σ_s in random rooms at Site A, B and C in LoS and nLoS scenarios are found to be normally distributed as shown in Fig. 4.10.

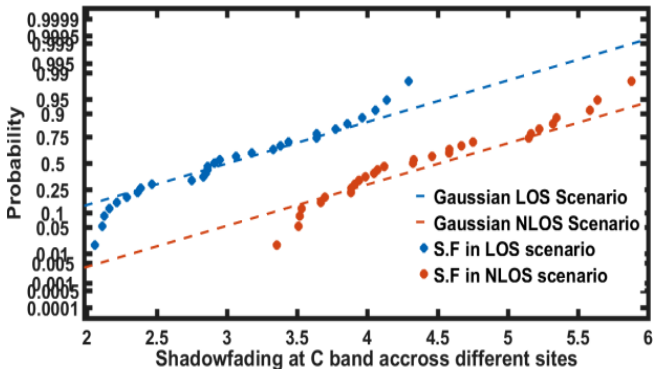

Fig. 4.10 Probability of the statistical mean μ of the standard deviation σ_s of the shadow fading in random multiple rooms at Site A, B and C in LoS and nLoS scenarios and found to be normally distributed.

Pathloss exponent(α): Pathloss exponent α distributed normally $(\mu_\alpha, \sigma_\alpha)$for spatial variations in any specific site. The exponent α in C, X and Ku band at Site-A for different Tx-Rx

alignments is depicted in Fig. 4.11. It is noted that at higher frequencies the losses and subsequently the exponents also increase.

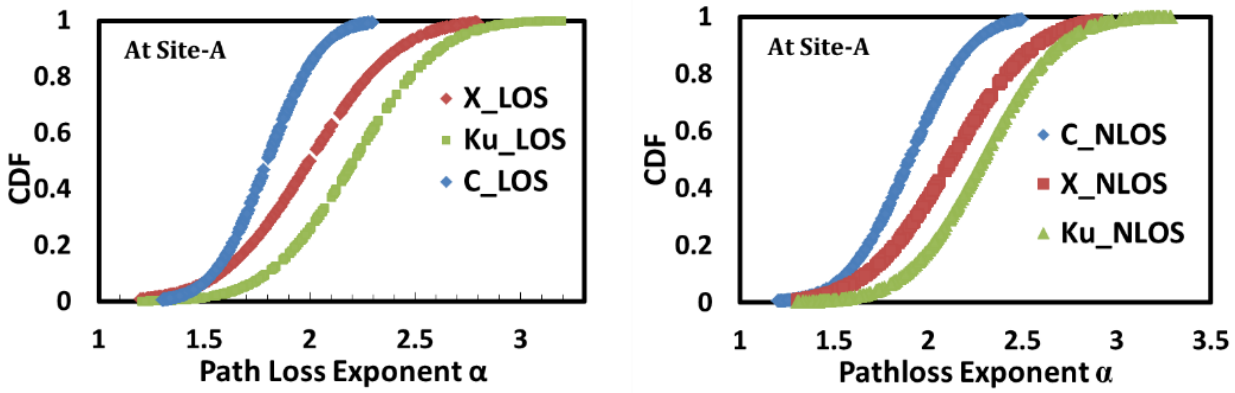

(a) (b)

Fig. 4.11 CDF plot of α for C, X and Ku band at Site-A for (a) LOS and (b) nLOS scenarios.

Fig. 4.12 shows the variation of α for C band at Site-A, Site-B and Site-C at LoS and nLoS respectively. In nLoS scenarios the exponent is increased slightly due to the non-existence of any direct path between the Tx-Rx antennas. Site-A depicts the largest variation in the loss exponent, whereas Site-B has the least fluctuation.

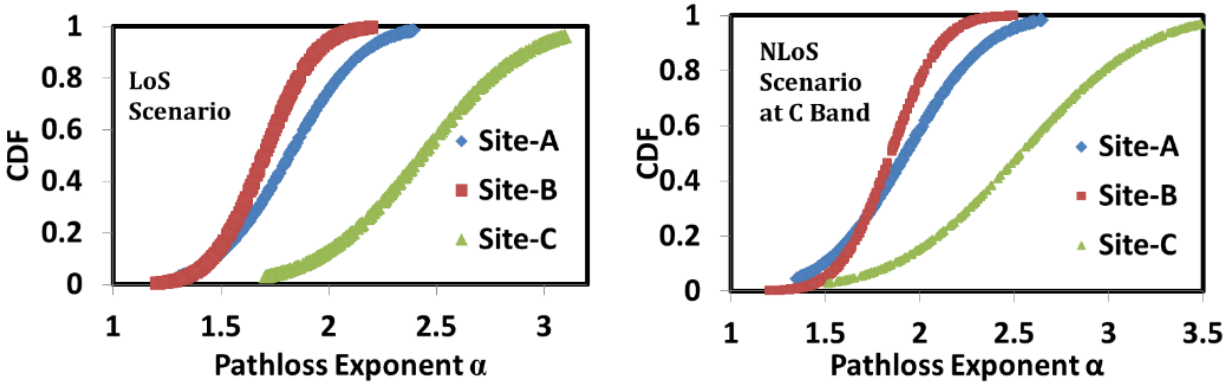

(a) (b)

Fig. 4.12 CDF plot of α at C band at Site-A for (a) LOS and (b) nLOS scenario

Fig. 4.13 shows the path loss exponent for multiple random locations in Site-A, B and C are normally distributed. For nLOS conditions the exponents are slightly larger.

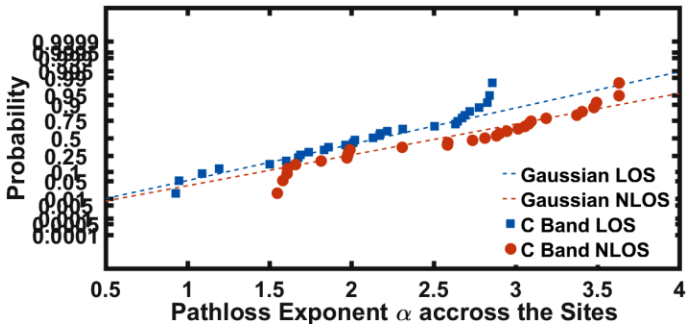

Fig. 4.13 Probability distribution of pathloss exponent in multiple indoor environments in Site A, B and C respectively in LoS and NLoS scenarios along with the normally distributed line.

4.4.3 Large Scale Pathloss Model

A simple large scale statistical path loss model for UWB propagation in indoor environments is proposed based on data from 14K measured samples in the C, X, and Ku bands for LoS and nLoS situations. The intercept point remains invariable as discussed earlier. Pathloss exponents are shown to be normally distributed, $\mathcal{N}(\mu_\alpha, \sigma_\alpha)$. Hence loss exponent is represented as follows.

$$\alpha = \mu_\alpha + k_1\sigma_\alpha \tag{4.17}$$

where k_1 is a zero-mean Gaussian variate of unit standard deviation N[0,1]. Shadow fading $\mathcal{X}_\sigma$is also follow Gaussian distribution with zero mean.

$$\text{Thus, } \mathcal{X}_\sigma = k_2\sigma \tag{4.18}$$

We observe that the standard deviation of shadow fading is a random variable and normally distributed over all the measurement locations as discussed in the last section.

$$\text{Hence, } \sigma = \mu_s + k_3\sigma_s \tag{4.19}$$

k_2 and k_3 in (4.18) and (4.19) are zero-mean Gaussian variate of unit standard deviation N[0,1]. Rearranging (4.16) to (4.19) the pathloss equation can be rearranged as follows.

$$Path_{Loss}(d)|_{dB} = PL_0 + 10\alpha \log\left(\frac{d}{d_0}\right) + \mathcal{X}_\sigma(d)$$

$$= PL_0 + 10(\mu_\alpha + k_1\sigma_\alpha)\log\left(\frac{d}{d_0}\right) + k_2\sigma$$

$$= PL_0 + 10(\mu_\alpha + k_1\sigma_\alpha)\log\left(\frac{d}{d_0}\right) + k_2(\mu_s + k_3\sigma_s)$$

$$=[PL_0 + \underbrace{10\mu_\alpha \log\left(\frac{d}{d_0}\right)}_{1^{st}}] + \{\underbrace{10k_1\sigma_\alpha \log\left(\frac{d}{d_0}\right) + k_2\mu_s + k_2k_3\sigma_s}_{2^{nd}}\} \quad (4.20)$$

The 1st and 2nd term of (20) represents the median path loss and random variation. The 2nd term is not exactly Gaussian as $(k_2 \times k_3)$ shows non-Gaussian nature. However, this product is negligibly small in comparison to other two Gaussian terms. Thus the 2nd term can be estimated to zero mean random variate. Standard deviation of the 2nd term is derived as follows.

$$\sigma_{variance} = \sqrt{100{\sigma_\alpha}^2(\log\left(\frac{d}{d_0}\right))^2 + {\mu_s}^2 + {\sigma_s}^2}$$

Thus, using this proposed statistical model as derived in (4.20) the received signal can be simulated using the statistical variations of different large-scale parameters listed in Table 4.4.

4.5 Frequency Domain Channel Model

In the previous section large scale fading is characterized by frequency and distance dependent statistical models. In this section the small-scale variations of the CTFs are investigated using frequency domain Autoregressive (AR) process to model the small scale indoor fading channel. In general, the time domain AR process is applied for spectral estimation [38]. Similar approach is invoked in frequency domain to model the measured complex frequency responses in an indoor propagation channel [7, 10, 14]. Complex CTFs can be represented by r^{th} order AR process as illustrated in (4.21) [16].

$$H(f_n, t; d) = \sum_{i=0}^{r} A_i H(f_{n-r}, t; d) + N(f_n) \quad (4.21)$$

where, n: 1,2,3, ... N; N is the total frequency samples of the VNA (1601samples), $H(f_n, t; d)$ is the complex CTF of n^{th} sample at distance d and A_i is the complex model coefficient. $N(f_n)$ is the n^{th} sample of the independent and identically distributed $(i.i.d)$ complex white noise process with zero-mean and σ_N^2 variance. Consequently, $H(f_n, t; d)$ is represented by an all-pole linear Infinite Impulse Response filter (IIR) in (4.22), where the input of the filter is the white Gaussian process [19]. The transfer function of the AR process is derived in (4.23).

$$H(z) = \sum_n H(f_n)\, Z^{-n} \tag{4.22}$$

$$G(z) = {H(z)}\Big/{N(Z)}$$

$$G(z) = \frac{1}{1-\sum_{i=0}^{r} A_i z^{-i}} = \prod_{i=1}^{r} \frac{1}{1-A_i z^{-1}} \tag{4.23}$$

The AR coefficients A_i can be derived using Ordinary Least Square procedure or from the solution of method of moment-based Yule-Walker equations. These processes are well established and discussed in detail in the open literature [17]. In brief, the solution can be obtained by taking the autocorrelation of (4.21) as follows.

Thus, $R_{HH}(q) = \sum_{i=1}^{r} H(f_n)H(f_{n-q})$

$$= \sum_{i=1}^{r} A_i R_{HH}(q-i) + \sigma_N^2\, \delta(q)$$

{ $\delta(.)$ Is the delta function}

Putting $q = -q$, $\quad R_{HH}(-q) = \sum_{i=1}^{r} A_i R_{HH}(i-q) + \sigma_N^2\, \delta(-q), \quad q > 0$

$$= \sum_{i=1}^{r} A_i R_{HH}(i-q) \tag{4.24}$$

Further the variance of the white noise excitation σ_N^2 is derived by putting $q = 0$;

$$R_{HH}(0) = \sum_{i=1}^{r} A_i R_{HH}(i) + \sigma_N^2\, \delta(0)$$

$$\sigma_N^2 = R_{HH}(0) - \sum_{i=1}^{r} A_i R_{HH}(q) \tag{4.25}$$

It is noted that the proposed AR model does not includes any initial condition hence the complexities are decreased with respect to the previously proposed AR models [9].

4.5.1 Order selection of the AR model

In the literature authors have suggested many methods to find the orders of AR process such as SVD (singular value decomposition) [40] and AIC (Akaike's Information Criterion). The AIC method is represented in (4.26) and well discussed in [16].

$$AIC = \log(l) + 2n/N \tag{4.26}$$

where l is the loss function, n and N are the number of estimated parameters and data respectively. In a nutshell, as the model order increases, the AIC value decreases. It is also noted that AIC values change insignificantly beyond a certain higher order, and this order number is chosen for the optimal model estimation. It is also noticed that as the model's order increases, so does its complexity; consequently, a tradeoff between model order estimation and complexity is asserted.

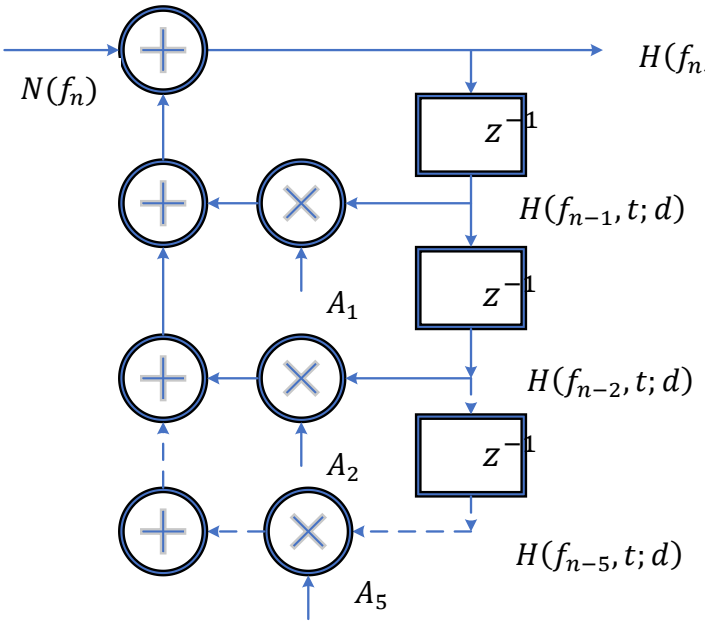

$$\begin{aligned} H(f_n, t; d) + \\ A_1 H(f_{n-1}, t; d) + \\ Aa_2 H(f_{n-2}, t; d) + \\ A_3 H(f_{n-3}, t; d) + \\ AH(f_{n-4}, t; d) + \\ A_5 H(f_{n-5}, t; d) = N(f_n) \end{aligned} \tag{4.27}$$

Fig. 4.14(a) Schematic representation of IIR filter model of the 5th order AR process as derived in (4.27)

It is suggested in the literature [10] that a 2nd order AR process is sufficient to model the indoor and underground tunnel environment to characterize an UWB channel. Chandra et al. proposed a 5th order AR model [7] within a vehicular environment. Authors in [7] compare the

measured PDP with the computer simulated 2nd and 5th order model data. It shows that 5th order model data matches very well with the measured data, specifically the power peaks of the received power of the first and subsequent clusters; but slightly delayed in case of 2nd order AR model. In our work we abstain from rigorous derivation of partial autocorrelation and subsequent AIC to find the order number; rather proceed with 5th order as proposed in most of the previous work for indoor channel modeling. The representation of the 5th order model is shown in (4.27).

I. Characterization of the model Parameters

The Poles of the model: Frequency domain AR model can be represented by the poles of its transfer function in (4.22). Each pole represents a cluster of reflectors where from the propagated signals get reflected. In time domain spectral estimation using AR process, the poles closer to the unit circle shows higher power at a specific frequency associated with the argument of the pole; thus, the frequency can be derived from the argument or angle of that pole [7, 14] as follows.

$$f_{pi} = \text{argument}(p_i) \Big/ (2\pi t_s) \tag{4.28}$$

where p_i is the p-th pole and t_s is the sampling period. Subsequently in frequency domain approach, the poles closer to the unit circle depict significant power at the delay associated with the argument of the pole; thus, the delay associated with a specific pole [7, 14] is derived as below.

$$delay_{pi} = \text{argument}(p_i) \Big/ (2\pi f_s) \tag{4.29}$$

where f_s represents the sampling frequency. The poles closer to the unit circle have larger impact on the cumulative power of the power delay profiles (PDP). The power of the poles reduced gradually as shift away from the unit circle. The amplitude and phase of each pole of the 5th order AR model is derived from the transfer function of the AR filter and listed in Table V for C, X and Ku in LoS and nLoS scenarios at SITE-A. The poles are considered for the Tx-Rx separation at 2, 4, 6, 8 and 10 m respectively. It is important to note that poles are distinctly

located in five different areas where each area defines the multipath cluster. It's important to note that as the number of poles increases, the argument of the poles increases as well, resulting in an increase in the required time to reflect from the specific cluster. The poles are also shifted away from the unit circle with increasing delay, indicating that the poles have smaller amplitude. Poles with longer delays and smaller amplitudes have a minor contribution to the model parameters. It's worth noting that when operating frequencies rise, the pole disperses, the amplitude decreases hence the poles move away from the unit circle, as seen in Fig. 4.14(b).

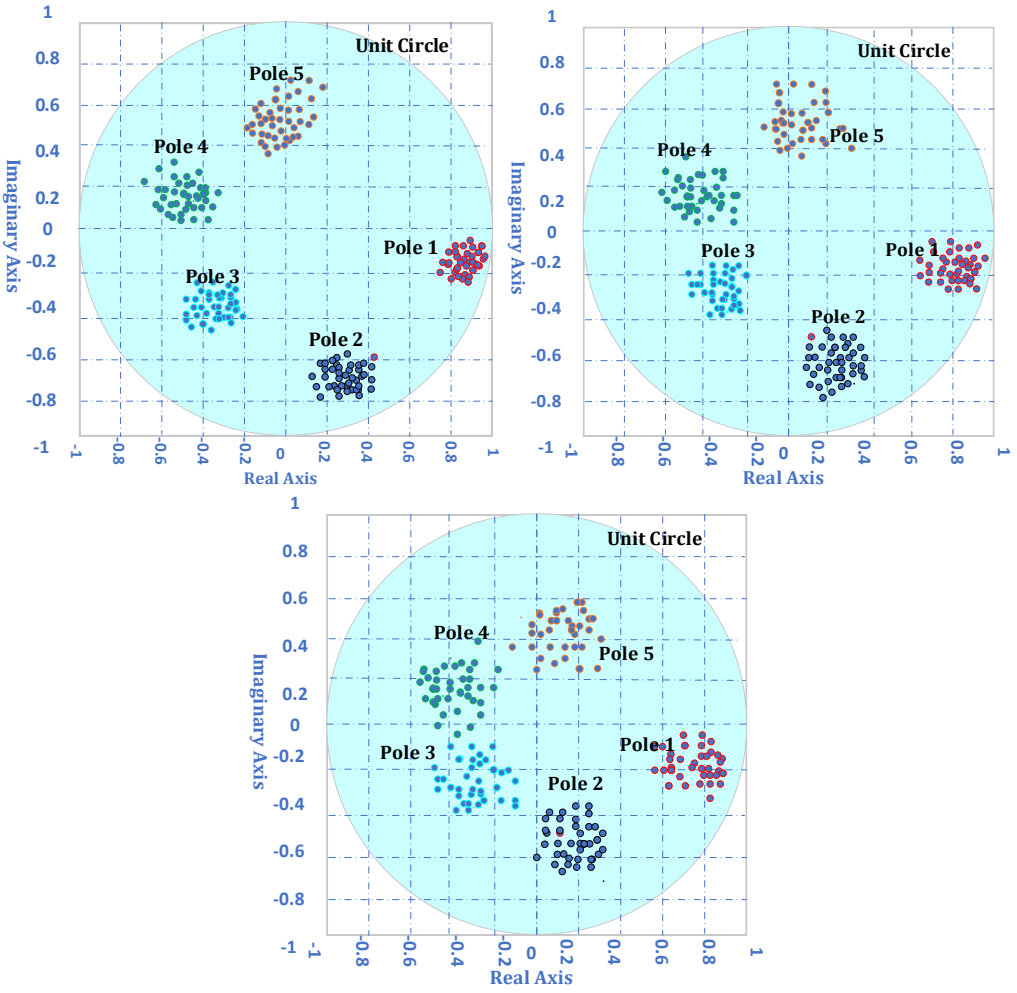

Fig. 4.14(b) Complex Z–plane scatter plot of 5th order AR model of C, X and Ku band LOS scenarios.

It's important to note that the poles in SITE-A are the most dispersed due to the presence of numerous scatterers at the Laboratories, whilst the corridors in SITE-B are the least dispersed due fewest scatterers. Many of these places may contain a considerable number of clusters, but

the transmitted signal is dispersed or reflected (many times) in the path where the overall contribution of these MPCs to the cumulative PDP are negligible, therefore ignored.

TABLE 4.5: AMPLITUDE AND PHASE OF EACH POLE OF THE 5TH ORDER AR MODEL FOR C, X AND KU BAND AT **LOS** SCENARIO

Freq. and Alignment	Tx-Rx Gap (m)	IID Noise variance	Poles Amplitude					Poles Phase				
			$\|p_1\|$	$\|p_2\|$	$\|p_3\|$	$\|p_4\|$	$\|p_5\|$	$rad\ p_1$	$rad\ p_2$	$rad\ p_3$	$rad\ p_4$	$rad\ p_5$
C Band And LOS scenario	2	0.031854	0.9917	0.8767	0.8013	0.7102	0.6213	-0.1024	-1.7564	-2.892	2.3563	1.8901
	4	0.048703	0.9867	0.8871	0.7983	0.6951	0.6621	-0.2327	-1.8525	-2.2987	2.5629	1.7536
	6	0.059993	0.9921	0.8624	0.8761	0.6501	0.6011	-0.3478	-1.5567	-2.9043	2.1246	1.6730
	8	0.126358	0.9654	0.8431	0.8103	0.7011	0.5809	-0.1935	-1.6453	-2.8965	2.1035	1.5622
	10	0.111819	0.9756	0.8962	0.7503	0.6601	0.5533	-0.2015	-1.8957	-3.1021	1.9097	2.0014
X Band And LOS scenario	2	0.031403	0.8823	0.6134	0.5022	0.4897	0.3879	-0.2091	-1.8980	-3.0132	1.9903	1.0912
	4	0.034295	0.8711	0.6632	0.5591	0.4011	0.4022	-0.1930	-2.1093	-2.9981	1.7893	1.2034
	6	0.062599	0.8021	0.7012	0.5602	0.3901	0.4590	-0.1568	-2.6712	-2.8356	2.0178	1.3901
	8	0.074846	0.9045	0.7123	0.4971	0.4427	0.3709	-0.1927	-1.8945	-2.4783	2.1125	1.3452
	10	0.094372	0.8911	0.6539	0.5788	0.4711	0.3786	-1.1023	-1.7623	-3.0013	2.0183	1.5632
Ku Band And LOS scenario	2	0.056437	0.8051	0.7745	0.4423	0.3345	0.2214	-0.1309	-1.2674	-2.8934	2.9003	1.8963
	4	0.059015	0.7984	0.7046	0.3902	0.4209	0.3592	-0.2893	-1.7923	-1.8934	2.0456	1.5683
	6	0.061952	0.8820	0.6907	0.5390	0.4021	0.3103	-0.3278	-1.9091	2.9901	2.8945	1.9974
	8	0.0984646	0.8233	0.7305	0.5582	0.3734	0.2904	-0.7893	-2.2673	-3.1066	2.2351	2.1061
	10	0.1625745	0.7756	0.6890	0.4284	0.3906	0.3401	-1.0123	-2.0912	2.9879	1.9034	2. 0034

TABLE: 4.6 AMPLITUDE AND PHASE OF EACH POLE OF THE 5TH ORDER AR MODEL FOR C, X AND KU BAND AT **NLOS** SCENARIO

Freq. and Alignment	Tx-Rx Gap (m)	IID Noise variance	Poles Amplitude					Poles Phase				
			$\|p_1\|$	$\|p_2\|$	$\|p_3\|$	$\|p_4\|$	$\|p_5\|$	$rad\ p_1$	$rad\ p_2$	$rad\ p_3$	$rad\ p_4$	$rad\ p_5$
C Band And nLOS scenario	2	0.1455036	0.9834	0.8032	0.7745	0.6902	0.5129	-0.1561	-1.8934	-2.6734	2.7845	1.4562
	4	0.1817289	0.9735	0.8523	0.7763	0.8034	0.7021	-0.2561	-1.7845	-2.3471	2.7882	1.6653
	6	0.1493972	0.9839	0.8203	0.8201	0.8890	0.5204	-0.4351	-1.6731	-2.9901	2.4523	1.5671
	8	0.1487003	0.9766	0.8022	0.7590	0.7103	0.5572	-0.5682	-1.7821	-2.6735	2.0034	1.3212
	10	0.2062462	0.9482	0.9012	0.8837	0.7506	0.6688	-0.3671	-1.9967	-3.0451	1.8956	1.8914
X Band And nLOS scenario	2	0.1033449	0.9023	0.6501	0.6893	0.5094	0.4021	-0.2271	-2.1452	-2.9995	1.9903	0.9912
	4	0.1595339	0.8893	0.7034	0.4803	0.4426	0.6565	-0.2034	-2.3619	.78311	1.7893	1.0034
	6	0.1785711	0.7906	0.7123	0.6245	0.5205	0.6670	-0.2893	-2.8748	-2.4321	2.0178	0.9901
	8	0.1611253	0.9201	0.7967	0.5807	0.4072	0.4108	-0.3903	-2.0983	-2.9197	2.1125	0.9452
	10	0.1680049	0.7934	0.8022	0.5572	0.5901	0.3909	-1.0017	-1.9673	3.0061	2.0183	1.4521
Ku Band And nLOS scenario	2	0.1201249	0.7834	0.5994	0.3945	0.3084	0.4120	-0.1783	-1.3782	-2.7634	2.7659	1.7851
	4	0.1547589	0.9031	0.8126	0.6023	0.3399	0.2790	-0.3482	-1.8970	-1.9839	1.9878	1.4072
	6	0.1561856	0.8934	0.7309	0.4892	0.4098	0.4044	-0.6581	-1.7869	2.5672	2.5673	1.8760
	8	0.1455036	0.8367	0.7745	0.5901	0.4691	0.3788	-0.9981	-2.1183	2.9988	2.0121	1.0045
	10	0.1817289	0.7936	0.6923	0.4439	0.2901	0.3167	-1.1097	-2.3289	-2.7896	2.0099	1.9932

It is interesting to observe that the amplitude variation of the poles in each cluster are negligible hence the poles amplitudes can be represented simply by taking the average of all the poles in any specific cluster. Thus, the averaged poles for 5th order AR process for C, X and Ku bands are shown below for LoS scenarios for SITE-A.

Poles for nLoS scenarios are also derived in similar way. Also, the pole arguments are related with the corresponding delay of the clusters using (4.30). It is noted that the phase of the poles at each cluster is gradually increasing in nature; hence the phases are presented using linear regression line based on Tx and Rx separation. The lines for C, X and Ku bands at three different sites for LoS scenario are shown below. The lines for nLoS condition are also derived in similar way.

$$\left.\begin{array}{l} SITE-A \quad |P_n^{C\ Band}| = \begin{pmatrix} 0.9823 \\ 0.8731 \\ 0.7027 \\ 0.6833 \\ 0.6037 \end{pmatrix}, \ |P_n^{X\ Band}| = \begin{pmatrix} 0.8702 \\ 0.6688 \\ 0.5394 \\ 0.4389 \\ 0.3997 \end{pmatrix}, \ |P_n^{Ku\ Band}| = \begin{pmatrix} 0.8168 \\ 0.7178 \\ 0.4716 \\ 0.3843 \\ 0.3042 \end{pmatrix} \\ SITE-B \quad |P_n^{C\ Band}| = \begin{pmatrix} 0.9352 \\ 0.8450 \\ 0.8934 \\ 0.8390 \\ 0.8211 \end{pmatrix}, \ |P_n^{X\ Band}| = \begin{pmatrix} 0.8392 \\ 0.7192 \\ 0.6932 \\ 0.6502 \\ 0.6262 \end{pmatrix}, \ |P_n^{Ku\ Band}| = \begin{pmatrix} 0.8277 \\ 0.7234 \\ 0.7630 \\ 0.6972 \\ 0.5941 \end{pmatrix} \\ SITE-C \quad |P_n^{C\ Band}| = \begin{pmatrix} 0.9569 \\ 0.7781 \\ 0.5781 \\ 0.5170 \\ 0.5041 \end{pmatrix}, \ |P_n^{X\ Band}| = \begin{pmatrix} 0.8657 \\ 0.6790 \\ 0.4998 \\ 0.4892 \\ 0.3767 \end{pmatrix}, \ |P_n^{Ku\ Band}| = \begin{pmatrix} 0.8345 \\ 0.6091 \\ 0.4672 \\ 0.4011 \\ 0.3245 \end{pmatrix} \end{array}\right\}$$

$$for\ n = 1, 2, 3, 4, 5 \tag{4.30}$$

$$\left.\begin{array}{l} \text{SITE-A} \left\{\begin{array}{l} P_d^C = -0.0676 \times d + 2.617 \\ P_d^X = -0.0738 \times d + 1.432 \\ P_d^{Ku} = -0.0915 \times d + 1.309 \end{array}\right. \\ \text{SITE-B} \left\{\begin{array}{l} P_d^C = -0.0284 \times d - 2.331 \\ PP_d^X = -0.0341 \times d + 0.092 \\ P_d^{Ku} = -0.0501 \times d + 2.114 \end{array}\right. \\ \text{SITE-C} \left\{\begin{array}{l} P_d^C = -0.0391 \times d + 1.997 \\ P_d^X = -0.0489 \times d + 0.552 \\ P_d^{Ku} = -0.0699 \times d + 0.0054 \end{array}\right. \end{array}\right\} \tag{4.31}$$

II. Input Noise of the Model

The AR process is initiated by the zero mean complex Gaussian noise as shown in (4.27) and the corresponding variances are listed in Table 4.4. It can be assessed from the table that the variance is slightly increased with the TX-Rx separation and independent of frequency variation.

It is well established that Tx-Rx separation and LOS/nLoS scenarios affect the large-scale fading parameters instead of small-scale parameters; hence observed minimal variation of the variance. Thus, the variance for three different bands and LoS/nLoS scenarios is represented using a single distance dependent regression line. Basically, insignificant variation of the variance in multiple operating bands and Tx-Rx separation is noted; hence the average of the exponent and interception values is taken to represent the single regression line as below.

$$(\sigma_n^2)_C = 0.0083 \times d + 0.0096 \tag{4.32}$$

This approach also reduces the numbers of the input parameters hence significantly reduces the complexities of the model.

4.6 Computer Simulation and Model Validation

4.6.1 Distance dependent Large Scale Pathloss Model estimation based on frequency domain measurement.

I. *Estimation of PL_0, α, and $\mathcal{X}_\sigma$:* From the scattering plot of the distance dependent empirical path loss data and subsequent least square linear fit line the statistical values of PL_0, α, and $\mathcal{X}_\sigma$ are derived and listed in Table 4.4.

II. *Formulation statistical model:* From the above estimation α and $\mathcal{X}_\sigma$ are found to be normally distributed in different locations. Also, the standard deviation of $\mathcal{X}_\sigma$ is normally distributed; hence a distance dependent statistical pathloss model is devised based on above analysis and shown in (4.20).

III. *Generating Model Data:* The statistical values mentioned in table 4.4 and the extracted data from the plots (Fig. 4.8 and Fig. 4.9) are used in the proposed large-scale model (4.20) to generate synthetic model pathloss data based on the type of the site, operation frequency, and alignment (LoS/ nLoS).

4.6.2 Estimation of complex CTF or $H(f)$ using proposed frequency domain channel model

In this proposed model the complex CTFs are presented as $H(f) = \overline{H(f)}.|H(f)|$; hence we separately derive the mean $|H(f)|$ and small scale CTF variation $\overline{H(f)}$. In the final step the derived values are cascaded to find the complete model that can be used to simulate CTFs. Below steps are taken to achieve the same.

I. $|H(f)|$ *Estimation:* From the CTF plot of different frequency bands and alignment scenarios (LOS/nLOS) the values for A and γ are derived and listed in Table 4.4. Subsequently these values are put in (4.11) to estimate the simulated $|H(f)|$.

II. $\overline{H(f)}$ *Estimation:* The small-scale variation or $\overline{H(f)}$ of the complex CTFs are derived using the proposed 5th order AR model. The steps to derive the $\overline{H(f)}$ are mentioned below.

   a) In the 1st step, The CTFs are represented by a 5th order AR process (4.22-4.23). Subsequently the transfer function of the AR process is presented where the input is IID Gaussian noise variance (4.25) of 1601 samples (VNA sample length). These transfer functions are represented by all pole linear IIR filter.

   b) The complex Poles of the transfer function of the IIR filter of the AR model are derived and the amplitude and phase of the poles are mentioned in (4.30) and (4.31) respectively for different operating bands and LoS/nLoS scenarios.

   c) Subsequently, the transfer function $H(z)$ is formed using the derived poles. By taking the inverse Z-transform, $\overline{H(f)}$ is obtained for a single frequency sample. Taking the summation for N (1601) samples $\overline{H(f)}$ is derived.

III. Finally, we estimate the complete CTF or $H(f)$ by cascading the derived values as mentioned

$$H(f) = \overline{H(f)}.|H(f)|$$

4.7 Model Validation in Frequency and Time Domain

In this step, we simply evaluate the goodness of fit of the synthetic model data with the empirical data to validate the proposed models in both frequency and time domain respectively.

4.7.1 Model validation in Frequency domain

C band CTF for LOS scenario at SITE-A is simulated using the above model and compare to empirical data as shown in Fig. 4.15(a). We have noticed close similarities between the responses. As shown in the picture, the least square linear fit lines between measured and simulated CTFs have a close intersection point and exponent value. The frequency domain channel model is also validated by comparing the simulated and measured coherence bandwidth (Bc), which is the range of frequency responses over which the CTFs' Auto-Correlation Function (ACF) [18] peak is 3dB lower, as shown in Fig. 4.15. (b).

$$R(\Delta f) = \int_{-\infty}^{\infty} H(f)H^{*}(f+\Delta f)\,\delta f$$

4.7.2 Model validation in Time domain

Time domain channel response is established by comparing the simulated and measured PDPs. In Fig. 4.16(a) the simulated and measured PDPs for LoS and NLoS scenarios in C band at SITE-A is illustrated. It is interesting to observe that the time of arrival of the MPCs from different clusters is largely similar though there is slight deviation in the amplitudes.

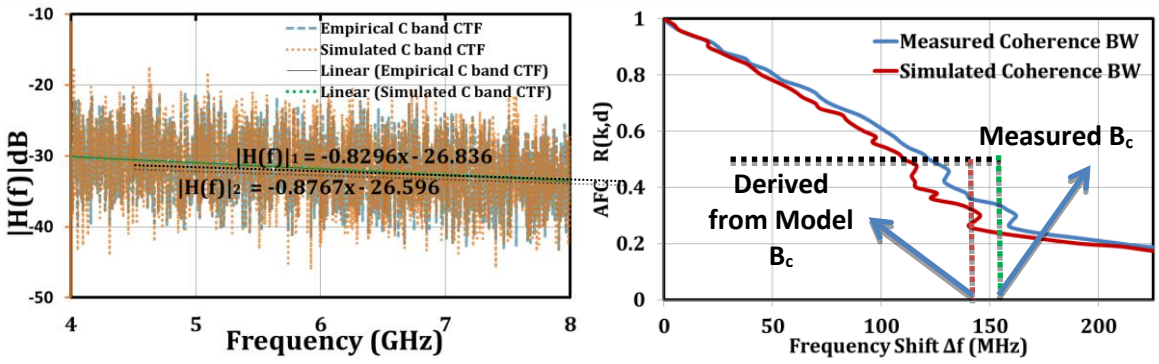

(a) (b)

Fig. 4.15 Comparison of Model and empirical data of (a) CTF and, (b) Coherence bandwidth at SITE-A in LoS and nLoS scenarios in C band operation

Many tradeoffs are made while determining the model parameters, which resulted in a minor disparity in the responses. We have validated the model further for root mean square delay spread (τ_{rms}), which is the measure of the second central moment of the delay profile. The CDF plot of τ_{rms} depicts very close similarity as illustrated in Fig. 4.16(b).

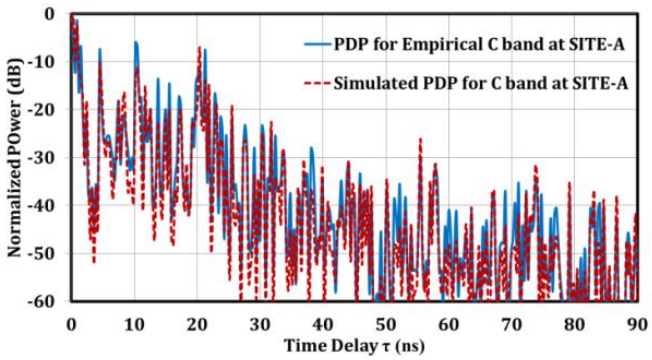

(a)

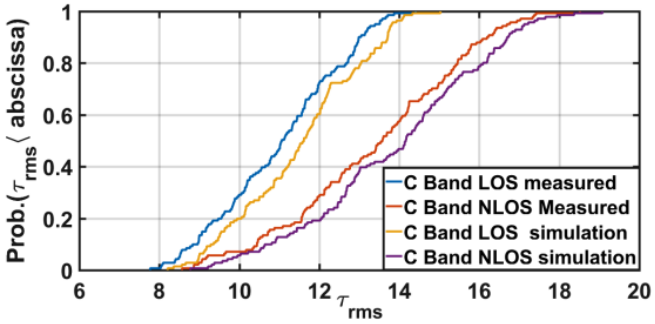

(b)

Fig. 4.16 Measured and simulated C band LOS Channel Transfer Function (CTF)

The simulated frequency domain channel characteristics such as coherence Bandwidth or correlation functions or CTF appear to be closer to the measured values than the time domain (such as delay spread or CIR) channel parameters since all of the measurements are done in the frequency domain. Due to the presence of a direct path, the excess delays in LOS scenarios are impacted much more than in nLOS situations.

4.8 Conclusion

In present communication scenarios it's crucial to characterize and analyze the indoor propagation channel to get accurate Channel State Information (CSI) before designing effective communication systems. On the other way, UWB communication is becoming attractive due to large bandwidth, resilience to deep fading, and low power consumption. It is also implemented for high-speed, short-range communication in future UDN contexts. Thus, characterization and modeling of these UWB channels are essential. A comprehensive propagation measurement

campaign is conducted in a university indoor static environment in C, X and Ku band using terminal independent frequency domain approach. Distance and frequency dependent statistical investigations are made for important parameter extraction from the measured terminal independent complex CTFs. The large-scale distance dependent pathloss fading model for coverage prediction and frequency domain AR model for BER and SINR prediction are proposed subsequently. The existence of poles in the transfer function of the AR process depicts the presence of clusters in the propagation path. Also, the position of the poles in the unit circle defines the amplitude, phase and delays of the MPCs reflected from the cluster of reflectors. Further the models are validated in frequency and time domain. For frequency domain validation, empirical PDPs and coherence bandwidth are compared with synthetic model data and found to be quite similar. Similar results are observed when CIRs and RMS delay spreads are evaluated for time domain validation of the designed models. The proposed model is simple to implement as it performs well enough with lesser parameters. The model is also computationally easier than available models to simulate intricate frequency responses in an indoor environment in recent and future heterogeneous network domain.

The investigations on wireless channel characterization and modeling provide significant insights regarding the channel behavior in present network architecture and environments. This would provide important observations to develop advanced antennas for upcoming 5G ecosystem. The essence of reconfigurable antennas can also be assessed from the observations discussed in this chapter. Few important aspects are pointed below.

1. Channel behavior alters with operating frequency band and bandwidth.
2. Wideband signals are immune to fading comparative to narrowband signals.
3. In higher frequencies the channel behavior changes remarkably. The signal attenuation, loss, fluctuation, and distortion increase due to increase in number of scatterers.
4. With increased scatterers and reflectors at higher frequencies the possibilities of signal distortion increase due to interference.

The importance of designing high gain reconfigurable antennas in coming time can clearly be assessed from the above discussions. Author has made an approach to overcome the mentioned wireless channel adversities in coming 5G cellular domain from an antenna

perspective. Thus, in the subsequent chapters author predominantly focused on the investigations of high gain compact reconfigurable antennas to significantly alleviate those issues.

References:

[1] J. Zhang, A. A. Glazunov and J. Zhang, "Wireless Performance Evaluation of Building Layouts: Closed-Form Computation of Figures of Merit," in IEEE Transactions on Communications, vol. 69, no. 7, pp. 4890-4906, July 2021, doi: 10.1109/TCOMM.2021.3074546.

[2] Chia-Chin Chong and Su Khiong Yong, "A generic statistical-based UWB channel model for high-rise apartments," in IEEE Transactions on Antennas and Propagation, vol. 53, no. 8, pp. 2389-2399, Aug. 2005, doi: 10.1109/TAP.2005.852505.

[3]https://www.radiall.com/products/rf-cable-assemblies/low-loss-high-frequency-flexible-cable-assembly-shf-range.html

[4] https://www.keysight.com/us/en/support/E5071B/ena-rf-network-analyzer.html

[5] J. McLean, H. D. Foltz and R. Sutton, "The effect of frequency-dependent radiation pattern on UWB antenna performance," IEEE Antennas and Propagation Society Symposium, 2004., 2004, pp. 2540-2543 Vol.3, doi: 10.1109/APS.2004.1331891.

[6] S. J. Howard and K. Pahlavan, "Autoregressive modeling of wide-band indoor radio propagation," in IEEE Transactions on Communications, vol. 40, no. 9, pp. 1540-1552, Sept. 1992, doi: 10.1109/26.163575.

[7] A. Chandra et al., "Frequency-Domain In-Vehicle UWB Channel Modeling," in IEEE Transactions on Vehicular Technology, vol. 65, no. 6, pp. 3929-3940, June 2016, doi: 10.1109/TVT.2016.2550626.

[8] D. Wang, Y. Cao, L. Zheng and Z. Du, "A Note on "Performance Analysis of UWB Systems over the IEEE 802.15.3a Channel Model"," in IEEE Transactions on Communications, vol. 60, no. 12, pp. 3909-3910, December 2012, doi: 10.1109/TCOMM.2012.101912.120002.

[9] G. D. Durgin, and T. S. Rappaport, “Theory of multipath shape factors for small-scale fading wireless channels,” IEEE Trans. AntennasPropagat., vol. 48, no. 5, pp. 682-693, May 2000.

[10] S. J. Howard and K. Pahlavan, "Autoregressive modeling of wide-band indoor radio propagation," in IEEE Transactions on Communications, vol. 40, no. 9, pp. 1540-1552, Sept. 1992, doi: 10.1109/26.163575.

[11] H. Hashemi, “The indoor propagation channel,” Proc. IEEE, vol. 81, pp. 943–968, July 1993.

[12] T. S. P. See and Z. N. Chen, "Experimental Characterization of UWB Antennas for On-Body Communications," in IEEE Transactions on Antennas and Propagation, vol. 57, no. 4, pp. 866-874, April 2009, doi: 10.1109/TAP.2009.2014595.

[13] A. Sani et al., "Experimental Characterization of UWB On-Body Radio Channel in Indoor Environment Considering Different Antennas," in IEEE Transactions on Antennas and Propagation, vol. 58, no. 1, pp. 238-241, Jan. 2010, doi: 10.1109/TAP.2009.2024969.

[14] S. S. Ghassemzadeh, R. Jana, C. W. Rice, W. Turin and V. Tarokh, "Measurement and modeling of an ultra-wide bandwidth indoor channel," in IEEE Transactions on Communications, vol. 52, no. 10, pp. 1786-1796, Oct. 2004, doi: 10.1109/TCOMM.2003.820755.

[15] Suiyan Geng, S. Ranvier, Xiongwen Zhao, J. Kivinen and P. Vainikainen, "Multipath propagation characterization of ultra-wide band indoor radio channels," 2005 IEEE International Conference on Ultra-Wideband, 2005, pp. 11-15, doi: 10.1109/ICU.2005.1569948.

[16] H. Tong, "More on autoregressive model fitting with noisy data by Akaike's information criterion (Corresp.)," in IEEE Transactions on Information Theory, vol. 23, no. 3, pp. 409-410, May 1977, doi: 10.1109/TIT.1977.1055706.

[17] Hui-Min Zhang and P. Duhamel, "On the methods for solving Yule-Walker equations," in IEEE Transactions on Signal Processing, vol. 40, no. 12, pp. 2987-3000, Dec. 1992, doi: 10.1109/78.175742.

[18] Y. Zhang, J. Zhang, D. Dong, X. Nie, G. Liu and P. Zhang, "A novel spatial autocorrelation model of shadow fading in urban macro environments", Proc. IEEE Glob. Telecommun. Conf., vol. Dec., pp. 1-5, 2008.

[19]https://www.ieee802.org/15/pub/04/15-04-0662-02-004a-channel-model-final-report-r1.pdf

Chapter 5
Dual Band Penta-Polarized Reconfigurable Planar Antenna

5.1 Introduction

Wireless channel behavior in different environmental scenarios is studied in the previous chapter. Time and frequency domain channel matrices such as RMS delay spread, doppler spread, doppler spectrum and coherence bandwidth that would provide significant channel state information are carefully observed. Large and small-scale fading models proposed in the last chapter can be employed in specific environment under consideration to derive important channel matrices and subsequently the ultimate channel nature. Signal degradation in an ultra-dense environment in the upcoming generation is inevitable due to interference [1-2]. The models would predict severe signal distortion, low SINR and extremely high BER due to the coexistence of large number of wireless nodes operating in constrained spectrum.

Multifunctional antennas have largely been studied to integrate multiple services and have rarely considered for interference mitigation applications [3]. Furthermore, reconfigurable antennas those which are investigated in recent literature show alarming concerns for practical realization (discussed in chapter 2B section:2.2.6). In this chapter an antenna perspective approach is investigated to counter co-channel interference by incorporating simple agile antennas in trans-receiver system.

A compact low profile ($\leq 0.01\lambda_0$, λ_0 is operating wavelength) single-layered dual-band agile microstrip antenna is studied. Both reconfigurable bands can further be reconfigured with five switchable polarization states. The structural simplicity, compactness, and ease of fabrication make the antenna suitable for a wide range of applications. Key advantages and novelty of the proposed design are outlined as below.

1) As per the authors' knowledge, there is very little literature available for penta-polarization antennas operating in two distinct bands. Most of the works reported so far have dealt with triple/quad polarization antennas. We address this very issue and present a

reconfigurable penta-polarization dual band antenna. The proposed antenna has ten reconfigurable states that would provide a higher degree of freedom to the antenna designer with ample design/reconfigurable choices.

2) Most of the reconfigurable antennas in the available literature are designed with complex feed networks, multiple SMA feeds, bulky multi-layered structures, and complex asymmetric antenna assemblies. In comparison, our proposed antenna is significantly compact ($0.5\lambda_0 \times 0.5\lambda_0 \times 0.01\lambda_0$), coplanar, single-layered, and excited using a single SMA feed. It has the advantage of being simple and miniaturized. Consequently, it can be easily interfaced with other transceiver systems.

3) The Antenna design procedure outlined in the current work is simple and based on physical equivalent circuit-based workflow. This makes the design workflow easily scalable to any other frequency yielding quick design cycles for any application in the 5G ecosystem.

4) Proposed antenna system is principally aimed at mitigating the problem of co-channel and intersystem interference in present 5G heterogeneous and ultra-dense wireless architecture. Degrees of freedom in the present design can be employed toward a smart system with outage minimization and link throughput stabilization in future communication systems.

5.2 Theory

5.2.1 Frequency Reconfigurability

A fundamental mode square ring with inner and outer edge length of a and b is designed to operate at lower frequency band f1 as shown in Fig. 5.1(a). Subsequently, the ring encloses a square patch and is coupled using PIN diodes to form a complete square patch that operates at higher band f2 as shown in Fig. 5.1(b). The resonant frequencies are derived from well-established expressions as illustrated in (5.1) and (5.2) respectively [4]. Four PIN diodes are placed between the inner square patch and the outer ring as presented in Fig. 5.1. The diodes (D1, D2, D3 and D4) are turned ON and OFF respectively to realize dual band operation of the antenna.

$$f1 = \frac{c}{2(a+b+2\times g)\sqrt{\varepsilon_{eff}}} \tag{5.1}$$

$$f2 = \frac{c}{2a\sqrt{\varepsilon_{eff}}} \tag{5.2}$$

where ε_{eff} is the effective dielectric constant of the substrate and g is the inner gap between the two patches as depicted in Fig. 5.1(c).

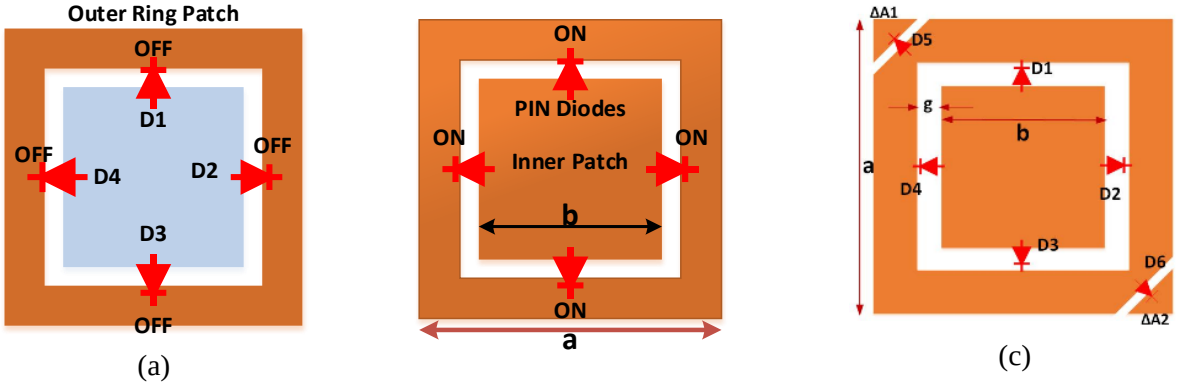

Fig. 5.1 Prototype antenna structures for dual frequency operation. The Orange color sections of the antennas portrays the excited sections of the antenna (a) Outer ring for Lower Frequency band f1, (b) Complete Square patch for higher frequency band f2 and (c) corner truncation and corresponding areas

5.2.2 Penta Polarization Agility at dual frequencies

The diagonal corners of a square patch are truncated to excite fundamental orthogonal modes (TM_{01} and TM_{10}) to generate circular polarization. The area of the truncated corner is to satisfy (5.3) to realize the orthogonal modes [4].

$$\frac{2\Delta A}{A} = \frac{1}{2Q_0} \tag{5.3}$$

where Q_0 is the unloaded quality factor of the orthogonal modes, ΔA is the total area of truncated corners and A is the patch area. Dimensions of the truncated corner are derived from the stated equation. Orthogonal microstrip feed lines as illustrated in Fig. 5.2 are designed to excite the antenna using a single SMA feed connected at the termination of the feed line. The position of the feed with respect to the surface current perturbation plays an important role in determining the sense of rotation of current on the patch surface. For instance, if the truncated corners are positioned at +45° and +225° with reference to the vertical feed; the antenna radiates Left-Handed CP wave. Similarly Right-handed CP signals are radiated for horizontal feed excitation

where the truncated corners are positioned at -45° and -225° with reference to the feed. Basically, corner truncation and subsequent perturbation caused the fundamental mode to split into two orthogonal modes (TM_{10} and TM_{01}) with slightly different frequencies [4] as mentioned in (5.4) to (5.7) for f1 and f2 band respectively.

$$f_x = f_1\left(1 - \frac{2\Delta A}{A}\right) \tag{5.4}$$

$$f_y = f_1 \tag{5.5}$$

where, $\Delta A = \Delta A1 + \Delta A2$ is the total area of the truncated portion and $A = a^2 - (b+2\times g)^2$ is the total area of the outer ring as illustrated in Fig. 5.1(a). Similarly, the orthogonal frequencies for complete square patch are derived as below.

$$f_x^1 = f_2\left(1 - \frac{2\Delta A}{A1}\right) > f_x \tag{5.6}$$

$$f_y^1 = f_2 > f_y \tag{5.7}$$

where $A1 = a^2$, area of the total square patch as shown in Fig. 5.1(b). The etched corners are connected with the truncated patches using PIN diodes to generate dual LP. The adjacent edge feeds are activated successively to realize horizontal (HP) and vertical polarization (VP) respectively as depicted in Fig. 5.2(a) and 5.2(b) at f1 band. In conjunction, simultaneous activation of both the feed with equal magnitude and phase realizes 135˚ slant LP states at the same band as illustrated in Fig. 5.2(c). Penta polarization reconfigurability at f2 band is also attained by similar feed configuration as shown in Fig. 5.2(f) to 5.2(j).

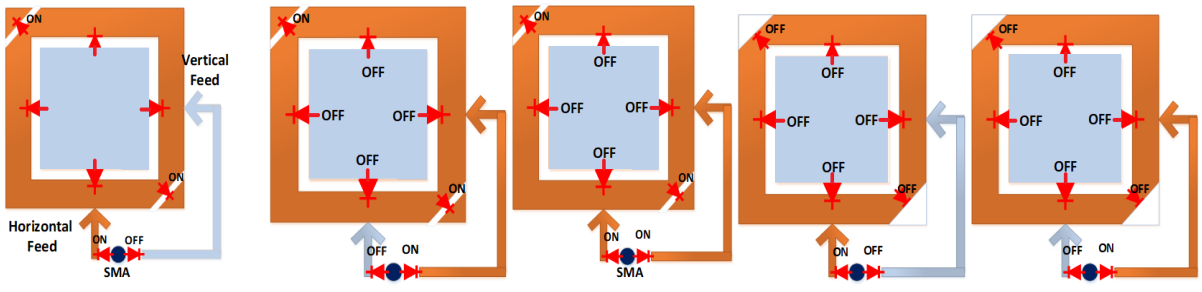

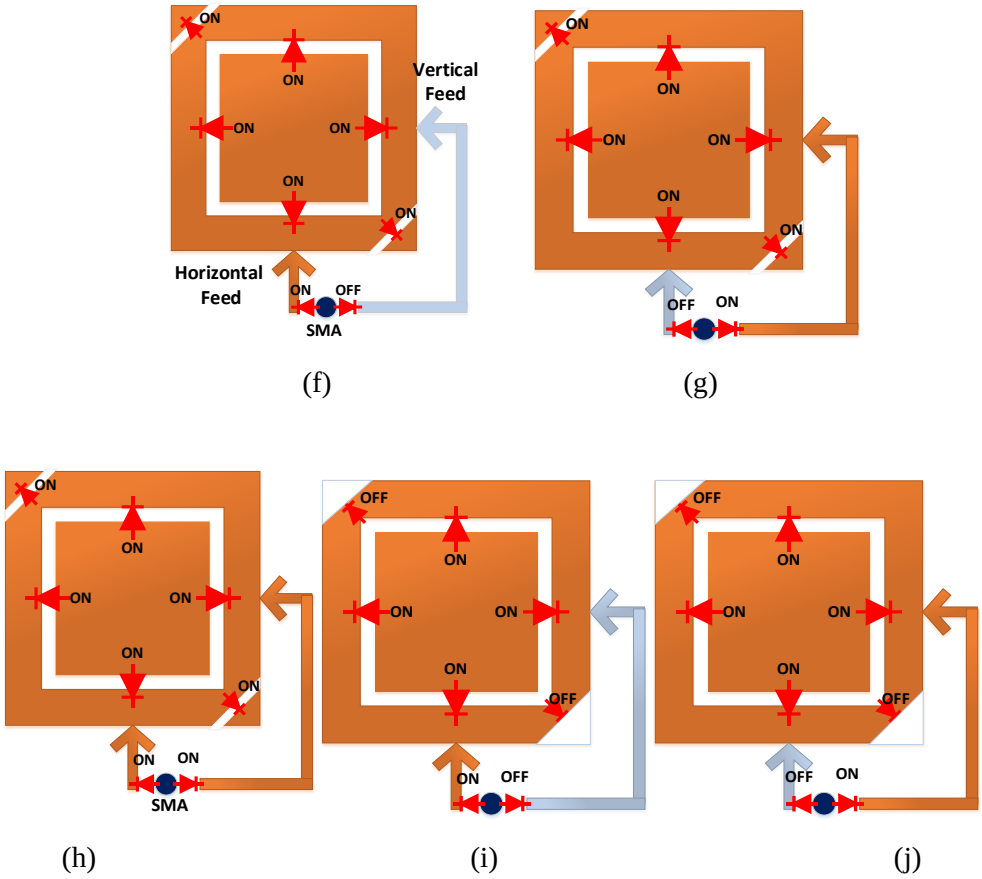

Fig. 5.2 Realization of five reconfigurable polarization states at lower band f1 (a) Vertical Polarization (VP), (b) Horizontal Polarization (HP), (c) 45° slant Polarization, (d) Left Hand CP (LHCP) and (e) Right hand CP (RHCP), also five polarization states at f2 band (f) Vertical Polarization (VP), (g) Horizontal Polarization (HP), (h) 45° slant Polarization, (i) Left Hand CP (LHCP) and (j) Right hand CP (RHCP).

A prototype antenna is designed to reconfigure at 5.2GHz and 5.8GHz respectively. Furthermore, the antenna is designed to operate at five distinct polarization states (dual CP, VP, HP and 135˚ slant) based on the theory discussed so far and portrayed in Fig. 5.3(a). The equivalent circuit models of the PIN diode for forward and reverse bias conditions are presented in Fig. 5.3(b). The corresponding dimension of the designed antenna is shown in Table 5.1.

Table 5.1: DIMENSIONS OF PROTOTYPE ANTENNA (ALL IN **mm**)

Parameters	a	b	x	t	Ln1	Ln2	Gx	Ln9
Dimensions	12	6.7	5.1	0.2	8.2	13.06	35	0.707
Parameters	m	n	p	q	g	r	wf80	wf126
Dimensions	2.1	0.374	0.1	0.1	0.141	0.5	0.9	0.32

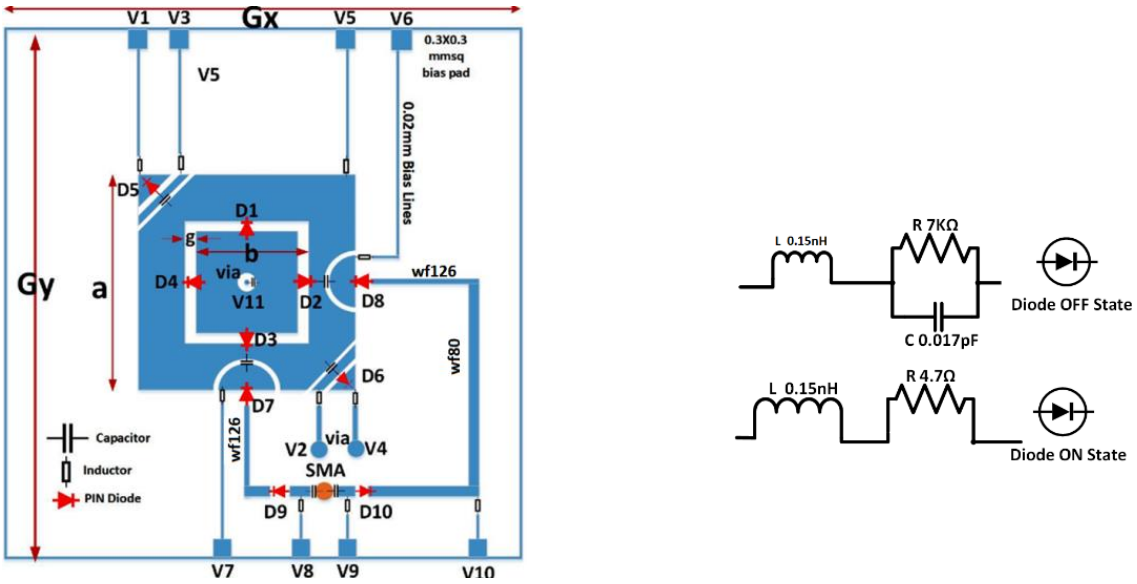

(a) (b)

Fig. 5.3 (a) Complete designed prototype antenna and (b) Forward and reverse biased diode equivalent circuit model.

5.2.3 Penta Polarization agility at lower band f1 (5.2GHz)

Diodes D1 to D4 are turned OFF to excite the patch at lower band f1 as depicted in Fig. 5.1(c). Subsequently D5 and D6 are turned ON to radiate linear polarized wave. Vertical edge of the reconfigurable orthogonal feed lines is activated by forward biasing D7 and D9 respectively to generate VP wave while D8 and D10 are kept in reverse bias condition. Subsequently the biasing conditions are just reversed to realize the HP state. Contrarily, D7 to D10 are kept ON exciting the orthogonal edges simultaneously for 135˚ slant LP generation. Furthermore, D5 and D6 are turned OFF to realize CP states. In the similar way, vertical and horizontal feeds are activated sequentially to radiate LHCP and RHCP wave respectively. The surface current distributions on the patch surface for dual CP states for T/4 successive time period are illustrated in Fig. 5.4(a) and 5.4(b) respectively. Also, the diode states for five distinct polarization reconfigurability at two different reconfigurable frequencies are illustrated in Table 5.2.

Table 5.2: DIODE STATES FOR DUAL BAND AND PENTA POLARIZATION MODES

Freq.	Pol. States	D1, D2, D3, D4	D5 & D6	D7&D9	D8&D10
f1 Lower Band 5.2GHz	VP	Off	On	On	Off
	HP	Off	On	Off	On
	45	Off	On	On	On
	RHCP	Off	Off	Off	On
	LHCP	Off	Off	On	Off
f2 Higher Band 5.8GHz	VP	On	On	On	Off
	HP	On	On	Off	On
	45	On	On	On	On
	RHCP	On	Off	Off	On
	LHCP	On	Off	On	Off

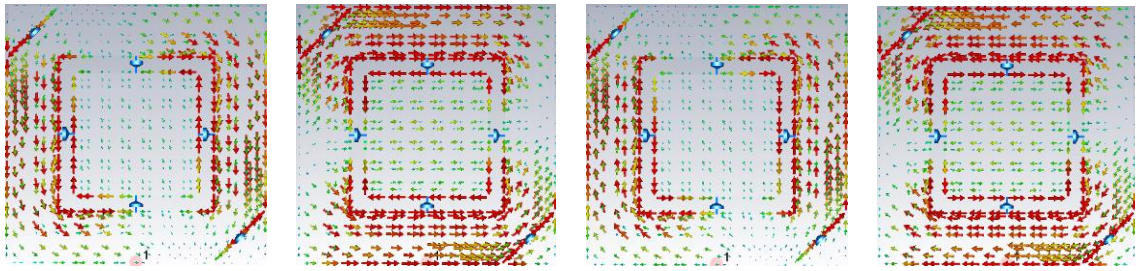

t=0 t=T/4 t=T/2 t=3T/4

(a) RHCP

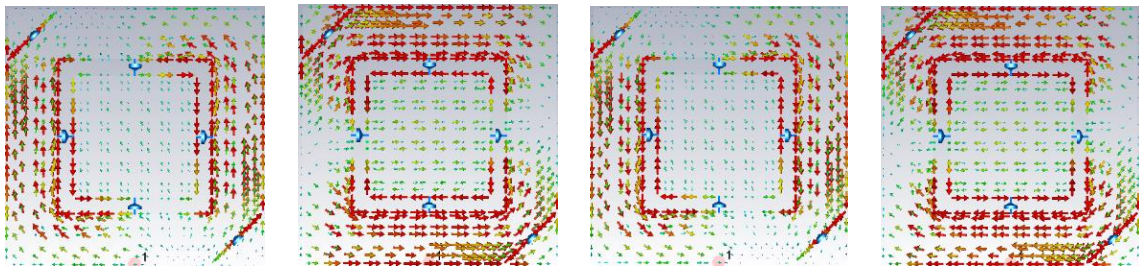

t=0 t=T/4 t=T/2 t=3T/4

(b) LHCP

Fig. 5.4 Surface current distribution on the patch antenna at lower f1 band (a) LHCP and (b) RHCP

5.2.4 Penta Polarization agility at higher band f2 (5.8GHz)

D1 to D4 are turned ON to excite the patch at higher band f2. Subsequently D5 and D6 are turned ON to operate at LP states. Vertical edge feed of the orthogonal feed lines is activated

by forward biasing D7 and D9 respectively to generate vertically polarized wave while D8 and D10 are kept in reverse bias condition. Contrarily, D7 to D10 are kept ON exciting the orthogonal edges simultaneously for 45˚ slant LP generation. Furthermore, D5 and D6 are kept OFF to realize CP states. In the similar way, vertical and horizontal feeds are activated sequentially to radiate LHCP and RHCP wave respectively. The surface current distributions on the patch surface for dual CP states for T/4 successive time periods are illustrated in Fig. 5.5(a) and 5.5(b) respectively. Surface current distributions for 45º slant polarization states at both the bands are depicted in Fig. 5.5(c). Current traverses a comparatively longer path at outer ring hence resonates at lower operating band f1, subsequently the complete square patch excites at higher fundamental resonance (f2) due to comparatively shorter current path as illustrated in Fig. 5.4 and Fig. 5.5 respectively.

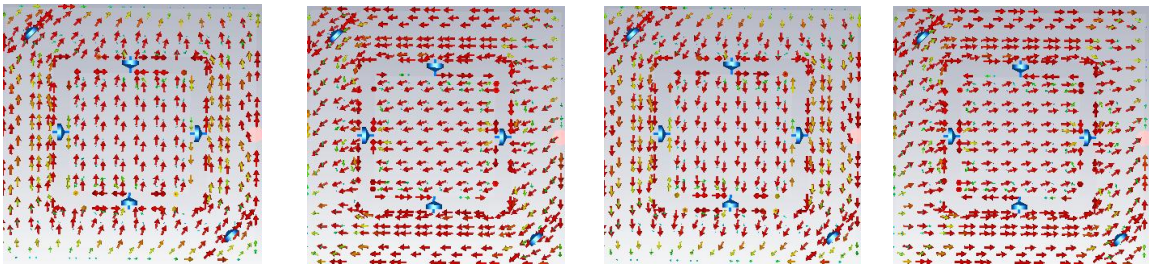

t=0 t=T/4 t=T/2 t=3T/4

(a) RHCP

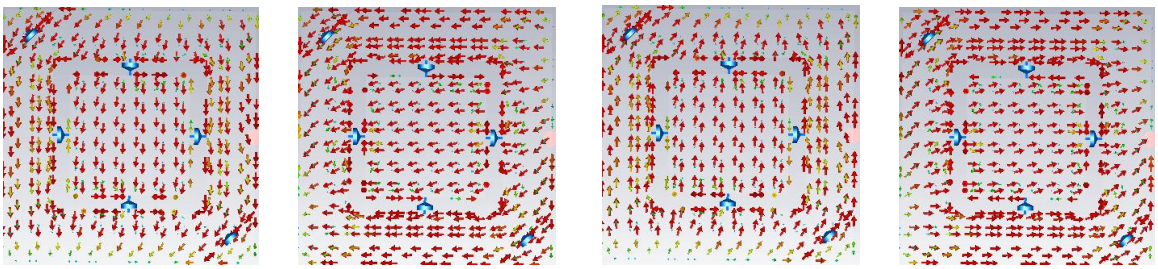

t=0 t=T/4 t=T/2 t=3T/4

(b) LHCP

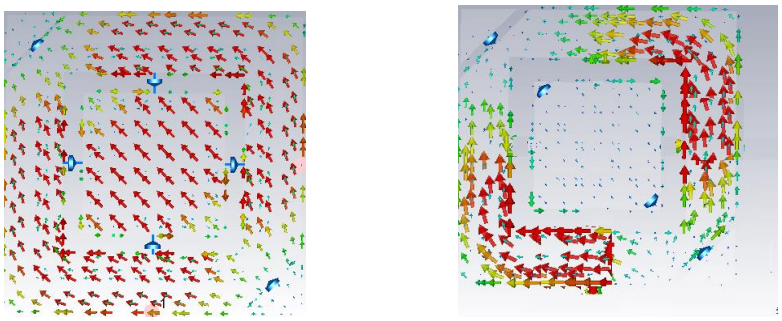

(c) 45˚ slant LP

Fig. 5.5 Surface current distribution on the patch antenna at f2 higher band (a) LHCP, (b) RHCP and (c) 45º slant polarization state at f2 and f1 bands respectively.

5.3 Analysis and observations on CP and 45º Slant polarization

The relative amplitude and phase of the far-field orthogonal electric components, i.e., E_θ & E_φ in the broadside beam (θ= φ=0º) at both the principal (φ=0º & 90º) planes are investigated. From the prototype design, $|E_\theta/E_\varphi|$ at the broadside far field for dual CP states are shown in Fig. 5.6(a) for θ variation at φ=0º & 90º planes at f2 band. It is noticed that the ratio remains within ±1dB along the Half Power Beamwidth (HPBW ±50º). Fig. 5.6(b) represents the phase difference i.e., $\angle(E_\theta - E_\varphi)$ is nearly ±90º for LHCP and RHCP respectively. The broadside axial ratios for CP states for dual sense of rotation at f2 band for θ variation at both the principal planes are found to be within 3dB for the HPBW as depicted in Fig. 5.7. For brevity, the plots only for RHCP states are shown in the below figures as for both the circular polarization states the mentioned plots are similar in nature.

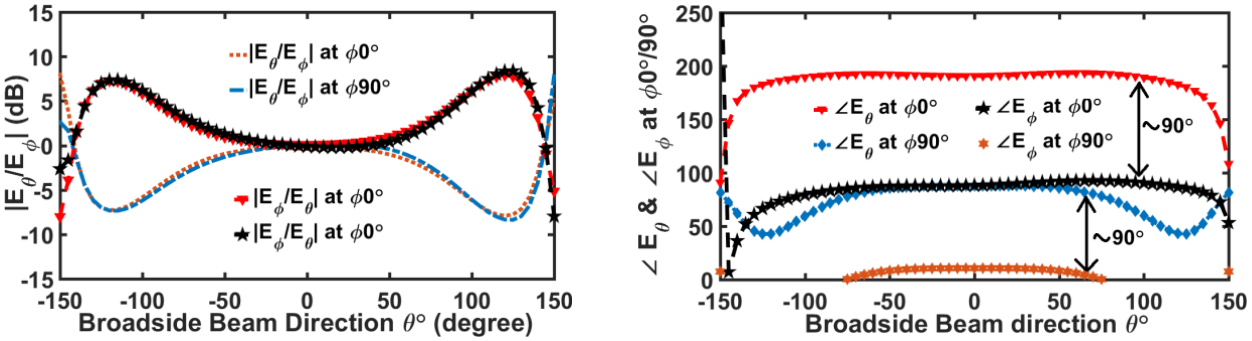

(a) (b)

Fig. 5.6 Far-field E_θ and E_φ component at broadside direction at φ=0º & 90º plane for RHCP state (a) E_θ and E_φ component ratio at φ=0º & 90º plane, and (b) Phase angle of E_θ and E_φ components at both principal planes.

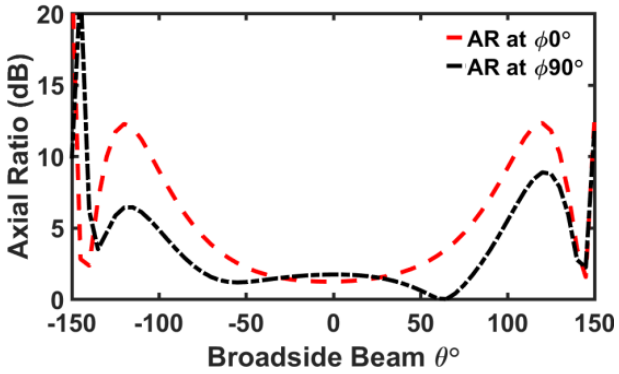

Fig. 5.7 Far-field 3dB axial ratio at broadside direction at φ=0° & 90° plane for RHCP polarization.

Similarly, $|E\theta/E\varphi|$ and $\angle\,(E\theta - E\varphi)$ at broadside far-field for 135° polarization for θ variation at φ=0° & 90° planes are shown in Fig. 5.8(a) and (b) respectively. It is observed that $|E\theta/E\varphi|$ is laid within ±1dB in both the planes for the HPBW (±55°) shows nearly equal amplitude. Also, the phase difference $\angle\,(E\theta - E\varphi)$ of the components for both the planes are remain within 0°-10° or π (equal but oppositely directed phase) as shown in Fig. 5.8(a). Similar results are observed for f1 band also, hence not shown for brevity.

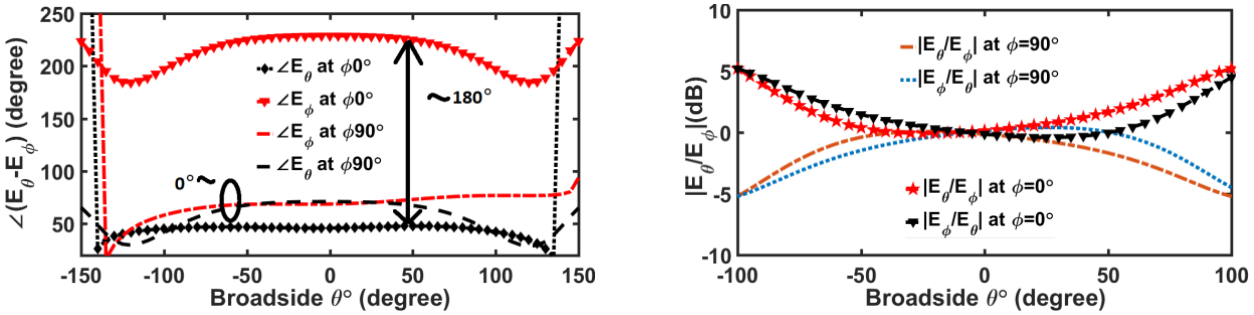

Fig. 5.8 Far-field E_θ and E_φ component at broadside direction at φ=0° & 90° plane for 45° slant polarization states (a) Phase angle E_θ and E_φ at both planes, and (b) E_θ and E_φ component ratio at φ=0° & 90° plane

5.4 Design of the feed network

Orthogonal edge impedances of the patch for all five polarization states are derived from the simulation as shown in Fig. 5.9 for f1 (5.2GHz) and f2 (5.8GHz) band respectively. The Impedance behavior is found to be identical for dual LP or dual CP states at specific band due to antenna symmetry hence only HP and RHCP states are shown in figure for brevity. The resonances for slant polarization are shifted slightly in the lower frequency due to minor

increment in current path along the diagonal of the patch. The real part of the input impedances (Z_{real}) of the CP and LP states are varied from 300Ω to 200Ω and 250Ω to 400Ω respectively in both the bands as shown in Fig. 5.9(a) and 5.9(b) respectively. Microstrip feed lines connected with the orthogonal edges of the patch are terminated with 50Ω coax SMA using quarter wave matching sections. The difference in length between the microstrip feed lines connected with the adjacent patch edges are chosen either to be equal or difference by multiple of wavelength to provide equal phase. The wavelength for designing the quarter wave sections of both the frequency band is taken at 5.5GHz. From the observations on the impedance behavior of different states, 300Ω edge impedance is considered for all the states to design the feed network. Subsequently, 155Ω quarter wave impedance transformer sections are used to transform the orthogonal edge impedance nearly to 80Ω and finally terminated at 50Ω SMA coax feed. Furthermore, the adjacent feed lines are excited simultaneously (for 135° slant LP) and a parallel connection of 80Ω at the coax feed end provides 40Ω load. It is observed from simulation that Z_{real} of all the reconfigurable states are varied within the range of (50-100) Ω with negligible imaginary input impedances (Z_{img}) and exhibits enough -10dB matching for all the states.

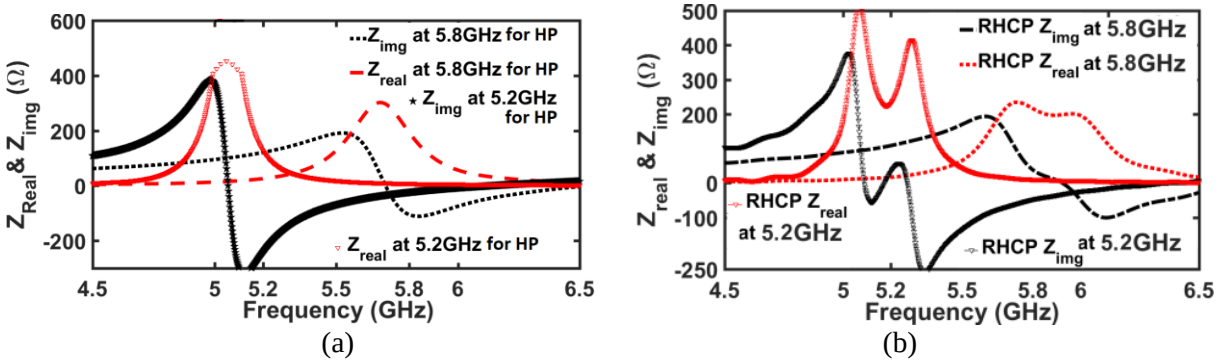

Fig. 5.9 Complex input impedances at the orthogonal edges of the prototype patch at 5.2GHz and 5.8GHz band for (a) Horizontal Polarization and (b) RHCP state

Higher order modes in the proximity of the fundamental mode are also resonated at the CP states due to the intermodal power coupling as depicted in the impedance plots. Though the modal significance of those unintended modes is negligible; hence do not have significant effect on antenna performances except increasing the impedance bandwidth. Furthermore, switching diodes and lumped elements are connected with the antenna to achieve reconfigurability. Hence the impedances are slightly altered, and further tuning of the length and width of the different

feed sections are performed to get optimized -10dB matching along with other antenna parameters.

Fabricated prototype antenna is shown in Fig. 5.10. Switching PIN diodes and biasing capacitors or inductors are shown along with bias lines and pads.

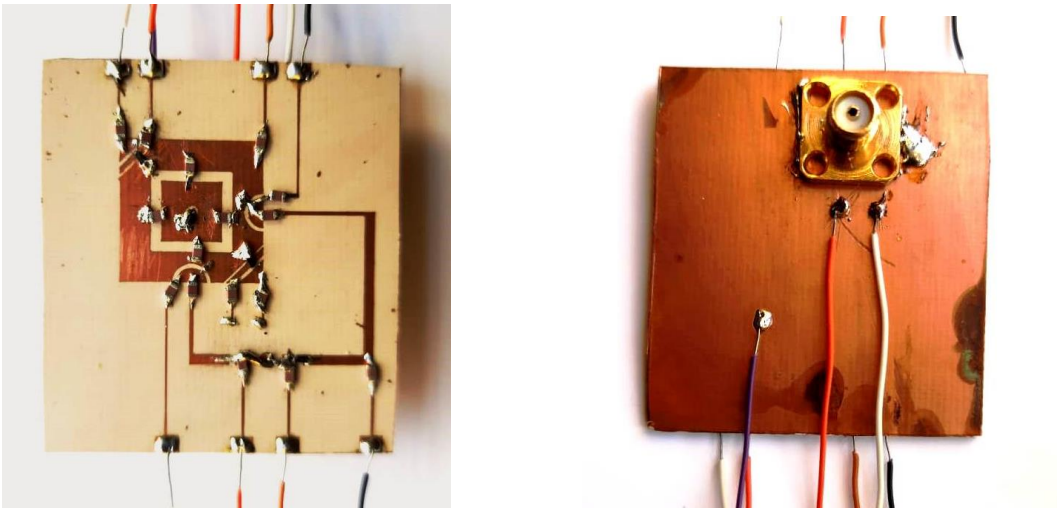

(a) (b)

Fig. 5.10 Fabricated prototype antenna (a) Top view and (b) Bottom view

5.5 Design of the bias network

PIN diodes from Avago Technologies (Model No. HPND-4005 SMD 01005) [5] are used for switching mechanism. The switches have got very low capacitances (C = 0.017 pF) and resistances (R = 4.7 Ω) in the OFF and ON states. The equivalent diode models for forward and reverse bias states are mentioned in Fig. 5.3(b). It also exhibits low package parasitic which would have minimum adverse effects on the isolation. It also shows very less insertion loss (0.4 dB). Very thin DC bias lines (0.1mm) are placed on the design to connect the DC sources with different antenna sections for proper biasing and terminated at 0.3mm×0.3mm bias pads for better coupling management. The complete design and fabricated prototype are shown in Fig. 5.3 and 5.10 respectively. A 0.9V DC supply between the anode and the cathode using two distinct DC sources will turn the diode ON with a bias current of ~ 20 mA. A voltage of 0V is sufficient to turn the diode OFF, but -8V DC is applied to firmly reverse bias the diode with a higher

reverse voltage in order to increase the isolation in the OFF state by reducing the diode internal capacitance. A 47nH inductor is used as RF choke to block RF component to the DC source while 33pF series capacitance is used for RF continuity as marked in the antenna layout in Fig. 5.3 and shown in the fabricated antenna. Diode biasing states are mentioned in Table 5.3 for all ten reconfigurable states.

TABLE 5.3: DIODE BIASING STATES FOR DIFFERENT RECONFIGURABLESTATES

Freq.	Polarization States	V_1& V_2	V_3& V_4	V_5, V_6& V_7	V_8	V_9	V_{10}	D_1 to D_4	D_5 & D_6	D_7 & D_9	D_8 & D_{10}
f1	VP	0	+3	0	+3	-10	-10	OFF	ON	ON	OFF
	HP	0	+3	0	-10	+3	-10	OFF	ON	OFF	ON
	45˚	0	+3	0	+3	+3	-10	OFF	ON	ON	ON
	RHCP	0	-10	0	+3	-10	-10	OFF	OFF	ON	OFF
	LHCP	0	-10	0	-10	+3	-10	OFF	OFF	OFF	ON
f2	VP	0	+3	0	+3	-10	+3	ON	ON	ON	OFF
	HP	0	+3	0	-10	+3	+3	ON	ON	OFF	ON
	45˚	0	+3	0	+3	+3	+3	ON	ON	ON	ON
	RHCP	0	-10	0	+3	-10	+3	ON	OFF	ON	OFF
	LHCP	0	-10	0	-10	+3	+3	ON	OFF	OFF	ON

5.6 Parametric Study

5.6.1 Variation of lengths of the truncated corner

The length of the truncated corners is varied to attain optimum 3dB axial ratio as shown in Fig. 5.11. for both the frequency bands. The area of the opposite truncated portions of the patch are varied along the variation of the corner length to satisfy (5.5) to excite TM_{01} and TM_{10} orthogonal modes. Though no significant variation in AR is noted for the variation of the gap (between truncated corner and the patch) width and the corresponding plot is not shown for brevity.

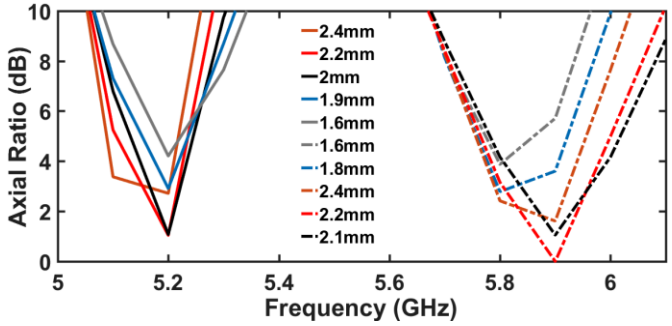

Fig. 5.11 Variation of 3dB axial ratio for the variation of truncated corner length

5.6.2 Inter patch gap ‘g’ variations

The current traversing path along the length of the patch for the lower frequency band is varied due to the variation of gap width between the inner patch and outer ring. As the dimension of the outer side of the outer patch remains fixed hence no significant variation of the higher resonance is observed. The lower resonance at 5.2GHz is varied largely along the variation of the inner side of outer patch and illustrated in Fig. 5.12(a). Hence tuning of this gap is required to align the lower band at desired frequency. Contrarily, the tuning of the higher band is controlled by the length of the outer patch according to (5.1), as discussed in section 5.2.2.

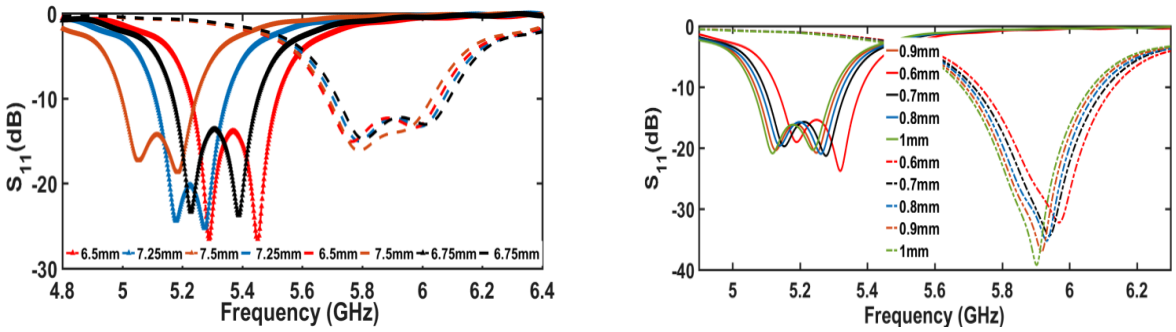

(a) (b)

Fig. 5.12 (a) Variation of reflection coefficient S_{11} for RHCP state at both frequency band for the variation of the width of the gap ‘g’ between inner square patch and the outer square ring and (b) Variation of reflection coefficient S_{11} for LHCP state at both the frequency band for the variation of width of 80Ω transmission line in the feed network.

5.6.3 Impedance Matching by feed length and width variation

The impedances of each microstrip lines in the feed network are varied by tuning the width and length of each section to tune the impedance matching. For example, the width of 80Ω impedance line is varied and the corresponding matching is depicted as shown in Fig. 5.12(b). Hence all the sections in the feed network are varied in length and width to achieve optimum -10dB impedance matching.

5.7 Measurement and Discussion

Measurements of the fabricated antenna are performed in an anechoic chamber using Agilent E5071B-VNA. 3D computational technique (FDTD) based commercial electromagnetic structure simulator; CST of version v.19 [6] is used for the complete simulation of the antenna. Two stable DC voltage sources are used to bias the PIN diodes. A standard ridged TEM Horn antenna (0.3-18GHz) is used to measure the far-field radiation characteristic for LP states. CP antennas of known specifications are used to measure radiation characteristics of CP states of the prototype antenna. The SMA feed is covered with RF absorbers to ensure least coupling of external spurious radiation which could cause ripples in the measured pattern. RF choke is used in DC bias lines and aluminum foil is used to cover the external bias lines along with the DC supply to prevent external RF noise. Though few discrepancies in the measured S_{11}, realized gain and pattern are observed. These deviations can be attributed to many factors such as improper soldering and non-identical lumped elements which misaligned the symmetric nature of the structure. Parasitic effects of the diodes and incorporating simple circuit model in the simulation environment also offsets the results.

5.7.1 Reflection Coefficient (S_{11})

Simulated and measured S_{11} plots are shown in Fig. 5.13. 10dB reflection and % of fractional bandwidth for all states are presented in Table 5.4. Dual CP or dual LP states at any specific frequency band are observed to be similar due to antenna symmetry. Higher order modes in the vicinity of fundamental mode are also resonated due to inter modal power coupling hence increasing the impedance bandwidth at those states as shown in the Fig. 5.13(a), (b), (d), and (e) respectively. The reasons for slight discrepancies in the results have already been discussed.

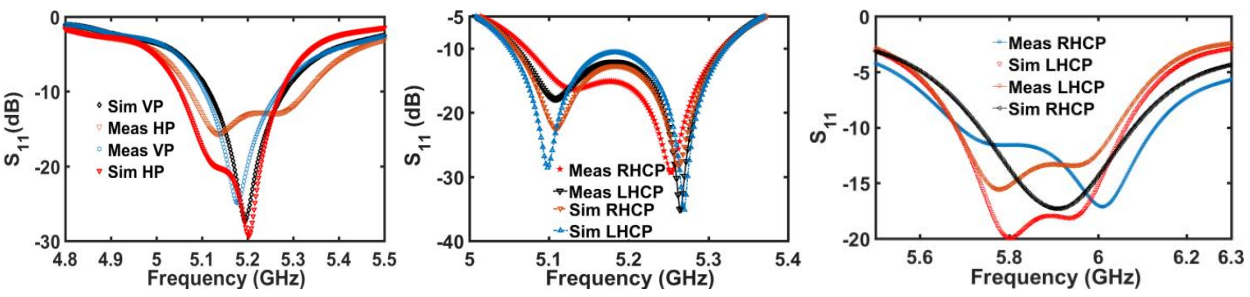

(a) (b) (c)

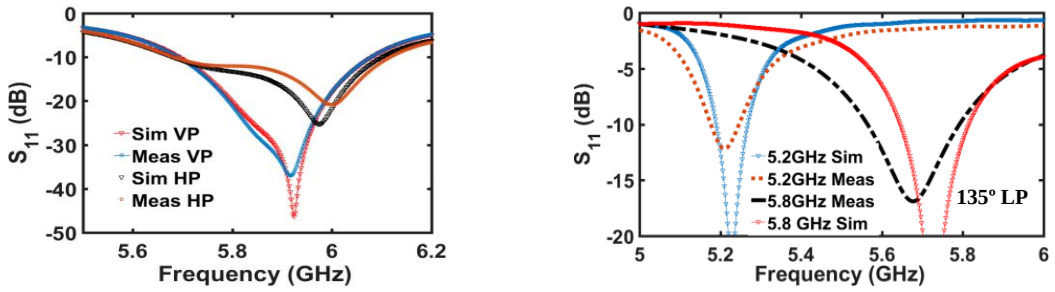

(d) (e)

Fig. 5.13: Reflection coefficient (S11) for all five polarization states at 5.2GHz and 5.8GHz band (a) 5.2GHz LP states, (b) 5.2GHz CP states, (c) 5.8GHz CP states, (d) 5.8GHz LP states and (e) 5.2GHz and 5.8GHz band 45° LP states.

5.7.2 3dB Axial Ratio bandwidth

3dB axial ratio bandwidth for LHCP and RHCP states at both the operating bands are shown in Fig. 5.14(a) and 5.14(b) respectively. The plots depict good agreement between simulated and measured results. The corresponding simulated and measured 3dB bandwidths are shown in Table 5.4. It is also noted that AR bandwidths also covers the WLAN operating bandwidth of each band. Slight offset in the measured results is due to various factors that has already been discussed in previous sections.

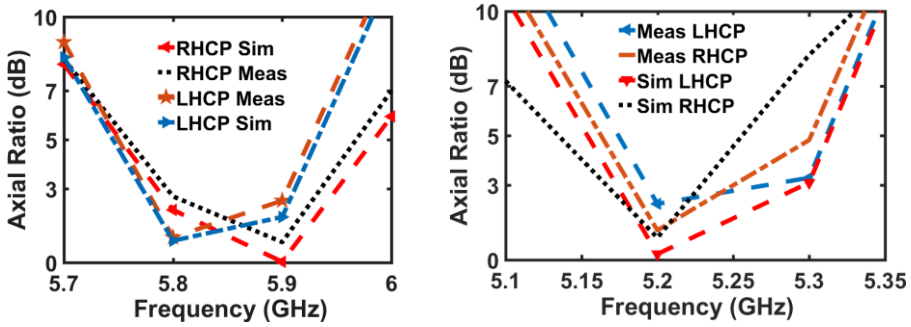

(a) (b)

Fig. 5.14 Simulated and measured 3dB Axial Ratio for CP states at both the frequency bands (a) 5.8GHz (f2) and (b) 5.2GHz (f1) band.

5.7.3 Realized Gain (dBi) and total antenna efficiency (%η)

The simulated and measured realized gain for different polarization states at 5.8GHz and 5.2GHz bands are observed to vary between the range of 6 to 7.5 dBi and 5 to 7 dBi respectively

as shown in Fig. 5.15(a) and presented in Table 5.4. The measured realized gain for all the states is found to be stable within 2dBi in both the bands. Forward biased diodes draw larger current hence incur larger ohmic losses which further combines with the dielectric and conduction losses and reduce the overall realized gains and antenna efficiencies at different states. Thus, comparatively lesser gains are observed for the states with larger number of diodes at ON mode. As ON state diodes provide larger losses hence CP states are having larger efficiencies with respect to LP states, whereas 45° slant polarization exhibits least efficiency due to maximum ON state diodes as shown in Fig. 5.15(c). The simulated efficiencies are shown in Table 5.4 and found to vary between 80 to 90 % & 70 to 80% respectively for 5.2GHz and 5.8GHz bands respectively. D1 to D4 diodes are kept ON realizing 5.8GHz band as shown in Fig. 5.1(a) thus it shows even further decrease in efficiency.

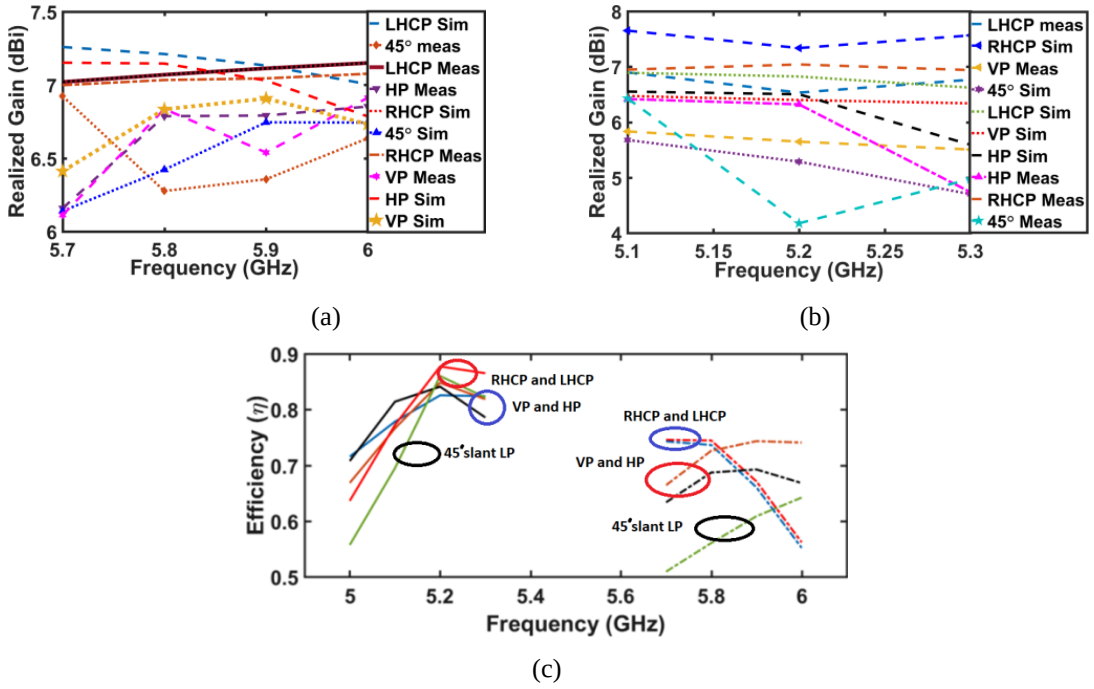

Fig. 5.15 (a) Simulated and measured Realized Gain (dBi) at 5.8GHz, (b) Simulated and measured Realized Gain (dBi) at 5.2GHz and (c) Total Antenna efficiency for different polarization state at both the frequency bands

5.7.4 Far-field radiation characteristics

Simulated and measured normalized far-field radiation patterns (RP) for all the polarization states at both the frequency bands are shown in Fig. 5.16 at φ = 0° & 90° planes. RP for all states is

observed to radiate at broadside direction without any sidelobes and least front to back ratios. Below -18dB and -15dB cross-pol levels are noted for LP and CP states respectively at both the bands principal planes. For 135° slant LP the cross-pol is measured below -15dB as shown in figure for 5.8GHz and 5.2GHz band respectively. Minor shift in the measured results can be explained due to fabrication tolerance, coupling of external noise in bias lines/wires and measurement difficulties as multiple wires were attached to the antenna for biasing.

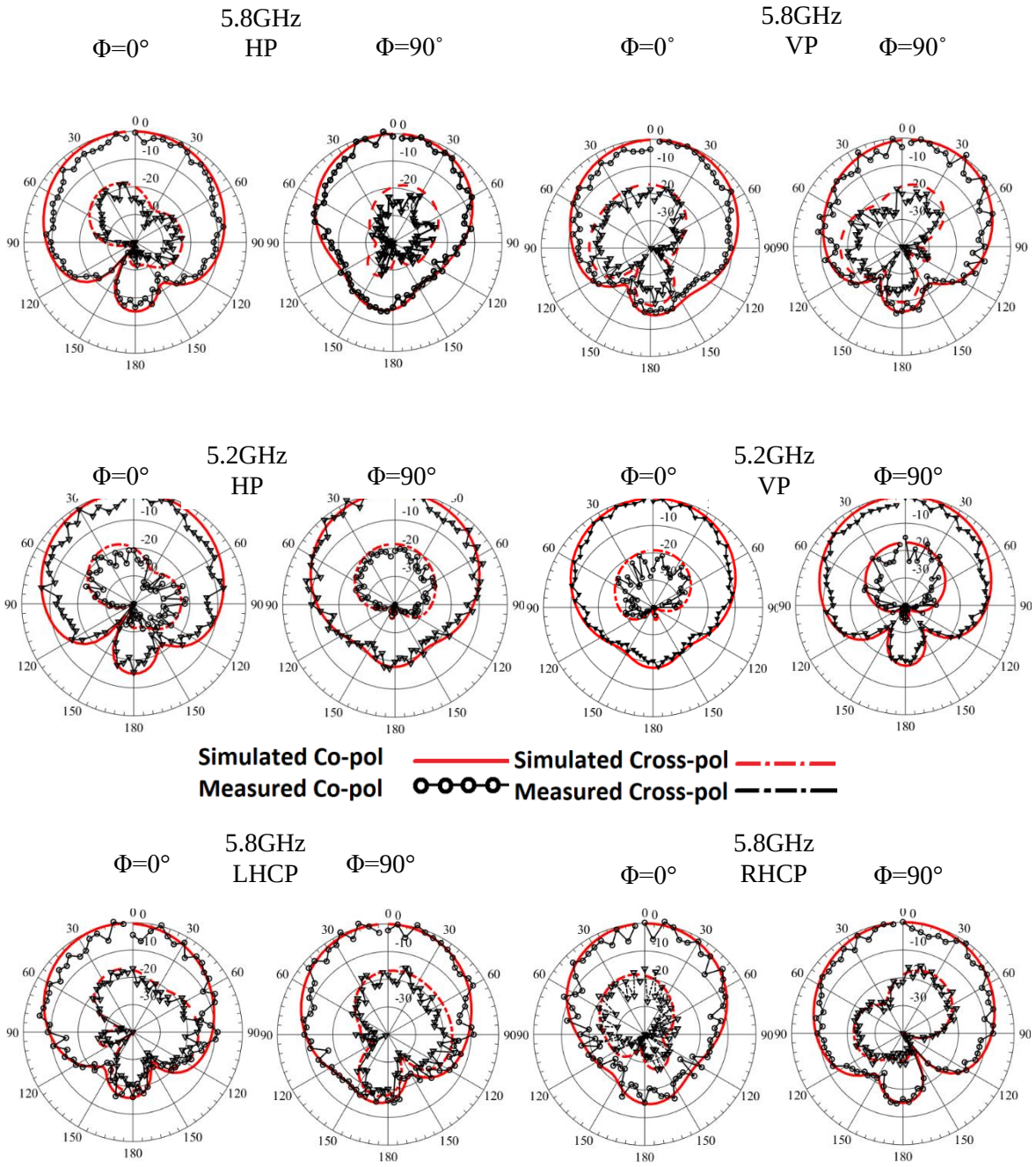

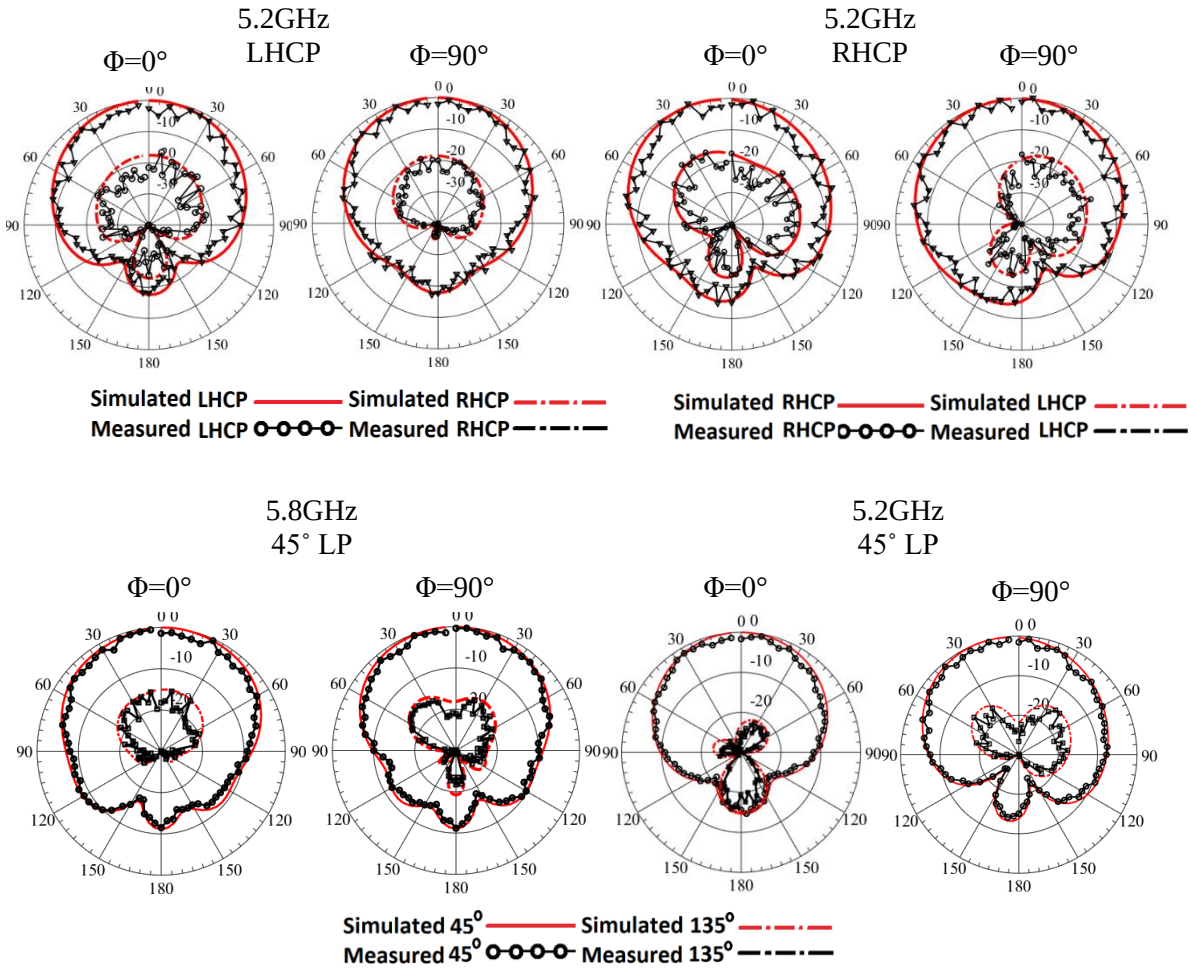

Fig. 5.16 Simulated and Measured far field normalized radiation pattern at Φ=0˚ and Φ=90˚ plane for all ten reconfigurable states. Co-pol and X-pol for LP states, RHCP and LHCP for CP states and 45 º/135 º angle plots for slant LP states are shown.

TABLE 5.4: SIMULATED AND MEASURED ANTENNA PARAMETERS

Polarization State	-10dB Impedance BW (MHz/%)		3dB Axial Ratio BW (MHz)		Realized Gain at φ = 0°, θ= 0° (dBi)		Antenna Efficiency (%)
			For 5.2GHz Band (f1)				
	S	M	S	M	S	M	S
HP	315/1.5	321/3			5.64	5.04	84
VP	269/2.3	290/1.7			6.82	6.67	84
45	78/1.5	70/1.4			6.52	5.63	82
RHCP	322/3.2	256/5	122	103	7.04	5.8	86
LHCP	316/3.1	222/4.3	76	80	6.5	5.94	87
			For 5.8GHz Band (f2)				
HP	428/2.6	441/3.6			7.1	6.9	74
VP	380/2.7	410/4			7.1	6.7	73
45	168/3	231/4			7.2	6.5	56
RHCP	448/6.7	438/7.6	163	149	7.14	6.3	68
LHCP	417/6.7	445/7.6	131	107	7	6.3	73

S: Simulation M: Measured

5.8 Comparison and Discussion

A comparative study of the performances between the proposed antenna with the recently published works is illustrated in this section. The values of different antenna parameters are organized in Table 5.5. It is observed in the literature that mostly a combination of maximum quad polarization reconfigurability operating up-to three frequency bands is reported as shown in the table. Few studies have demonstrated polarization agility for a single band continuous tuning range [8, 12, 17]. Koul *et al.*, proposed an antenna with multiple frequency bands operating in different polarization states [9]. To achieve triple/quad polarization states operating in multiple frequency bands, authors incorporate complex multilayer structures and feeding arrangements [11, 15] incompatible with practical and industrial applications. Antennas with large footprint area and profile are also proposed for achieving frequency and polarization agility [7,8, 11, 14]. Ge *et al.*, uses large number of switching diodes (48 nos.) to generate quad polarization reconfigurability in three different bands [15]. So far only a single article in literature has discussed about penta-polarization reconfigurability and that too at single frequency band **[**16]. The proposed design is a multilayered meta-surface inspired bulky antenna with 15 diodes that makes the prototype difficult to fabricate for practical implementation.

TABLE 5.5: PERFORMANCE COMPARISON WITH RECENTLY REPORTED FREQUENCY AND POLARIZATION AGILE ANTENNAS

Ref.	f_0(GHz)	Pol. Agility	Freq. Agility	Sub. Layers	Diodes Used	% Imp. BW	Footprint Area (λ_0^2)	Antenna Height(λ_0)	Peak Gain
[14]	5.7	4	1	3	4 SDPT	23/27(LP & CP)	2.64×2.83	0.062	9.9-10.3
[15]	2.25-2.45	4	3	1	48 PIN	33.9	0.86 × 0.78	0.01	4.7
[12]	2.4-3.6	3	1	1	12 VARACTORS	40 Tuning (CP and LP)	1.2 × 1.1	0.04	2.6-7.3
[13]	2.2-3	2	4	3	32 PIN, 24Varactor	NA	2×0.67	0.18	-1 to 9
[16]	5.2	5	1	2	15 PIN	28	1.21×1.21	0.06	8.2
[10]	5.2/5.8	4	2	1	6 PIN	3.5/3.6	1×1.1	0.08	3
[11]	8-11.2	3	1	2	NA	33 tuning	2.5×2.5	0.725	16.5
[7]	3.5/5.2	2	2	2	4 PIN	21.7/25	1.4×1.4	0.1	6.86/8.14
[8]	3.6-4	4	1	1	2 VARACTORS	10 tuning	1.4×1.4	0.01	5-10
[9]	5.2/5.7	3	2	1	7 PIN	4-8	1.1×1	0.04	5.81
This Work	**5.8/5.2**	**5**	**2**	**1**	**10 PIN**	**7-31(LP, CP)**	**0.5×0.5**	**<0.01**	**5-7.5**

Most of the recently proposed designs are having noticeable concerns such as complex feed network, multiple SMA feed, multilayer bulky structures, complex and asymmetric design which pose significant difficulties in practical and industrial implementations. In comparison, the proposed antenna is a single layer, single feed, planar, compact structure with exceedingly low

profile (>0.01λ), reconfigurable at dual frequency bands and each band can be further operated in five distinct polarization states.

5.9 Conclusion

RF front in present communication era is playing a pivotal role to uphold the most advanced and latest technology-based applications. The gradual deployment of innumerous RF nodes in existing and upcoming 5G ecosystem catalyzed ISI and co-channel interference issues. Selecting a suitable operating state from ten distinct available states (based on predefined SINR and Received Signal Strength threshold of the communication link) can significantly reduce ISI, co-channel interference, and channel multipath issues in recent 5G ecosystem or in any existing ultra-dense RF environments. Hence an antenna perspective approach would provide additional degree of freedom to the system designer along with signal processing and communication front to mitigate these issues. In this chapter a compact simple dual-band penta-polarization agile single layer and single feed MSA is proposed for the first time in the literature to mitigate those issues from an antenna perspective approach. Subsequently a prototype Penta-polarized MSA operates at 5.2GHz, and 5.8GHz bands are fabricated and measured with satisfactory results. Few discrepancies are noted and can be attributed to the fabrication tolerance, non-symmetric soldering, and non-exact circuit model of the PIN diodes. Though low loss, higher accuracy RF or MEMS switch can be used to enhance the antenna performance. This design methodology also provides insight into the behavior of the equivalent circuit model in terms of resonance frequency which would be useful to translate the structure at other frequency bands for diverse applications. The proposed antenna can be further modified and improved to incorporate more numbers of reconfigurable states using compact, single layered and single SMA feed. In the next chapter, further investigation in this direction is continued.

References

[1] O. T. H. Alzubaidi et al., “Interference Challenges and Management in B5G Network Design: A Comprehensive Review,” Electronics, vol. 11, no. 18, p. 2842, Sep. 2022, doi: 10.3390/electronics11182842.

[2] N. Bhushan et al., "Network densification: the dominant theme for wireless evolution into 5G," in IEEE Communications Magazine, vol. 52, no. 2, pp. 82-89, February 2014, doi: 10.1109/MCOM.2014.6736747.

[3] Mohanta, Harish Chandra; Kouzani, Abbas; Mandal, S K (2019): Reconfigurable antennas and their applications. Deakin University. Journal contribution. https://hdl.handle.net/10536/DRO/DU:30134727

[4] Ramesh, G., Prakash, B., Inder, B., Apisak., Ittipihoon.: “Circularly polarized microstrip antenna and techniques in microstrip antenna design handbook,” Norwood (MA): Artech House; 2001.

[5] https://www.mouser.in/ProductDetail/Broadcom-Avago/HPND-4005

[6] https://www.3ds.com/de/produkte-und-services/simulia/produkte/cst-studio-suite

[7] Z. Nie, H. Zhai, L. Liu, J. Li, D. Hu and J. Shi, "A Dual-Polarized Frequency-Reconfigurable Low-Profile Antenna With Harmonic Suppression for 5G Application," in IEEE Antennas and Wireless Propagation Letters, vol. 18, no. 6, pp. 1228-1232, June 2019, doi: 10.1109/LAWP.2019.2913170.

[8] M. Ikram, N. Nguyen-Trong and A. Abbosh, "A Simple Single-Layered Continuous Frequency and Polarization-Reconfigurable Patch Antenna Array," in IEEE Transactions on Antennas and Propagation, vol. 68, no. 6, pp. 4991-4996, June 2020, doi: 10.1109/TAP.2019.2952461.

[9] R. K. Singh, A. Basu and S. K. Koul, "A Novel Reconfigurable Microstrip Patch Antenna With Polarization Agility in Two Switchable Frequency Bands," in IEEE Transactions on Antennas and Propagation, vol. 66, no. 10, pp. 5608-5613, Oct. 2018, doi: 10.1109/TAP.2018.2860118.

[10] Y. P. Selvam, L. Elumalai, M. G. N. Alsath, M. Kanagasabai, S. Subbaraj and S. Kingsly, "Novel Frequency- and Pattern-Reconfigurable Rhombic Patch Antenna With Switchable Polarization," in IEEE Antennas and Wireless Propagation Letters, vol. 16, pp. 1639-1642, 2017, doi: 10.1109/LAWP.2017.2660069.

[11] C. Ni, M. S. Chen, Z. X. Zhang and X. L. Wu, "Design of Frequency-and Polarization-Reconfigurable Antenna Based on the Polarization Conversion Metasurface," in IEEE Antennas and Wireless Propagation Letters, vol. 17, no. 1, pp. 78-81, Jan. 2018, doi: 10.1109/LAWP.2017.2775444.

[12] J. Hu, X. Yang, L. Ge, Z. Guo, Z. -C. Hao and H. Wong, "A Reconfigurable 1 × 4 Circularly Polarized Patch Array Antenna With Frequency, Radiation Pattern, and Polarization Agility," in IEEE Transactions on Antennas and Propagation, vol. 69, no. 8, pp. 5124-5129, Aug. 2021, doi: 10.1109/TAP.2020.3048526.

[13] N. Nguyen-Trong, L. Hall and C. Fumeaux, "A Frequency- and Polarization-Reconfigurable Stub-Loaded Microstrip Patch Antenna," in IEEE Transactions on Antennas and Propagation, vol. 63, no. 11, pp. 5235-5240, Nov. 2015, doi: 10.1109/TAP.2015.2477846.

[14] J. Hu, Z. -C. Hao and W. Hong, "Design of a Wideband Quad-Polarization Reconfigurable Patch Antenna Array Using a Stacked Structure," in IEEE Transactions on Antennas and Propagation, vol. 65, no. 6, pp. 3014-3023, June 2017, doi: 10.1109/TAP.2017.2695529.

[15] L. Ge, Y. Li, J. Wang and C. -Y. -D. Sim, "A Low-Profile Reconfigurable Cavity-Backed Slot Antenna With Frequency, Polarization, and Radiation Pattern Agility," in IEEE Transactions on Antennas and Propagation, vol. 65, no. 5, pp. 2182-2189, May 2017, doi: 10.1109/TAP.2017.2681432.

[16] P. Liu, W. Jiang, S. Sun, Y. Xi and S. Gong, "Broadband and Low-Profile Penta-Polarization Reconfigurable Metamaterial Antenna," in IEEE Access, vol. 8, pp. 21823-21831, 2020, doi: 10.1109/ACCESS.2020.2969488.

[17] H. H. Tran, C. D. Bui, N. Nguyen-Trong and T. K. Nguyen, "A Wideband Non-Uniform Metasurface-Based Circularly Polarized Reconfigurable Antenna," in IEEE Access, vol. 9, pp. 42325-42332, 2021, doi: 10.1109/ACCESS.2021.3066182.

Chapter 6
Tri-band Penta-Polarization Reconfigurable Planar Antenna

6.1 Introduction

A dual band Penta-polarization reconfigurable antenna is discussed in the previous chapter in the context of interference mitigation in UDN environment in 5G scenario. The proposed prototype antenna operates in ten distinct reconfigurable states. In this chapter an extension of the previous work is presented. The antenna is modified to operate in three different frequency bands and each band can further be reconfigured to operate in five polarization states. Thus, the antenna, operating in fifteen different states would provide the system designers ample choice of reconfigurability to counter signal distortions due to interference. The protype design depicts the following advantages.

1. The proposed planar antenna is compact and low profile ($0.9\lambda_0 \times 0.9\lambda_0 \times 0.01\lambda_0$) with fifteen different reconfigurable states. It is sensible to point out that such agile antennas are rarely investigated in the open literature so far.

2. This design can be scaled to different frequencies in 5G bands; hence scalability makes the proposed design appropriate for a very large variety of applications in upcoming heterogeneous network.

3. The antenna provides great flexibilities to the system designers with fifteen distinct reconfigurable states to attain optimum signal quality in electromagnetically dense environments by increasing the possibilities to nullify co-channel signal interference. In upcoming telecom-regime, the proposed antenna is suitable for diverse applications due to its simple design, ease of fabrication, compactness, and scalability.

6.2 Antenna Design Concept

6.2.1 Concept behind Frequency Agility

The simple design is shown in Fig. 6.1 where a square patch is enclosed by an outer square ring. The inner patch as depicted by highlighted section in Fig. 6.1(a) is designed to operate at higher frequency band i.e., 5.8GHz (f1). Subsequently, the outer ring is interfaced with the inner patch using switching diodes and forms a larger complete patch operates at a lower frequency band i.e., 2.45GHz (f2) as illustrated by the highlighted sections in Fig. 6.1(b). The lowest operating band f3 (1.8GHz) is generated by exciting the outer square ring separately as highlighted in Fig. 6.1(c). Two rectangular slots are cut in the adjacent edges of the outer ring to allow feed lines to connect with the inner patch as shown in Fig. 6.1. Orthogonal microstrip feed lines are connected with the adjacent patch edges to excite different antenna sections using switching diodes and bias network to initiate multiple reconfigurable states as per requirement. As shown in Fig. 6.2(f), f1 and f2 are obtained from the edge lengths of the inner and outer square patches as depicted by (6.1) & (6.2) respectively. The lowest frequency band f3, due to larger current path on the outer ring patch surface is derived by (6.3). These expressions are very well established in the literature [1].

$$f1 = \frac{c}{2b\sqrt{\varepsilon_{eff}}} \qquad (6.1) \qquad f2 = \frac{c}{2a\sqrt{\varepsilon_{eff}}} \qquad (6.2) \qquad f3 = \frac{c}{2(a+b)\sqrt{\varepsilon_{eff}}} \qquad (6.3)$$

where a and b are the edge lengths of inner and outer patch and ε_{eff} represents the effective dielectric constant of the substrate.

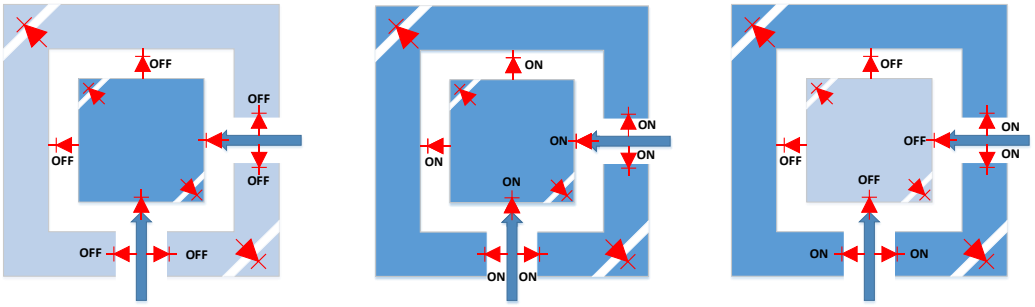

(a) (b) (c)

Fig. 6.1 Prototype antenna structures for three reconfigurable bands with suitable diode biasing conditions, (a) f1, (b) f2, and (c) f3

Switching diodes are used to excite the vertical and horizontal feed line as shown in Fig. 6.2. Vertical line is excited to realize VP and LHCP states while horizontal feed is activated to generate HP and RHCP states. Subsequently, the feed lines are excited together to generate a 45° linear polarization state as pictured in Fig. 6.2.

6.2.2 Polarization Reconfigurability

The diagonal corners of a square MSA are truncated to generate the orthogonal modes, i.e., TM_{10} and TM_{01} respectively to initiate circular polarization. This is a well devised technique and thoroughly detailed in the literature [16]. The area of the truncated corners is related with the quality factor of the antenna using (6.4) to initiate the CP states [2].

$$\frac{Total\ Area\ of\ the\ Truncated\ corner\ (2*\Delta A)}{Total\ Area\ of\ the\ square\ patch\ (A)} = \frac{1}{2*Quality\ Factor(Q0)} \tag{6.4}$$

In the proposed design, corners of the inner and outer patches are cut as pictured in Fig. 6.1 & 6.2 to get CP states in all operating bands. The frequencies of the orthogonal modes of the near square patch antenna for f1 band are given in (6.5) & (6.6) respectively.

$$f_x = f_1\left(1 - \frac{2\Delta B}{B}\right) \tag{6.5}$$

$$f_y = f_1 \tag{6.6}$$

$$Q_0 = f_0/\Delta f \tag{6.7}$$

where, $\Delta B (= \Delta B1 + \Delta B2)$ is the overall area of both the diagonal corners as shown in Fig. 6.2(f.) Also, $B = b^2$ is the total area as shown in Fig. 6.2(f). Subsequently, the orthogonal frequencies for combined square patch (for f2 band) and the outer ring (f3 band) as highlighted in Fig. 6.2 are devised below.

$$f_x^2 = f_3\left(1 - \frac{2\Delta A}{A1}\right) < f_x^1 = f_2\left(1 - \frac{2\Delta A}{A}\right) < f_x, \quad f_y^2 = f_3 < f_y^1 = f_2 < f_y \tag{6.8}$$

where, $\Delta A = \Delta A1 + \Delta A2$, area of the total truncated sections of the outer ring and $A = a^2$ (total area of the combined patch) while considering combined inner-outer patch for f2 operation

as illustrated in Fig. 6.2(f). Subsequently, $A1 = b^2 - w^2$ where w is the inner edge length of the outer ring patch for f3 band operation. The truncated corners of the outer square ring patch are shared by f2 and f3 operating bands. The values of Q_0 for five distinct polarization states at each band are derived from the simulated Z_{real} using (6.7).

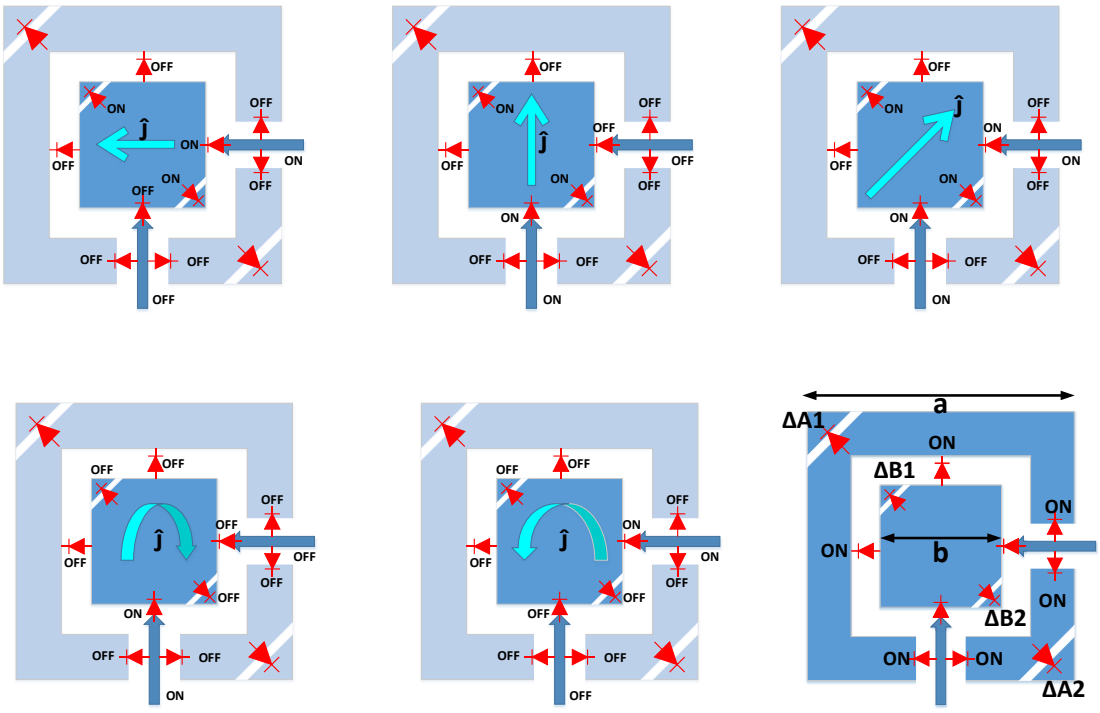

Fig. 6.2 Illustration of the orientation of surface currents on the prototype antenna at f1 band for Penta polarization states, (a) HP, (b) VP, (c) 45° slant (d) LHCP, (e) RHCP and (f) prototype antenna structure using suitable biasing network

These derived Q_0 values are used to find the length of the truncated corner (ΔA) of the outer ring for band 2 and band 3 using (6.4) and found to be 6.63mm and 7.12mm respectively. The lengths of the truncated corners are slightly different as the bands are slightly different (f2=2.45GHz and f3=1.8GHz). If we design the antenna with outer ring patch corner length 6.63mm, which is derived for f2 band then a proper 3dB AR value is observed for LHCP or RHCP states at f2 band, but AR deteriorates in case of f3 band as depicted in Fig. 6.3(a). Similarly, considering a corner length of 7.12mm (which is derived for f3 band), the design exhibits proper 3dB AR of both the CP states at f3 frequency band while the AR at f2 band for both the CP states deteriorates as depicted in the Fig. 6.3(b). As both the polarization states depict similar results, only the LHCP state is shown in the plots for necessary illustration. It is observed that AR for

both CP states in f2 and f3 band is primarily dependent on the lengths of the inner (w) and outer (a) sides of the outer ring patch along with corner length (y) and corner slot width (x). Detail marking on antenna sections are clearly shown in Fig. 6.7(a).

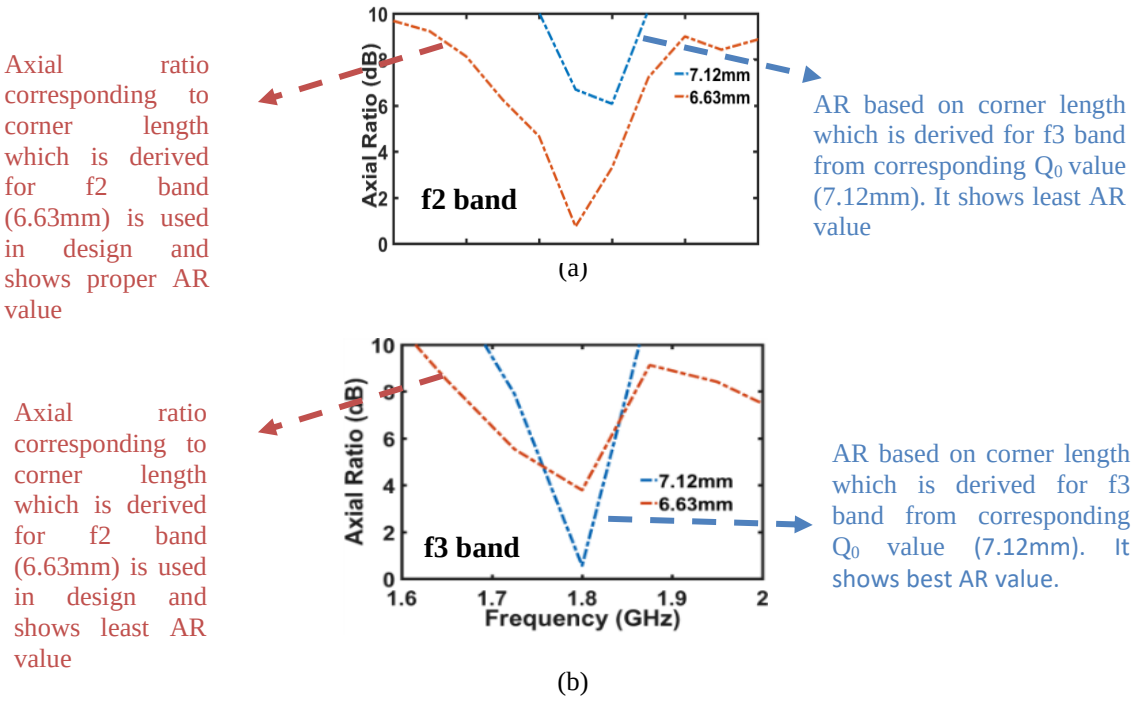

Fig. 6.3 LHCP Axial Ratios based on corner lengths which are derived from the Q_0 values of the f2 and f3 bands (a) AR at f2 band corresponding to 6.63mm and 7.12mm corner lengths and, (b) AR at f3 band corresponding to 6.63mm and 7.12mm corner lengths.

Complete parametric optimization of the above parameters is performed to achieve optimum 3dB AR in all CP states in both the frequency bands. It is noted that at the truncated length of 6.8mm along with the other optimized parameters, the AR for all CP states at both bands depict suitable results which are illustrated in section 6.4. Fig. 6.3 illustrates the generation of five distinct polarization states at f1 band by selectively choosing the vertical and horizontal feed lines using proper switching diodes and biasing network. Subsequently, 45° linear polarization is attained by exciting both the feed lines together with equal phase and amplitude as shown in Fig. 6.3(c).

Diode biasing states for penta polarization reconfigurability at three different bands are listed in Table 6.1.

TABLE 6.1: DIODE BIASING FOR TRI-BAND PENTA POLARIZATION STATES

Freq.	Pol. States	D1 & D2	D3& D4	D5	D6	D7& D8	D9 &D15	D10 & D11	D12 & D13	D14
f1	VP	Off	Off	On	Off	Off	Off	Off	Off	On
	HP	Off	Off	Off	On	Off	On	Off	Off	Off
	45°	Off	Off	On	On	Off	On	Off	Off	On
	RHCP	Off	Off	Off	On	Off	On	Off	Off	On
	LHCP	Off	Off	On	Off	Off	Off	Off	Off	On
f2	VP	On	On	On	Off	On	Off	On	On	On
	HP	On	On	Off	On	On	On	On	On	Off
	45°	On	On	On	On	On	On	On	On	On
	RHCP	Off	Off	Off	On	On	On	On	Off	On
	LHCP	Off	On	On	Off	On	Off	On	Off	On
f3	VP	On	Off	Off	Off	On	Off	On	On	On
	HP	On	Off	Off	Off	On	On	On	On	Off
	45°	On	Off	Off	Off	On	On	On	On	On
	RHCP	On	Off	Off	Off	On	On	On	Off	Off
	LHCP	On	Off	Off	Off	On	Off	On	Off	On

6.2.3 Polarization Agility at f1 band

Polarization agility at f1 band is achieved using specific diode biasing conditions illustrated in Table 6.1. Surface currents of the inner patch for RHCP and LHCP states are shown in Fig. 6.4 for T/4 successive time periods. This portrays the shortest $\lambda/2$ current path subsequently represents upper frequency band (f1=5.8GHz).

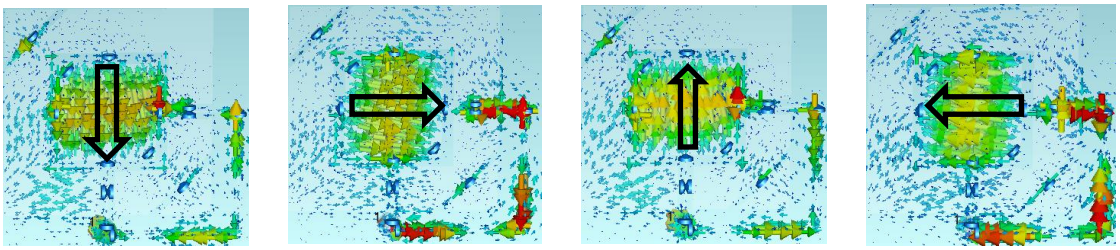

t=0 t=T/4 t=T/2 t=3T/4

(a)RHCP

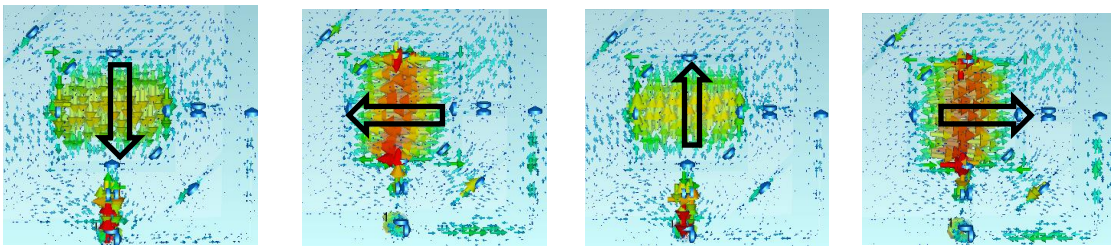

t =0 t=T/4 t=T/2 t=3T/4

(a)LHCP

Fig. 6.4 Current distribution on the MSA surface for successive T/4 time at f1 band for (a) RHCP and (b) LHCP

6.2.4 Polarization Agility at f2 band

Five reconfigurable polarization states at f2 band are achieved using the diode biasing conditions as illustrated in Table 6.1. Surface current of the combine patch for RHCP and LHCP states are shown in Fig. 6.5 for successive T/4 time periods at f2 band (2.45GHz).

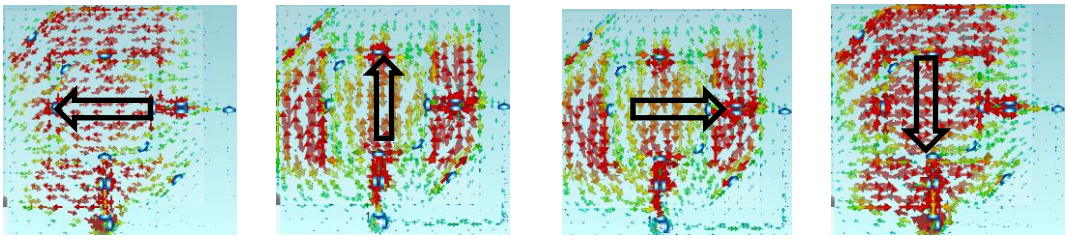

t=0 t=T/4 t=T/2 t=3T/4

(a)LHCP

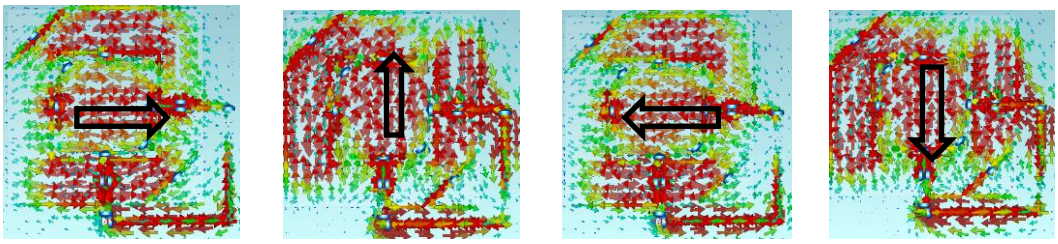

t=0 t=T/4 t=T/2 t=3T/4

(a)RHCP

Fig. 6.5 Current distribution on the MSA surface for successive T/4 time at f2 band for (a) LHCP and (b) RHCP

6.2.5 f3 band polarization Agility

Penta-polarization agility at f3 band is attained by introducing the diode biasing states as presented in Table 6.1. Surface current of the complete patch (patch contains inner square and outer ring antennas using diode) for RHCP and LHCP states are shown in Fig. 6.6 for successive T/4 time periods at f3 band (1.8GHz).

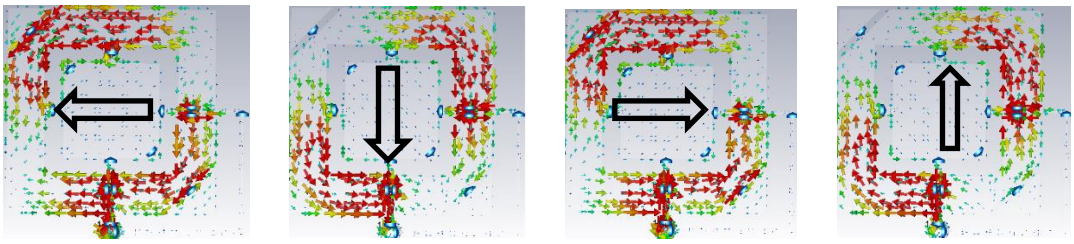

t=0 t=T/4 t=T/2 t=3T/4

(a)RHCP

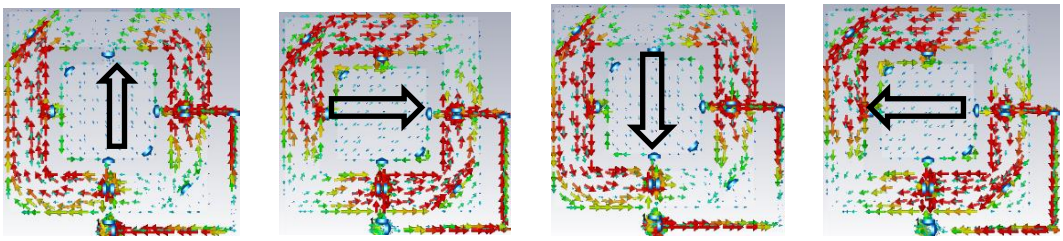

t=0 t=T/4 t=T/2 t=3T/4

(a)LHCP

Fig. 6.6 Current distribution on the MSA surface for successive T/4 time at f3 band for (a) RHCP and (b) LHCP

The designed and fabricated prototype antenna is shown below in Fig. 6.7.

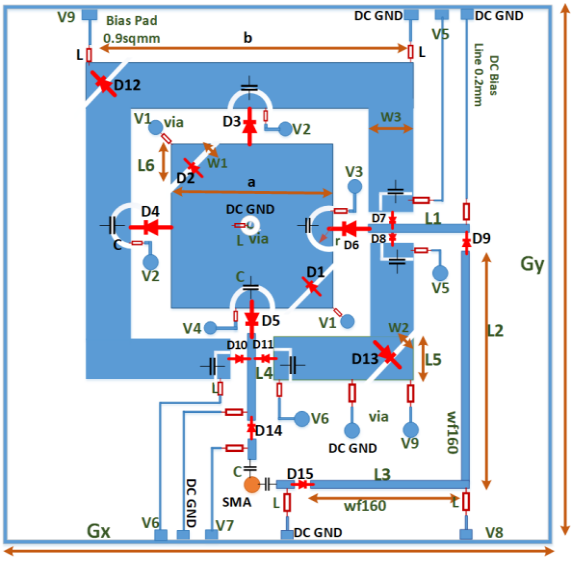

(a)

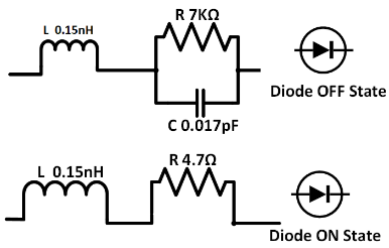

(b)

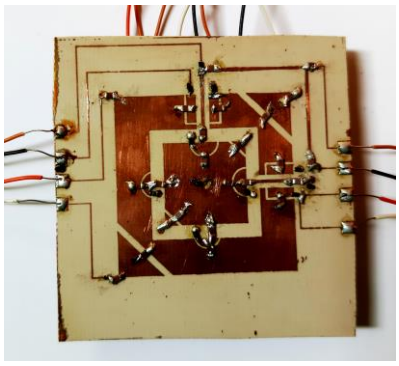

(c)

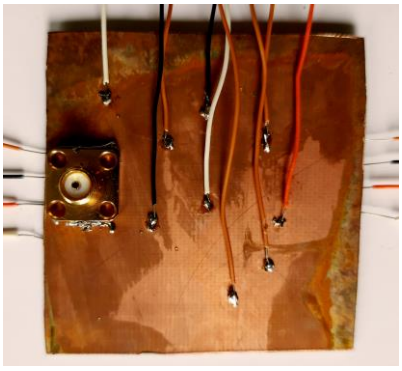

(d)

Fig. 6.7 (a) Antenna diagram with complete feed network, switching diodes and bias network, fabricated prototype antenna (b) Equivalent diode model, (c) Top view and (d) Bottom view. *Gx=Gy=50, a=12.5, b=27.2, L1=10.55, L2=15.73, L3=16.17, L4=8.2, L5=6.8, L6=1.3, W1=1, W2=0.32, W3=5.8, r=3, and wf160= 0.2 (in mm)*

The phase and magnitudes of the radiated electric components are analyzed in the broadside direction for the clarity of understanding of different polarization states. Fig. 6.8(a) illustrates the ratios of the $|E_\theta/E_\varphi|$ in dB in both the principal planes φ=0° & 90° respectively at RHCP and LHCP states at f2 frequency band. The plot depicts that the ratios lie within ±1.5dB exhibiting nearly equal magnitude along the Half Power Beamwidth (HPBW ±53°) of the pattern. In conjunction, the relative phase differences between the orthogonal components i.e., $\angle(E_\theta - E_\varphi)$ in the principal planes are nearly ±90° throughout Half Power Broadside beam as shown in Fig. 6.8(b). Hence, the phase and magnitude of E_θ *and* E_φ is found appropriate for both LHCP and RHCP generation. The axial ratio along the broadside direction within HPBW is found within 3dB value in both the principal planes as illustrated in Fig. 6.9(a).

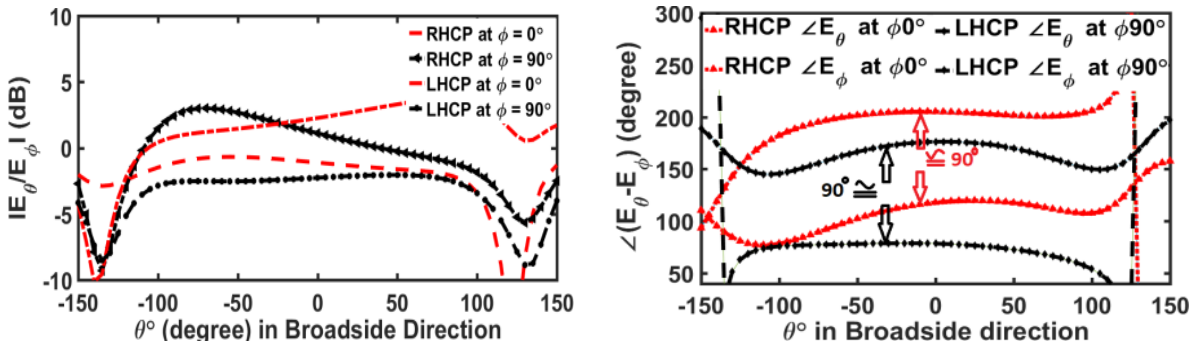

(a) (b)

Fig. 6.8 (a) Simulated amplitude ratios of $|E_\theta/E_\varphi|$component, (b) simulated Phase of $\angle(E_\theta - E_\varphi)$ for dual CPs at φ=0° & 90° plane at f2 operating band

The relative phase and ratio of the orthogonal components E_θ *and* E_φ are also observed for 45° slat polarization state. The $|E_\theta/E_\varphi|$ in dB is found to remain within ±1dB while the phase difference $\angle(E_\theta - E_\varphi)$ at φ=0° & 90° planes is nearly zero ($\angle E_\theta = \angle E_\varphi$) along the HPBW at boresight direction as illustrated in Fig. 6.9(b). Similar observations are noted for f1 and f3 bands also, hence not shown for brevity.

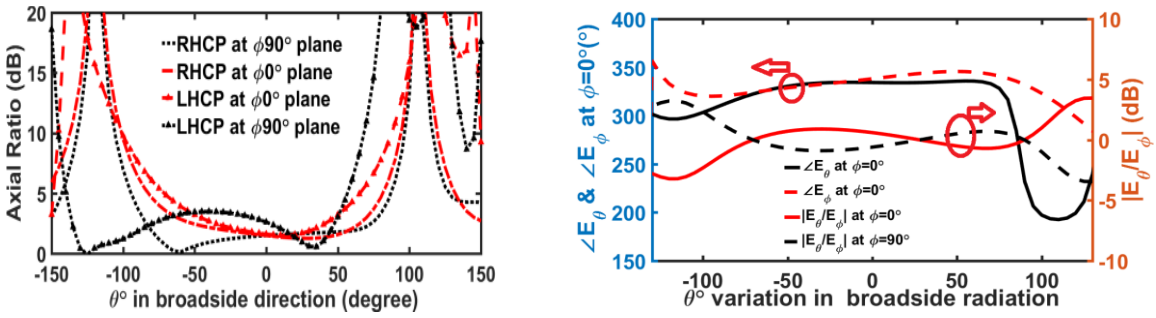

(a) (b)

Fig. 6.9 (a) Simulated Axial Ratios of the components at the farfield at φ=0° & 90° plane at f2 operating band and (b) Simulated amplitude of E_θ and E_φ component ratios and Phase of E_θ and E_φ components for 45° slant polarization at φ=0° & 90° plane

6.3 Prototype Antenna Design

To validate the proposed theory, a MSA operates at 1.8GHz (f3), 2.4GHz (f2) and 5.8GHz (f1) bands is designed and fabricated. These bands can further be reconfigured to generate penta-polarization states using proper biasing networks presented in the subsequent sections. Roger AD430 substrate with dielectric constant ε_r=4.3, loss tangent $\tan\delta$=0.002 and height h=30mil is used to fabricate the antenna. The complete layout with marking and dimension of the simulated antenna is shown in Fig. 6.7. The fabricated antenna is also presented in the figure. Finite Difference Time Domain (FDTD) based commercial 3D electromagnetic structure simulator; CST of version v.19 [3] is used for the complete simulation of the antenna.

6.3.1 Antenna feed network design and optimization

The impedance of the horizontal and vertical edges for fifteen distinct reconfigurable states are deduced from simulation results. Fig. 6.10(a-c) illustrates the real and imaginary impedances of all fifteen states. It is interesting to observe that for any frequency band the impedance behavior of CP or LP states are similar to great extent due to antenna symmetry. The real part of the impedances is noticed to vary between the range of 100-250Ω as depicted in the Fig. 6.10. Correspondingly, the imaginary parts are noticed to remain nearly zero (~0j). A judicious approach is made by considering the average edge impedance around 160Ω for all operating modes. Quarter wave matching sections are used to transform the impedance to 80Ω at the coax end as illustrated in Fig. 6.7(a). The input impedance at the junction of the two feed

lines is observed to vary within the range 50-100Ω which would mismatch slightly with the 50Ω coax feed but delivers enough matching to provide -10dB reflection bandwidth for all the states. A slight offset in the impedances is noted after including the bias network in the design. Additional optimization of the feed network is done to achieve optimum impedance matching.

a.

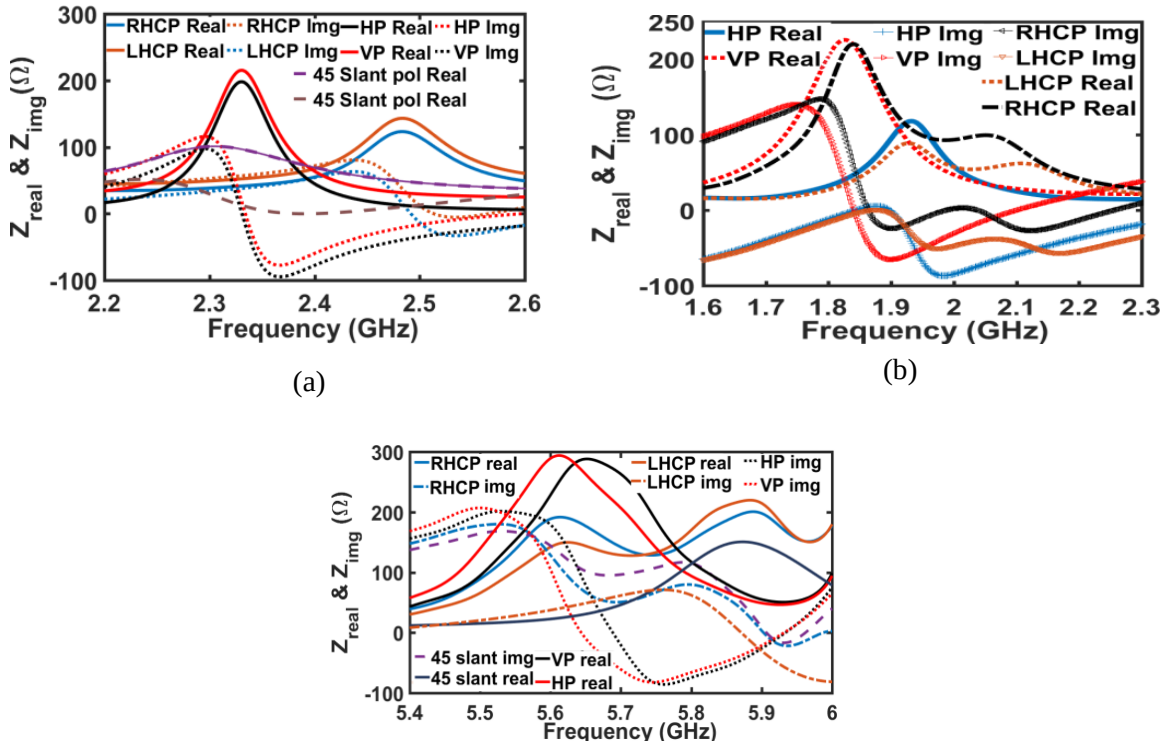

Fig. 6.10 Real and Imaginary part of the edge impedances of the prototype antenna for multiple polarization states at, (a) f1 (b) f2 and (c) f3 band.

6.3.2 Biasing Network

Switching PIN diodes (model HPND-4005, Avago Technology) [4] are incorporated in the design for the switching mechanism. In forward and reverse bias conditions the diode equivalent circuit with the corresponding values of the series and parallel resistor R, inductor L and capacitor C are shown in Fig. 6.7(b). These switches exhibit low package parasitic along with improved isolation and insertion loss (0.4dB). For proper diode biasing and coupling management, DC bias lines of width 0.2mm and 0.3×0.3mm^2 bias pads are designed with proper layout on the antenna as shown in Fig. 6.7(a). 47nH series inductors are placed on the bias line

to block RF component to the sources. Subsequently, series capacitances (33pF) are incorporated in the bias network for RF signal continuity. The bias network and subsequent components are shown in the antenna diagram and also in the fabricated antenna in Fig. 6.7.

6.4 Measurement and Discussion

The radiation and impedance characteristics of the fabricated antenna are measured using VNA Agilent E5071B. Few precautionary measures are taken while conducting the measurement in an anechoic chamber. Spurious radiations from the open feed are prevented by covering with absorbers whereas the external DC wires are wrapped with aluminum foil to avoid further radiations which may couple with the antenna radiation and cause pattern distortion. Despite of the precautions, minute inconsistencies between the measured and simulated results are observed. These discrepancies are attributed to improper soldering while fabricating the antenna and integrating crude circuit model of the diodes in the simulation environment.

6.4.1 Reflection co-efficient (S_{11})

The 10dB Impedance bandwidth for all fifteen operating modes is detailed in Table 6.2. Due to antenna symmetry, the input impedances (Z_{in}) and reflection coefficients for both the CP (RHCP & LHCP) and LP (VP & HP) states are observed to be comparable at any specific frequency band as illustrated in Fig. 6.12. In general, a single fundamental resonance for LP and dual orthogonal resonances for CP states are observed when the antenna is excited using individual orthogonal SMA feeds as depicted in Fig. 6.11(a). Similar trend is observed in all polarization states at three frequency bands while exciting the antenna using single SMA attached at the end of the coplanar edge feed microstrip lines. However, two additional higher harmonics in proximity of the fundamental mode in HP and RHCP states at f1 band are observed as depicted in Fig. 6.11(a-b).

This exception is observed in the real impedance plot at HP and RHCP states in f1 band as illustrated in Fig. 6.11(b). Interestingly these higher order modes are not present when the antenna is excited by individual orthogonal feeds as shown in Fig. 6.11(a). Surface wave excitation and coupling from the orthogonal microstrip feed lines excites these unintended higher order modes. Since the modal significance of the fundamental mode is found to be dominant, its

characteristic is prominent over the band. As a result, the antenna performance remains unaltered except the increment of impedance bandwidth of those specific states.

Excitation using individual SMA at each orthogonal edge

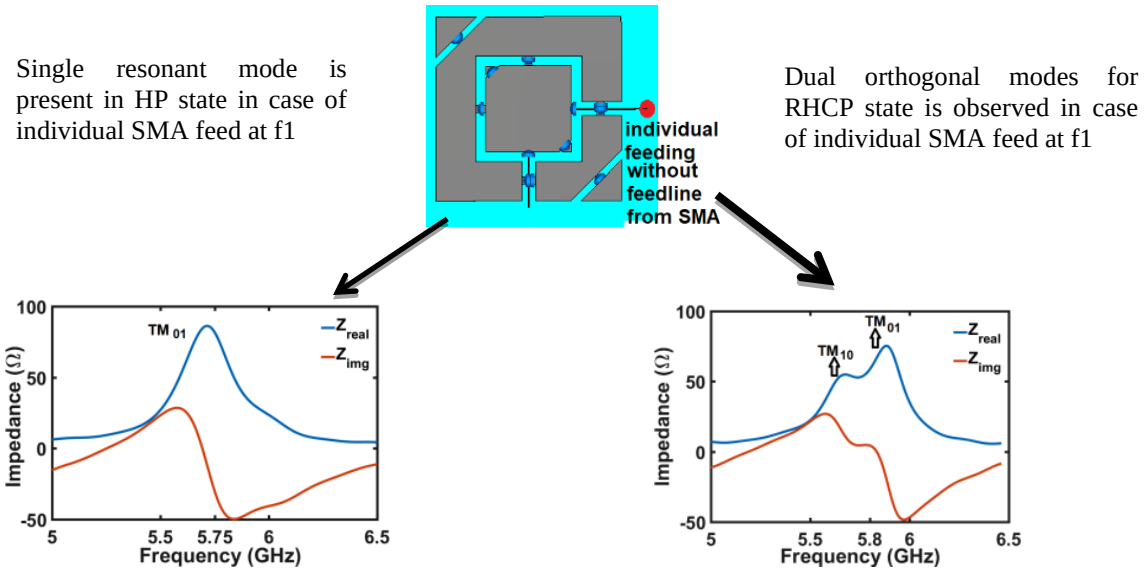

Fig. 6.11 (a) Designed Antenna with individual orthogonal SMA feed and corresponding resonances at f1 (5.8GHz band)

Excitation using Coplanar Orthogonal Feed Lines with single SMA

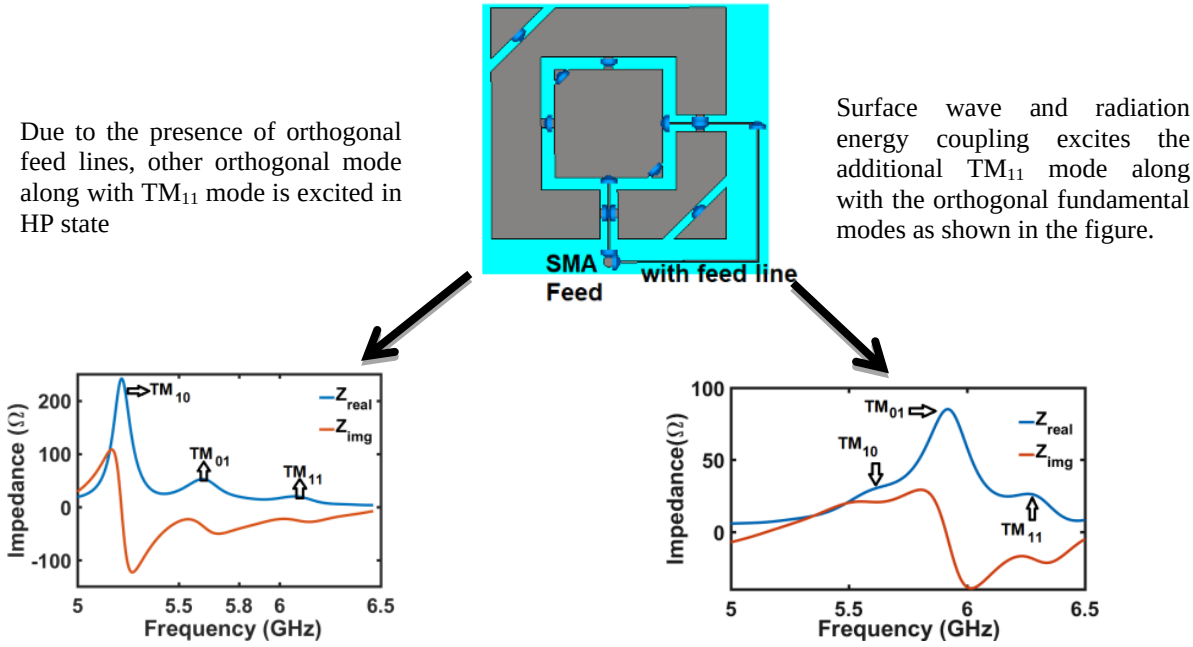

Fig. 6.11 (b) Antenna with orthogonal microstrip line feed with corresponding resonances at f1 band

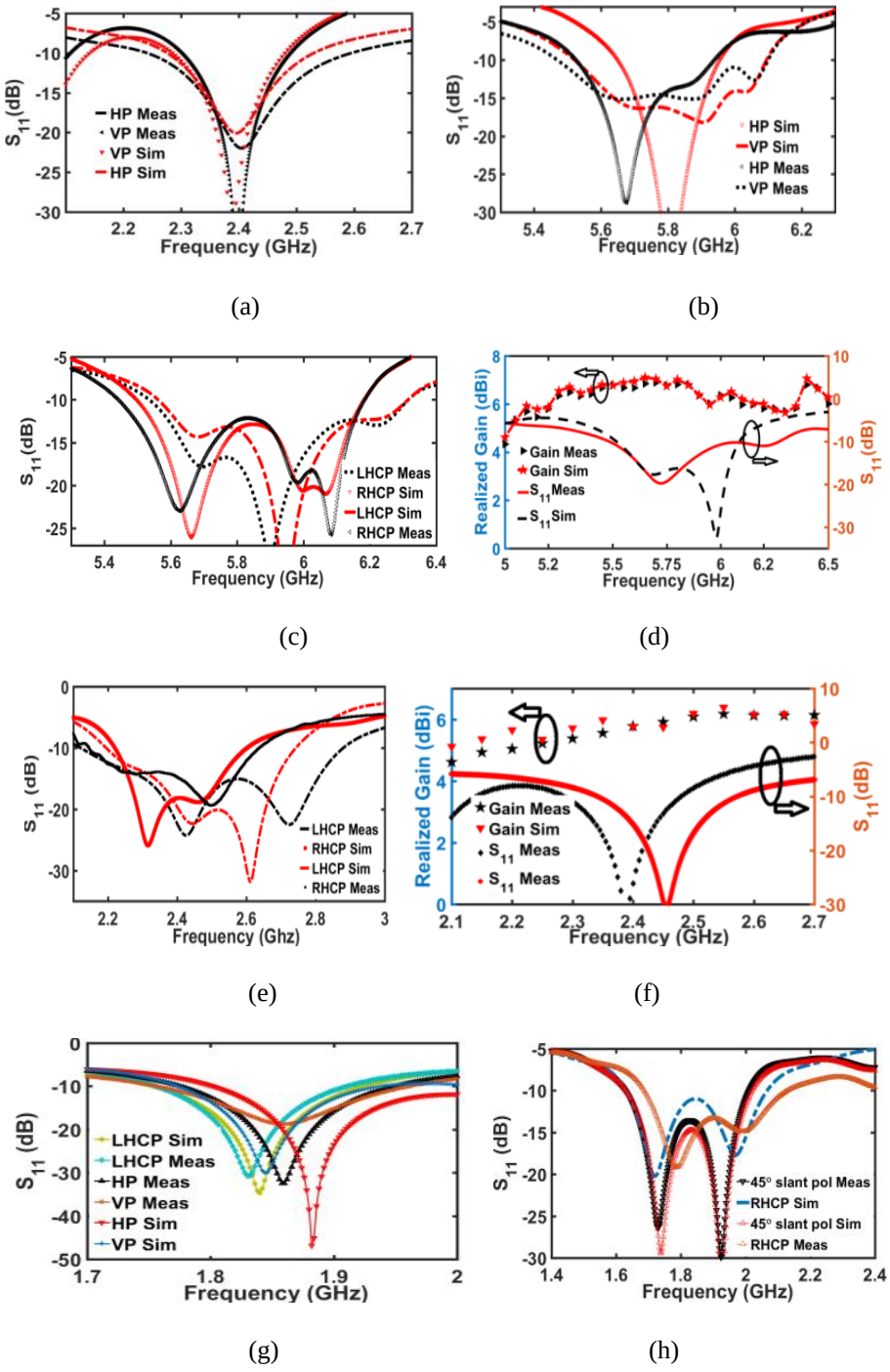

Fig. 6.12 Simulated and measured reflection coefficients S_{11} for all polarization states (a) LP at f1, (b) CP at f1, (c) LP at f2, (d) 45° slant S_{11} and realized gain at f1, (e) CP at f2, (f) 45° slant S_{11} and realized gain at f2, (g) LP and LHCP sates at f3 and, (h) RHCP and 45° slant states

6.4.2. Radiation Pattern

Fig. 6.13 illustrates the antenna radiation pattern for fifteen reconfigurable conditions at φ = 0° and φ=90° planes. The measurement technique of the CP and 135° slant polarization states are briefly discussed in the previous chapter. Due to antenna symmetry, the pattern for LP or CP states operating in any given band is identical. Thus HP, LHCP with 45° slant polarization states for each band are shown for brevity. Co and X-pol for 45° slant is measured at φ = 45° and φ=135° planes respectively.

Cross polarization levels are measured below -15dB for all modes in φ = 0° and φ=90° planes. HPBWs are measured to be nearly ±50° with slight variation for all the states in both the planes as depicted in the figures. Pattern invariance with negligible side lobe and X-pol level is also noted in few states for comparatively wide impedance bandwidth which is already illustrated in Fig. 6.12. Minute offsets in the measured patterns can be attributed to a variety of factors that have already been discussed in previous section. The radiation patterns at three operating bands are presented below.

At 2.45GHz band

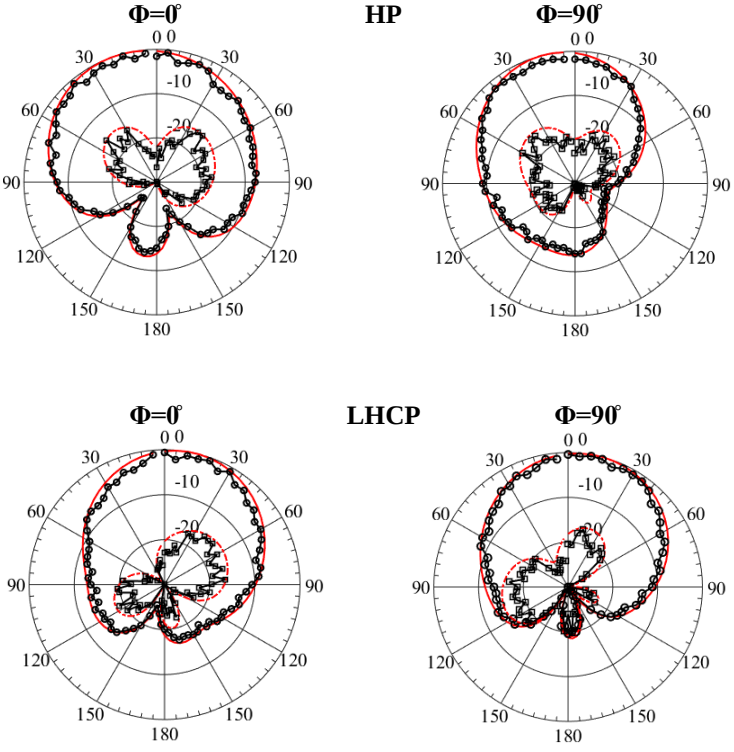

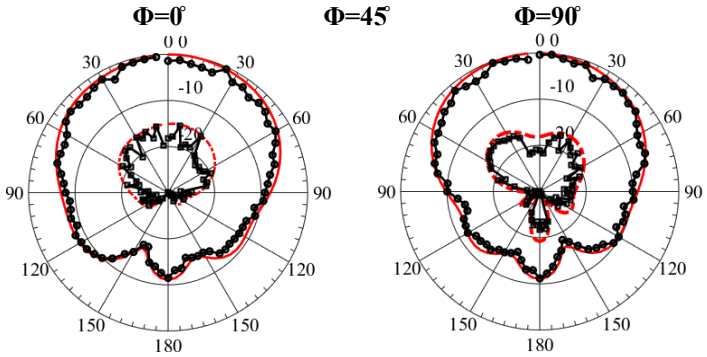

At 5.8GHz Band

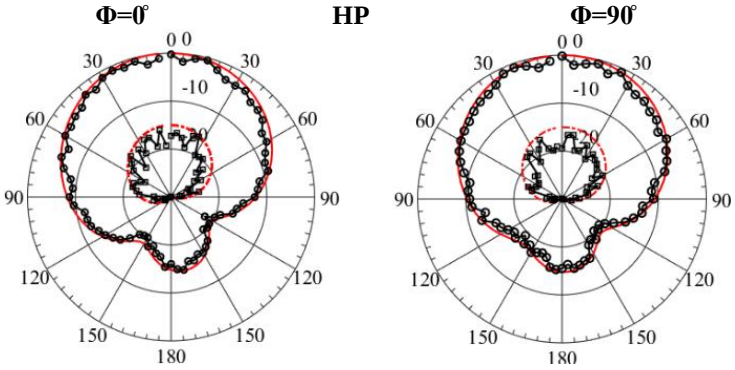

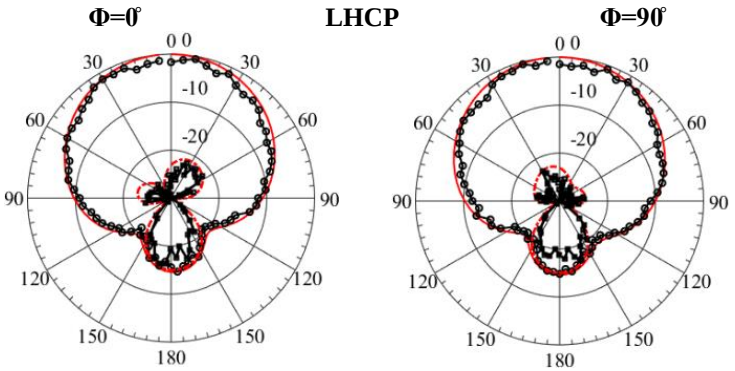

At 1.8GHz Band

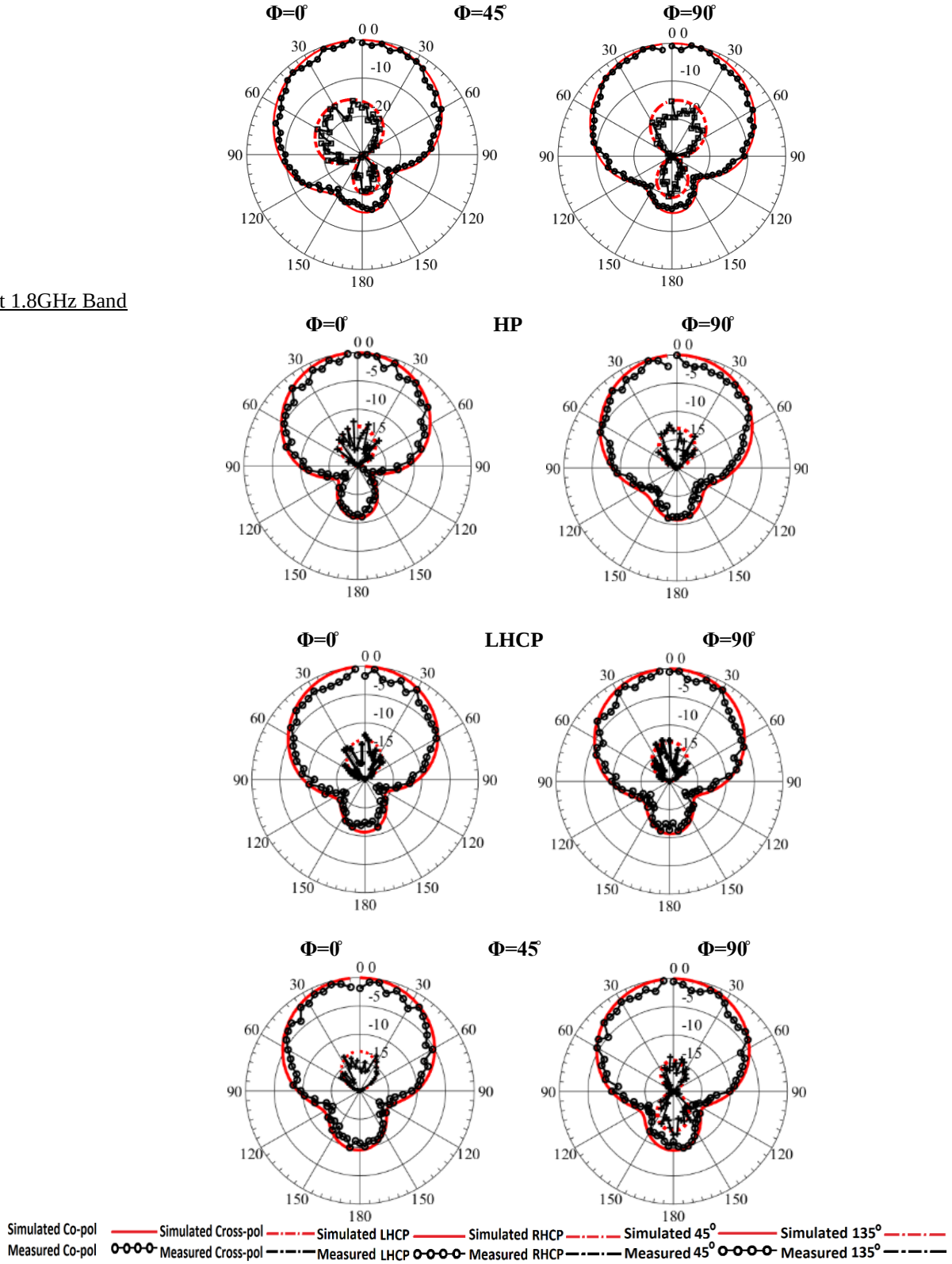

Fig. 6.13 Simulated and measured Co and x-pol pattern for (HP), (LHCP), and 45° slant φ=0° and φ=90° at 2.45GHz, 5.8GHz and 1.8GHz band

6.4.3. Realized Gain

Realized gains for all the reconfigurable states are depicted in Fig. 6.14, Fig. 6.12(d) & 6.12(f) respectively. The corresponding values are tabulated in Table 6.2. It is observed that broadside gains for all states are varied in the range of 5-7.2dBi in both the principal planes. Simulated realized gains for both dual LPs and dual CPs for a specific band are largely similar due to antenna symmetry. The measured gains are slightly reduced primarily due to dielectric, conduction, diode and lumped element losses.

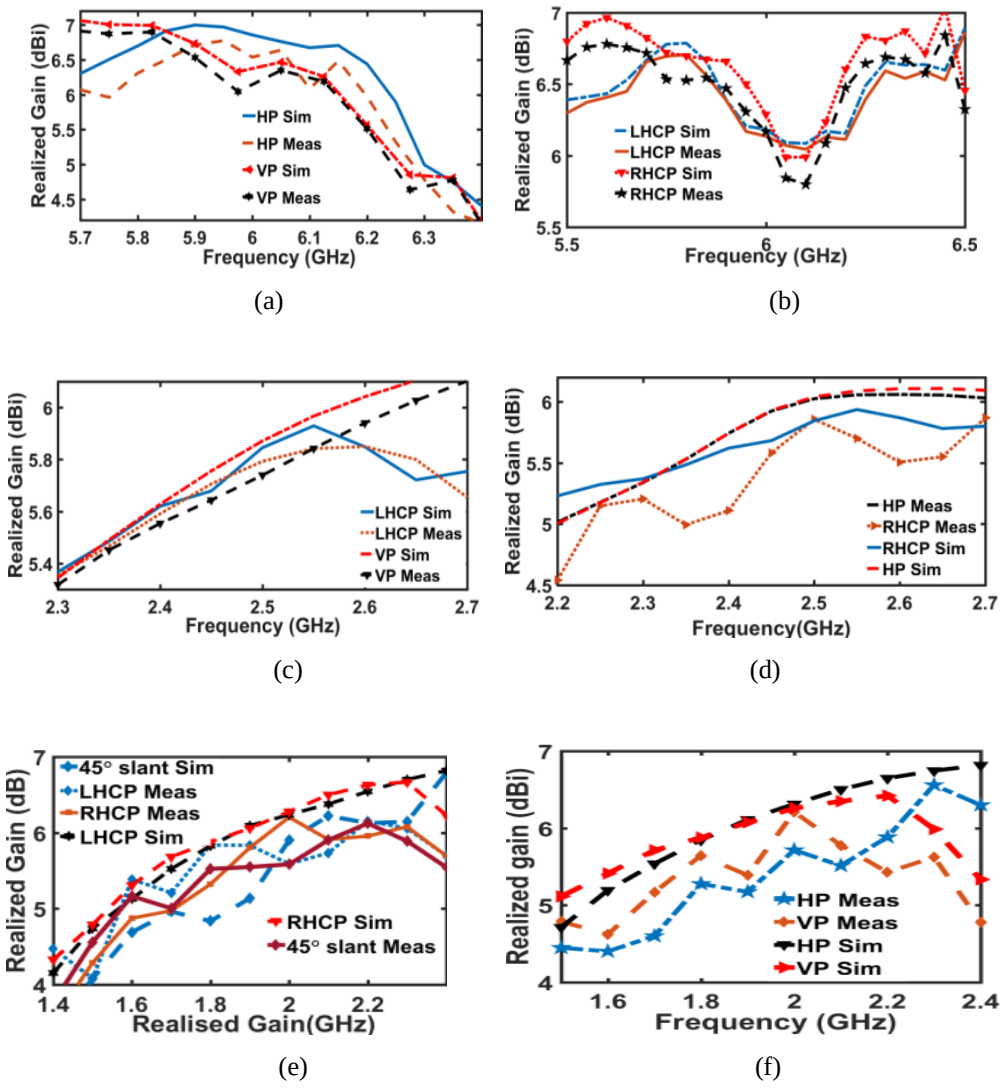

Fig. 6.14 Realized gain for all reconfigurable states, (a) LP states at 5.8GHz, (b) CP states at 5.8GHz, (c) VP and LHCP states for 2.45GHz, (d) HP and RHCP states for 2.45GHZ, (e) Dual CP and 45° slant for 1.8GHz and (f) LP for 1.8GHz band; Meas: Measured, Sim: Simulated

6.4.4 Axial Ratio

Fig. 6.15 illustrates the simulated and measured AR bandwidth for the dual CP states at three frequency bands. Subsequently the values are tabulated in Table 6.2 and show good agreement. Small discrepancies in the simulated and measured AR bandwidth are attributed to many influences as mentioned earlier.

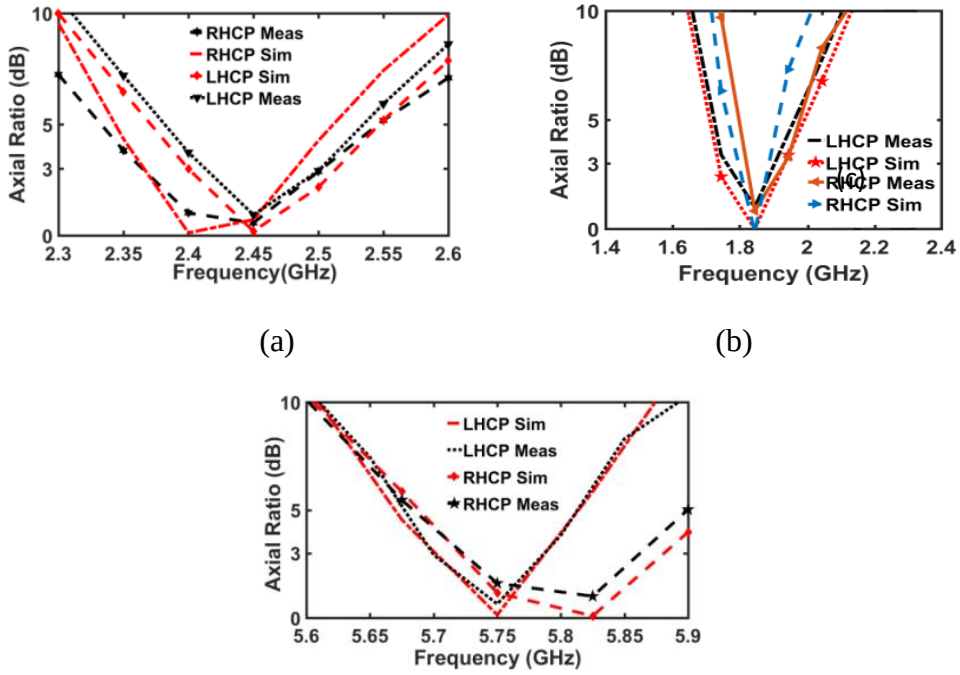

Fig. 6.15 Simulated and measured 3dB AR bandwidths of dual CP states at, (a) 2.45GHz, (b) 1.8GHz, and (c) 5.8GHz

6.4.5 Antenna Efficiencies:

Antenna efficiency reduces with the internal resistance of the switching devices. The PIN switches used in the design show large package parasitic capacitance and insertion loss. Diodes are biased to attain five different polarizations stated at three reconfigurable frequency bands as shown in Table 6.1. Due to the presence of these lossy diodes at different biasing conditions the efficiency of the antenna varies from 57% to 83% as shown in Fig. 6.16(a). Also, the usage of

lossy substrate introduces conduction and dielectric loss that further reduces the overall antenna efficiency. Forward biased diode draws larger forward current, hence increases the diode ohmic loss and thus reduces the efficiency further. Two, four and six diodes are turned ON subsequently to realize CP, LP, and 45° slant polarization states at f1 band as presented in Table 6.1. Thus, CP and 45° slant state shows highest and lowest efficiencies in the plot. Antenna efficiencies can be improved significantly by using low loss switches. Fabricating the antennas using low $\tan\delta$ (loss tangent) substrate also increases the total efficiency. Fig. 6.16(b) depicts the total antenna efficiencies for five different polarization states at f1 band using low loss switches and substrates. It shows clearly that η (%) has improved remarkably which varies from 88 to 97% for different polarization states at f1 band. In other frequency bands (f2 and f3) similar improvement with slight variations in total efficiencies are observed but not shown for brevity.

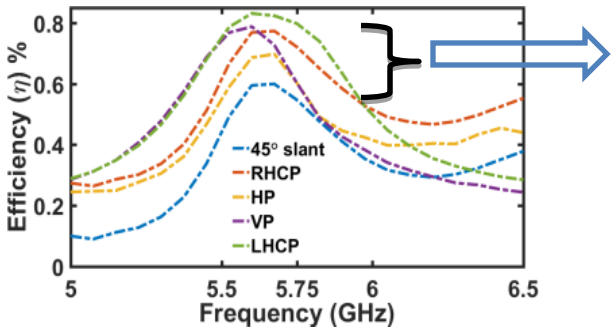

Antenna efficiencies (η) are seen to vary between 57-83% for lossy PIN switches used in the design and fabrication. Also, it decreases along with the increase of diode ON states to attain a specific polarization.

(a)

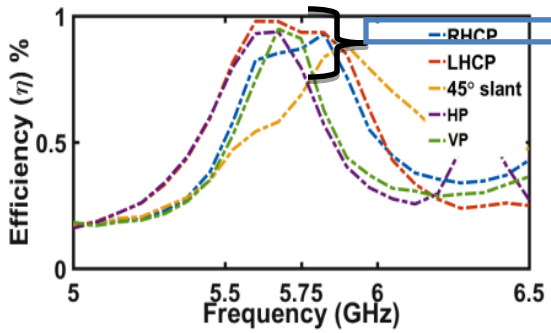

Antenna efficiencies (η) are increased significantly and seen to vary between 88-97% by incorporating low loss MEMS switches and substrate with low loss tangent or conduction loss.

(b)

Fig. 6.16 Total Antenna efficiencies (η%) in f1 band operation using (a) lossy PIN Diodes and (b) Loss less PIN diodes in the antenna design

6.5 Comparison and Discussion

In this section, the authors compare the proposed antenna with recently published works in the literature and subsequently discuss the advantages and novelty based on antenna flexibility, compactness, and overall performances. Researchers in the open literature suggested maximum up-to quad polarization states in three distinct frequency bands. It's worth noting that most authors in the open literature [7, 15-32] use multi-feed, multi-layered, and bulky structures, as well as complicated designs. To achieve frequency and pattern reconfigurability, authors in literature use a relatively broad footprint area in few cases [13, 14]. Also, a numbers of research articles published recently [6, 12] have shown continuous frequency tuning with multi polarization reconfigurability. A dual polarized microstrip aperture array operates at three distinct frequency bands are illustrated in [8].

TABLE 6.2: SIMULATED AND MEASURED ANTENNA PARAMETER VALUE

Pol. State	Impedance BW(-10dB)		Axial Ratio BW (3dB)		Realized Gain (dB)	
			For 2.4 GHz Band (f2)			
	S(MHz/%)	M(MHz/%)	S(MHz)	M(MHz)	S	M
HP	195/8	250/10			5.95	5.9
VP	190/8	350/14.3			5.75	5.65
45° Slant	233/9.5	200/8.2			7.15	6.93
RHCP	542/22	758/31	110	150	5.73	5.49
LHCP	609/25	571/23.3	120	90	5.7	5.8
			For 5.8 GHz Band (f1)			
	S(MHz/%)	M(MHz/%)	S(MHz)	M(MHz)	S	M
HP	306/5.3	415/7.2			6.71	6.43
VP	433/7.5	630/11			7	6.89
45° Slant	674/11.8	390/6.8			6.8	6.64
RHCP	683/12	645/11	170	130	6.75	6.51
LHCP	750/13	765/13.3	90	110	6.81	6.73
			For 1.8 GHz Band (f3)			
	S(MHz/%)	M(MHz/%)	S(MHz)	M(MHz)	S	M
HP	210/11.7	190/10.6			6.1	5.2
VP	170/9.4	210/11.7			6.05	5.8
45° Slant	400/22	380/21			5.75	5.3
RHCP	420/23	430/24	90	120	5.96	5.44
LHCP	170/9.4	190/10.6	170	130	5.87	5.12

S: Simulated M: Measured

In [9] authors employ an exceedingly large numbers of PIN switches (48) to attain four reconfigurable polarization states in three different operating bands. In [5] authors demonstrate various reconfigurable polarization states over a broad frequency range. Penta polarization reconfigurability utilizing a metasurface inspired MSA slot antenna has only been proposed in

one study so far [11]. Recent proposals in the literature have visible flaws, such as complicated feed networks, multilayer assembly, and multiple SMA feeds, which would make real-world implementation difficult. The proposed antenna, on the other hand, has a number of distinct advantages, including a substantially smaller structure. From an RF aspect, the proposed design can be implemented into the transceiver system to alleviate SINR, BER, or fluctuating RSS concerns. As a result, the antenna is well suited for sophisticated multifunctional applications as well as preventing interference and multipath difficulties in electromagnetically dense situations.

TABLE 6.3: ANTENNA PARAMETER COMPARISON BETWEEN PROPOSED AND RECENTLY PUBLISHED WORKS

Ref.	No. of Flexibilities	Resonant (GHz)	Frequency Agility	Substrate Layers (nos.)	Polarization Agility	Peak Gain	% Impedance BW	Footprint Area ($\lambda_0 d^2$)	No. of Diodes	Antenna Height(λ_0)
[5]	8	5.2/5.8	2	1	4	3	3.5/3.6	1×1.1	6 PIN	0.08
[14]	3	8-11.2	1	2	3	16.5	33 tuning	2.5×2.5	NA	0.725
[17]	6	5.2/5.7	2	1	3	5.81	4-8	1.1×1	7 PIN	0.04
[12]	4	5.7	1	3	4	9.9-10.3	23/27(LP & CP)	2.64×2.83	4 SDPT	0.062
[13]	4	3.5/5.2	2	2	2	6.86/8.14	21.7/25	0.78×0.87	4 PIN	0.1
[10]	10	5.2/5.8	2	1	5	5-7.5	7-31(LP, CP)	0.5×0.5	10PIN	<0.01
[9]	12	2.25-2.45	3	1	4	4.7	33.9	0.86 × 0.78	48 PIN	0.01
[16]	3	3.6-4	1	1	3	5-10	10 tuning	1.4×1.4	2 VARACTORS	0.01
[20]	3	2.4-3.6	1	1	3	2.6-7.3	40 Tuning (CP and LP)	1.2 × 1.1	12 VARACTORS	0.04
[6]	8	2.2-3	4	3	2	-1 to 9	NA	2×0.67	32 PIN, 24 Varactor	0.18
[11]	5	5.2	1	2	5	8.2	28	1.21×1.21	15 PIN	0.06
This Work	**15**	**5.8/2.4/1.8**	**3**	**1**	**5**	**5.1-7**	**6.8-31(LP,CP)**	**0.96×0.96**	**15 PIN**	**<0.01**

6.6 Conclusion

Wireless front is gradually getting denser due to the deployment of many nodes in close proximity to enhance data and network coverage to cater to a wide range of advanced and real-time applications. Due to the constraint in the available wireless spectrum, there is significant overlapping of operating frequency bands which causes co-channel and Inter-system interference resulting in low SINR and high BER. Signal multipath in the wireless channel on the other hand creates random fluctuation in the RSS. In this article authors put forward a method to mitigate these issues from the RF viewpoint. Also, the approach would certainly provide greater flexibilities to the system designers with fifteen available reconfigurable states to counter these concerns. A compact, simple reconfigurable MSA with five polarization states at each of three reconfigurable frequency bands is designed with a single layer and feed. For the validation of the proposed theory a prototype MSA operates at 1.8GHz, 2.4GHz, and 5.8GHz is designed and fabricated. The simulated antenna is measured for fifteen reconfigurable states and acceptable results are observed. The design can also be scaled to other operating bands, hence applicable for wide range of applications. The antenna can readily be combined with conventional transceiver systems due to its single feed and compact structure. Therefore, design simplicity, compactness, fabrication ease and optimum performance makes the proposed design very suitable in the ultra-dense environment in 5G ecosystem.

References

[1] Garg Ramesh, Bhartia Prakash, Bahl Inder, Ittipihoon Apisak. Circularly polarized microstrip antenna and techniques in microstrip antenna design handbook. Norwood (MA): Artech House; 2001.

[2] Joseph Helszajn, "Circular Polarization in Parallel Plate Waveguides," in Microwave Polarizers, Power Dividers, Phase Shifters, Circulators, and Switches , IEEE, 2019, pp.37-47, doi: 10.1002/9781119490104.ch3.

[3] https://www.3ds.com/de/produkte-und-services/simulia/produkte/cst-studio-suite

[4] https://www.mouser.in/ProductDetail/Broadcom-Avago/HPND-4005

[5] Y. P. Selvam, L. Elumalai, M. G. N. Alsath, M. Kanagasabai, S. Subbaraj and S. Kingsly, "Novel Frequency- and Pattern-Reconfigurable Rhombic Patch Antenna With Switchable

Polarization," in IEEE Antennas and Wireless Propagation Letters, vol. 16, pp. 1639-1642, 2017, doi: 10.1109/LAWP.2017.2660069.

[6] J. Hu, X. Yang, L. Ge, Z. Guo, Z. -C. Hao and H. Wong, "A Reconfigurable 1 × 4 Circularly Polarized Patch Array Antenna With Frequency, Radiation Pattern, and Polarization Agility," in IEEE Transactions on Antennas and Propagation, vol. 69, no. 8, pp. 5124-5129, Aug. 2021, doi: 10.1109/TAP.2020.3048526.

[7] Z. Nie, H. Zhai, L. Liu, J. Li, D. Hu and J. Shi, "A Dual-Polarized Frequency-Reconfigurable Low-Profile Antenna With Harmonic Suppression for 5G Application," in IEEE Antennas and Wireless Propagation Letters, vol. 18, no. 6, pp. 1228-1232, June 2019, doi: 10.1109/LAWP.2019.2913170.

[8] S. -S. Zhong, Z. Sun, L. -B. Kong, C. Gao, W. Wang and M. -P. Jin, "Tri-Band Dual-Polarization Shared-Aperture Microstrip Array for SAR Applications," in IEEE Transactions on Antennas and Propagation, vol. 60, no. 9, pp. 4157-4165, Sept. 2012, doi: 10.1109/TAP.2012.2207034.

[9] L. Ge, Y. Li, J. Wang and C. -Y. -D. Sim, "A Low-Profile Reconfigurable Cavity-Backed Slot Antenna With Frequency, Polarization, and Radiation Pattern Agility," in IEEE Transactions on Antennas and Propagation, vol. 65, no. 5, pp. 2182-2189, May 2017, doi: 10.1109/TAP.2017.2681432.

[10] Pal, Joydeep., Patra, Kaushik., and Gupta, Bhaskar.: “A low profile single feed compact dual-band penta-polarization agile microstrip antenna for interference mitigation in point-to-point link in Ultra-Dense environment, “in AEU - International Journal of Electronics and Communications, Vol. 150,

[11] P. Liu, W. Jiang, S. Sun, Y. Xi and S. Gong, "Broadband and Low-Profile Penta-Polarization Reconfigurable Metamaterial Antenna," in IEEE Access, vol. 8, pp. 21823-21831, 2020, doi: 10.1109/ACCESS.2020.2969488.

[12] J. Hu, Z. -C. Hao and W. Hong, "Design of a Wideband Quad-Polarization Reconfigurable Patch Antenna Array Using a Stacked Structure," in IEEE Transactions on Antennas and Propagation, vol. 65, no. 6, pp. 3014-3023, June 2017, doi: 10.1109/TAP.2017.2695529.

[13] Z. Nie, H. Zhai, L. Liu, J. Li, D. Hu and J. Shi, "A Dual-Polarized Frequency-Reconfigurable Low-Profile Antenna With Harmonic Suppression for 5G Application," in

IEEE Antennas and Wireless Propagation Letters, vol. 18, no. 6, pp. 1228-1232, June 2019, doi: 10.1109/LAWP.2019.2913170.

[14] C. Ni, M. S. Chen, Z. X. Zhang and X. L. Wu, "Design of Frequency-and Polarization-Reconfigurable Antenna Based on the Polarization Conversion Metasurface," in IEEE Antennas and Wireless Propagation Letters, vol. 17, no. 1, pp. 78-81, Jan. 2018, doi: 10.1109/LAWP.2017.2775444.

[15] Ghaffar, F. A., Vaseem, M., Roy. L. and Shamim, A.: "Design and Fabrication of a Frequency and Polarization Reconfigurable Microwave Antenna on a Printed Partially Magnetized Ferrite Substrate," in IEEE Transactions on Antennas and Propagation, vol. 66, no. 9, pp. 4866-4871, Sept. 2018, doi: 10.1109/TAP.2018.2846796.

[16] M. Ikram, N. Nguyen-Trong and A. Abbosh, "A Simple Single-Layered Continuous Frequency and Polarization-Reconfigurable Patch Antenna Array," in IEEE Transactions on Antennas and Propagation, vol. 68, no. 6, pp. 4991-4996, June 2020, doi: 10.1109/TAP.2019.2952461.

[17] R. K. Singh, A. Basu and S. K. Koul, "A Novel Reconfigurable Microstrip Patch Antenna With Polarization Agility in Two Switchable Frequency Bands," in IEEE Transactions on Antennas and Propagation, vol. 66, no. 10, pp. 5608-5613, Oct. 2018, doi: 10.1109/TAP.2018.2860118.

[18] Anantha, Bharathi, et al. “A Novel Single Feed Frequency and Polarization Reconfigurable Microstrip Patch Antenna.” AEU - International Journal of Electronics and Communications, vol. 72, 2017, pp. 8–16., https://doi.org/10.1016/j.aeue.2016.11.012.

[19] J. Hu and Z. -C. Hao, "Design of a Frequency and Polarization Reconfigurable Patch Antenna With a Stable Gain," in IEEE Access, vol. 6, pp. 68169-68175, 2018, doi: 10.1109/ACCESS.2018.2879498.

[20] N. Nguyen-Trong, L. Hall and C. Fumeaux, "A Frequency- and Polarization-Reconfigurable Stub-Loaded Microstrip Patch Antenna," in IEEE Transactions on Antennas and Propagation, vol. 63, no. 11, pp. 5235-5240, Nov. 2015, doi: 10.1109/TAP.2015.2477846.

[21] W. Li, Y. M. Wang, Y. Hei, B. Li and X. Shi, "A Compact Low-Profile Reconfigurable Metasurface Antenna With Polarization and Pattern Diversities," in IEEE Antennas and Wireless Propagation Letters, vol. 20, no. 7, pp. 1170-1174, July 2021, doi: 10.1109/LAWP.2021.3074639.

[22] C. Zhou, B. Wang and H. Wong, "A Compact Dual-Mode Circularly Polarized Antenna With Frequency Reconfiguration," in IEEE Antennas and Wireless Propagation Letters, vol. 20, no. 6, pp. 1098-1102, June 2021, doi: 10.1109/LAWP.2021.3073417.

[23] Pal, Joydeep., Patra, Kaushik. and Gupta, Bhaskar. :"A TM 03 mode reduced side lobe high-gain printed antenna array in K band for UDN and IoT applications in 5G," in International Journal of RF and Microwave Computer-Aided Engineering.30. 10.1002/mmce.22414.

[24] Arbelaez, A., Goode, I., Gomez-Cruz, J., Escobedo, C. and Saavedra, C. E.: "Liquid Metal Reconfigurable Patch Antenna for Linear, RH, and LH Circular Polarization with Frequency Tuning," in Canadian Journal of Electrical and Computer Engineering, vol. 43, no. 4, pp. 218-223, Fall 2020, doi: 10.1109/CJECE.2019.2904898.

[25] Y. Liu, Q. Wang, Y. Jia and P. Zhu, "A Frequency- and Polarization-Reconfigurable Slot Antenna Using Liquid Metal," in IEEE Transactions on Antennas and Propagation, vol. 68, no. 11, pp. 7630-7635, Nov. 2020, doi: 10.1109/TAP.2020.2993110.

[26] Bharathi, Anantha, et al. “A Quad-Polarization and Frequency Reconfigurable Square Ring Slot Loaded Microstrip Patch Antenna for WLAN Applications.” AEU - International Journal of Electronics and Communications, vol. 78, 2017, pp. 15–23., https://doi.org/10.1016/j.aeue.2017.05.015.

[27] J. Liu, J. -Y. Li, R. Xu and S. -G. Zhou, "A Reconfigurable Printed Antenna With Frequency and Polarization Diversity Based on Bow-Tie Dipole Structure," in IEEE Transactions on Antennas and Propagation, vol. 67, no. 12, pp. 7628-7632, Dec. 2019, doi: 10.1109/TAP.2019.2934775.

[28] Yang, L. S., et al. “Polarization Reconfigurable Slot Antenna for 5.8 GHz Wireless Applications.” AEU - International Journal of Electronics and Communications, vol. 101, 2019, pp. 27–32., https://doi.org/10.1016/j.aeue.2019.01.022.

[29] Mani, Manoj, et al. “Frequency Reconfigurable Stepped Impedance Dipole Antenna for Wireless Applications.” AEU - International Journal of Electronics and Communications, vol. 115, 2020, p. 153029., https://doi.org/10.1016/j.aeue.2019.153029.

[30] Prakash, Tarun, et al. “A Reconfigurable Active Microstrip Antenna for Agile Switching: Pattern, Beamwidth, and Multibeam.” AEU - International Journal of Electronics and Communications, vol. 149, 2022, p. 154181., https://doi.org/10.1016/j.aeue.2022.154181.

[31] A. Bhattacharyya, J. Pal, K. Patra and B. Gupta, "Bandwidth-Enhanced Miniaturized Patch Antenna Operating at Higher Order Dual-Mode Resonance Using Modal Analysis," in IEEE Antennas and Wireless Propagation Letters, vol. 20, no. 2, pp. 274-278, Feb. 2021, doi: 10.1109/LAWP.2020.3048444.

[32] Ullah, Sadiq, et al. “Design, Fabrication and Measurement of Triple Band Frequency Reconfigurable Antennas for Portable Wireless Communications.” AEU - International Journal of Electronics and Communications, vol. 81, 2017, pp. 236–242., https://doi.org/10.1016/j.aeue.2017.07.028.

Chapter 7
Higher Order Mode Planar 2D Array for High Gain Applications in 5G Ecosystem

7.1 Introduction

A high gain antenna can provide a proficient way to alleviate the multi-path fading and low SINR issues by aligning the high-power beam towards the direction of the intended receiver; hence shunting out the interference and noise sources which results in increased SINR, larger diversity gain and improved data throughput in the RF link [1, 2]. With the advancement of 5G, mmWave and terahertz (THz) antenna systems are being investigated extensively for ultra-high data rate communication [3]. Fabrication accuracy is reaching down to micron level for these high-frequency bands which demand high accuracy and precision. Low Temperature Co-fired Ceramic (LTCC) or other high-precision techniques can be employed to design high-frequency antennas with significantly small components [4, 5]. However, these techniques incur additional complexities because of fabrication misalignment and dense packaging of very small components. In conjunction, the overall manufacturing costs are increased by an appreciable amount. Hence, electrically large RF devices with simple fabrication and low sensitivity to fabrication tolerance operating at mmWave frequencies without any compromise in performance have become important in these scenarios [6].

Furthermore, the realization of highly directional beams with wide bandwidth from low profile planar radiators has always been one of the most challenging issues faced by the antenna community. Different gain enhancement methods have been traditionally employed to enhance the radiation performance. Patch antennas are usually printed on substrate materials that normally have low permittivity, which limits the feasibility of gain enhancement methods by varying substrate parameters. Another efficient technique is to excite Microstrip antennas to operate in Higher-Order broadside Modes (HOMs) [7]. This approach can efficiently mitigate both fabrication tolerance and low gain issues. Due to enlarged spacing between the two radiating slots the overall footprint area of these HOM antennas is increased. Side Lobe Levels

of these antennas are also increased. The SLL can be reduced by decreasing the overall size of the patch at resonance by increasing the permittivity of substrate [8]. However, this technique suffers from increased Q factor (Quality Factor) which reduces impedance bandwidth. Another technique is to incorporate slots on the HOM patches to perturb the out of phase currents or reshaping the patches to operate in their fundamental mode to minimize SLL.

Array configuration is another efficient way to increase antenna gain [9]. The realized gain of an antenna can further be increased by designing an array using array elements operating at higher order modes. This technique has rarely been discussed in the open literature. In this chapter a 2D patch array operates at TM_{03} broadside radiated mode is investigated.

7.2 TM_{mn} Mode Analysis

The radiated far-fields of patch antenna are calculated from the magnetic currents ($\vec{M}_s$) on patch periphery over an infinite ground plane. Fig. 7.1 shows for TM_{11}, TM_{21} and TM_{30} modes in a rectangular patch where the black and red arrows represent current directions along ±x and ±y axis respectively. These Higher Order Modes (HOM) have different amplitudes and out-of-phase currents around patch periphery, as shown in Fig. 7.1(a), 7.1(b) and 7.1(c). Relative amplitudes of the magnetic currents at the patch edges determine the far-field radiation pattern. Four apertures on the periphery of the rectangular patch are shown in the fig. 7.1(d). The interior electric field in the lossy cavity is given by the following well established equation [10].

$$E_Z = \sum_m \sum_n A_{mn} \psi_{mn}(x, y) \tag{7.1}$$

Here A_{mn} and ψ_{mn} are the modal amplitude and the Eigen function of the $(m,n)^{th}$ mode. The corresponding magnetic current is given by the following equation as defined in (7.2).

$$\widehat{M_s} = -\hat{n} \times \widehat{E_z} \tag{7.2}$$

Electric vector ($\hat{F}$) potential for the patch aperture is derived using (7.1-7.4) by applying the free space Green's function. These expressions are very well established in the literature.

$$
\begin{aligned}
&\hat{F}_{(x+L)} = (\hat{y})\frac{\mu_0}{4\pi}\frac{e^{-jk_0 r}}{r}2h\{\sin c(k_0 h\cos\theta)\}\\
&\sum_m\sum_n E^2_{mn}\left[\frac{W}{2}\left\{e^{jQ_+\left(Y_0+\frac{W}{2}\right)}\right\}\sin c\left(Q_+\frac{W}{2}\right)+\left\{e^{jQ_-\left(Y_0+\frac{W}{2}\right)}\right\}\sin c\left(Q_-\frac{W}{2}\right)\right]e^{jk_0(x_0+L)\sin\theta\cos\phi}\\
&\hat{F}_{(x)} = (-\hat{y})\frac{\mu_0}{4\pi}\frac{e^{-jk_0 r}}{r}2h\{\sin c(k_0 h\cos\theta)\}\\
&\sum_m\sum_n E^1_{mn}\left[\frac{W}{2}\left\{e^{jQ_+\left(Y_0+\frac{W}{2}\right)}\right\}\sin c\left(Q_+\frac{W}{2}\right)+\left\{e^{jQ_-\left(Y_0+\frac{W}{2}\right)}\right\}\sin c\left(Q_-\frac{W}{2}\right)\right]e^{jk_0 x_0\sin\theta\cos\phi}\\
&\hat{F}_{y} = (\hat{x})\frac{\mu_0}{4\pi}\frac{e^{-jk_0 r}}{r}2h\{\sin c(k_0 h\cos\theta)\}\\
&\sum_m\sum_n E^3_{mn}\left[\frac{L}{2}\left\{e^{jP_+\left(Y_0+\frac{W}{2}\right)}\right\}\sin c\left(P_+\frac{W}{2}\right)+\left\{e^{jP_-\left(Y_0+\frac{W}{2}\right)}\right\}\sin c\left(P_-\frac{W}{2}\right)\right]e^{jk_0 y_0\sin\theta\sin\phi}\\
&\hat{F}_{(y+W)} = (\hat{x})\frac{\mu_0}{4\pi}\frac{e^{-jk_0 r}}{r}2h\{\sin c(k_0 h\cos\theta)\}\\
&\sum_m\sum_n E^4_{mn}\left[\frac{L}{2}\left\{e^{jP_+\left(Y_0+\frac{W}{2}\right)}\right\}\sin c\left(P_+\frac{W}{2}\right)+\left\{e^{jP_-\left(Y_0+\frac{W}{2}\right)}\right\}\sin c\left(P_-\frac{W}{2}\right)\right]e^{jk_0(y_0+W)\sin\theta\sin\phi}
\end{aligned}
\qquad (7.3)
$$

where,

$$
\begin{aligned}
E^1_{mn} &= \frac{E_0\psi_0\cos(k_m x_0)\psi_{mn}(x_0 y_0)}{k^2-k^2_{mn}}G_{mn}\\
E^2_{mn} &= \frac{E_0\psi_0\cos\{k_m(x_0+L)\psi_{mn}(x_0 y_0)}{k^2-k^2_{mn}}G_{mn}\\
E^3_{mn} &= \frac{E_0\psi_0\cos(k_n y_0)\psi_{mn}(x_0 y_0)}{k^2-k^2_{mn}}G_{mn}\\
E^4_{mn} &= \frac{E_0\psi_0\cos\{k_n(y_0+W)\}\psi_{mn}(x_0 y_0)}{k^2-k^2_{mn}}G_{mn}
\end{aligned}
\qquad (7.4)
$$

And,

$$
\begin{aligned}
Q^{\pm} &= k_0\sin\theta\sin\varphi\pm k_n\\
P^{\pm} &= k_0\sin\theta\cos\varphi\pm k_m
\end{aligned}
$$

The total relative vector potential in x and y directions are derived from the equation 7.1- 7.4 simply by taking the vector addition as follows.

$$F_x = \hat{F}_x + \hat{F}_{x+L} \tag{7.5}$$

$$F_y = \hat{F}_y + \hat{F}_{y+W} \tag{7.6}$$

k_0 is the wavenumber in the free space and ε_0 is the dielectric constant. Hence the far-field radiation pattern for rectangular patch is derived using (7.7 & 7.8) respectively [10-13].

$$E_\theta = j\omega\eta_0 \left(F_x \sin\varphi - F_y \cos\varphi \right) \tag{7.7}$$

$$E_\varphi = j\omega\eta_0 \left(F_x \cos\theta\cos\varphi + F_y \cos\theta \sin\varphi \right) \tag{7.8}$$

Antenna directivity is derived from the following relation.

$$D(\theta,\varphi) = 4\pi \frac{\left|E_\theta(\theta,\varphi)\right|^2 + \left|E_\varphi(\theta,\varphi)\right|^2}{\int_0^{2\pi}\int_0^{\pi} \left(\left|E_\theta(\theta,\varphi)\right|^2 + \left|E_\varphi(\theta,\varphi)\right|^2 \right) \sin\theta d\theta d\varphi} \tag{7.9}$$

Patch antennas designed with a specific aspect ratio (length to width) can support both fundamental and higher order modes. Judicious feeding is required to excite a specific mode to couple maximum input power to the concerned mode only. Input excitation is likely to get coupled with other modes which might be excited partially due to improper feeding and may degrade the overall antenna performance. Modal analysis of a rectangular patch shows that few specific higher order modes radiate in broadside direction with increased directivity. Fig. 7.2 depicts 3D radiation pattern of a rectangular patch excited in TM_{20}, TM_{22}, TM_{30}, TM_{31}, and TM_{32} modes respectively. It is important to observe that TM_{30} mode depicts broadside radiation.

7.2.1 Broadside radiating Modes

The internal electric field distributions up to the fifth harmonic are studied carefully. Phase reversal of the electric field along the patch length aligns the magnetic currents in the same direction along the parallel apertures as shown in Fig. 7.1(e). This incurs a broadside radiated beam in the radiation pattern. On the other hand, the electric field in the parallel path apertures along the width aligns in same direction; hence the corresponding magnetic currents are in opposite direction cancelling the broadside far-filed radiation. It is observed that with higher modes, the pattern also changes in shape with increased number of side lobes of varying

amplitude. It has been observed that, for m = 0 or n = 0 and m = n = 1, 3, 5, …, (2n + 1), the corresponding TM_{mn} modes radiate in the broadside direction. Other resonant modes radiate in non-broadside directions.

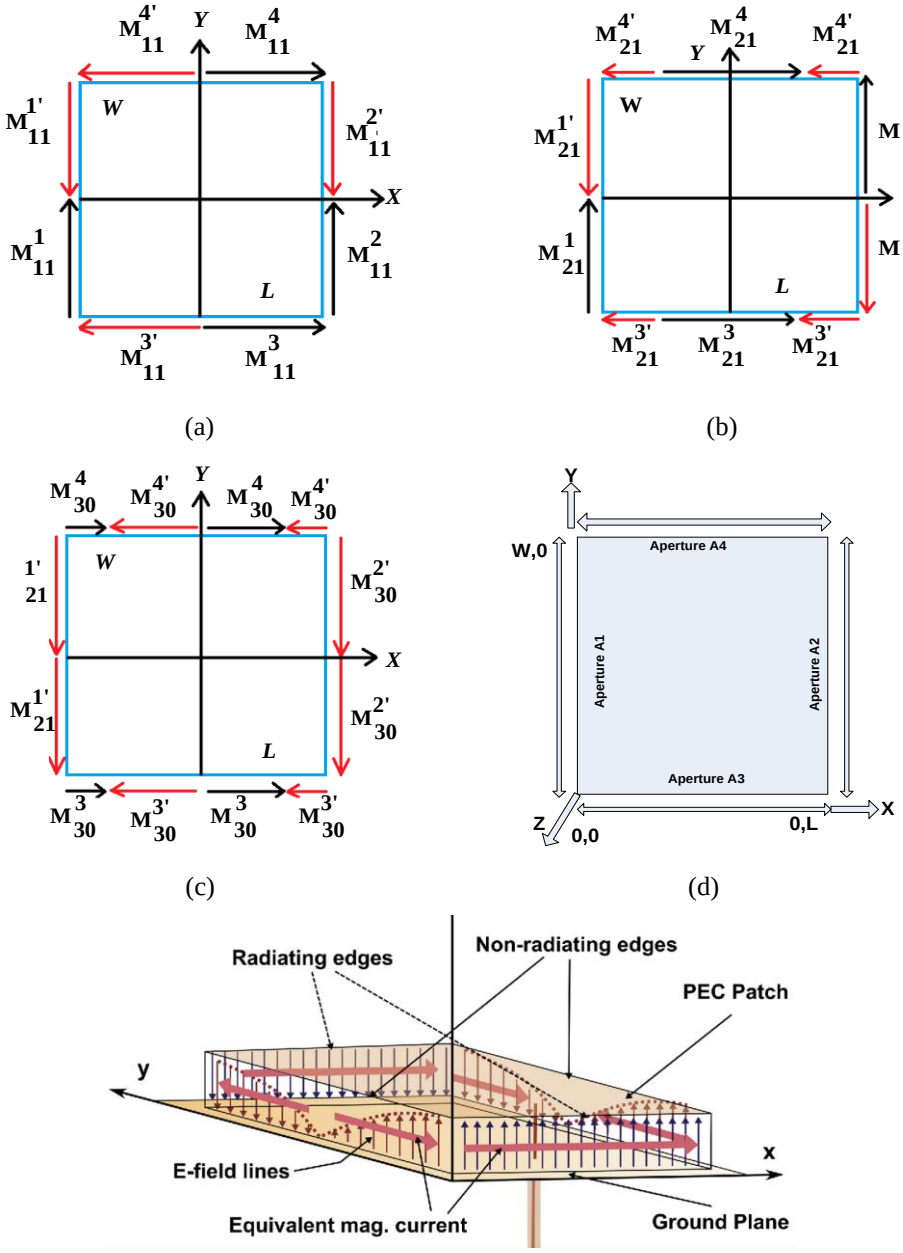

Fig. 7.1 Equivalent Magnetic current at patch periphery of different higher order modes in rectangular patch (a) TM_{11} (b) TM_{21} (c) TM_{30} and (d) radiating and non-radiating apertures of patch and (e) Electric fields in the patch cavity and magnetic currents on the patch periphery

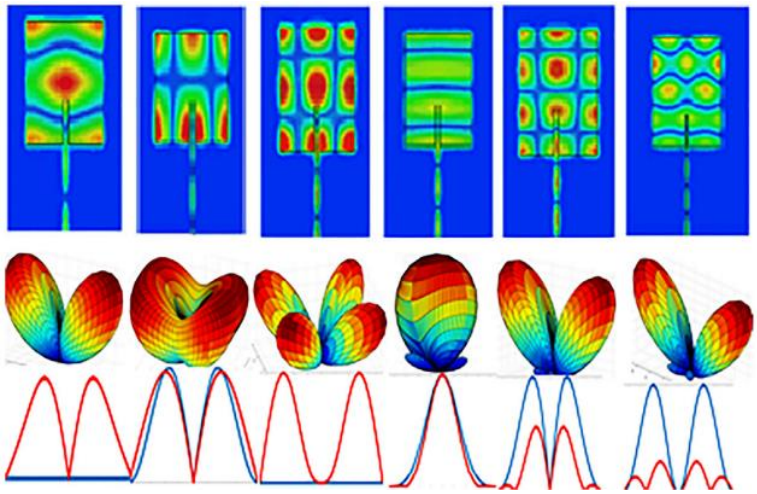

Fig 7.2 Simulated electric fields on the patch and respective 3D & 2D (in two principal planes) radiation patterns for first few higher order resonant modes at 22GHz: (a) TM_{02}, (b) TM_{11}, (c) TM_{22}, (d) TM_{03},, (e) TM_{32}, and (e) TM_{33}

The modal resonant frequencies and input impedance of a patch antenna are represented by the following expressions [13].

$$F_r = \frac{c}{2\pi\sqrt{\varepsilon_r}}\sqrt{k_m^2 + k_n^2} \tag{7.10}$$

$$Z_{in} = -j\omega\mu_0 \sum_{m=0}^{\infty}\sum_{n=0}^{\infty} \frac{\psi_{mn}^2(x_0, y_0)}{k_0^2 - k_{mn}^2} G_{mn} \tag{7.11}$$

Fig. 7.3 represents all resonant frequencies up to TM_{33} mode using (7.10-7.11) and arranged in Table 7.1.

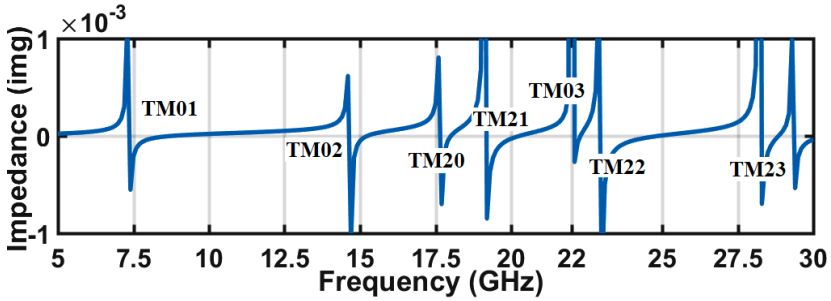

Fig. 7.3 Modal frequencies up to TM_{33} mode for TM_{01} f_0= 7.3GHz

TABLE 7.1
RESONANT MODES AND CORRESPONDING MODAL FREQUENCIES OF RECTANGULAR PATCH

Resonant Modes	Higher Order Modes resonant frequencies (GHz)			
TM01	3.140138	4.710207	6.280276	7.333399
TM02	6.280276	9.420413	12.56055	14.6668
TM03	9.420413	14.13062	18.84083	**22.0002**
TM10	3.880077	5.755225	7.601157	8.826119
TM11	4.991539	7.43698	9.859992	11.47515
TM12	7.382198	11.03933	14.68145	17.11769
TM13	10.18819	15.25769	20.31636	23.70462
TM20	7.760153	11.51045	15.20231	17.65224
TM21	8.371406	12.4369	16.44847	19.11492
TM22	9.983078	14.87396	19.71998	22.95031
TM23	12.20509	18.22539	24.20924	28.20656
TM30	11.64023	17.26568	22.80347	26.47836
TM31	12.05634	17.89664	23.65249	27.47512
TM32	13.22637	26.03393	30.2691	30.2691
TM33	14.97462	29.57998	34.42546	34.42546

HOMs at comparatively higher frequencies are closer to each other as shown in Fig. 7.3. This imposes an additional challenge to excite an intended HOM as the probability of excitation of unintended modes also increases. Input power couples with nearby modes which degrades the antenna efficiency considerably. For example, TM_{03} is required to be excited at 22 GHz. From the modal frequency plot (Fig. 7.3), it is found the fundamental resonant frequency (TM_{01}) should be at 7.33 GHz to excite TM_{03} mode at 22GHz (Table 7.1). The distribution of modal resonant frequencies shows that TM_{13}, TM_{22}, and TM_{03} modes reside in close proximity as illustrated in Fig. 7.4. This certainly increases intermodal power coupling which adversely affects antenna efficiency and far-field pattern.

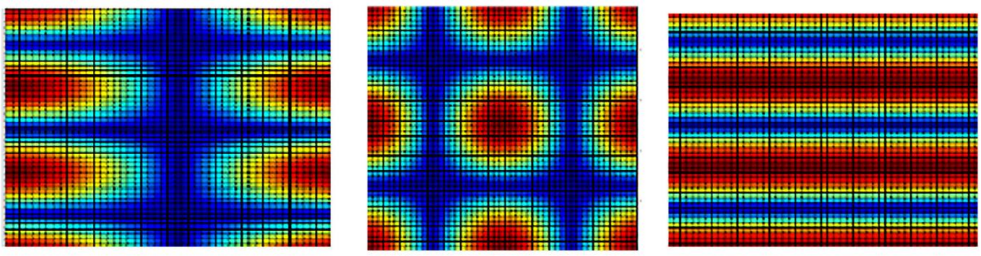

(a) (b) (c)

Fig. 7.4 Electric field distribution within the cavity for (a) TM13, (b) TM22, and (c) TM03 modes

The feed excitation is given at the voltage maxima of TM_{03} mode by observing the electric filed plots of overlapping fields (TM_{13}, TM_{22}, and TM_{33}). It is well known that modal significance provides the exact figure of power coupling in different modes than the graphical electric field plots. The feed location has been optimized to attain maximum modal amplitude at TM_{03} mode. The modal coupling coefficients for TM_{03} mode excitation has been given in Table 7.1. It is noted that the TM_{03} modal amplitude is very high with respect to the other modes for the chosen feed location. Although in practical scenarios when probe feed is connected at the specific patch location, it would certainly couple some power to the nearby overlapping modes causing minute deviations of the simulated key parameters.

7.2.2 Non-Broadside radiating Modes

TM_{mn} modes for m=0 or n=0 and m=n=1,3, 5, …..(2n+1) radiate in the broadside direction, whereas the rest are non-broadside radiating modes. Broadside radiating modes have in-phase magnetic current and odd multiples of λ/2 separation between the radiating edges (λ is the operating wavelength). Oppositely directed magnetic currents in the non-radiating edges cancel out the radiation in broadside direction. This is shown in Fig. 7.1(c) for TM_{03} mode. For fundamental mode (TM_{01}) excitation, the in-phase magnetic currents in the parallel apertures along $\pm$ L/2 are observed whereas out of phase currents are aligned along $\pm$ W/2 as depicted in Fig. 7.1(e). This eventually leads to broadside radiation. However, the $\vec{M}_s$ for non-broadside patch radiators, the out of phase $\vec{M}_s$ do not cancel out completely. Concurrently, radiating slots of the patch antenna behave as array elements and can be considered as two element array configurations for further analysis.

Phase difference between two uniformly excited non-directional radiators is $\psi = \beta d\cos\varphi + \alpha$. The phasor sum of the fields at far filed is $E = E_0\left(1 + ke^{i\psi}\right)$ and the magnitude of the total field is given by $E = E_0\left|\left(1 + ke^{i\psi}\right)\right|$. Thus, the total electric field magnitude is given by

$$E_T = 2E_0\cos\left(\frac{\pi d\cos\varphi}{\lambda} + \frac{\alpha}{2}\right) \tag{7.12}$$

For the out of phase currents $\alpha = \pi$, and from the above equation, it is evident that the total field in the broadside direction ($\theta = \varphi = 0°$) is zero since the Array Factor (AF) puts a null in the

broadside direction. Fig. 7.1(a) & 7.1(b) illustrate $\vec{M}_s$ for TM_{13} and TM_{22} non-broadside modes. As the mode number increases the number of side lobes increase in different θ and φ directions with varying amplitudes**.**

7.3 Design of Patch antennas at 22 GHz

7.3.1 Why 22GHz

Significant research has been done by competent authorities [14] and a compact documentation regarding atmospheric losses of electromagnetic radiation has been prescribed for very wide range of frequencies including UV, visible, infrared, terahertz, and mmWave regions. Results shows that the mmWaves can penetrate the opaque atmosphere (haze, fog, clouds, dust, smoke, and light rain) where electro-optical and infrared systems normally fail. For most applications, the operation of ground-based systems is limited to seven RF spectrum windows. These RF windows (W1 to W7) are defined in the proposed report in [14]. The report illustrates that the Oxygen molecules in the atmosphere have a permanent magnetic moment which absorb power during interaction with the incident electromagnetic field. The interaction produces a family of rotation and absorption lines in the vicinity of 60 GHz and at 119 GHz [14]. Similarly, the water vapor molecules have an electric dipole which interacts with the incident radiation to produce rotational absorption at 22.2 GHz, 183.3 GHz, and 324 GHz frequencies. Thus, variation of power loss occurs while propagating through open atmosphere as shown in Fig 7.5. A high atmospheric loss window at 22 GHz is present which is avoided for long-distance wireless communications. For the short-range non-Line of Sight (nLoS) or LoS Point to Point / Multipoint (P2PM) communication this unused frequency band can be suitably employed. In recent 5G cellular domain many advanced services such as Internet of Things (IoT), Vehicle to Vehicle (V2V) communication or Vehicle to Everything (V2X) communication can be deployed in the K band. This band can also cater high speed and reliable data transfer due to the availability of sufficient spectrum bandwidth. The most advantageous part is that the network coverage will be completely localized in 22GHz. This would in turn reduces the co-channel interference with neighboring cells by naturally restricting its coverage. An automatic gain

control mechanism can be incorporated in the antenna system to overcome further degradation of the propagated signal strength due to rain and dew or in case of other atmospheric adversities.

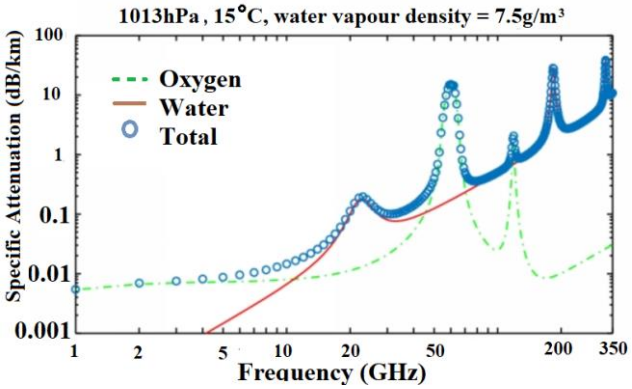

Fig. 7.5 Atmospheric losses of electromagnetic wave at different frequencies due to Oxygen and water molecules in the atmosphere

7.3.2 Design and Fabrication of Antennas

The design, simulation and fabrication of the K band prototype planar antenna and arrays operating at fundamental and higher order broadside mode are investigated in this section. For a comparative study and observation antennas and arrays operating at 22GHz in TM_{03} mode are studied. TM_{03} mode is chosen as this is the very next broadside radiating mode to TM_{10} (fundamental mode). Other higher order broadside modes (TM_{50}, TM_{05}, and TM_{70} and so on) can also be utilized for further gain enhancement with proper feeding. Though these antennas exhibit very large footprint area and hence avoided in most applications. A Finite Difference Time Domain based (FDTD) 3D commercial electromagnetic simulator, Computer Simulation Technologies (CST) microwave suite [15] is used for the simulation. Arlon AD430 substrate with material properties; permittivity (ε_r) 4.3, loss tangent ($\tan\delta$) 0.002 and substrate thickness (h) 30 mils (0.762 mm) is for antenna fabrication. In HOMs, the effective substrate height is increased; hence the substrate with lowest thickness is chosen for the design. We have used very low profile ($\geq 0.1\lambda$) and low loss Arlon AD430 substrate (according to market and laboratory availability). The substrate height (0.762 mm) is very low with respect to λ (approximately $\lambda/12$ at f = 22 GHz). This in-turn reduced the cross polarization, as the antennas generate higher cross polarization in HOMs.

I. Fundamental mode single antenna

A TM_{01} mode patch antenna as shown in Fig. 7.6(a) is designed (4.1884 × 2.77 mm^2) with comparable size to the commonly available SMA connector (1.3 mm center conductor diameter). This introduces adverse effects on the overall antenna radiation and impedance performance. Microstrip corporate feed is used because the patch edge has high impedance that eventually mitigates the radiation from the feed in mmWave frequencies. A quarter-wave impedance matching section is used to match the antenna. Antenna edge impedance is calculated to be 238.5 Ω. Hence the characteristic impedance of the quarter-wave matching section turns out to be 109.2 Ω. The length of the quarter-wave section 7/4 mm. Simulated and measured S_{11} and radiation pattern (at Φ = 0, Φ = 90 planes) plots are shown in Fig. 7.6(b) and Fig. 7.7 respectively. The cross-polarization level at both E/H plane is less than 30dB. Simulated peak S_{11} at resonance and % of fractional bandwidth is observed at −52 dB and 8.6% (from 21.224 GHz to 23.112 GHz) respectively. Corresponding measured values are −46 dB (at 21.8 GHz) and 11.2% (from 20.8 GHz to 23.27 GHz) respectively. The simulated real and imaginary parts of the input impedance at resonance are noted at 50.23 Ω and −j0.5 Ω, while in measurement it is observed to be 50.7 Ω and j0.19 Ω respectively. The slight discrepancy is primarily due to the feeding probe and metal soldering. The broadside simulated and measured realized gains are 7.47 and 6.45dBi, respectively, with 90% simulated antenna efficiency as depicted in Fig. 7.10.

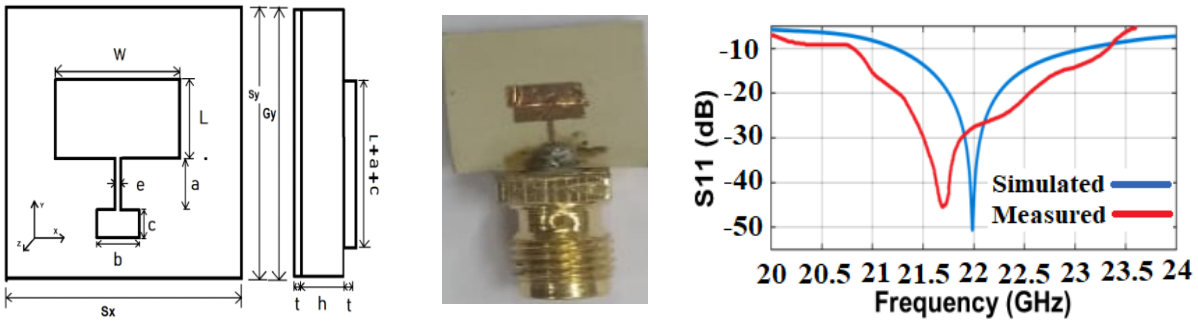

(a) (b) (b)

Fig. 7.6 (a) Geometry of single element, (b) fabricated Antenna (c) simulated & measured S_{11} in TM_{01} mode

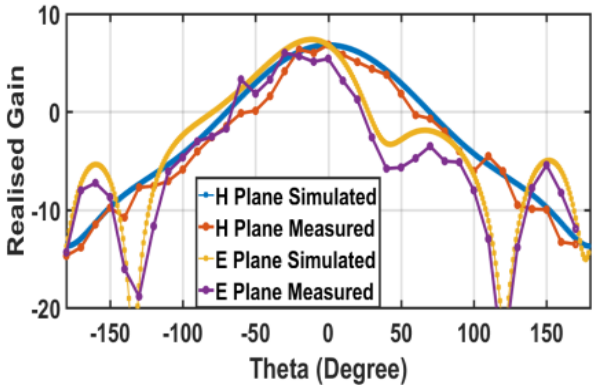

Fig 7.7 Single element TM_{01} mode Radiation pattern in $\Phi=0^0$, $\Phi=90^0$ plane

II. TM_{03} mode single element antenna

The resonant frequency for TM_{03} mode antenna is given in (6.5) where the wavenumbers *km* and *km* are given by $k_m = {}^{m\pi}/_{L} = {}^{3\pi}/_{L}\,(m = 3)$ and by $k_n = {}^{n\pi}/_{W} = 0\,as\,(n = 0)$ where L and W is the length and width of the path antenna element. Hence resonance frequency is given in (7.13)

$$F_r = \frac{c}{2\pi\sqrt{\varepsilon_r}}\sqrt{({}^{3\pi}/_{L})^2} \tag{7.13}$$

The length L of the TM_{03} mode patch element can be calculated directly from the above equation for any specific operating frequency. The width of the patch needs to access from fundamental mode equations [16, 17] and optimized further for optimum antenna performances. A single patch antenna operating at 7.3 GHz at fundamental mode (TM_{01}) excites the TM_{03} mode at 22 GHz which is already elaborated in the previous sections. The center conductor of the SMA probe is placed at maxima of the electric field at patch surface of TM_{03} where the other nearby modes TM_{32}, TM_{13}, and TM_{22} are having nulls. This process of choosing proper feeding location eventually reduces the coupling of input power to other modes. The geometry and corresponding dimension are shown Fig. 7.8(a) and Table 7.2. The simulated S_{11} and fractional bandwidth is noted at −57.3 dBm (at 22 GHz) and 2.3% (from 21.7 GHz to 22.2 GHZ), respectively. Corresponding measured parameters are observed at −39 dBm (at 22.1 GHz) and 3.0% (from 21.75GHz to 22.4 GHz) respectively. The simulated and measured S_{11} and radiation pattern at broadside direction in both the principal planes (Φ = 0°and Φ = 90°) plots are shown in Fig.

7.8(b) and 7.9 respectively. The cross polarization is shown to be less than 25 dBm in both E/H plane. The measured and simulated realized gains in the broadside direction of the patch are 8.73 and 8.91 dBi respectively as demonstrated in Fig. 7.10. The simulated real and imaginary parts of the input impedance of the antenna are obtained as 49 Ω and j0.1 Ω, respectively. In measurement, these values are observed around 47.6 Ω and −j1.29 Ω which showed a very close impedance matching at 22 GHz. A slight mismatch occurs due to the probe soldering that alters the overall patch input impedance.

(a) (b) (c)

Fig. 7.8 TM_{03} mode (a) Geometry of single element, (b) fabricated antenna, and (c) simulated & measured S_{11}

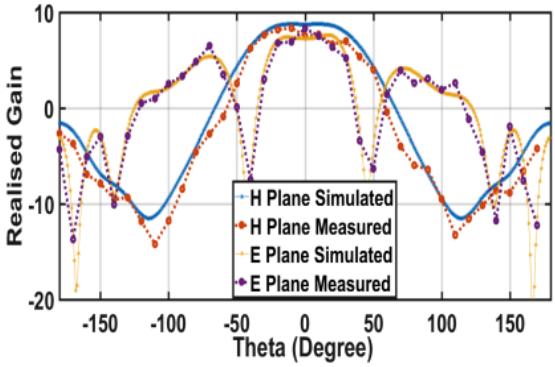

Fig. 7.9 Single element TM_{03} mode patch simulated & measured radiation patterns in broadside direction in $\Phi=0^0$, $\Phi=90^0$ planes

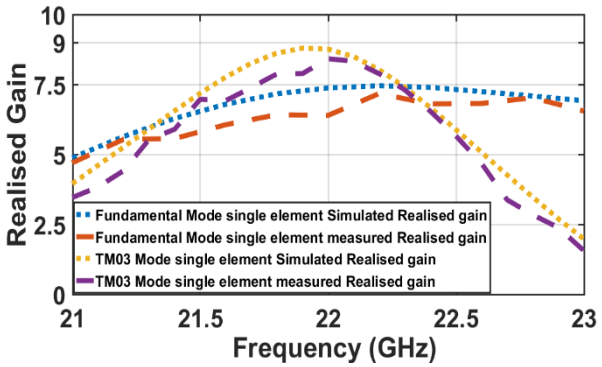

Fig. 7.10 Gain Vs Frequency plot of Single element Fundamental and higher order modes (TM03)

TABLE 7.2
DIMENSIONS OF TM_{01} & TM_{03} SINGLE ELEMENT PATCH

Modes	Ground Length Gx	Ground Width Gy	Substrate Length Sx	Substrate Width Sy	λ/4 length (e)109.2Ω
TM01	13	13	13	13	1.75
TM03	10	10	10	10	
	Substrate Height (h)	Patch Thickness(t)	Patch Length (L)	Patch Width(W)	λ/4 width (a) 109.2Ω
TM01	0.762	0.004	2.77	4.1884	0.2
TM03	0.762	0.004	7.4982	9.118	

7.3.3 Design of fundamental mode array

I. Design of feed network

TM_{01} patch elements are symmetrically positioned in X and Y directions. Microstrip line feed is used to feed the array elements. T-junction power dividers are used to excite the elements by equal signal amplitude and phase. Patch edge impedance is found to be 238.5 Ω. Impedance matching has been achieved using intermediate quarter wave impedance transformer sections. A 140 Ω quarter-wave matching section is connected with the edge of the patch elements to convert the impedance to 100 Ω and, the impedance at the center of the microstrip line of two oppositely connected 100 Ω (parallel connected impedance) microstrip lines being 50 Ω. Due to area constraint, the feed probe is not connected to this 50 Ω section; instead, it is extended to the edge of the substrate using 100 and 71 Ω quarter-wave matching sections and finally connected to the source probe as shown in Fig. 7.11(a).

II. Parametric optimization of feed network

CST [15] integrated optimization techniques such as Particle Swarm Optimization (PSO) and Genetic Algorithm (GA) are used for array feed network optimization. Lengths and corresponding widths of different feed sections are optimized to get desired 50Ω impedance matching (Fig. 7.11). Inter-elemental spacing of the array elements are optimized for maximum broadside radiation and low SLL. E-plane SLL value is optimized to −13.4 dB (Fig. 7.14) for m = 0.625 and n = 0.75 (inter-element spacing in X and Y directions respectively in terms of λ). The simulated array operates from 21.142 GHz to 23.916 GHz with 2.774 GHz (12.6%) impedance bandwidth. The measured S_{11} and % of fractional bandwidth are noted to be −35 dBm (at 21.22 GHz) and 18.72% (20.34 GHz - 24.46 GHz) respectively as shown in Fig. 7.13(a). Such wide bandwidth attributes to the slight overlapping of the nearby mode. The simulated and measured realized gain values are 9.613 and 9.32 dBi respectively as shown in Fig. 7.16(a) with 92% simulated total antenna efficiency is noted. The Half Power Beam Width (HPBW) is noted to be 40° and 60° respectively in Φ0 and Φ90 planes (Fig. 7.15) with less than 27 dB cross polarization level. Simulated and measured real and imaginary parts of the input impedance are (51.9 Ω, j2.2 Ω) and (40 Ω, j4 Ω) respectively. The dimension of different array sections is listed in Table 7.3.

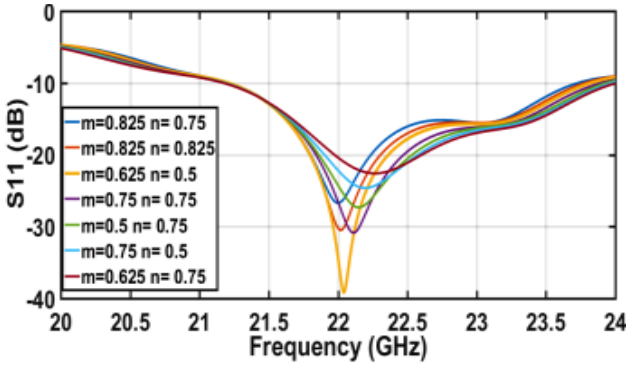

Fig. 7.11 TM01 2×2 array S_{11} variations with feed sections width variations

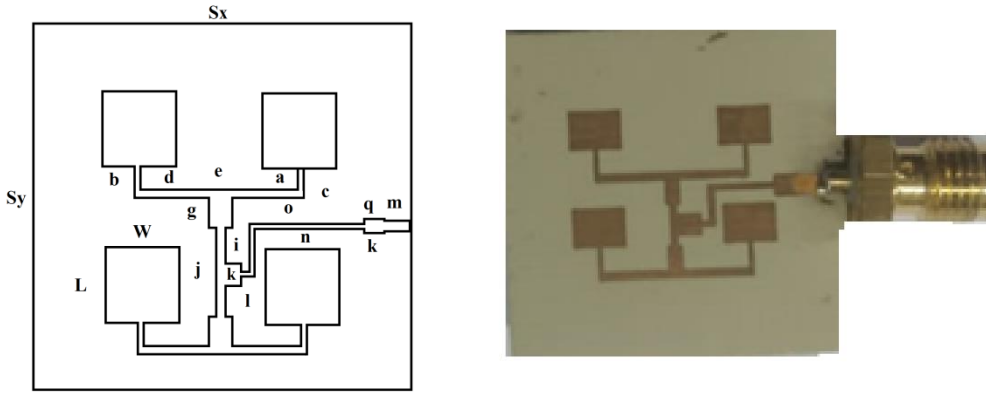

(a)

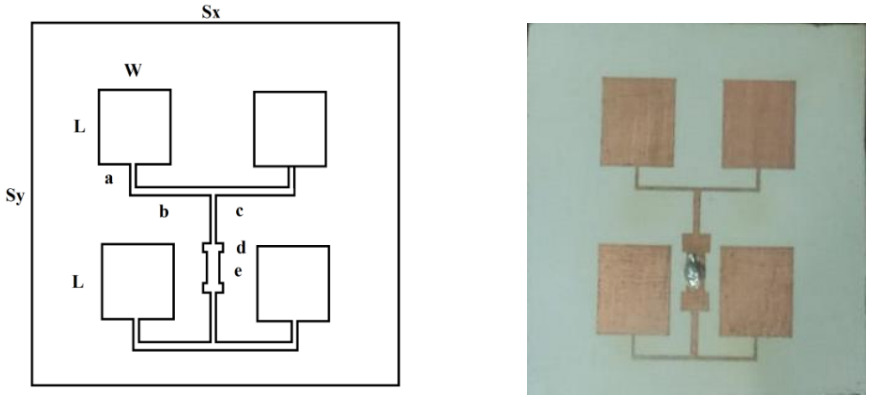

(b)

Fig. 7.12 Geometry design with fabricated prototype of the antenna (a) Fundamental mode 2×2 array and (b)TM_{03} mode 2×2 array

TABLE 7.3

DIMENSION OF TM01 & TM03 2×2 ARRAY

Parameters	**Gx**	**Gy**	**Sx**	**Sy**	**W**	**L**	**q**
TM01 2×2 array	25	25	25	25	3.7	2.83	
TM03 2×2 array	30	30	30	30	7.6	9.2	
Parameters	**a**	**b**	**c**	**d**	**e**	**g**	**o**
TM01 2×2 array	0.34	0.4	0.6	0.6	1	1.75	4.725
TM03 2×2 array	0.38	0.4	0.8	2	3		
Parameters	**i**	**j**	**k**	**l**	**m**	**n**	**r**
TM01 2×2 array	0.45	0.2	1.75	2.587	3.45	0.45	1.44

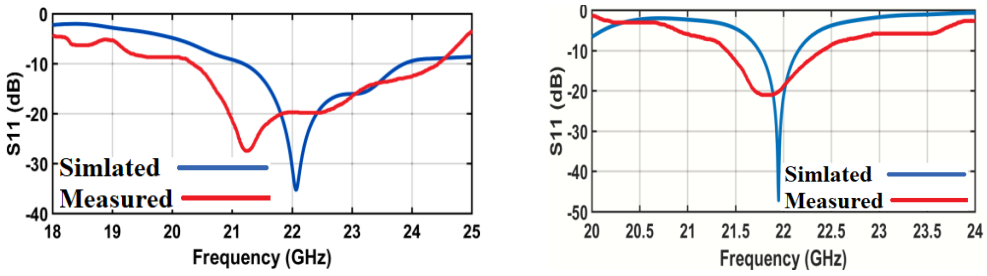

(a) (b)

Fig. 7.13 Simulated and measured S_{11} (a) TM_{01} and, (b)TM_{03} mode 2×2 array

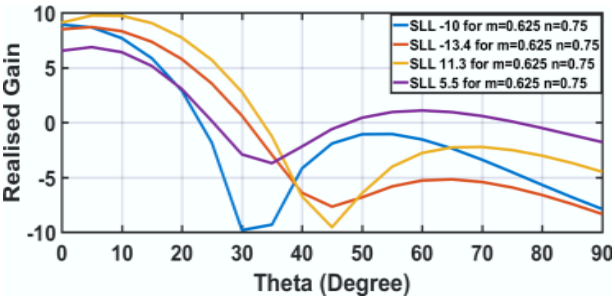

Fig. 7.14: TM_{01} mode 2×2 array E-plane side lobe variation

7.3.4 Simulation and fabrication of TM_{03} mode 2 × 2 array

Feed design for TM_{03} mode array followed the same approach as described for the fundamental array in previous section. Array elements are designed at fundamental (TM_{01}) 7.33 GHz and excited at TM_{03} mode using edge feed microstrip lines such that other nearby modes are largely suppressed so that the power coupling with nearby modes is minimized. Optimization techniques inbuilt in the CST simulation software have been used to find the optimum inter elemental separation for maximum broadside radiation, low SLL, and high gain. For m = 0.625 λ and n = 0.51 λ, the SLL in E and H-plane are noted at below13.2 dB and −14.6 dB respectively as illustrated in Fig. 7.15 and 7.17.

The simulated and measured S_{11} is observed at −47.65 dB at 21.93 GHz and −20.25 dB at 21.89 GHz respectively as shown in Fig. 7.14(b). The measured and simulated % of fractional bandwidth is noted around 3% (21.653GHz -22.31 GHz) and 5.14% (21.36 GHz-22.49 GHz) respectively.

The total simulated antenna efficiency is marked at 86% for TM_{03} mode antenna. The simulated and measured realized gains are found to be 16.2 dBi and 15.5 dBi respectively at 22 GHz as plotted in Fig. 7.16(b).

The Simulated and measured values of real and imaginary input impedance are observed at (37.9 Ω, −j1.7 Ω) and (31.45 Ω, −j4.23 Ω) respectively. All simulated and measured antenna parameters for single and 2 × 2 array operate at TM_{01} and TM_{03} modes are tabularized in Table 7.4.

The comparison shows an 82% increment of measured realized gain in contrast with the fundamental array. Impedance b/w of HOM array is more than 1 GHz (5.14%) which is well suited for UDN and IoT applications in 5G. Also, the side lobes appeared at HOM array has been reduced significantly in E/H plane (13.2 dB and 14.6 dB in each plane) as depicted in Fig. 7.17.

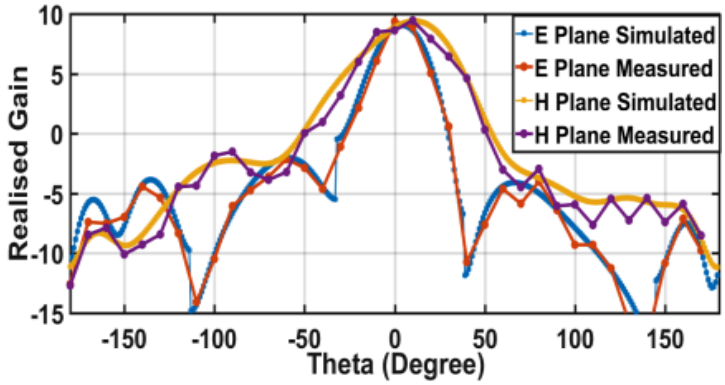

Fig. 7.15 TM01 mode 2×2 array simulated and measured E/H plane pattern

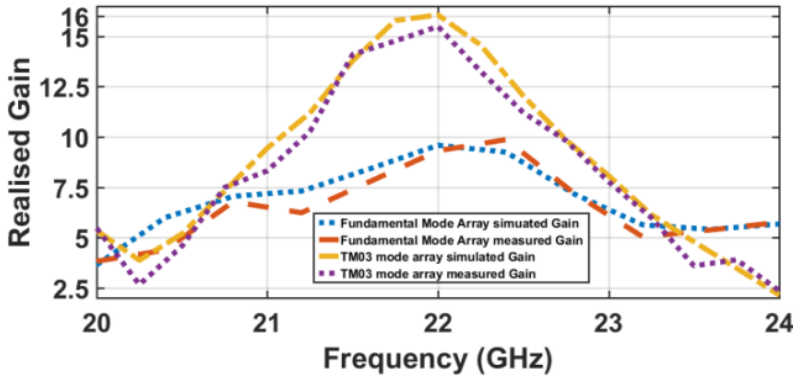

(a)

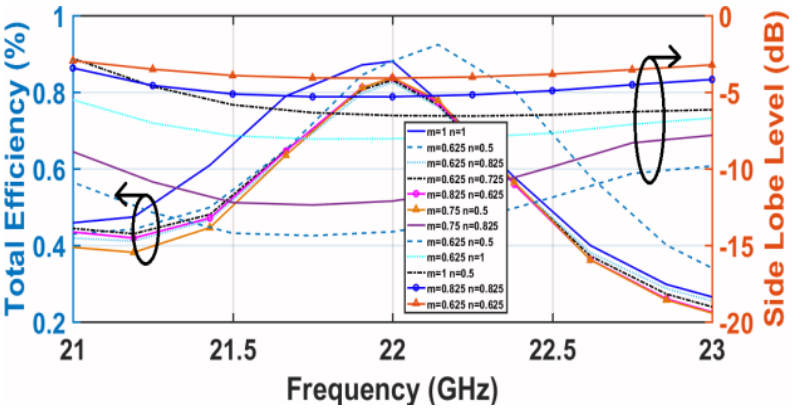

(b)

Fig. 7.16. Simulated and measured (a) realized gain vs frequency plot of single element fundamental and TM_{03} mode patch antenna array (b) E-plane side lobe variation with inter elemental space variations and total simulated antenna efficiencies.

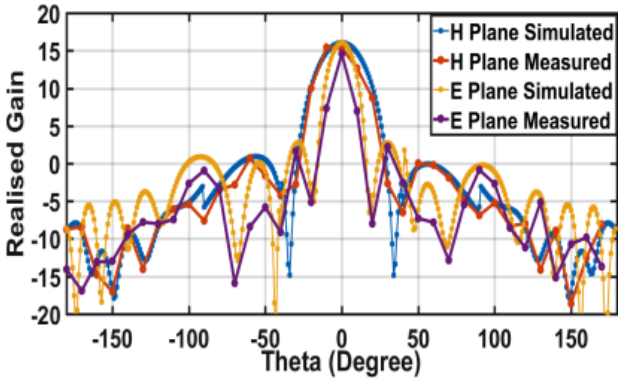

Fig. 7.17 TM_{03} mode 2×2 array simulated and measured E and H plane radiation pattern

TABLE 7.4

TM_{01} AND TM_{03} ANTENNA AND ARRAY SIMULATED AND MEASURED RESULTS COMPARISON

Patch geometry	Real-estate Sq-mm	Impedance BW (%)		Realized Gain		HPBW Degree		μ_{eff} (%)
		S	M	S	M	S E/H-plane	M E/H-plane	
TM01 single patch	2.77× 4.1884	8.6	11.2	7.47	6.5	66/83	59/77	90
TM01 2×2 array	14.4× 12.66	12.6	18.72	9.61	9.32	40/60	38.6/57	92
TM03 Single patch	7.4982× 9.118	2.3	3	8.91	8.73	67/84	65/81	90.07
TM03 2×2 array	17.0964× 23.836	2	5.14	16.2	15.5	20/36	18.2/31	86

μ_{eff} total antenna efficiency, HPBW half power beamwidth, S, M simulated and measured values

7.4 Discussion

Table 7.5 shows the performance of the proposed antenna in comparison with several recently reported higher-order single element and array antennas. In [18, 19, 20], author has proposed higher-order annular ring, stacked ring, and slotted circular patch antennas with a reasonable gain and other parameters. Though the measured % of fractional impedance bandwidth is very low (2%). Also, the antennas have very low aperture efficiency. In [21], microstrip square patch antenna having extremely low impedance BW (0.3%) has been proposed. A single element single layered patch operated at TM_{50} mode has been investigated in [22] that showed 3% impedance bandwidth using dual SMA feed. Author has proposed large ground slots for single element antenna with comparatively low SLL value (12.8dB /7 dB in E and H planes) in [23, 24]. In [25- 27], authors have proposed rectangular patch higher-order array with larger interelement spacing (1.47λ0). In [25], an antenna operating at higher order mode is studied. The antenna showed large ground size (48 λ_0) with complex GCPW-SICL feeding arrangement. Reference [26] proposed a multilayer Partially Reflected Surface inspired antenna for SLL reduction. Though the antenna showed high antenna profile and complex CPW-SIW feeding arrangement. In [27], a new strategy for mitigating high SLL is proposed with nine individual SMA coax connector to feed nine individual array elements. The structure introduced additional complexities in system integration. A 2 × 2 fundamental mode antenna arrays with a gain of 7.3 dBi and impedance bandwidth of only 2.3% is presented in [28] despite of its small inter-element spacing (0.8 λ_0). In this chapter, a TM_{03} mode 2D (2 × 2) array is presented. The proposed array shows sufficiently high measured realized gain, i.e., 15.5 dBi. The -10dB impedance bandwidth is also measured around 2GHz. Suitable E/H plane side lobes are measured (13.2/14.6 dB below). The HPBW of the broadside beam is measured around 18.2° and 31° in E/H planes. The measured aperture efficiency (58.34%) is noted to be significantly good. Thus, in contrast with the others work, the designed TM03 mode 2D array depicts more suitable gain-BW product, HPBW, aperture efficiency, and broadside pattern at 22 GHz frequency. Hence, the antenna can suitably be incorporated in different 5G applications, specifically for IoT (required high gain and low BW) in an Ultra-Dense Network environment (low co-channel interference required that is supported by inherent property of 22 GHz channel).

TABLE 7.5
A COMPARATIVE STUDY ON RECENT WORKS OF HIGHER ORDER MODES ANTENNA AND ARRAY

Ref	Resonant modes/ Frequency	Realized Gain	Ground Size	Relative BW	Element Spacing	Feeding Techniques	SLL	Aperture Efficiency
(18) Single element and layer	TM12/9.96	10.9	$3.14\lambda^2$	>1.5	NA	SMA	17.5	31.4
(19) Single element and layer	TM13/9.96	9.9	$3.08\lambda^2$	1.2	NA	SMA	17	25.2
(20) Single element and layer	TM12/9.94	13.06	$5.52\lambda^2$	1.56	NA	SMA	20	29.13
(21) Single element and layer	TM30/4.2	12.7	$2.37\lambda^2$	0.3	NA	SMA	18.6	62.48
(22) Single element and layer	TM50/5.96	11.5	$2.37\lambda^2$	3	NA	Dual SMA	17	47.47
(23) Single element and layer	TM70/7.3	16	$4.84\lambda^2$	3.8	NA	SMA coax	12.8	65.25
(24) Single element and layer	TM30/2.6	14.6	$5.3\ \lambda^2$	15.2	NA	Single SMA	7	43.04
(25) 1×8 array Single layer	TM50/22.3	19	$48\ \lambda^2$	7.8	$1.4\ \lambda$	GCPW-SICL	22	12.75
(26) 2×2 array3 layer	TM30/21	16.3	$24\ \lambda^2$	3.4	$1.47\ \lambda$	CPW-SIW	15.5	13.86
(27) 3×3 array Single layer	TM50/6	14.8	NM	6.67	NM	Nine (9) SMA	27	NM
(28) 2×2 array3 layer	TM01/24	7.4	$3.2\lambda^2$	2.3	$0.8\ \lambda$	Edge feed SMA	NM	13.67
This work2×2 array1 layer	**TM03/22**	**15.5**	**$6.6\ \lambda^2$**	**5.14**	**$1.1\ \lambda$**	**Single SMA**	**14.6**	**58.34**

7.5 Conclusions

In this chapter, a TM_{03} mode high gain antenna array operating at 22 GHz is proposed. This band is quite suitable for UDN/IoT applications because of its high atmospheric loss window [14] which would naturally mitigate co-channel interference. Designing of a planar array using antenna elements excited in higher order modes is studied in comparison with recently published works. It has been observed that the proposed single layered, single feed compact antenna array is convenient for IoT and UDN applications in 5G domain with significantly high gain and reduced SLL. The proposed antennas and arrays have been fabricated and measured for radiation and impedance characteristics. The parameters are found to be satisfactory with enhanced realized gain. In comparison with other published works our proposed antenna array showed marked improvement in gain with fewer antenna elements (2 × 2), reduced footprint area and structural simplicity. Therefore, the proposed array antenna could be a good candidate for future 5G applications in UDN and IoT scenarios.

References:

[1] K. M. S. Huq, S. A. Busari, J. Rodriguez, V. Frascolla, W. Bazzi and D. C. Sicker, "Terahertz-Enabled Wireless System for Beyond-5G Ultra-Fast Networks: A Brief Survey," in IEEE Network, vol. 33, no. 4, pp. 89-95, July/August 2019, doi: 10.1109/MNET.2019.1800430.

[2] S. Haghighatshoar and G. Caire, "The beam alignment problem in mmWave wireless networks," 2016 50th Asilomar Conference on Signals, Systems and Computers, 2016, pp. 741-745, doi: 10.1109/ACSSC.2016.7869144.

[3] T. Koch and A. Lapidoth, "On Multipath Fading Channels at High SNR," in IEEE Transactions on Information Theory, vol. 56, no. 12, pp. 5945-5957, Dec. 2010, doi: 10.1109/TIT.2010.2080995.

[4] A. C. F. Reniers, Q. Liu, M. H. A. J. Herben and A. B. Smolders, "Review of the accuracy and precision of mm-wave antenna simulations and measurements," 2016 10th European Conference on Antennas and Propagation (EuCAP), 2016, pp. 1-5, doi: 10.1109/EuCAP.2016.7481973.

[5] U. Ullah, N. Mahyuddin, Z. Arifin, M. Z. Abdullah and A. Marzuki, "Antenna in LTCC Technologies: A Review and the Current State of the Art," in IEEE Antennas and Propagation Magazine, vol. 57, no. 2, pp. 241-260, April 2015, doi: 10.1109/MAP.2015.2414668.

[6] Silver S. Microwave Antenna Theory and Design. New York, NY: McGraw Hill; 1949 chap 23. Zhong SS, Lo YT. Single-element rectangular microstrip antenna for dual-frequency operation. Electron Lett. 1983;19: 298-300.

[8] P. Juyal and L. Shafai, "A Novel High-Gain Printed Antenna Configuration Based on T12 Mode of Circular Disc," in IEEE Transactions on Antennas and Propagation, vol. 64, no. 2, pp. 790-796, Feb. 2016, doi: 10.1109/TAP.2015.2506724.

[9] Yingjie Jay Guo; Richard W. Ziolkowski, "A Perspective of Antennas for 5G and 6G," in Advanced Antenna Array Engineering for 6G and Beyond Wireless Communications , IEEE, 2022, pp.1-22, doi: 10.1002/9781119712947.ch1.

[10] Constantine A. Balanis, "Microstrip Antennas: Analysis, Design, and Application," in Modern Antenna Handbook , Wiley, 2008, pp.157-200, doi: 10.1002/9780470294154.ch4.

[11] James JR, Hall PS. Characteristics of microstrip patch antennas and some methods of improving frequency agility and bandwidth. Handbook of Microstrip Antennas. London, UK: Peregrinus; 1989 chap 3.

[12] Bahl IJ, Bhartia P. Microstrip Antennas. Norwood, MA: Artech House; 2001.

[13] Garg R, Bhartia P, Bhal I, Ittipiboon A. Microstrip Antenna Design Handbook. Artech House Inc; 2001. 40. Crane RK, Dissanayake AW. ACTS propagation experiment: attenuation distribution observations and prediction model comparisons. Proc IEEE. 1997;85(6):879-892.

[14] R. K. Crane and A. W. Dissanayake, "ACTS propagation experiment: attenuation distribution observations and prediction model comparisons," in Proceedings of the IEEE, vol. 85, no. 6, pp. 879-892, June 1997, doi: 10.1109/5.598411.

[15] CST Computer Simulation Technology. http://www.cst.com

[16] Trevor S. Bird, "Microstrip Patch Antenna," in Fundamentals of Aperture Antennas and Arrays: From Theory to Design, Fabrication and Testing , Wiley, 2015, pp.137-147, doi: 10.1002/9781119127451.ch5.

[17] Debatosh Guha; Yahia M.M. Antar, "Printed Antennas for Wireless Communications," in Microstrip and Printed Antennas: New Trends, Techniques and Applications , Wiley, 2011, pp.215-261, doi: 10.1002/9780470973370.ch8.

[18] P. Juyal and L. Shafai, "A Novel High-Gain Printed Antenna Configuration Based on T12 Mode of Circular Disc," in IEEE Transactions on Antennas and Propagation, vol. 64, no. 2, pp. 790-796, Feb. 2016, doi: 10.1109/TAP.2015.2506724.

[19] P. Juyal and L. Shafai, "Gain Enhancement in Circular Microstrip Antenna via Linear Superposition of Higher Zeros," in IEEE Antennas and Wireless Propagation Letters, vol. 16, pp. 896-899, 2017, doi: 10.1109/LAWP.2016.2613996.

[20] P. Juyal and L. Shafai, "Sidelobe Reduction of TM12 Mode of Circular Patch via Nonresonant Narrow Slot," in IEEE Transactions on Antennas and Propagation, vol. 64, no. 8, pp. 3361-3369, Aug. 2016, doi: 10.1109/TAP.2016.2576503.

[21] X. Zhang, L. Zhu and Q. -S. Wu, "Sidelobe-Reduced and Gain-Enhanced Square Patch Antennas With Adjustable Beamwidth Under TM03 Mode Operation," in IEEE Transactions on Antennas and Propagation, vol. 66, no. 4, pp. 1704-1713, April 2018, doi: 10.1109/TAP.2018.2806220.

[21] Y. He, Y. Li, W. Sun, Z. Zhang and P. -Y. Chen, "Dual Linearly Polarized Microstrip Antenna Using a Slot-Loaded TM50 Mode," in IEEE Antennas and Wireless Propagation Letters, vol. 17, no. 12, pp. 2344-2348, Dec. 2018, doi: 10.1109/LAWP.2018.2874472.

[22] Ahmed Z, Ahmed MM. Sidelobe reduction and gain enhancement in higher order TM30 and TM70 mode rectangular patch antennas via partial notch loading. IET Microw Antennas Propag. 2019;13(12):1955-1962.

[23] J. Anguera, A. Andújar and J. Jayasinghe, "High-Directivity Microstrip Patch Antennas Based on TModd-0 Modes," in IEEE Antennas and Wireless Propagation Letters, vol. 19, no. 1, pp. 39-43, Jan. 2020, doi: 10.1109/LAWP.2019.2952260.

[24] Y. Zhang, W. Cao, Z. Qian, S. Shi and W. Peng, "Low Grating Lobe Array Antenna With Electrically Large Property Based on TM50 Mode," in IEEE Access, vol. 7, pp. 32897-32906, 2019, doi: 10.1109/ACCESS.2019.2903169.

[25] Sezgin Ördek, Ahmet Kizilay, "Electrically large aperture horn array antenna with low side lobe level for Ku-band frequency", Microwave and Optical Technology Letters, 2022.

[26] H. Yang et al., "A New Strategy to Design Microstrip Antenna Array With Low Side-Lobe Level and High Gain," in IEEE Access, vol. 7, pp. 152715-152721, 2019, doi: 10.1109/ACCESS.2019.2948098.

[27] M. Poggiani, F. Alimenti , P. Mezzanotte , et al. 24-GHz patch antenna array on cellulose-based materials for green wireless Internet applications. IET Sci Meas Technol. 2014;8(6):342-349.

[28] Jayasinghe JMJW, Anguera J, Uduwawala DN, Andújar A. Highdirectivity genetic microstrip patch antenna. Int J Electron Lett. 2016;4(3):279-286. https://doi.org/10.1080/21681724.2015.1034189.

Chapter 8
Penta-Polarization Agile Higher Order Planar Antenna

8.1 Introduction

Signal to interference and Noise ratio (SINR) of a RF link can be improved by increasing the gain of the terminal antennas [1]. The transmit power of an antenna can also be efficiently used by higher antenna gain [2]. It has also been noted that with increased gain the beamwidth of the antenna is reduced; hence can be precisely aligned to the intended user without interfering surrounding signals. Thus, signal interference can also be reduced to some extent [3]. The reconfigurable antennas proposed so far have shown low realized gain that varied in the range of 5-8dBi. Thus, gain enhancement in reconfigurable antennas make the system way more suitable in recent scenarios in terms of power efficiency and reduced signal degradation [4].

In this chapter an effective approach to enhance the gain of the penta-polarization reconfigurable antenna is investigated. So for the proposed antennas are designed to operate in fundamental modes. The design of antennas is further improved and excites to operate in higher order broadside mode without tempering the simplicity of the structure.

In this chapter, a compact, high gain, single-layered penta-polarization reconfigurable MSA operating at TM_{03} mode is investigated possibly for the first time in the literature. A prototype antenna is analyzed, fabricated, and measured to validate the proposed theory.

8.2 Theory

8.2.1 Higher Order Mode MSA

The radiating edges of patch antennas operating in TM_{0n} or TM_{n0} modes (n is the modal index) are $n\times\lambda/2$ apart along the patch length and radiates similar to $n\times\lambda/2$ mode dipole (λ is the wavelength of TM_{0n} mode) [5, 6]. Side-lobe Levels (SLL) present in the radiation pattern vary in numbers and amplitude depending upon the modal index of the radiating mode [7]. Large magnitude of the SLL can be attributed to the existence of $\lambda/2$ out of phase current sections

between in-phase $\lambda/2$ current strips on the patch surface as illustrated in Fig.8.1 (a-b). The equivalent magnetic current ($\vec{M}$) at the radiating edges are equal and out of phase for even modal index (n) and hence cancel out the far-field radiation placing null in the broadside direction. Conversely, for odd n, broadside far-field radiation is combined. Hence TM_{0n} modes with odd n radiate in the broadside direction providing significantly higher gain at the expanse of higher SLL and larger aperture area.

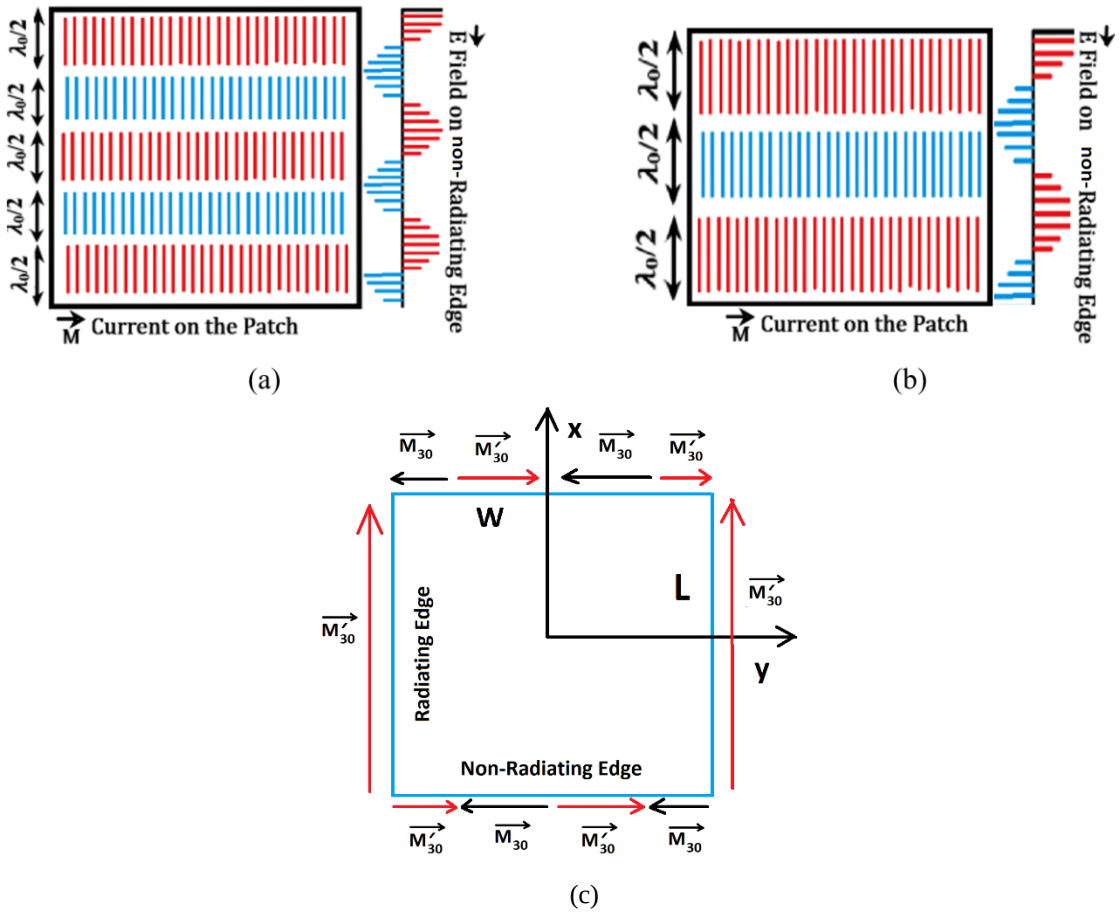

Fig. 8.1 Surface current on the patch antenna with red and blue lines indicate $\lambda/2$ opposite directed current strips and E filed on the non-radiating edge of the patch in (a) TM_{05}, (b) TM_{03} mode operation, and (c) TM_{03} mode equivalent magnetic currents ($\vec{M}$) at patch edges with red and black arrows indicate opposite directed currents.

For an example, equivalent magnetic currents, $\vec{M}$ in the radiating and non-radiating edges of TM_{03} and TM_{05} are aligned in-phase and out of phase respectively as shown in Fig. 8.1(c) which results in addition of far filed radiation in the broadside direction as depicted in

Fig. 8.2(a). The presence of multiple $\lambda/2$ sections along the patch length resembles the analogy of an array of multiple (obtained from the modal index) dipole radiators separated by $\lambda/2$. The number of side lobes in the E-plane is primarily due to the array factor formed by the hypothetical dipole radiators separated by $\lambda/2$ [7]. Few techniques such as shorting vias or slots can be incorporated to perturb the surface current distribution on the patch and realign the current as broadside radiating modes so that these modes also radiate in the broadside direction [8, 9].

8.2.2 Reduction in SLL of Higher Order MSA

Consecutive $\lambda/2$ sections on the patch surface are having oppositely directed current generating the side lobes at TM_{0n} modes. These $\lambda/2$ sections are removed to make the current distribution unidirectional, similar to that of the fundamental mode, hence reducing the SLL with the expense of slightly reduced gain due to reduced aperture area. Out of phase $\lambda/2$ section (at the center on the patch) in TM_{03} mode and alternate $\lambda/2$ sections in case of TM_{05} mode are removed partially to reduce the SLL significantly as shown in Fig. 8.2.

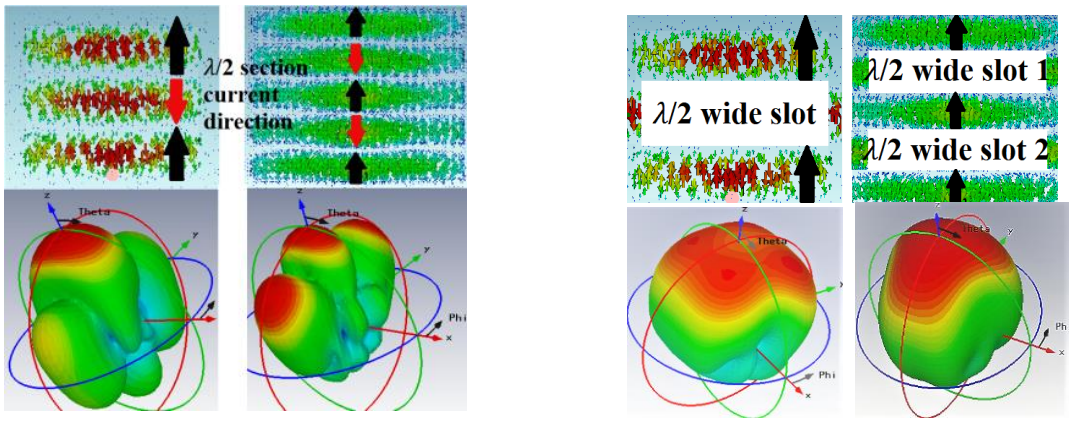

(a) (b)

Fig. 8.2 Surface current and 3D radiation pattern for TM_{03} and TM_{05} mode patch (a) without $\lambda/2$ slot etched, (b) with $\lambda/2$ slot etched.

8.3 Analysis on TM_{03} mode square MSA

A square patch antenna operating at TM_{03} mode is synthesized using the design procedure discussed in previous chapter (Chapter 7, Section: 7.3.1). Orthogonal modes (TM_{03} and TM_{30}) are excited along the length and width of the patch to generate CP states; hence a square slot is cut at the center of the patch to minimize the side lobes in dual CP states (RHCP and LHCP). The slot length is tuned further for optimum radiation performance at the designed frequency.

8.3.1 Effect of slot on input impedance

As the slot area increases, the current paths on the patch surface become longer, shifting the input impedances at the orthogonal edges at low resonances. However, the impedance values have remained nearly unchanged as shown in Fig. 8.3(a). The etched slot on the patch results in an inductive loading in the edge impedances; therefore, the imaginary part moves from capacitive to inductive region and improves impedance matching, as shown in Fig. 8.3(b). It is also observed in Fig. 8.3 that the TM_{22} mode resides adjacent to TM_{03} mode and varies in frequency with the changing slot area and increases the impedance bandwidth. The far-field pattern and overall antenna efficiency of the intended mode might be compromised due to inter-modal power coupling. Though TM_{22} mode has negligible modal significance and hence it has least adverse effect on the performances of the intended mode (TM_{03}).

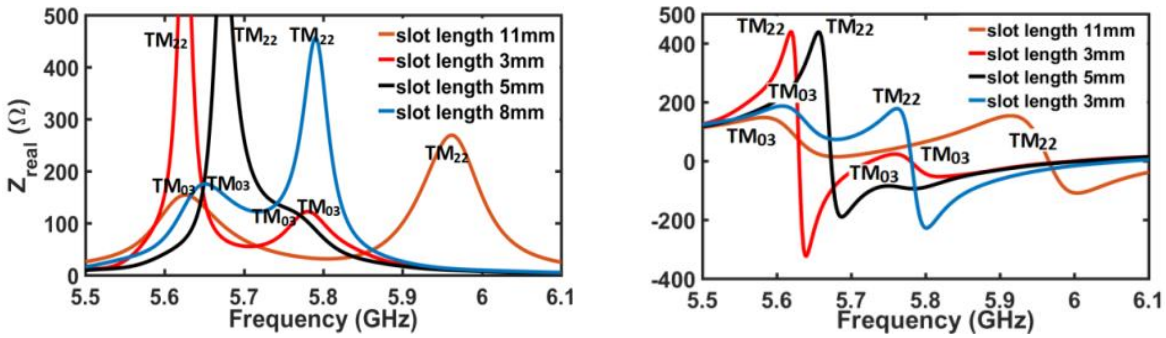

(a) (b)

Fig. 8.3 TM_{03} mode input impedance for different slot length (a) Real, and (b) Imaginary part

8.3.2 Effect of slot on Antenna gain

As a result of varying the slot area, the resonance frequencies are shifted, reducing gain both at the designed frequency (5.8GHz) and at the shifted resonances. Fig. 8.4 shows the realized gain at 5.8GHz which reduces gradually for varying slot lengths across the patch width in TM_{03} and TM_{05} modes. The reduction of the gain at those shifted resonances is attributed to the reduced aperture due to increasing slot area.

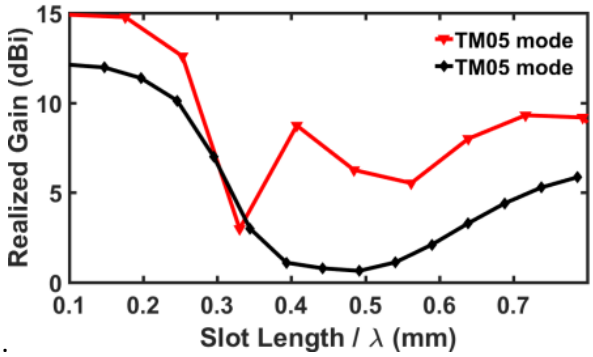

Fig.8.4 Realized Gain of TM03 and TM05 mode antennas for varying slot width.

There is an apparent phase difference between upper and lower $\lambda/2$ sections of the patch when the slot length is substantial (nearly equal to the patch width) causing marginal beam tilt in the $\varphi=90^{\circ}$ plane. The dimensions of the slot must therefore be optimized to balance acceptable SLL, gain, and beam tilt. This can be achieved by adjusting the patch and slot dimensions simultaneously.

8.3.3 Effect of slot on Side-lobe

An optimal antenna performance can be achieved using $\lambda/2\times\lambda/2$ slot area with minimum SLL at $\varphi=0^{\circ}$ & 90° planes. Increasing the slot area reduces dielectric and conduction losses, resulting in an improvement in radiation and total efficiency. The SLL plots for a specific frequency for TM_{03} & TM_{05} modes at the $\varphi=0^{\circ}$ & 90° plane is shown in Fig. 8.5. It is observed that SLL in both the planes are lower at TM_{03} than TM_{05} mode. This can be attributed to the presence of a smaller number of out of phase $\lambda/2$ current strips compared TM_{05} mode. SLL at TM_{03} and TM_{05} modes for 0.5λ slot length is less than -13dB and -20dB respectively in both the principal planes as shown in plots.

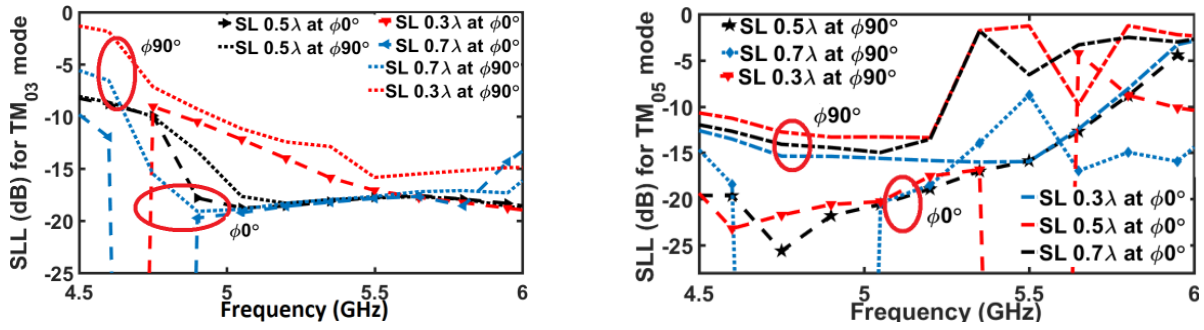

(a) (b)

Fig. 8.5 Side lobe levels (SLL) at φ=0° & 90° planes for varying slot lengths for (a) TM_{03} and (b) TM_{05} mode

8.4 Design of TM_{03} mode polarization agile MSA

Corner truncation and subsequent perturbation of patch surface current caused each higher order mode to split into two orthogonal (TM_{0n} & TM_{n0}) modes with slightly different frequencies as defined in (8.1 & 8.2) respectively [7] to realize CP states.

$$f_x = f\left(1 - \frac{2\Delta A}{A}\right) \tag{8.1}$$

$$f_y = f \tag{8.2}$$

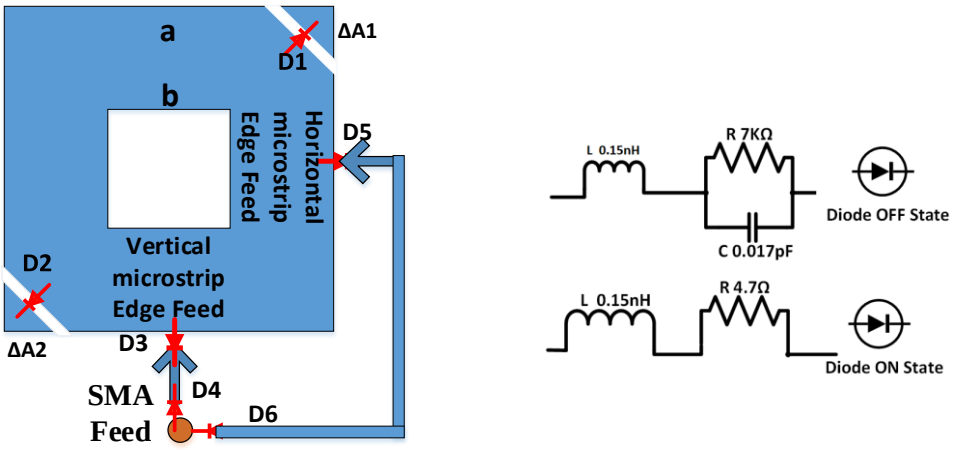

Fig. 8.6 (a) Simple antenna structure for polarization diversity, and (b) Diode equivalent model for forward and reverse bias condition.

ΔA ($\Delta A1 + \Delta A2$) is the total area of the truncated portion and $A = (a^2 - b^2)$ is the total area of the square patch subtracting the central cut area as shown in Fig. 8.6(a). The area of the truncated corners is derived from (8.3) to achieve orthogonal modes to generate CP [7]. The length of the corners can be derived from the mentioned equation.

$$\frac{2\Delta A}{A} = \frac{1}{2Q_0} \tag{8.3}$$

Reconfigurable orthogonal feed lines connected to the patch edges as illustrated in Fig. 6a are excited individually to attain RHCP and LHCP respectively. PIN diodes are connected at the truncated corners to retain the original patch structure as shown in the figure. Feeds are excited individually in this configuration to realize vertical and horizontal polarization states (VP & HP) respectively. Simultaneous excitation of both feeds with equal phase and amplitude generates 45° slant linear polarization state.

Table 8.1 present the DC bias conditions for six PIN diodes for five distinct achievable polarization states at TM_{03} mode operation.

TABLE 8.1. DIODE BIAS CONDITION FOR PENTA-POLARIZATION STATES

Polarization	D_1& D_2	D_3& D_4	D_5& D_6
VP	ON	ON	OFF
HP	ON	OFF	ON
45° Slant	ON	ON	ON
LHCP	OFF	ON	OFF
RHCP	OFF	OFF	ON

D: PIN Diodes

The sense of rotation of the patch surface current clearly depicts the generation of RHCP and LHCP waves for specific switching conditions mentioned in Table 8.1. $|E_\theta/E_\varphi|$ at φ=0° & 90° planes are laid within ±1.5dB and $\angle (E_\varphi \sim E_\theta) = 90°$ is observed for circular polarization as shown in Fig. 8.7(a). It depicts equal amplitude components with 90° phase difference. $\angle E_\varphi$ leads in one case where LHCP wave is radiated and simultaneously the leading of $\angle E_\theta$ initiates RHCP. Axial Ratio (AR) at broadside far field in both the principal planes is less than 3dB through the Half Power Beam-width (HPBW±30°) as represented in Fig. 8.7(b). $|E_\theta/E_\varphi|$ at φ=0° & 90° plane is laid within ±2 dB and $\angle(E_\varphi \sim E_\theta) = 0°$ represents far field electric components with equal amplitude and phase generating 45° slant polarized wave as shown in Fig. 8.7(c).

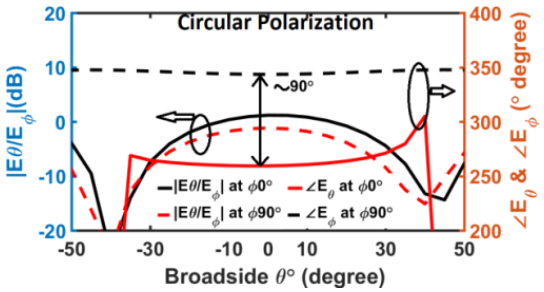

(a)

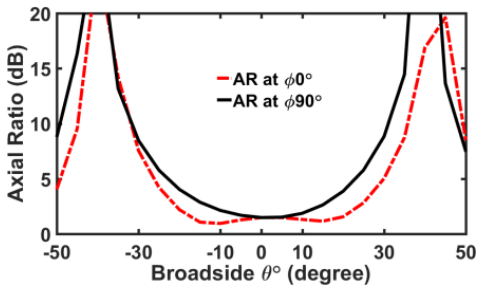

(b)

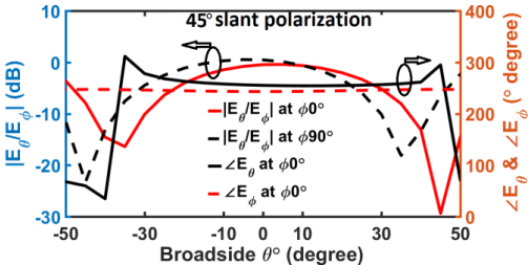

(c)

Fig. 8.7 (a) $|E_\theta/E_\varphi|$at φ=0° & 90° plane and ∠ $(E_\varphi \sim E_\theta)$for LHCP, (b) AR in the HPBWat φ=0° & 90° plane for LHCP, and (c) $|E_\theta/E_\varphi|$at φ=0° & 90° plane and ∠ $(E_\varphi \sim E_\theta)$for 45° slant polarization

Current distribution on the patch surface for different polarization states are shown in Fig. 8. At T/4 time intervals the surface current distribution for RHCP and LHCP state is shown in Fig. 8.8 (a-b) whereas, 45° slant polarization at t=0 & T/2 time period is depicted in Fig. 8.8(c).

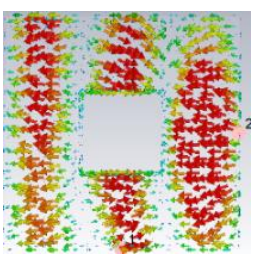

t=0

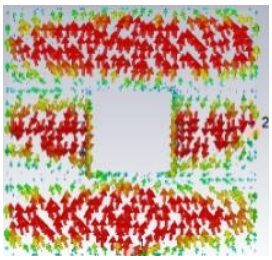

t = T/4

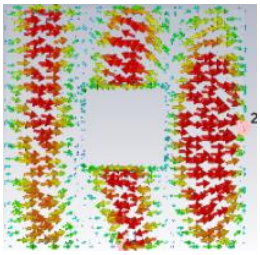

t = T/2

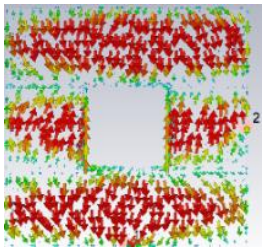

t = 3T/4

(a) LHCP

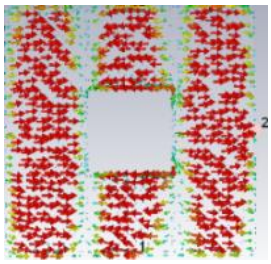

t=0

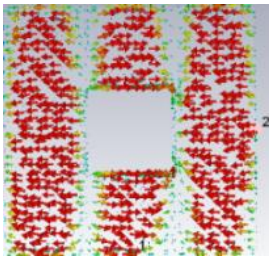

t = T/4

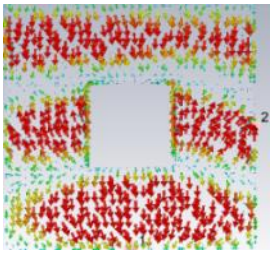

t = T/2

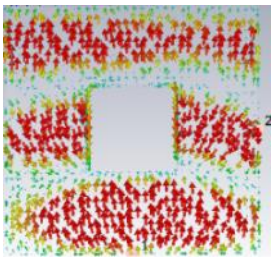

t = 3T/4

(b) RHCP

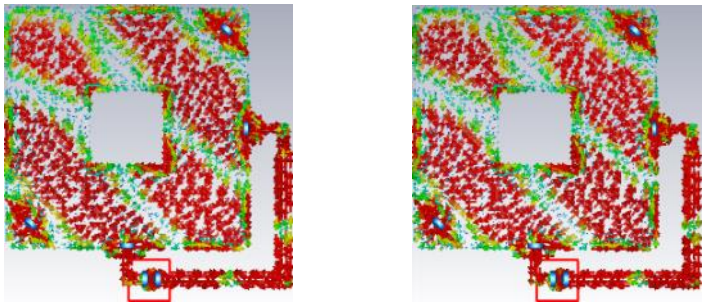

t = 0 t = T/2

(c) 45° Slant

Fig. 8.8 Generation of five different polarization states using corner truncation and feeding techniques and corresponding current direction, (a) Horizontal feed with corner truncation for LHCP, (b) vertical feed with corner truncation for RHCP and (c) 45° slant polarization with dual feed.

8.5 Design of the Feed Network

Input impedance of the orthogonal edges for distinct polarization states are found to be complex as the MSA is made square for CP generation at higher order mode as shown in Fig. 8.9(a-b). It is noted that the impedance behavior is greatly similar either for CP or LP states due to antenna symmetry. It is also observed that the real and imaginary parts of the impedances are varied within the range (55-80) Ω and (60-100) jΩ respectively. An average of the input impedances is taken while designing the feed lines as the impedances are not varied significantly. A series stub of specific width and length is connected with one of the MSA edges to transform the complex impedance to real impedance. Subsequently quarter wave sections are attached to transform the impedance to 70Ω and terminated at 50Ω coax feed. Despite slight impedance mismatch, it provides enough -10dB matching. Similar approach is opted for the feed line originating from the adjacent edge and transforms the MSA edge impedance to 70Ω. The parallel combination of these lines appears to be 35Ω at the time of simultaneous activation for 45° slant polarization. It is observed that though 35Ω+j0 terminal impedance is slightly mismatched with 50Ω SMA feed, it provides significantly good matching as well and shown in in S_{11} plots in Fig. 8.12. The adjacent feed lines are chosen either to be equal or different in length by multiple of λ to provide equal phase and amplitude to both the edges to attain 45° slant polarization state. The above approach is found suitable to attain -10dB impedance matching for all desired polarization states in a single layer single feed structure.

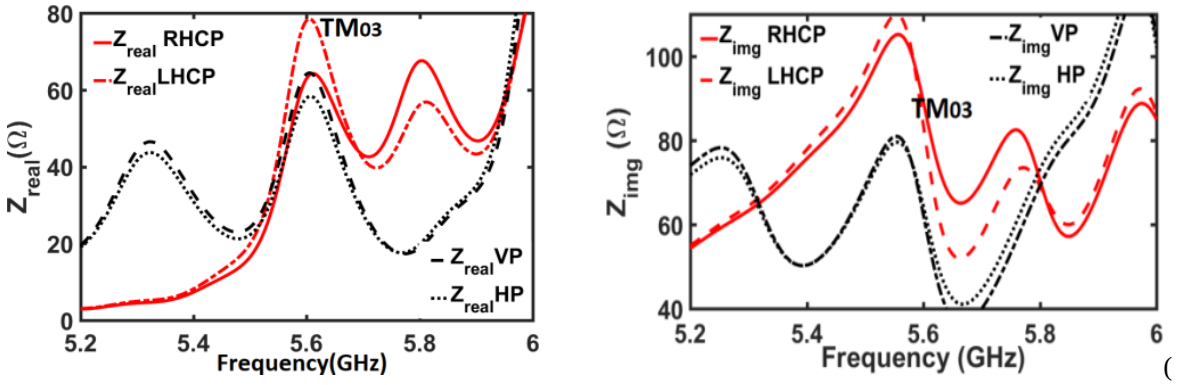

(a) (b)

Fig. 8.9 Input impedances (Z_{real} and Z_{img}) at the orthogonal edges of the TM_{03} mode MSA for different polarization states (a) CP (LHCP & RHCP), and (b) LP (VP & HP).

Layout of the prototype antenna along with the fabricated sample is shown in Fig. 8.10(a-b). All designed dimensions are mentioned in Table 8.2.

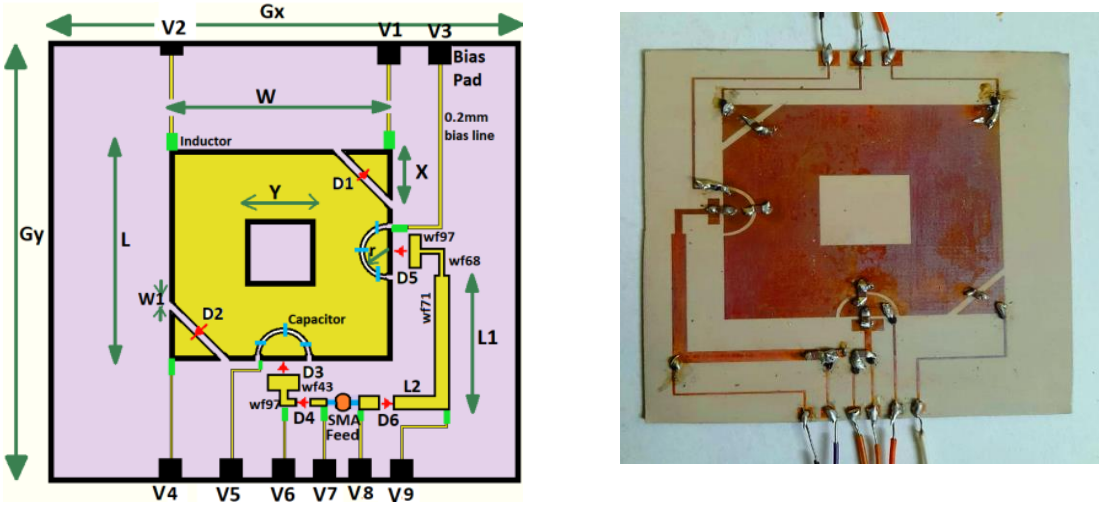

(a) (b)

Fig. 8.10 (a) Layout of the designed prototype TM_{03} mode reconfigurable penta-polarized patch antenna, and (d) fabricated prototype antenna

TABLE 8.2: DIMENSIONS OF DESIGNED ANTENNA (ALL ARE IN MM)

Parameters	**H**	**T**	**Gx**	**Gy**	**L**	**W**	**X**	**Y**
Values	1.6	0.004	60	60	39.5	39.7	8	13
Parameters	L2	L3	L4	L5	L6	L7	L9	L10
Values	18.99	1.05	1.05	1.92	3.52	2.4	3.52	4.52
Parameters	L11	Wf71	Wf43	Wf97	Wf68	W1	r	L1
Values	1.8	2	4.5	1	4.7	1	2.7	23.45

8.6 DC Biasing Network

PIN diodes from Avago Technologies (HPND-4005-beam-lead SMD 01005 package) [9] are used for the switching mechanism. The switches have got very low capacitances (C = 0.017 pF) in the OFF state and low resistances (R = 4.7 Ω) in the ON state. It also has low values of package parasitic with limited adverse effects on the isolation and insertion loss. Fig. 8(b) depicts the equivalent circuit of the diode in forward and reverse bias states. D1 and D2 are used to switch the truncated corners of the patch as shown in Fig. 8.10(a). DC voltage sources, V1 and V4 are connected to the opposite truncated corners while one of the opposite non-truncated corners of the patch is terminated at V2 to control the switching of D1 and D2 simultaneously. D3 and D4 are used in the vertical feed line and the switching is controlled by V5, V6 and V7 DC sources respectively. Whereas D5 and D6 are connected in the horizontal feed line and controlled by V8, V9 and V3 respectively. The corresponding DC values are tabulated in Table III. The sources V2, V6 and V9 are DC grounded and hence not tabulated.

Circular slots are cut at the adjacent edges around the orthogonal feeds; subsequently 33pF series capacitance (Murata Manufacturing) is used for DC block and RF continuity. Whereas 47nH inductor (Skyworks Inc.) is used as RF choke to block the RF to the DC source as shown in Fig. 8.10. DC bias lines of 0.15mm width are drawn to connect different antenna sections with DC sources for proper biasing. These lines are made very thin in comparison with the wavelength to attain high impedance and terminated at $3\times3mm^2$ bias pads for better coupling management.

TABLE 8.3: DC BIASING CONDITIONS FOR DIFFERENT POLARIZATION

Polarization	V1	V3	V4	V5	V7	V8	D1 D2	D3 D4	D5 D6
VP	+3	-10	+3	+3	+3	-10	ON	ON	OFF
HP	+3	+3	+3	-10	10	+3	ON	OFF	ON
45°	+3	+3	+3	+3	+3	+3	ON	ON	ON
RHCP	-10	+3	-10	-10	-10	+3	OFF	ON	OFF
LHCP	-10	-10	-10	+3	+3	-10	OFF	OFF	ON

A DC voltage drop of +0.9 V between the anode and the cathode will turn the diode ON with a bias current of ~ 20 mA. The insertion loss of the diode is around 0.4dB. A voltage of 0V

is sufficient to turn the diode OFF, but it is preferable to firmly reverse bias the diode with a higher reverse voltage (e.g., -10V) in order to increase the isolation in the OFF state by reducing the diode inner capacitance.

8.7 Measurement Results and Discussion

A prototype antenna operating at TM_{03} mode is fabricated at 5.8GHz band to validate the proposed theory and design methodology. FDTD based microwave simulator CST V.19 is used to simulate the antenna. Arlon AD430 substrate with ε_r 4.3, $\tan\delta$ 0.002 and height 30 mil is used for the design. Two stable DC voltage sources are used to bias the switches in accordance with different bias conditions as shown in Tables 8.3. The SMA feed is covered with RF absorbers to ensure least coupling of external spurious radiation which can cause ripples in the measured pattern. Aluminum foil is used to cover the external bias lines along with the DC supply to prevent external RF noise.

8.7.1 Reflection Co-efficient (S_{11})

Simulated and measured reflection coefficient S_{11} (dB) of all polarization states are plotted in Fig. 8.11(a-b) and 8.12(b). Impedance bandwidth for VP and HP modes are observed to vary between 14-17%. For 45° slant polarization state these results are found to be 24% and 16% respectively. Similarly, for RHCP and LHCP states, the simulated and measured S_{11} is found to vary between 12-12.5 % as depicted in the Fig. 8.11(b). The results are tabularized in Table 8.4. TM_{03} and TM_{13} are observed to couple around 5.8GHz band (TM_{03} at 5.85 and TM_{13} at 5.45GHz) increases the bandwidth in LP states. The modal significance of the TM_{03} mode is found to be dominant hence its characteristic is prominent over the band. Merging of three coexisting modes at 5.4GHz, 5.8GHz and 6.2GHz increases the impedance bandwidth of 45° slant polarization. A minor frequency offset is observed in the measured S_{11}. These discrepancies can be explained due to fabrication tolerance, considering approximate boundary condition (Artificial Boundary Condition) in the computational domain, simple circuit model of the diodes and parasitic effects of the packaged diodes along with manufacturer and soldering tolerance.

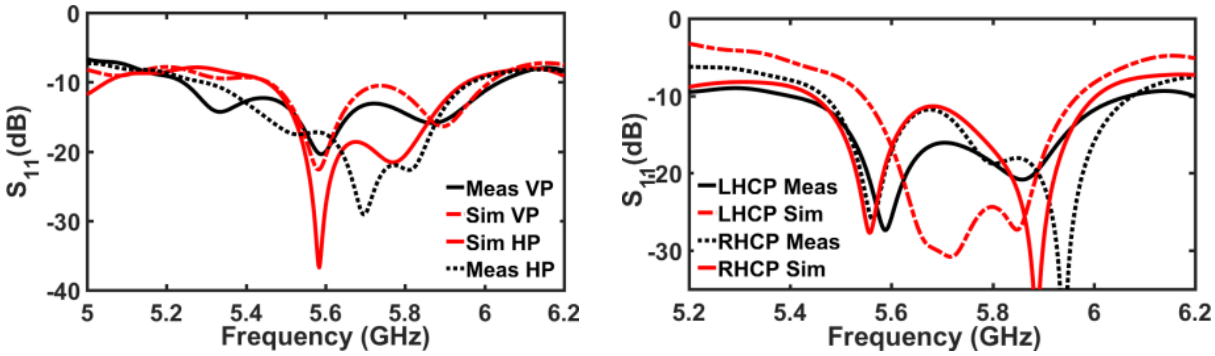

(a) (b)

Fig. 8.11 Simulated and Measured S_{11} for different polarization states. (a) LP & VP, and (b) LHCP, RHCP polarization states

8.7.2 dB Axial Ratio Bandwidth

3dB AR bandwidth is observed for both the CP modes in the broadside direction. Measured and simulated bandwidth for RHCP is 4.4% and 4% respectively, while it is 3.93% and 3.98% respectively for LHCP mode as illustrated in Fig. 8.12 (a). It is also observed that the entire AR bandwidth is lying within the impedance bandwidth presented in Table IV.

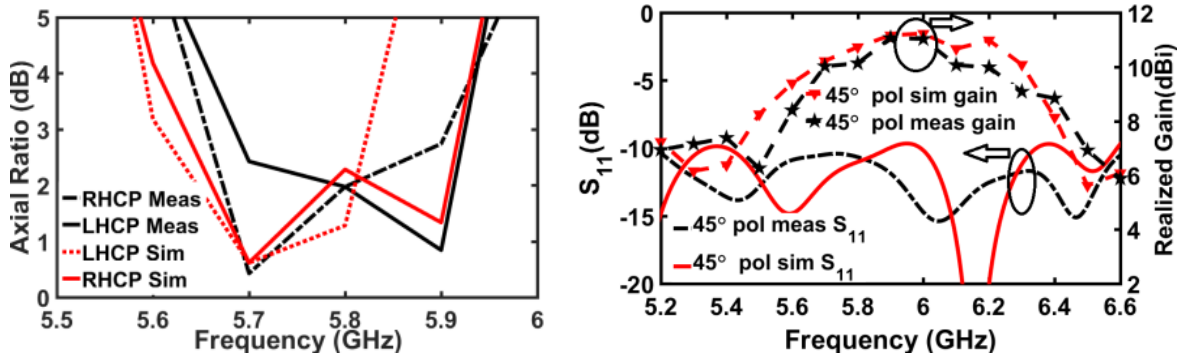

(a) (b)

Fig. 8.12 Simulated and measured 3 dB AR bandwidth for reconfigurable dual CP (LHCP and RHCP) states and (b) 45° slant polarization sates along with S_{11}

8.7.3 Realized Gain (dBi)

Simulated and measured realized gains for all the polarization states are depicted in Fig. 8.13 (a-b) and Fig. 8.12(c) respectively. The measured realized gains are observed to vary between 11.32-9.9dBi at 5.8GHz in the broadside direction and remain approximately constant throughout the impedance bandwidth (within 1.4dBi variation) as shown in the figures. A slight

reduction in measured gain is attributed to the insertion loss of PIN diodes, losses in lumped elements and also dielectric and conduction losses of the substrate.

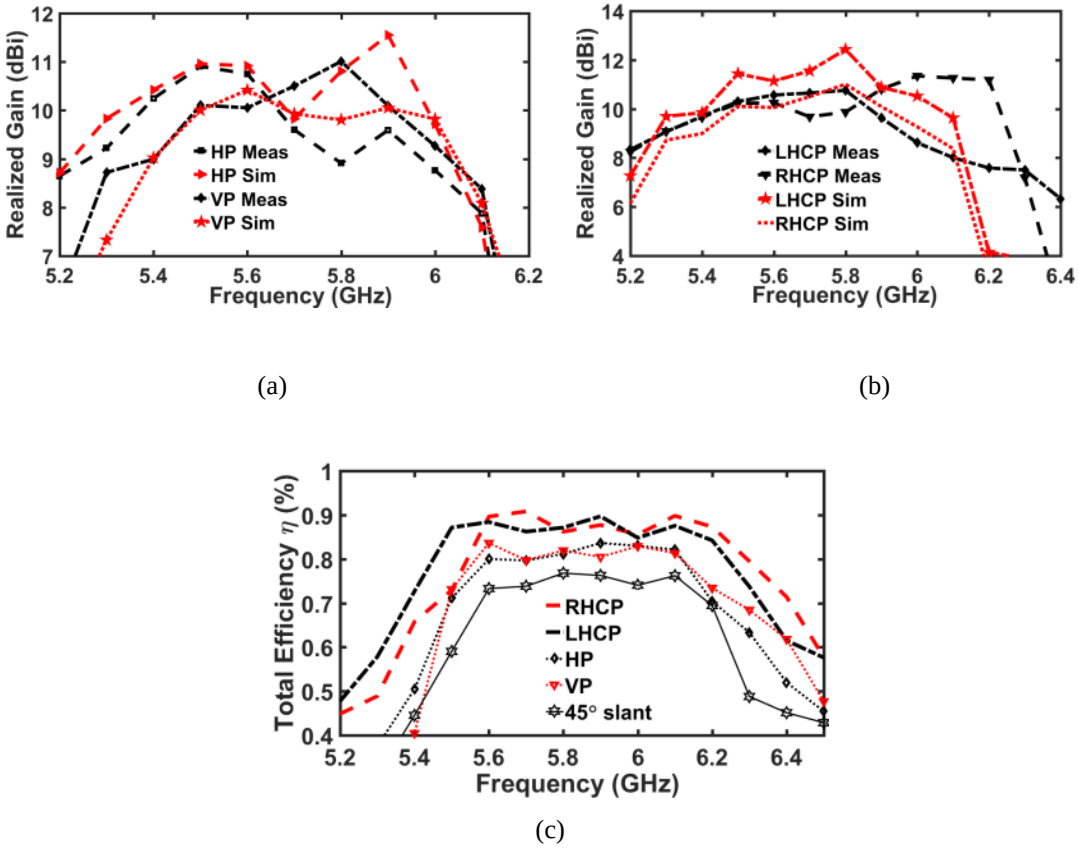

Fig.8.13 Simulated and Measured Realized Gain of (a) LP states, (b) Dual CP states, and (c) simulated antenna efficiency of different polarization states

8.7.4 Total Antenna Efficiency (%η)

Total simulated efficiency for LPs is varying between 80-85%, while it is nearly 75% in case of 45° slant polarization between 5.4-6.2GHz. Conversely the efficiencies lay between 85-90% for both CP states. Fig. 8.13(c) shows the efficiencies for different polarization states. Substrate loss along with impedance mismatch predominantly contributes for the reduction in antenna efficiency. Forward biased diode draws larger forward current, hence increases the diode ohmic loss and thus reduces the efficiency further. Two, four and six numbers of diode are turned ON subsequently to realize CP, LP and 45° slant polarization states

as presented in Table 8.2. Thus, CP and 45 slant state shows highest and lowest efficiencies in the plot. Low loss RF MEMS switches can be incorporated to increase the total efficiency further.

8.7.5 Radiation Pattern

Co and cross pole patterns for φ=0° and φ=90° planes are measured for multiple frequencies for comparatively wide impedance bandwidth to observe pattern invariance throughout the band. For LP states, the patterns are measured at 5.5GHz/5.8GHz and 5.6GHz/5.8GHz in φ=0° and φ=90° planes respectively, but only 5.8GHz patterns are shown in Fig. 8.14 for brevity. The measured and simulated cross-polarization (X-pol) and front to back ratio (FBR) is observed to be below -20dB and -15dB respectively.

As the impedance bandwidth for 45° slant polarization is about 16%, the pattern is measured for three different frequencies such as 5.6GHz, 5.8GHz and 6GHz respectively at 45° (co-pol) and 135° (X-pol) measured at both principal planes. X-pols are observed to be below -20dB. Due to the symmetry of the structure the simulated and measured RHCP and LHCP found great similarity in both the planes. Also, the X-pol and FBR are found to be less than -18dB. Slight discrepancies in the measured results are predominantly due to fabrication tolerance, noise susceptibility of DC cable from external sources, soldering of diodes and lumped elements which are not identical resulting throughout the fabricated antenna and creates asymmetries in the structure that affects the radiation patterns. The patterns for five distinct polarization states are plotted in the subsequent figure at 5.8GHz.

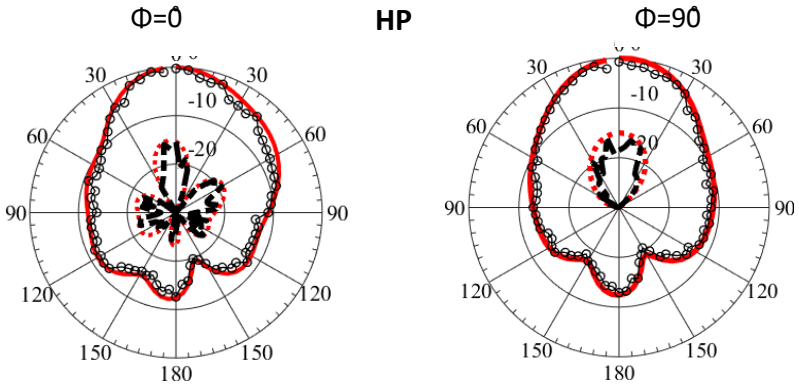

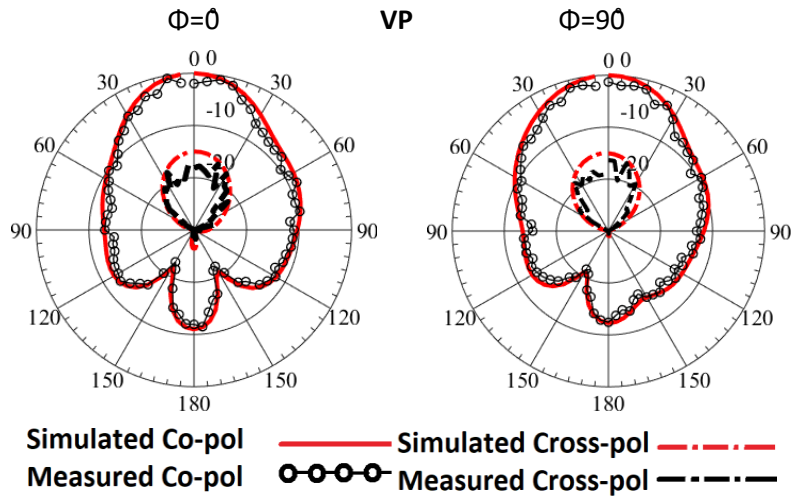
Φ=0̊
VP
Φ=90̊
0 0
30
-10
-20
60
90
120
150
180
Simulated Co-pol
Measured Co-pol
Simulated Cross-pol
Measured Cross-pol

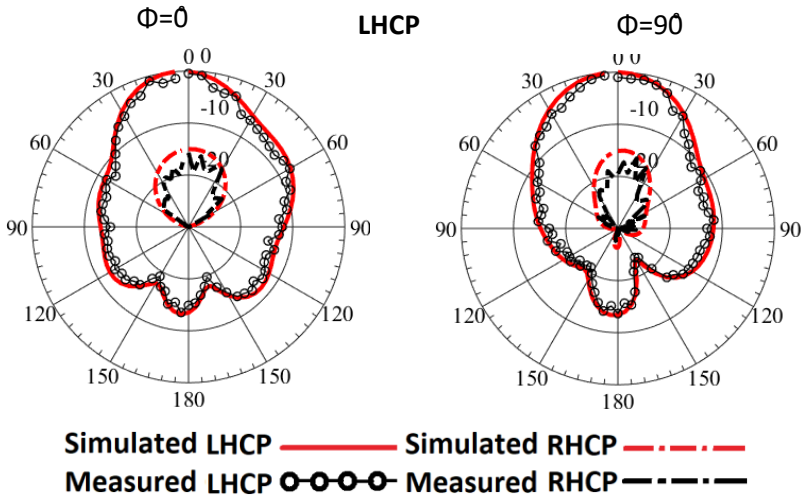
Φ=0̊
LHCP
Φ=90̊
0 0
30
-10
-20
60
90
120
150
180
Simulated LHCP
Measured LHCP
Simulated RHCP
Measured RHCP

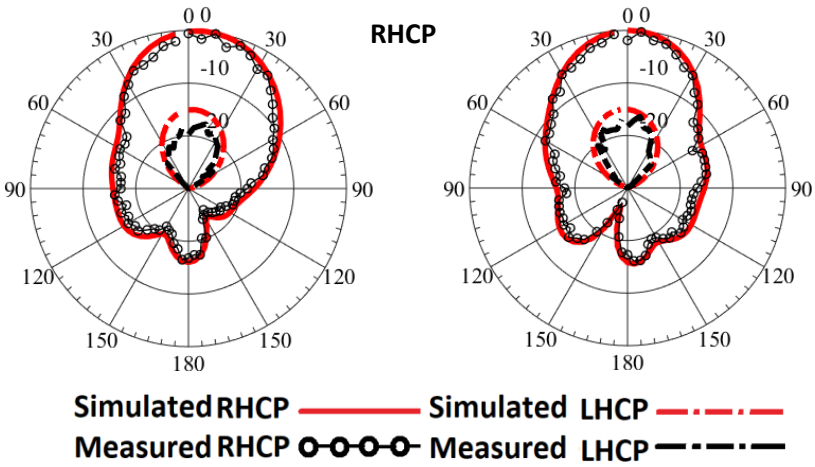
RHCP
0 0
30
-10
-20
60
90
120
150
180
Simulated RHCP
Measured RHCP
Simulated LHCP
Measured LHCP

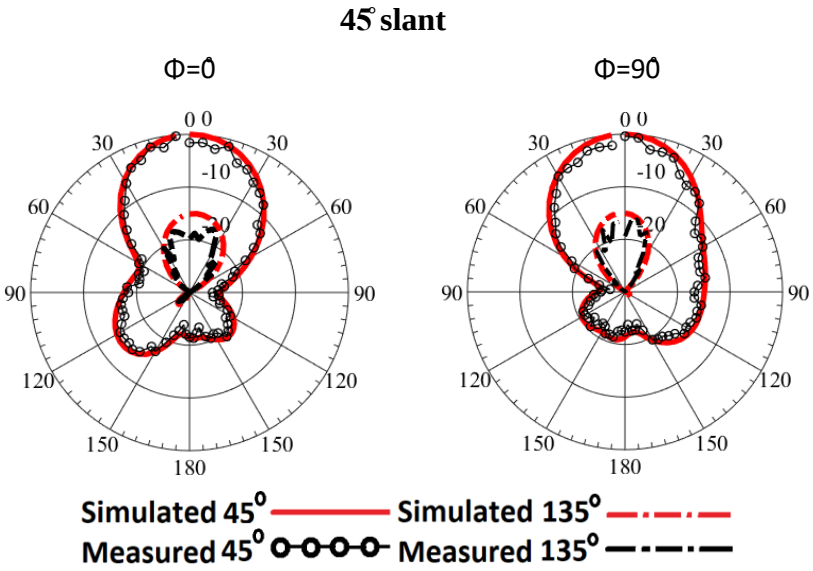

Fig. 8.14 Simulated and Measured Co-pol and cross-pol radiation pattern for all polarization states at φ=0° and φ=90° plane at 5.8GHz.

TABLE 8.4: SIMULATED AND MEASURED RESULTS OF DIFFERENT ANTENNA PARAMETERS AT PENTA-POLARIZATION STATES

Polarization States	Impedance BW (-10dB) (GHz) f1-f2/%		Axial Ratio BW (3dB) (GHz) f1-f2/%		Realized Gain at 5.8GHz at φ = 0°, θ= 0°		Antenna Efficiency
	Sim	Meas	Sim	Meas	Sim	Meas	Sim
HP	5.26-6.15/15.34	5.2-6.05/14.65	Na	Na	11.32	10.02	85
VP	5.3-6.2/15.5	5.22-5.92/12	Na	Na	11.02	10	82
45	5.16-6.52/23.4	5.45-6.45/17.2	Na	Na	10.8	10.3	78
RHCP	5.46-6.18/12.4	5.45-6/9/4	5.62-5.925/4	5.66-5.918/4.4	10.87	10.11	89
LHCP	5.32-6.13/14	5.3-6.07/13.3	5.69-5.921/3.98	5.602-5.83/3.93	10.1	9.9	91

Sim: Simulation, Meas: Measurement Result

8.8 Equivalent Circuit Model

Equivalent circuit models for RHCP, HP and 45° slant polarization stats are shown in Fig. 8.15(a-c). Models depict the coexistence of multiple higher order resonances along with TM_{03}. The frequency behavior of MSA can be modeled by parallel resonant circuit [7]. Its fundamental electrical parameters i.e., resistance, inductance and capacitance values for multiple modes can be computed from the knowledge of corresponding resonant frequencies (f_0) and quality factors (Q). In this study, the resistance at resonances is extracted from the full wave simulation while the inductance (L_{MSA}) and capacitance (C_{MSA}) of the antenna are calculated as below.

$$L_{MSA} = \frac{R}{\omega_0 Q} \qquad C_{MSA} = \frac{1}{\omega_0^2 L_{MSA}}$$

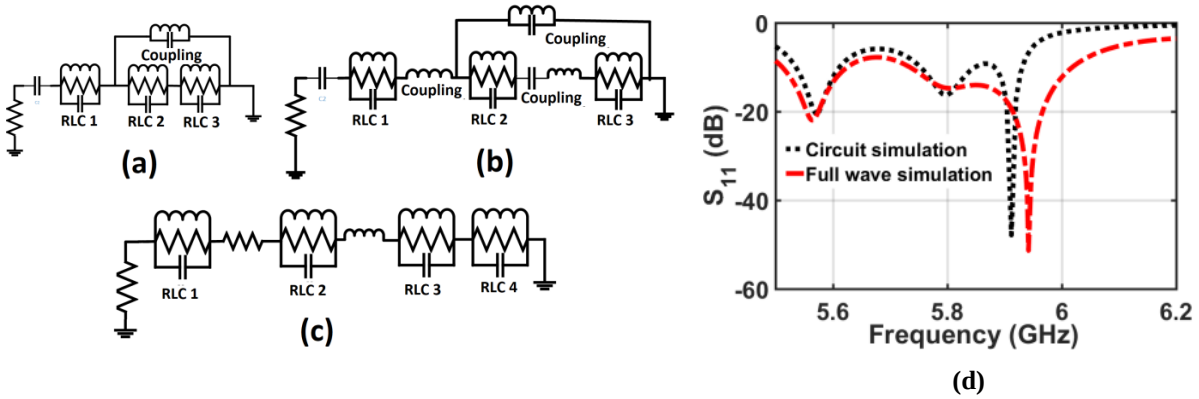

Fig. 8.15 Equivalent Circuit Model for (a) RHCP, (b) HP, (c) 45° Slant states, and (d) comparison between Full-wave and circuit simulation for RHCP

Fig. 8.15(a) shows RHCP mode equivalent circuit. It depicts the coexistence of three higher order resonances. Modes at higher frequencies are coupled inductively. For LP states the resonance modes are inductively and capacitively coupled as shown in Fig. 8.15(b) which increases the impedance bandwidth. Four distinct resonance modes are observed at 45° slant polarization within 5.2 to 6.2GHz band presented in Fig. 8.15(c). Comparison between full wave simulation and circuit simulation is shown in Fig. 8.15(d). Due to antenna symmetry other CP and LP states depicts similar models hence not shown for brevity.

8.9 Comparison and Discussion

A comparative study of the basic antenna parameters of recently published polarization agile antennas in the literature with the proposed work is presented in Table 8.5. In [21], a 2×2 tri-polarized reconfigurable array with multilayer SIW feed is presented. The design antenna array shows significantly large footprint area with three substrate layers. A dual feed multilayer high profile low gain tri-polarized antenna is proposed in [22]. In [23] low gain high profile multilayer complex structure with 12 diodes is presented for quad-polarization applications. A

multilayer high-profile quad-polarized antenna is shown in [26]. A tri-polarized multilayer structure with exceedingly large footprint area with 16 diodes is illustrated in [27].

Probably a single multilayer meta-surface inspired bulky antenna with 15 diodes for penta-polarization application is prescribed for the first time in the literature. It is observed in the literature that most of the recently proposed designs are having noticeable concerns such as complex feed network, multiple SMA feed, multilayer bulky structures, complex and asymmetric design which will find difficulties in practical and industrial implementations. In conjunction, we have proposed a high gain (due to higher order mode) single feed, single layer with exceedingly low profile (0.01λ) planar compact structure with reconfigurable penta-polarization antenna for the first time in the literature.

TABLE 8.5: COMPARATIVE STUDY OF RECENTLY PROPOSED ANTENNAS WITH OUR WORK

Ref.	f_0(GHz)	Pol. states (each)	Substrate layers	No. of Diodes	% Imp. BW	Footprint Area (λ_0^2)	Antenna Height, λ_0	Peak Gain
[11] 2×2array	3.5	3	3	3	10(LP) 18(CP)	1.65×2.05	0.25	14.7(LP) 14(CP)
[12]	2.45	3	single	4	33.9	0.79 × 1.05	0.21	8.2
[13]	3.9	3	single	2	18.4(CP) 8.7(LP)	1.6 Circular patch	0.08	10.6
[14]	5.8	3	2	4	7.1	0.56×0.56	0.037	6.63
[15]	2.2	4	2	12	28	0.3 Circular patch	0.1	1.9
[16]	3.5	4	3	6	53	0.92×0.92	0.1	10.9
[17]	2.55	3	2	16	1.6	3×3	0.3	9.6
[18]	2.45	4	2	8	9.5	0.57×0.57	0.06	7.7
[19]	1	4	2	6	2.5,5.8	0.7×0.4	0.02	7.6
[10]	5.2	5	2	15	28	1.21×1.21	0.06	8.2
This Work	5.8	5	single	6	14-23(LP, CP)	1.1×1.1	0.01	10.3

8.10 Conclusion

Co-channel and ISI issues are the most common adverse effects that degrade the quality of received signals and it would be multiplied further in upcoming UDN environment in 5G ecosystem. Hence an antenna perspective approach would provide additional degree of freedom to the system designer along with signal processing and communication front to mitigate these

issues. A compact single layer single feed high gain penta-polarization agile microstrip antenna excited at higher order broadside mode to attain higher gain is proposed. Subsequently a prototype antenna operates at 5.8GHz WLAN band is fabricated and measured with satisfactory results. This design approach also provides insight into the behavior of the circuit in terms of resonance frequency which would be useful to translate the structure at other frequency bands for diverse applications. With significantly larger gain, the proposed antenna high power transmission efficiencies in coming time which is one of the major advantages of 5G architecture.

References

[1] Y. K. Jang and J. D. Villasenor, "SINR improvement through reconfigurable antenna adaptation to handheld device orientation," 2010 IEEE Antennas and Propagation Society International Symposium, 2010, pp. 1-4, doi: 10.1109/APS.2010.5561233.

[2] T. A. H. Bressner, M. N. Johansson, A. B. Smolders and U. Johannsen, "High-Gain Lens-Horn Antennas for Energy-Efficient 5G Millimeter-Wave Communication Infrastructure," in IEEE Transactions on Antennas and Propagation, vol. 70, no. 5, pp. 3183-3194, May 2022, doi: 10.1109/TAP.2021.3137252.

[3] Dandanov, N., Al-Shatri, H., Klein, A. et al. Dynamic Self-Optimization of the Antenna Tilt for Best Trade-off Between Coverage and Capacity in Mobile Networks. Wireless Pers Communication 92, 251–278 (2017). https://doi.org/10.1007/s11277-016-3849-9

[4] Q. Umar Khan, M. Bin Ihsan, D. Fazal, F. Mumtaz Malik, S. Amin Sheikh and M. Salman, "Higher Order Modes: A Solution for High Gain, Wide Band Patch Antennas for Different Vehicular Applications," in IEEE Transactions on Vehicular Technology, vol. 66, no. 5, pp. 3548-3554, May 2017, doi: 10.1109/TVT.2016.2604004.

[5] Joydeep, Pal & Kaushik, Patra & Gupta, Bhaskar. (2020). A TM 03 mode reduced side lobe high-gain printed antenna array in K band for UDN and IoT applications in 5G. International Journal of RF and Microwave Computer-Aided Engineering.30. 10.1002/mmce.22414.

[6] A. Bhattacharyya, J. Pal, K. Patra and B. Gupta, "Bandwidth-Enhanced Miniaturized Patch Antenna Operating at Higher Order Dual-Mode Resonance Using Modal Analysis," IEEE Antennas and Wireless Propagation Letters, vol. 20, no. 2, pp. 274-278, Feb. 2021,doi: 10.1109/LAWP.2020.3048444.

[7] Ramesh, G., Prakash, B., Inder, B., Apisak., Ittipihoon.: "Circularly polarized microstrip antenna and techniques in microstrip antenna design handbook," Norwood (MA): Artech House; 2001.

[8] Q. U. Khan, D. Fazal and M. bin Ihsan, "Use of Slots to Improve Performance of Patch in Terms of Gain and Sidelobes Reduction," in IEEE Antennas and Wireless Propagation Letters, vol. 14, pp. 422-425, 2015, doi: 10.1109/LAWP.2014.2365588.

[9] https://www.mouser.in/ProductDetail/Broadcom-Avago/HPND-4005

[10] Y. Liu, Q. Wang, Y.Jiaand P. Zhu, "A Frequency- and Polarization-Reconfigurable Slot Antenna Using Liquid Metal," IEEE Transactions on Antennas and Propagation, vol. 68, no. 11, pp. 7630-7635, Nov. 2020,doi: 10.1109/TAP.2020.2993110.

[11] N. Zhu, X. Yang, T. Lou, Q. Cao and S.Gao, "Broadband Polarization-Reconfigurable Slot Antenna and Array With Compact Feed Network," IEEE Antennas and Wireless Propagation Letters, vol. 18, no. 6, pp. 1293-1297, June 2019,doi: 10.1109/LAWP.2019.2915650.

[12] Y. Shi, Y.Cai, X. Zhang and K. Kang, "A Simple Tri-Polarization Reconfigurable Magneto-Electric Dipole Antenna," IEEE Antennas and Wireless Propagation Letters, vol. 17, no. 2, pp. 291-294, Feb. 2018,doi: 10.1109/LAWP.2017.2786945.

[13] Q. Chen, J. Li, G. Yang, B. Cao and Z. Zhang, "A Polarization-Reconfigurable High-Gain Microstrip Antenna," IEEE Transactions on Antennas and Propagation, vol. 67, no. 5, pp. 3461-3466, May 2019,doi: 10.1109/TAP.2019.2902750.

[14] M. Li, Z. Zhang and M. -C. Tang, "A Compact, Low-Profile, Wideband, Electrically Controlled, Tri-Polarization-Reconfigurable Antenna With Quadruple Gap-Coupled Patches," IEEE Transactions on Antennas and Propagation, vol. 68, no. 8, pp. 6395-6400, Aug. 2020,doi: 10.1109/TAP.2020.2970073.

[15] Y. Cui, C. Qi and R. Li, "A Low-Profile Broadband Quad-Polarization Reconfigurable Omnidirectional Antenna," IEEE Transactions on Antennas and Propagation, vol. 67, no. 6, pp. 4178-4183, June 2019,doi: 10.1109/TAP.2019.2905987.

[16] H. H. Tran, N. Nguyen-Trong, T. T. Le, A. M. Abbosh and H. C. Park, "Low-Profile Wideband High-Gain Reconfigurable Antenna With Quad-Polarization Diversity," IEEE Transactions on Antennas and Propagation, vol. 66, no. 7, pp. 3741-3746, July 2018,doi: 10.1109/TAP.2018.2826657.

[17] W. Li et al., "Polarization-Reconfigurable Circularly Polarized Planar Antenna Using Switchable Polarizer," IEEE Transactions on Antennas and Propagation, vol. 65, no. 9, pp. 4470-4477, Sept. 2017,doi: 10.1109/TAP.2017.2730240.

[18] L. Kang, H. Li, B. Tang, X. Wang and J. Zhou, "Quad-Polarization-Reconfigurable Antenna With a Compact and Switchable Feed," IEEE Antennas and Wireless Propagation Letters, vol. 20, no. 4, pp. 548-552, April 2021,doi: 10.1109/LAWP.2021.3056549.

[19] H. Sun and Z. Pan, "Design of a Quad-Polarization-Agile Antenna Using a Switchable Impedance Converter," IEEE Antennas and Wireless Propagation Letters, vol. 18, no. 2, pp. 269-273, Feb. 2019,doi: 10.1109/LAWP.2018.2888843.

Chapter 9
Frequency and Pattern Reconfigurable Planar Antenna

9.1 Introduction

The trajectory of technological progress in the communication front is advancing at an extremely rapid pace, particularly in the wireless domain. It is emerging as one of the possible frontends in existing and upcoming 5G ecosystem to cater diverse multi facet advanced applications. In such scenarios, compact high gain multifunctional antennas are becoming highly desirable, which can dynamically modify antenna parameters such as operating frequency, polarization and pattern to achieve functional diversities [1]. Several interesting concepts have been proposed so far in the literature for single and multi-functional antennas [2-5]. With continuous deployment of innumerable RF nodes in close proximity in the impending heterogeneous network, multipath and Signal to Interference and Noise Ratio (SINR) has emerged as the most complicated concerns [6]. Alongside, high gain beam steerable antennas can provide a proficient way to alleviate the multi-path fading and increase SINR by aligning the high-power beam toward the direction of intended receiver; hence shunts out the interference and noise sources which results in higher SINR, larger diversity gain and improved data throughput in the network [7]. Researchers in the literature have largely focused on designing advanced multi-functional antennas specifically for frequency and pattern reconfigurable applications using different techniques. Those techniques are discussed in detail in the literature review chapter.

Therefore, in a nutshell most of the previously proposed antennas or antenna arrays depict multilayer high-profile structures with significantly large footprint area and low gain. Also, the proposed antennas are operated with complex feeding and biasing network.

In this chapter an approach has been to address those very issues. The chapter deals with the investigation of a very low profile TM_{03} mode 2D planar array with frequency and pattern reconfigurable functionalities.

The key advantages and novelty of the proposed array are outlined as below.

1) There is very little literature available for compact single layered single feed high gain miniaturized planar array with continuous frequency and 2-D beam scanning capabilities. In this chapter a single-layered, single feed, low profile (<0.01λ) miniaturized 2×2 planar MSA array operating at TM_{03} mode is studied to achieve significantly higher gain with continuous frequency tuning and beam scanning functionality.

2) The proposed array is designed using miniaturized patch elements (the resonant length of the patch is tactfully reduced by 22%); hence the overall footprint of the array is reduced remarkably. Also, the array is excited using a simple and single feeding structure; thus, it can be easily interfaced with transceiver systems.

3) The proposed antenna is scalable hence can be designed in other frequencies for different 5G applications. The antenna is principally aimed at mitigating the problem of low SINR, co-channel and intersystem interference in present day heterogeneous and ultra-dense wireless architecture.

Thus, the design simplicity, compactness and ease of fabrication along with optimum performance make the proposed multifunctional antenna very suitable for upcoming heterogeneous network architecture.

9.2 Antenna Design Theory

9.2.1 Analysis of Higher Order Mode MSA

The radiating edges of a patch antenna operating in TM_{0n} or TM_{n0} modes are n×λ/2 apart along the patch length and radiates like n×λ/2 length dipole (λ is the wavelength of TM_{0n} mode). Contrarily, Side lobes in the pattern vary in numbers and amplitude depending upon the modal indices. Large magnitude of the SLL can be attributed to the existence of λ/2 out of phase current between in-phase λ/2 current strips on the patch surface as illustrated in Fig. 9.1 & Fig. 9.2 (cited from the previous chapter) for TM_{03} and TM_{05} mode respectively. This phenomenon can also be analyzed as the array of two radiating apertures n×λ/2 apart along the patch length. Subsequently, the number of side lobes in the E-plane is primarily due to the array factor formed by these hypothetical radiators. From cavity model analysis it is observed that equivalent magnetic current ($\vec{M}$) at the radiating edges are equal and out of phase for even modal index n

and hence they cancel out the far-field radiation placing null in the broadside direction. Conversely, for odd n, broadside far-field radiation is combined. Hence TM_{0n} modes with odd n radiate in the broadside direction providing significantly higher gain at the expense of higher SLL and larger aperture area.

As an example, TM_{03} and TM_{05} modes are analyzed further. It is noted that $\vec{M}$ in the radiating and non-radiating edges are aligned in-phase and out of phase respectively as shown in Fig. 9.1(c) which results in addition of far filed radiation in the broadside direction with significantly large SLL as depicted in Fig. 9.2(a).

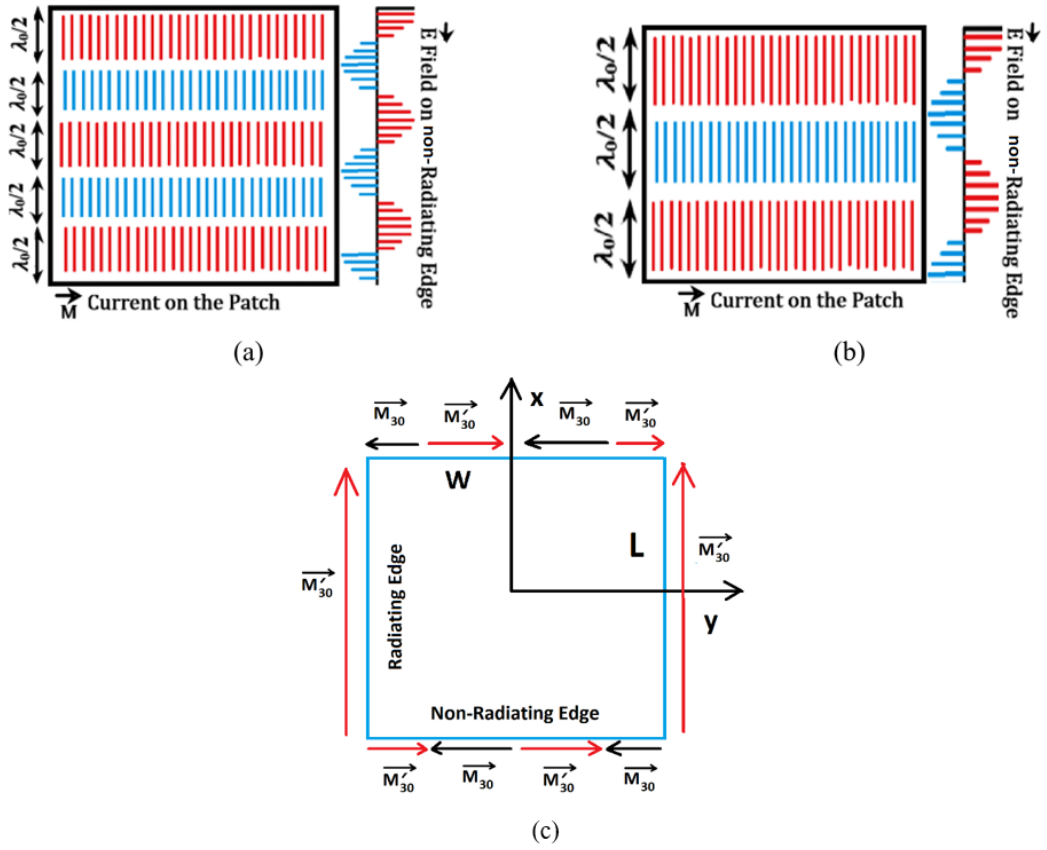

Fig. 9.1 Surface current on the patch antenna with red and blue lines indicate $\lambda/2$ opposite directed current strips and E filed on the non-radiating edge of the patch in (a) TM_{05}, (b) TM_{03} mode operation, and (c) TM_{03} mode equivalent magnetic currents ($\vec{M}$) at patch edges with red and black arrows indicate opposite directed currents.

9.2.2 SLL reduction of Higher Order MSA

Consecutive $\lambda/2$ sections on the patch surface are having oppositely directed current generating the side lobes at TM_{0n} modes. These $\lambda/2$ sections are removed to make the current

distribution unidirectional, similar to that of the fundamental mode, hence reducing the SLL with the expense of slightly reduced gain due to reduced aperture area. Out of phase $\lambda/2$ section (at the centre on the patch) in TM_{03} mode and alternate $\lambda/2$ sections in case of TM_{05} mode are removed partially to reduce the SLL significantly as shown in Fig. 9.2(b). It is observed that SLL in both the planes are reducing gradually with the increase of slot length. SLL for $\lambda/2\times$ (W-2) mm^2 slot area is observed less than -20dB at φ=0º and φ=90º planes, as shown in Fig. 9.3.

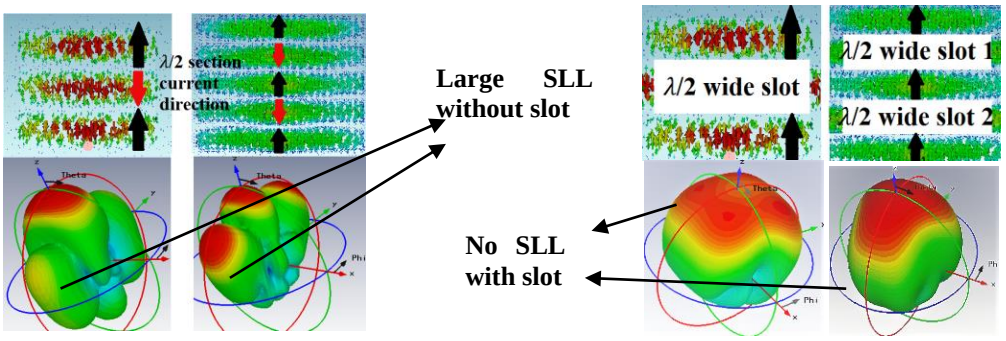

Fig. 9.2 Surface current distribution and corresponding radiation pattern for TM_{03} and TM_{05} mode MSA (a) With complete patch and (b) With $\lambda/2$ slots at out of phase current strips

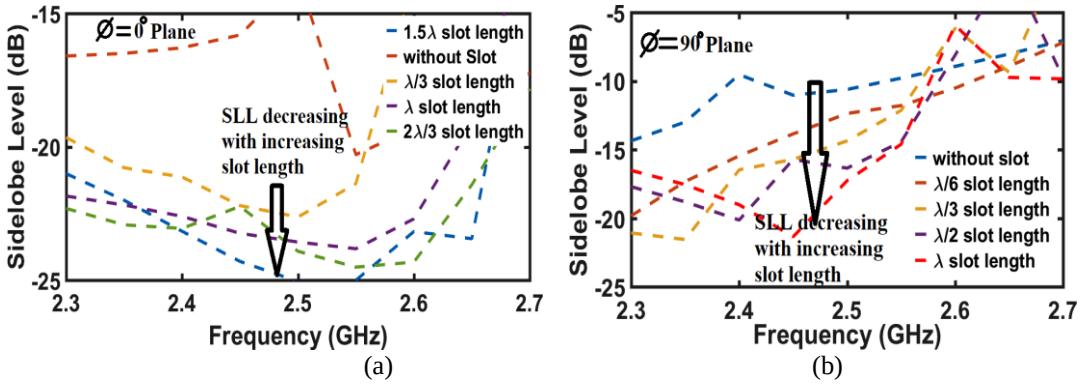

Fig. 9.3 SLL at (a) φ=0° & (b) 90° plane for varying slot lengths for TM_{03}

9.2.3 Effect of slot on input impedance

It is established that for fundamental resonance the input impedance decreases as the length of the slot increases and vice-versa [8]. Similar trend is also observed for TM_{0n} modes. The real part of the input impedances is reduced from 100Ω to 50Ω as the slot length varies from $\lambda/6$ to 1.5λ as shown in Fig. 9.4 and hence improves the impedance matching. It is also

interesting to note that the slot behaves differently to other non-broadside radiating modes. As an illustration, TM_{22} mode resides adjacent to TM_{03} is impacted inversely. The increasing slot length perturbs the current traversing path of TM_{22} mode largely and shifts the resonance towards higher frequencies along with increase in input impedances is observed as shown in the Fig. 9.4. Though from cavity model analysis it is noted that TM_{22} mode has small modal significance and hence it has least adverse effect on the intended mode (TM_{03}).

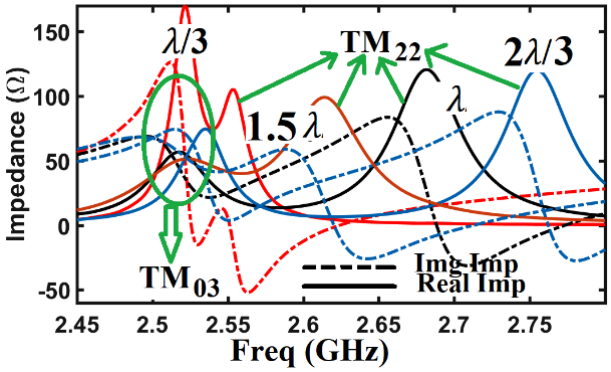

Fig. 9.4 Impact of varying slot length on $Re[Z_{in}]$ for TM_{03} mode patch

9.2.4 Effect of slot on Antenna gain

As a result of varying the slot area, the resonance frequencies are shifted slightly, reducing gain both at the designed frequency and at the shifted resonances. Fig. 9.5 shows the realized gains at 2.45GHz for varying slot lengths across the patch width in TM_{03} and TM_{05} modes reduce gradually. It is also noted that the gain of those modes (shifted to lower resonance frequencies due to increased slot area) are reduced due to the reduced aperture area.

Antenna efficiency increases at a specific frequency as the length of the slot increases. This is attributed due to the decrease in dielectric and conduction losses with increase in slot aperture.

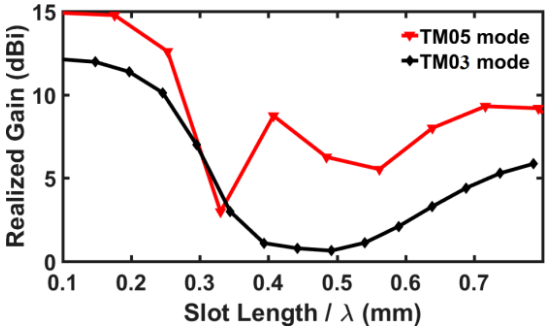

Fig. 9.5 Realized Gain for varying slot length of TM_{03} and TM_{05} mode

9.2.5 TM_{03} Mode MSA Miniaturization Mechanism

As discussed in previous section, the SLL of the TM_{03} mode is reduced significantly by removing the central portion of the patch (λ/2 wide). This essentially prevents the excitation of the out of phase current strip at the center of the patch leaving the other unidirectional current strips unperturbed. This configuration performs similar to an array of two in-phase current strips separated by λ/2, as shown in Fig. 9.6(b). Three thin λ/2 linkages carrying out-of-phase currents (with respect to two edge strips) are placed between the two strips to sustain the original current distribution on the structure. In the Autor's other work [9], the linkages are meandered maintaining the actual length (λ/2) and symmetricity of the structure, which essentially decrease the effective radiating length of the patch by λ/4 as shown in the Fig. 9.6(c), hence reduces the overall footprint area by 16%. The patch is miniaturized further by incorporating parabolic shaped λ/2 linkages between the outer λ/2 sections and reduces the non-radiating edge length by λ/3; thus miniaturized the footprint by 22% as illustrated in the Fig. 9.6(d).

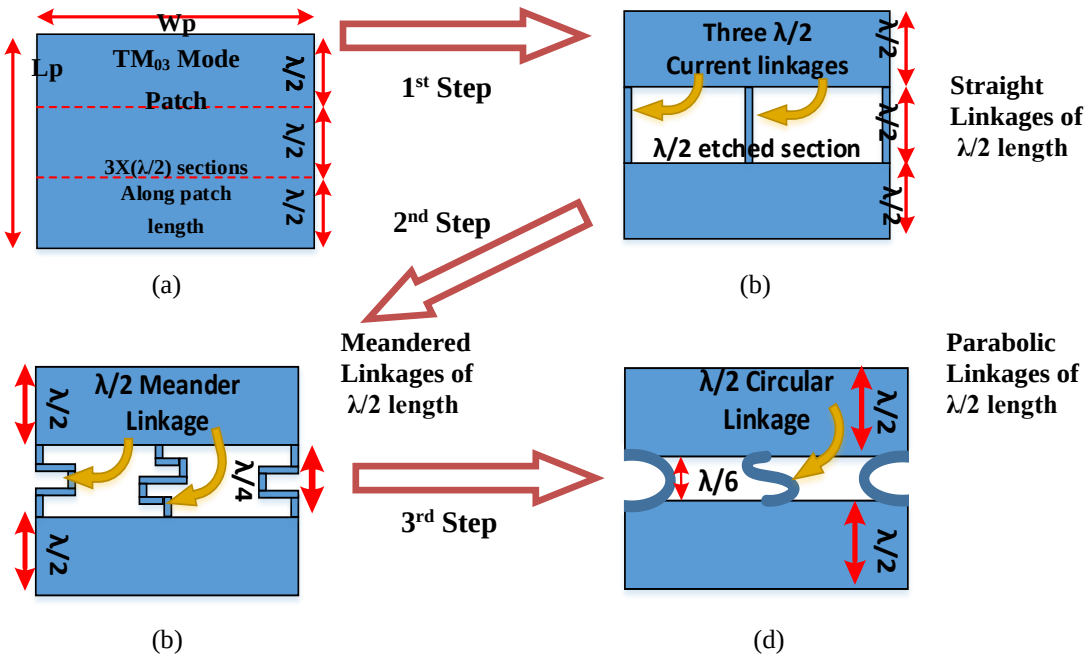

Fig. 9.6 Evolution of the miniaturized MSA element operating in TM_{03} mode (a) complete Patch, (b) $\lambda/2$ center etched patch with three straight $\lambda/2$ linkages, (c) miniaturized Patch with $\lambda/4$ meander linkage and (d) Further miniaturization with $\lambda/6$ curve linkages

Further reduction in area is possible but the overall antenna performance will be compromised due to the coupling between closely spaced upper and lower λ/2 current strips. The curved linkages reduce the unintended radiation as in the case of meandered linkages the edge radiation is high due to sharp bending; hence curve linkages increase the radiation efficiency and consequently the realized gain.

9.2.6. Effect of MSA element miniaturization on antenna parameters

I. Input impedance and resonance

TM_{03} mode resonance for the elements with straight [Fig. 9.6(b], curve [Fig. 9.6(d)] linkage and complete patch [Fig. 9.6(a)] are observed to be localized around 2.6GHz as depicted in the Fig. 9.7. The resonances remain fixed as the resonant lengths are kept same using λ/2 curve and straight linkages while minimizing the overall physical area. As the width of the slot reduces the real part of the input impedance also decreases as observed in the Fig. 9.7. An important observation is that only for meandered linkages [Fig. 9.6(c)] the TM_{03} mode resonance is shifted significantly towards lower frequency value. This is attributed to the coexistence of multiple sharp bending in the meander linkages that increases the overall electrical length of the patch and subsequently the current path shifts the resonance towards the lower frequency value.

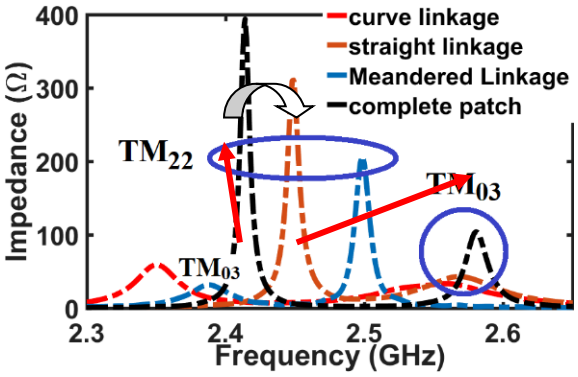

Fig. 9.7 Input impedances for different patch elements with straight, meandered and curve λ/2 linkages along with non-etched patch.

II. Antenna Gain and total antenna Efficiency (η %)

With the increase of the slot area the conduction and dielectric loss is reduced hence the η is increased compared to the patch without slot as shown in the Fig. 9.8. It is also noted that in

case of meandered linkage η reduces significantly despite of having wide center slot. This reverse phenomenon can be analyzed due to the radiation losses from the multiple sharp bending of the meander linkages. Contrarily, the element with curved linkage exhibits largest η due to least radiation loss. The directivity of all the elements reduces due to the slot which reduces the antenna aperture. Thus, maximum directivity is noted for the complete patch element [Fig. 9.6(a)], while element with meandered linkage shows minimum directivity as shown in the figure.

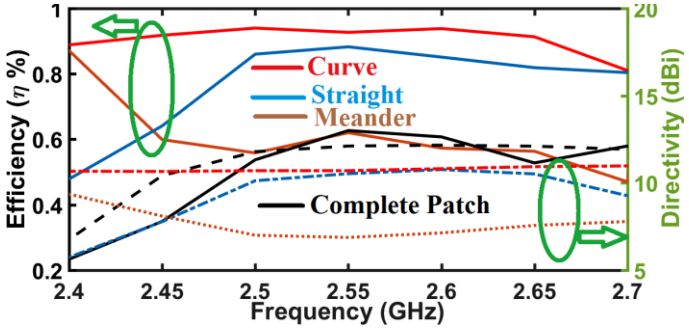

Fig. 9.8 Directivity and efficiency for different patch elements with straight meandered and curve linkages along with complete patch.

9.3 Array Configuration

A planar 2×2 array is designed using the miniaturized patch elements with curved linkages [Fig. 9.6(d)] operating at TM_{03} mode as shown in Fig. 9.9(a). Coplanar edge feed microstrip lines are used to excite the elements. Impedance of the radiating edges of the array elements are derived from the simulation and found to be (58.4+6.3j) Ω. Subsequently, quarter wave matching sections and T-junction power dividers are used to design the feed network as shown in Fig. 9.9. Consequently, the length and width of the feed lines are parameterized for best possible impedance characteristics. Also, the inter-elemental separation along X and Y axis is adjusted and optimized for optimum radiation characteristics.

9.3.1 Frequency Tuning Mechanism of the 2×2 array

It is well known that the equivalent circuit model of a MSA is a parallel RLC resonator. Thus, the resonant frequency of the MSA can be altered by varying L or C by changing antenna structure or by incorporating external reactive load to the antenna. Hence varactor diodes are

placed at the top radiating edges of the array elements as shown in Fig. 9.9. The capacitance of the diodes is varied by proper biasing, hence allowing the antenna to resonate within a specific tuning range. A hyper-abrupt Junction tuning varactor (model SMV1231 from Skyworks [10]) having low series resistance (2.5Ω) and low phase noise is used in this work. The capacitance varies from 0.466 pF to 2.35 pF applying reverse voltage from 15V to 0V. Nearly 11% frequency tuning about the center frequency (2.45GHz) is simulated using the full swipe of the varactor capacitance as shown in Fig. 9.10(b). It is observed that fundamental mode resonator exhibits larger tuning range in comparison with higher order modes (HOM) as these modes exhibit larger Q values [11].

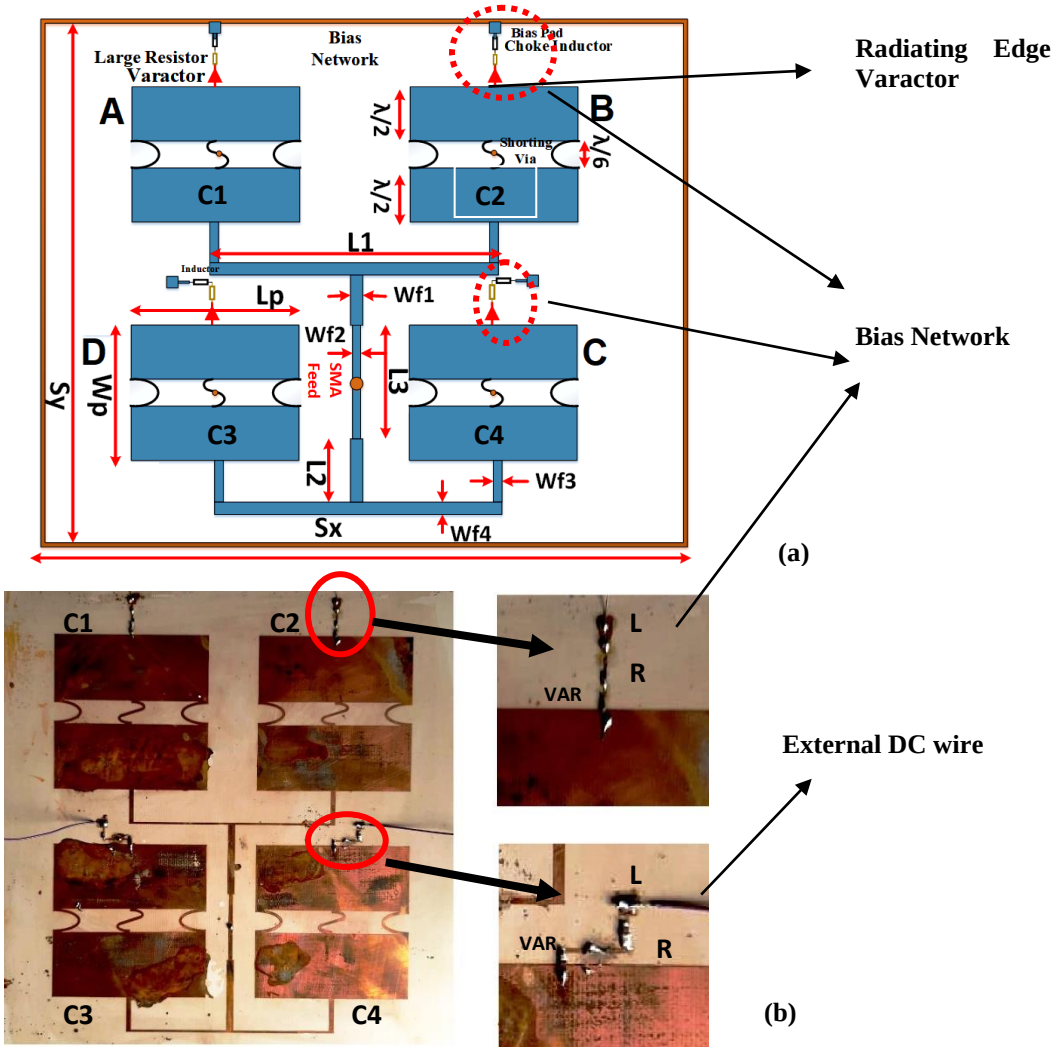

Fig. 9.9 (a)Top view of the designed 2×2 planar array, (b) Fabricated antenna array with biasing network *Array Dimensions: Sx=Sy=200, Lp=84, Wp= 66 , L1=89.58 , L2=30.36 , L3= 28.48 ,Wf1=3, Wf2=1.64, Wf3=1.94, Wf4=0.72(all in mm).* L, R and VAR represent Inductor, Resistor and Varactors respectively.

9.3.2 Pattern Reconfigurable Mechanism

Beam navigation feature is incorporated in the array by integrating relative phase difference between the array elements. Phase difference between the elements is obtained by suitably detuning the varactor capacitance which essentially modifies the effective electrical length by adding reactive load to the individual patch elements.

A specific resonance (f_0) within the tuning range can be attained by properly modifying the varactor capacitance C_0 in all the four elements which radiates in in-phase at broadside direction. By controlling the bias voltage, a slight variation in the capacitance $\pm\delta C$ between the adjacent patches along X or Y coordinates can be achieved thus the elements are slightly detuned with respect to relative phase. Thus, the detuned reactive loads (C+ δC) and (C- δC) provide relative phase difference between the adjacent patches which tilts the main beam towards the element with larger reactive values.

Concurrently, the excitation amplitude remains nearly same. Beam tilt angle is varied further by controlling the reverse bias voltage which varies the detuned capacitance. -10dB reflection coefficient for an arbitrarily chosen varactor capacitance C_0 in all the array elements result in a specific resonance at f_0 as shown in the middle plot of Fig. 9.10(a). The upper and lower plots depict the two extreme cases for detuned varactors $C_0 \pm \delta C$, so that the S_{11} at resonance $f_0 \pm \delta f_0$ is just below the −10 dB reference level as clearly illustrated in Fig. 9.10. Internal filed distributions within the patch elements remain unchanged for $C_0 \pm \delta C$ except relative phase of the fields.

In brief, the beam scanning within the entire frequency sweep can be summarized as follows. Firstly, any specific resonant frequency f_0 is chosen within the tuning range by suitably fixing the capacitance C_0 of all the four varactors using specific reverse bias voltage (V_R). Secondly, the adjacent diodes (as per the requirement of beam tilt at specific φ plane) are detuned gradually and the main beam starts tilting. In this process the resonant frequency shifts towards upper or lower frequencies depending upon the varactor capacitance values such as $C_0+\delta C$ or $C_0-\delta C$. Thus, δC values are changed gradually while maintaining -10dB (S_{11}) value as illustrated in Fig. 9.10(a). The maximum tilt angle is achieved at $C_0 \pm \delta C_{max}$.

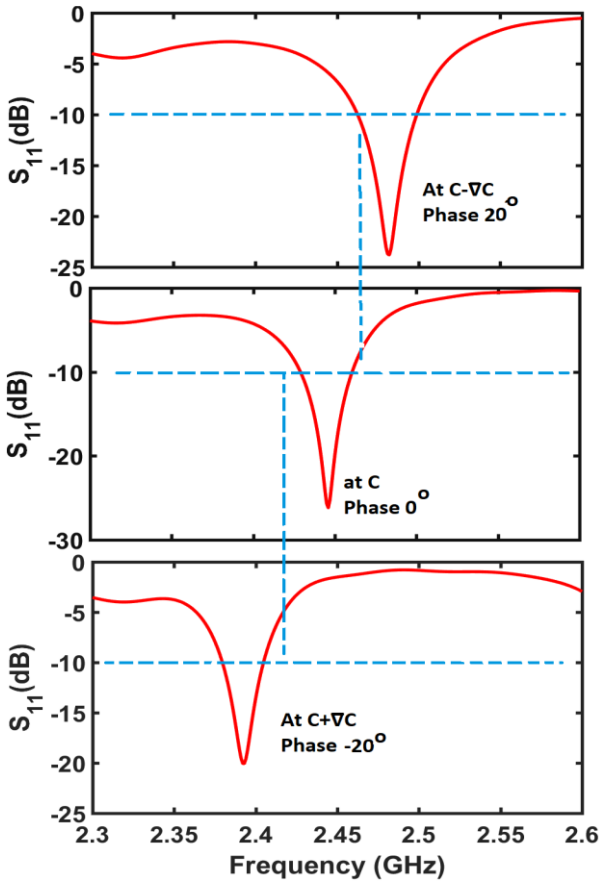

Extreme right of S_{11} maintaining -10 dB matching at varactor C_0-δC

S_{11} maintaining -10 dB matching at resonance f_0 Using varactor C_0

Extreme right of S_{11} maintaining -10 dB matching at varactor C_0+δC

(a)

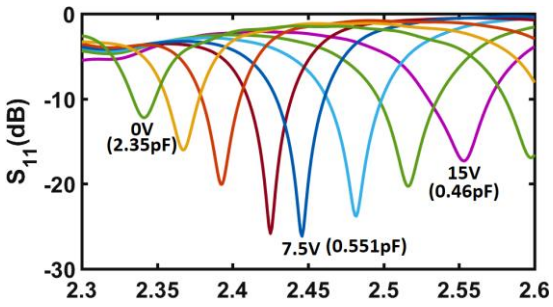

(b)

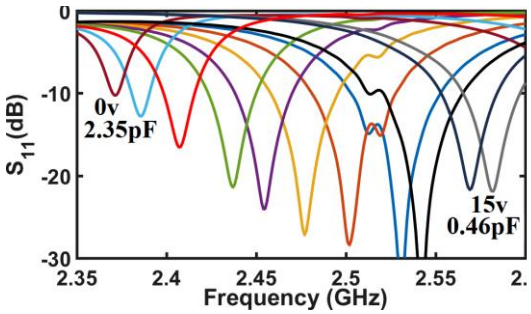

(c)

Fig. 9.10 (a) S_{11} variations for varactor capacitance C_0±δC. The middle graph represents S_{11} for C_0 and the upper/lower graphs are due to C_0- δC and C_0+ δC, S_{11} tuning range for varactor tuning for (b)Simulated and (c) measured S_{11}

9.3.3 2D Beam Scanning mechanisms

As shown in Fig. 9.9, the array elements are arranged along X and Y direction marked as A, B, C and D respectively. Beam scanning at φ=0º plane is achieved by suitably detuning the varactor capacitance in A/C and B/D element pairs along the X axis. Subsequently, scanning at φ=90º plane is realized by detuning in A/B and C/D element pairs along the Y axis. Contrarily, the direction of the pattern can be reversed by swapping the detuned varactor values by toggling the bias voltage. It is also observed that beam switching at φ= ±45º planes can be attained by detuning the diagonal elements of the array such as A/D or B/C element pairs. Subsequently, by detuning any two adjacent diodes with suitable reverse bias voltage, the beam can be tilted at ±θ directions at any φ plane. As an example, the values of four edge varactors are listed in Table 9.1 for main beam directions at different φ planes at 2nd quadrant of the 2D array geometry for maximum θ tilt.

TABLE 9.1: VARACTOR CAPACITANCES (PF) AT FOUR ARRAY ELEMENTS FOR DIFFERENT BEAM DIRECTIONS AT 1ST QUADRANT

C1	C2	C3	C4	Φ plane	θ tilt
2.35	2.35	0.5	0.5	90º	24º
2.35	0.3	0.6	0.5	100º	28º
2.35	0.4	0.8	0.5	110º	28º
2.35	0.5	1.1	0.5	120º	26º
2.35	0.55	1.3	0.5	130º	27º
2.35	0.5	1.7	0.5	140º	27º
2.35	0.45	1.9	0.5	150º	25º
2.35	0.44	2	0.5	160º	25º
2.35	0.47	2.15	0.5	170º	24º
2.35	0.5	2.35	0.5	180º	24º

For complete intuition, a plot of the array with detuned varactors and corresponding radiation pattern is illustrated in Fig. 9.11. The figure depicts the beam steerability at φ= ±45º, 90º, 0º planes. Patterns for other φ variations are not shown for brevity.

Beam scanning angle can be enhanced by reducing the inter-elemental separation between the array elements which subsequently reduce the effective aperture of the array, and hence its directivity. Parametric optimization is performed and found $\lambda_0/2$ spacing yield highest directivity with minimum grating lobes. Maximum achievable scan angle is severely influenced by coupling of radiated energy thru air or surface wave between the array elements which essentially reduces the required phase difference between the array elements. These effects can

be minimized by reducing the Patch width in expense of degraded directivity and impedance matching. A trade-off between optimum beam scanning angle and gain is opted while deriving the patch width. Alternately, coupling through feed network increases the scanning angle if optimized properly since the phase of the associated coupling coefficient can be conveniently controlled by varying the feed length which partly compensate the surface wave or air coupling.

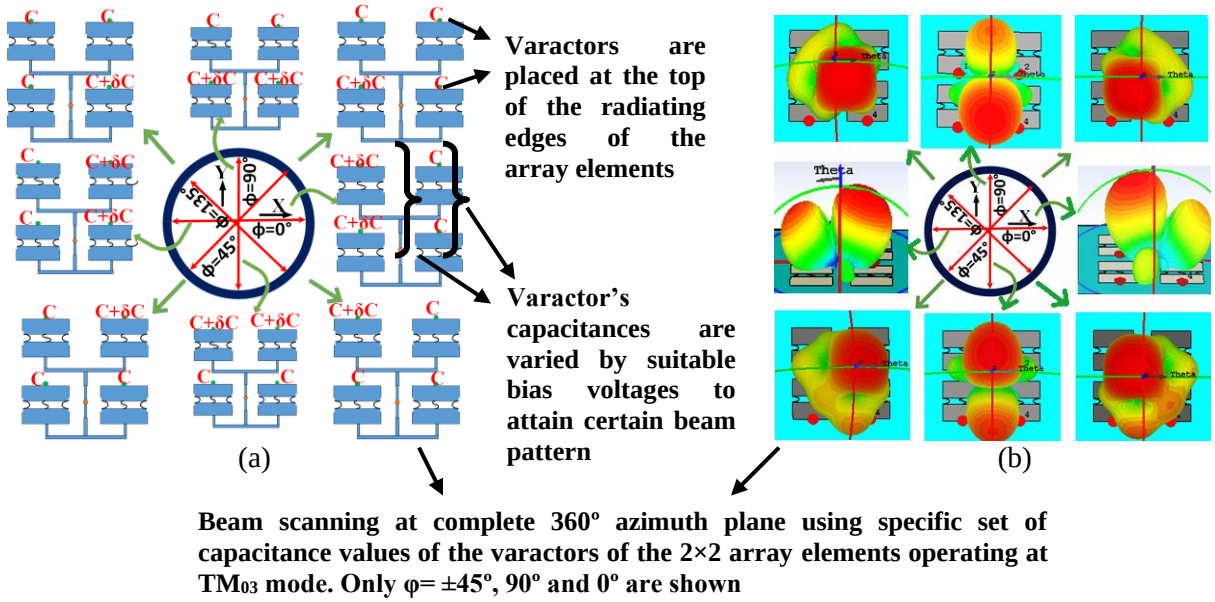

Fig. 9.11 (a) Configuration of radiating edge varactor capacitances at four array elements for main beam scanning at φ= 0°, 90°, ±45° planes and maximum ±θ tilt, (b) 3D radiation pattern at at φ= 0°, 90°, ±45° planes in accordance with the variations of the capacitance

Fig. 9.12 provides a complete illustration of selecting specific capacitance values of the varactor diodes by applying suitable reverse bias to attain specific beam directions in azimuth and elevation plane. Fig. 9.12(a) presents different capacitance values of the varactors of A & C and B & D element pairs for ±θ tilts at φ=0° plane. Subsequently, Fig. 9.12(b) & 9.12(c) illustrates the different capacitance points of different element pairs as circled in the array elements for ±θ tilts at φ=90° & 135° planes. Thus, the elevation of the main beam at any azimuth plane is possible by judiciously choosing the varactor capacitances of the array elements using suitable biasing.

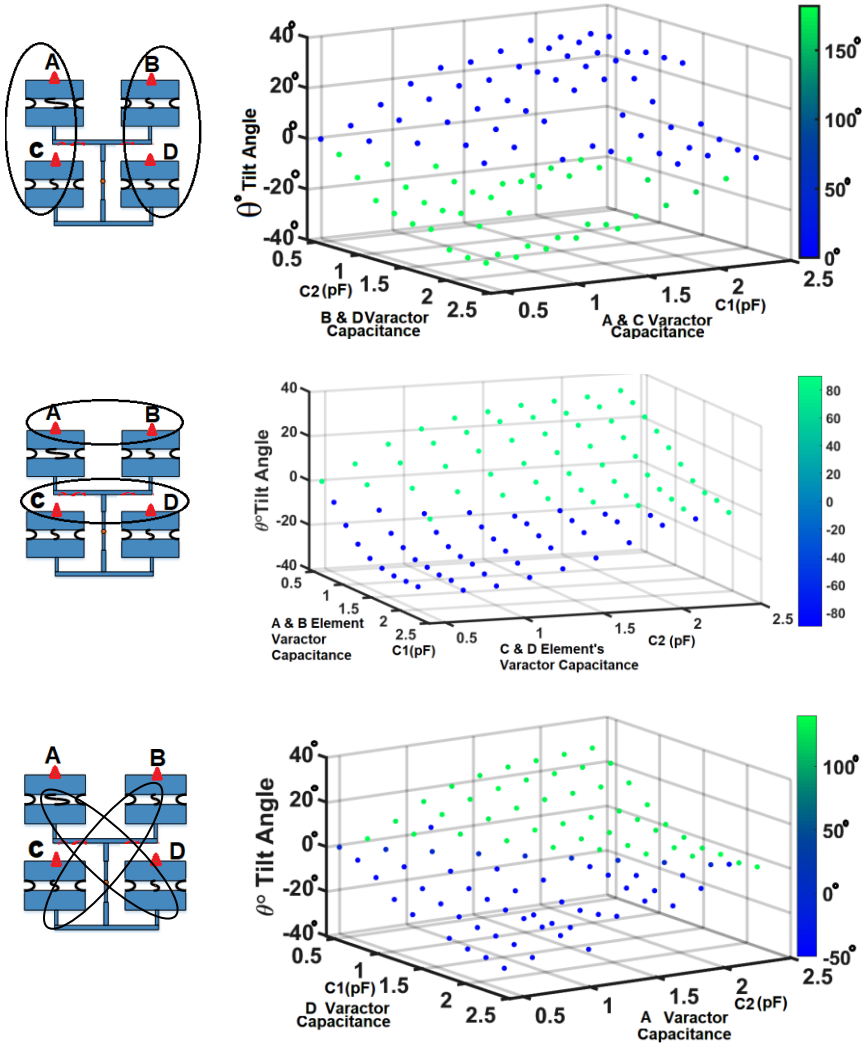

Fig. 9.12 Variation of four varactor capacitances at A, B, C and D array elements to realize beam direction at different Azimuth and elevation planes. (a) Beam direction at φ=0º and θ variation for capacitance values of the radiating edge varactors at A, C and B, D element pair, (b) Beam direction at φ=90º and θ variation for capacitance values of the radiating edge varactors at A, B and C, D element pair and (c) Beam direction at φ=±45º and θ variation for capacitance values of the radiating edge varactors at AD and BC element pair

Fig. 9.13 depicts the simulated normalized polar plots of the patterns at of 2.45 GHz for different tuning conditions of the varactor diodes. Fig. 9.13(a) shows that at any specific resonance within the frequency tuning range the maximum main beam elevation is θ_{max}= ±25º while the maximum tilt at elevation plane is θ_{max}= ±40º considering 3dB beamwidth (taking the HPBW). Also, a complete 360º beam scanning at azimuth plane is realized as shown in Fig.

9.13(b). The far field radiation is linearly polarized (the LP could be horizontal of vertically polarized based on the antenna alignment) with -25dB X-pol components.

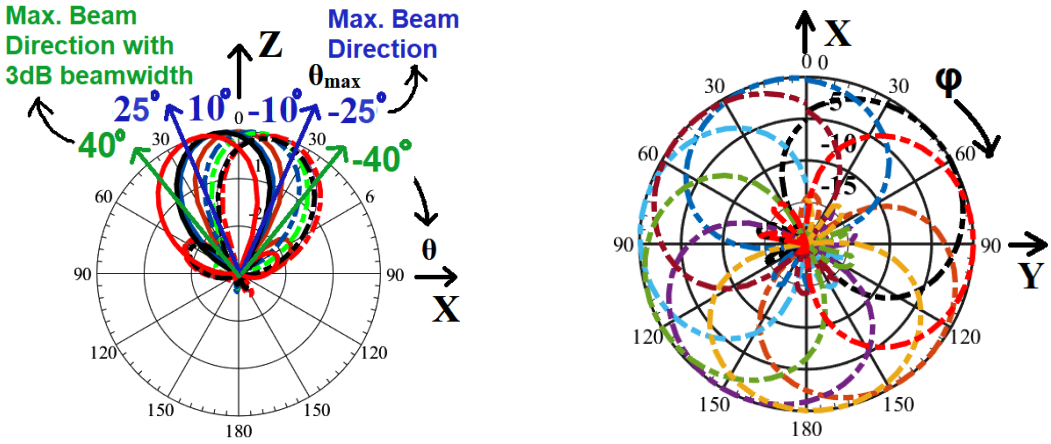

(a) (b)

Fig. 9.13 (a) Maximum Beam direction with and without 3dB beamwidth at elevation plane and (b) 360º scanning at azimuth plane for different capacitance values of the varactor diodes

9.4 Antenna array fabrication and Measurement

A prototype antenna array is designed at 2.45GHz band to validate the proposed theory. CST V.19, a FDTD based hybrid electromagnetic simulation solver tool is used to simulate the design. Roger RO404 substrate having dielectric constant ε_r=3.51, loss tangent $\tan\delta$=0.017 and height h=30mil is used to fabricate the antenna. The complete layout of the simulated antenna and the corresponding fabricated antenna is shown in Fig. 9.9. Series combination of 1 MΩ resistor and 47 nH inductor is used to bias the varactor diodes. Without disturbing the internal fields, a shorting via is placed at the center of each element to provide DC ground along with a 33-pF capacitor for RF continuity. Multiple 0.2mm DC bias lines are designed and are terminated at 0.3×0.3mm^2 bias pads for proper biasing and coupling management as shown in figures. Measurements are conducted in an anechoic chamber using Agilent E5071B VNA.

The SMA feed is covered with RF absorbers to ensure least coupling of external spurious radiation which could cause ripples in the measured pattern. RF choke is used in DC bias lines while aluminum foil is used to cover the external bias lines along with the DC supply to prevent external RF noise. Slight discrepancies in the measured results can be attributed to many factors such as improper soldering and non-identical lumped elements which misaligned the symmetric

nature of the structure. Parasitic effects of the diodes and incorporating simple circuit model of the varactor diode in the simulation environment also offset the measured results.

9.4.1 Reflection co-efficient (S_{11})

Simulated and measured frequency tuning for different reverse bias conditions along with corresponding varactor capacitances are shown in Fig. 9.10. Approximately 10 % tuning range is measured form 2.35GHz to 2.6GHz with slight shift towards higher frequencies. The reasons for slight discrepancies in the results are already discussed. As the sensitivity at TM_{03} mode is quite high hence the 10dB frequency tuning range is comparatively less with respect to fundamental resonance.

9.4.2 Antenna Efficiencies (η)

Antenna efficiency reduces with the internal reactance of the tuning devices. Thus, with increasing varactor capacitance larger current drifts thru the diodes exhibiting higher loss; hence antenna efficiency gradually reduces towards the lower frequency range due to larger varactor load. Fig. 9.14 shows that efficiency decreases from 82% to 58% as the varactor capacitance increases from 0.466-pF to 2.35-pF with decreasing reverse bias voltage from 15v to 0v. The varactors used in the design are having large package parasitic capacitance and insertion loss. Also, lossy substrate (tan δ=0.017) is used to fabricate the design introduces further conduction and dielectric loss that reduces the overall antenna efficiency. However, antenna efficiency can be improved by incorporating low loss varactors and low loss substrate in the design.

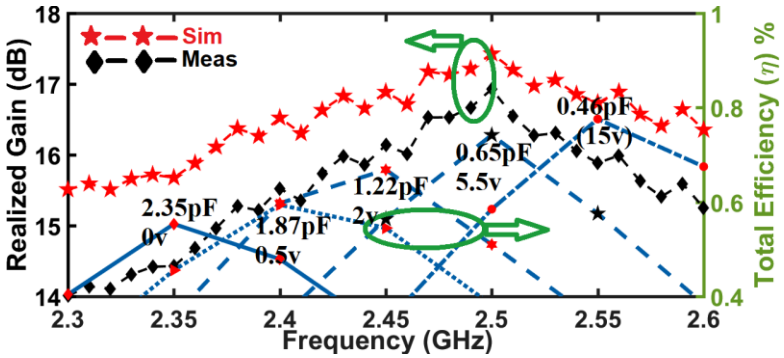

Fig. 9.14 Realized Gain and antenna efficiencies at broadside direction

9.4.3 Realized Gain

Fig. 9.14 shows the simulated and measured realized gain in different frequencies at broadside direction for varying varactor capacitances. Maximum 17.3dB realized gain is measured at 2.5GHz and the value is gradually reduced in the lower frequencies as antenna efficiency is also reduced gradually. Gain at three distinct frequency points within the tuning range (2.35GHz, 2.45GHz and 2.55GHz) is depicted in Fig. 9.15 for varying beam directions. It is discussed that to increase the tilt angle of the main beam the varactor capacitances need to detune further; correspondingly the realized gain reduces progressively due to degraded antenna efficiencies which is clearly portrayed in Fig. 9.15. It is observed that at higher resonance (2.55GHz) the gain is comparatively high due to larger efficiency as shown in Fig. 9.14. In any specific frequency within the tuning range, the measured gain is found to vary between 14dBi to 17.5dBi as the beam scans between θ= ±40º angle (including 3dB HPBW). The measured gains are reduced slightly due to dielectric, conduction, diode, and other lumped element losses.

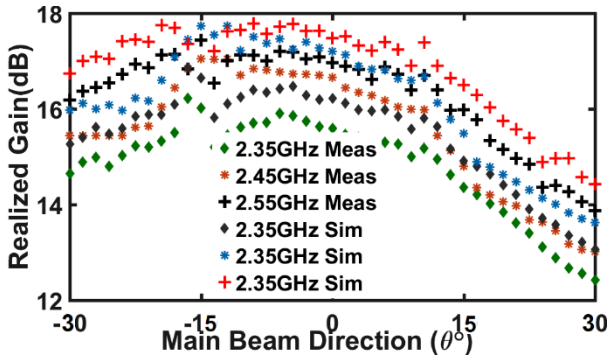

Fig. 9.15 Realized gain at 2.35GHz, 2.45GHz and 2.55GHz for varying main beam directions.

9.4.4 Radiation Pattern

The simulated and measured normalized radiation pattern at φ= 0º, 30º, 45º and 90º planes are shown in Fig. 9.17 for 2.45GHz and 2.55GHz respectively in both the principal planes. Patterns for other φ planes and frequencies are not shown for brevity. SLL and X-pol values are below -15dB and -20dB in both principal planes as illustrated in the figure. It is observed that SLL and X-pol levels increase slightly with increasing tilt angle and noted below -

12dB & -18dB in both principal planes which are still below the acceptable level as shown in the pattern plots.

In all φ planes maximum ±25º main beam scan angles (θ tilt) and ±40º beam tilt considering 3dB Half Power Beamwidths (HPBW) are measured as shown in Fig. 9.16. Direction of maximum radiation along the elevation plane in higher order modes are slightly reduced in comparison with fundamental mode due to higher Q value.

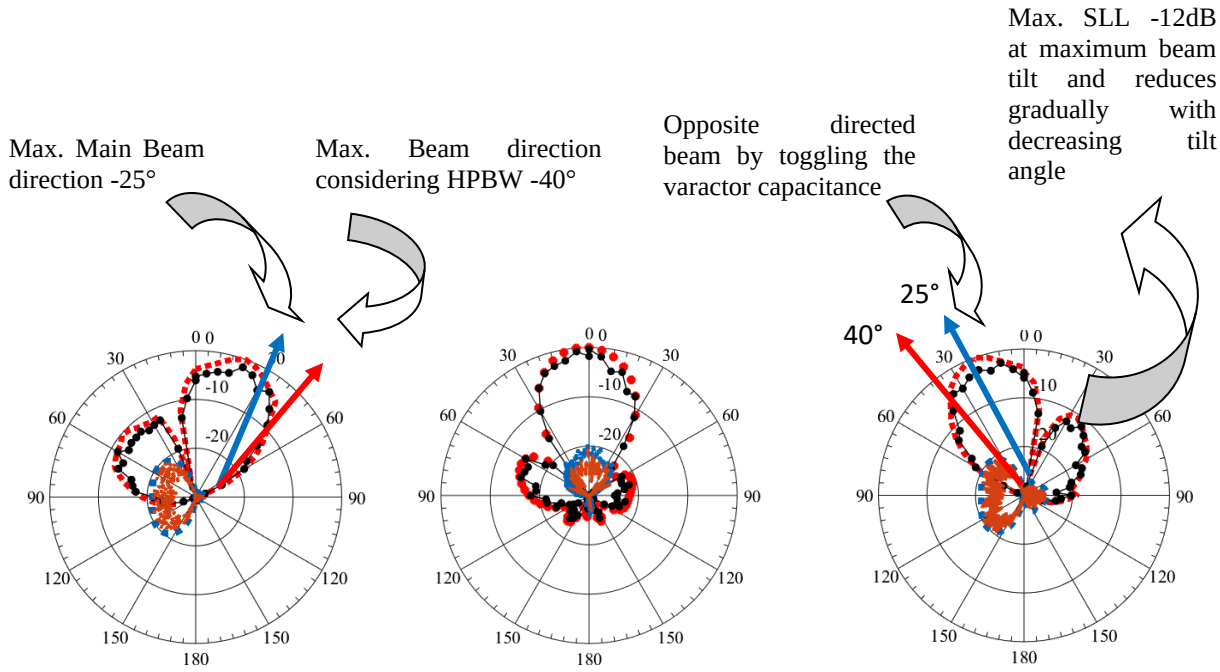

Fig. 9.16 E plane simulated and measured Co and X-pol Radiation pattern at φ = 90ºat 2.45GHz shown for tilt angle for main beam at ±25°and beam considering HPBW ±40°.

Pattern invariance with negligible SLL and X-pol level is noted in most of the cases. This fact can be attributed to the negligible adverse effects of the other co-existed higher order modes (TM_{22}) with TM_{03} mode hence the pattern purity remains unaltered for entire tuning band.

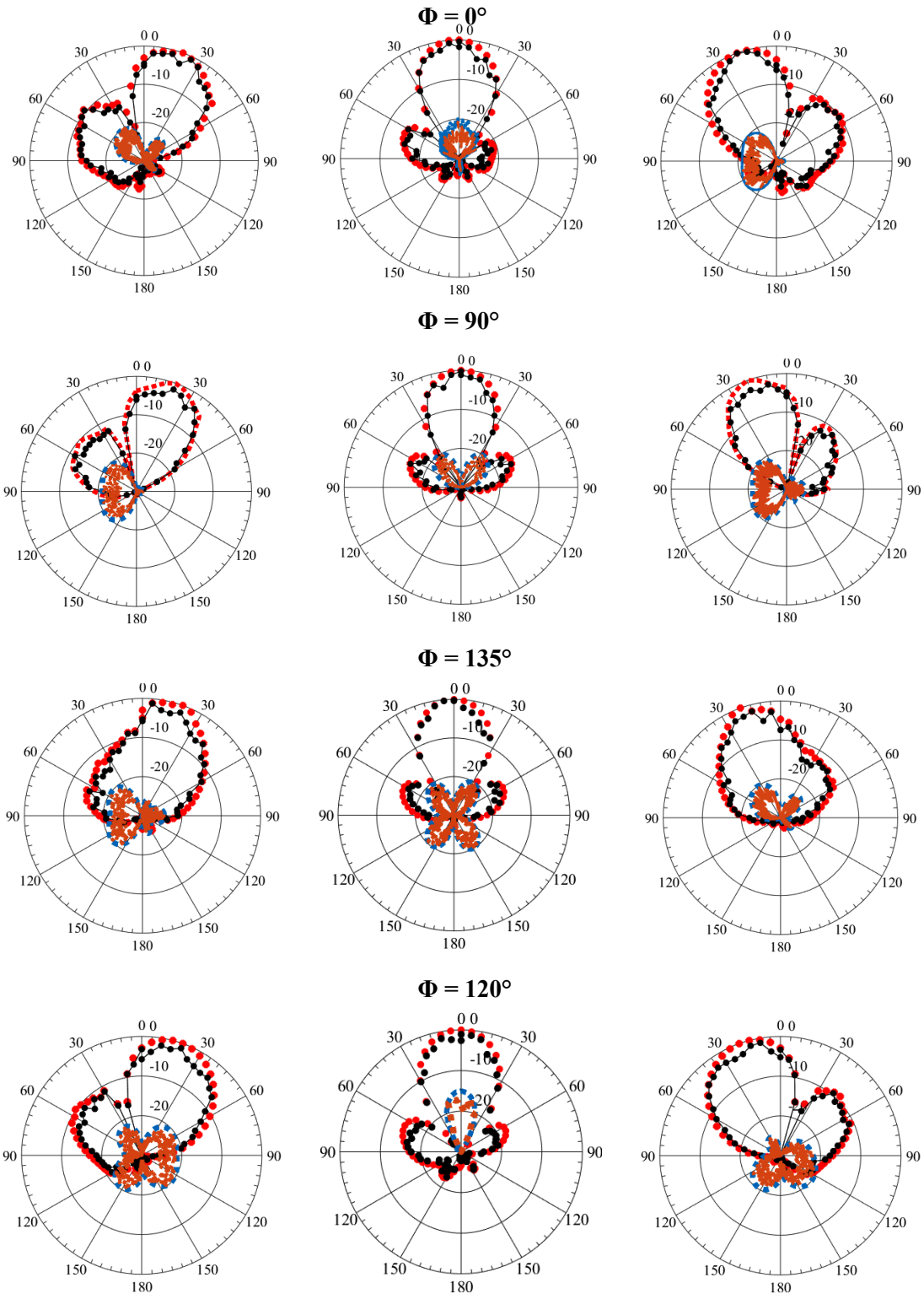
Φ = 0°
Φ = 90°
Φ = 135°
Φ = 120°
2.45GHz
Co-Pol Simulation
Co-Pol Measure
X-Pol Simulation
X-Pol Meas

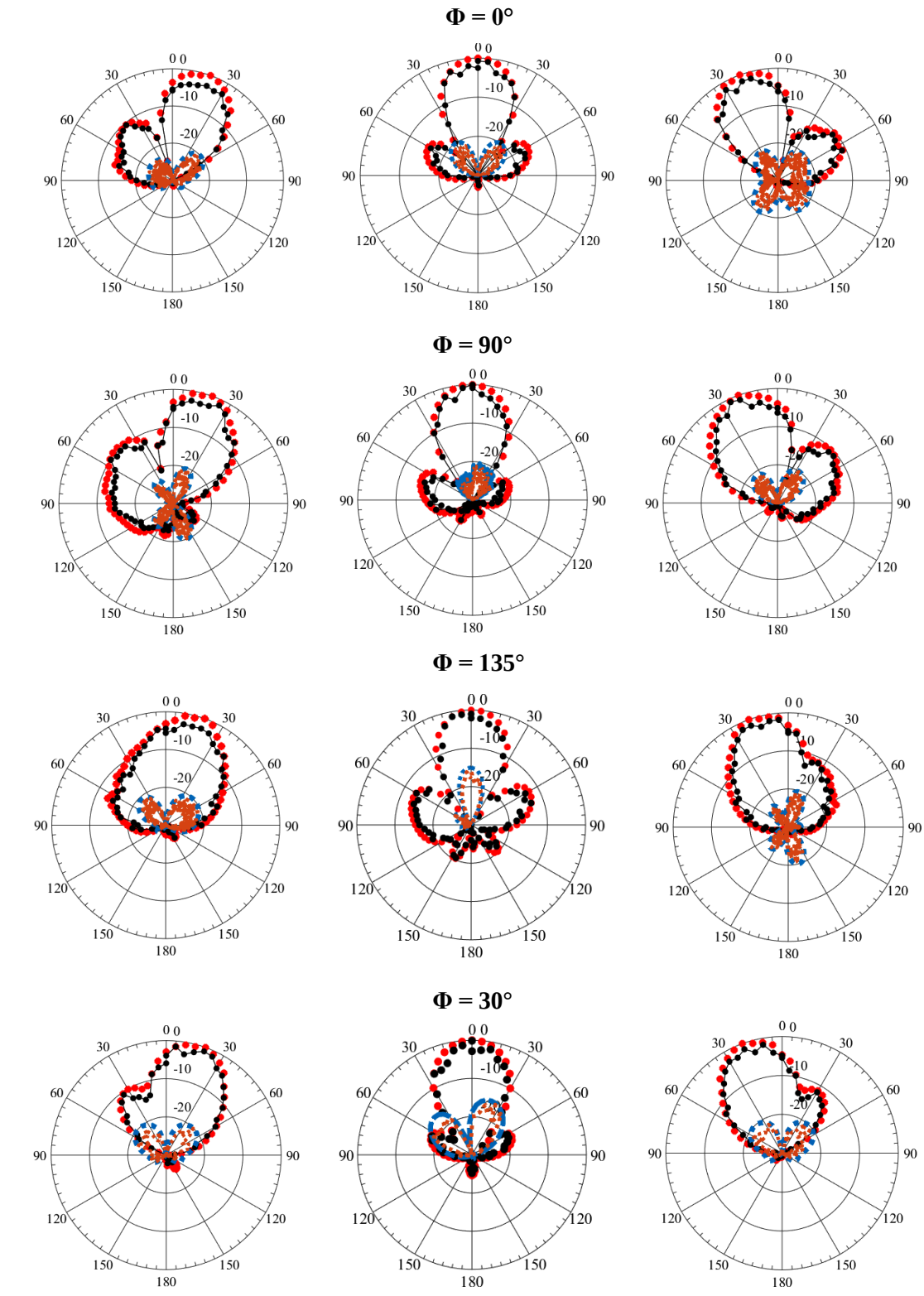
Φ = 0°
Φ = 90°
Φ = 135°
Φ = 30°
2.55GHz
Co-Pol Simulation
Co-Pol Measure
X-Pol Simulation
X-Pol Meas

Fig. 9.17 E plane simulated and measured Co and X-pol Radiation pattern at φ = 0º, 90º, 120º, 30º and 135º at 2.45GHz and 2.55GHz respectively. All plots are shown for maximum ±θ variation.

9.5 Comparison and Discussion

A comparative study of the recently proposed frequency and pattern reconfigurable antennas using MSA array and other planar and non-planar techniques in the literature is presented on performance and practical realization basis. A 1×2 microstrip monopole array is proposed very recently [12] which shows 2-D beam scanning at $0°< \Phi < 180°$, $0°< \theta < 90°$ (including 3dB beamwidth) with 8.2-11.1dBi gain in 5GHz band. Though dual port along with additional phase shifters are attached with two array elements to achieve the mentioned results. In [13] a 4×4 planar array is proposed at fixed 3.5GHz band that radiates six discrete beams at different φ planes. The antenna is fabricated on a large footprint area ($7.6\lambda_0 \times 5.1\lambda_0$). A 1×2 linear compact MSA array is proposed in [14] but limited to ±23º beam tilt only at φ=0º plane with 10% frequency tuning range and exhibits low gain (5.5-8.7dB) at 2.2GHz band. An 8×8 2D planar phased array [15] is designed at 5.2GHz band that scans ±80º (including 3dB beam) only at φ = 0º and 90º planes with a varying gain between 15.2-19.1dBi. It includes a very bulky and complex phase network for different phase combination with 64 discrete feed ports. Also, the antenna is fabricated on a very large footprint area ($5.2\lambda_0 \times 5.2\lambda_0$) and profile ($0.3\lambda_0$ or 10.508mm). In [16], a 1×9 multilayer MSA linear array backed by high impedance surface periodic structure exhibits ±60º beam scan at φ=0º plane with large footprint ($8.33\lambda_0 \times 1.31\lambda_0$) and profile ($0.19\lambda_0$ or 7.9mm). The antenna also exhibits wide gain variation (7dBi) with frequency and beam scan angles. A varactor loaded compact MSA is proposed in [17] with frequency tune and 360º beam scanning at φ=0º plane with exceedingly low gain around 2-2.51dBi. A low gain (5.6dBi) corrugated SIW based LWA operating at fixed 4.5GHz band is shown in [18]. The antenna exhibits θ= -41º to 31º beam scanning at E plane using very large number of diodes (40 Nos.). A 3-layer high profile complex 1×4 MSA array is proposed [19] for 2.15GHz to 2.99GHz frequency tuning and ±50º beam coverage in six discrete φ planes uses very large number of switching components (24 varactors and 32 PIN). A SIW based 4-port MSA is also proposed to [20] operate at 2.4GHz band exhibits 12 discrete beams at different fixed directions. Phase difference is applied to the port from external circuitry to achieve max ±30º tilt.

TABLE 9.2

A COMPARATIVE ANALYSIS OF RECENTLY PUBLISHED PATTERN AND FREQUENCY

Ref	Beam-Scan Antenna Configuration	Multi-functionality	Scanning Range	Realized Gain	Antenna Profile Height	RF Comp.	Operating Frequency	Substrate Layers and SMA Feed	Beam Tuning Mechanism
[12]	2D 1×4	B. S	$0°<\Phi<180°$ $0°<\theta<90°$	6.1-11.7	$1.2\lambda_0$	NA	5.2GHz	1 Layer 8 Port Feed	External Phase Network
[13]	2D 4×4	B. S	$\theta=\pm21°, \pm44°, \pm52°$ at six discrete ϕ planes	13.2-17.4	$0.02\lambda_0$	64 PIN	3.5GHz	1 Layer 1 Port Feed	Microstrip Line phase
[14]	1-D 1×2	F & B. S	$\theta=\pm23°$ at $\phi=90°$	6.5-8	$0.012\ \lambda_0$	2 Var.	2.2GHz	1 Layer 1 Port Feed	Varactor Detuning
[15]	8×8 2D	B. S	$\theta=\pm80°$at $\phi=90°, 0°$	15.2-19.1	$0.3\lambda_0$	NA	5.2GHz	3 Layer 64 Port Feed	Parasitic Pixel Layer
[16]	1-D 1×9	B. S	$\theta=\pm60°$ at $\phi=90°$	12.9-15.7	$0.19\lambda_0$	NA	3.5GHz	3 Layer Single feed	HIS PS
[17]	1-D	F & B. S	Azimuth 360°	2.34	$0.012\ \lambda_0$	4 Var.	2.45GHz	2 Layer 1 Port Feed	Varactor Detuning
[18]	1-D	F	$\theta=-41°$ to 31° at E plane	5.6	$0.028\lambda_0$	40PIN	4.5GHz	1 Layer 2 Port Feed	Corrugated SIW LWA
[19]	2-D 1×4	F & B. S	$\theta=\pm50°$ in five discrete ϕ planes	7	$0.018\ \lambda_0$	24 Var. 32 PIN	2.15-2.99GHz	3 Layer 1 Port Feed	Varactor Detuning and PIN switching
[20]	2D antenna	B. S	$\theta=-36°$ at 12 discrete ϕ plane	5.7-8.2	$0.02\ \lambda_0$	NA	2.45GHz	1 Layer 4 Port Feed	External Phase Network
This Work	**2D 2×2**	**F & B. S**	**$\theta = \pm 40°$ (including 3dB Beam width) 360° azimuth plane**	**14.5-17.1**	**$0.011\ \lambda_0$**	**4 Var**	**2.45GHz**	**1 Layer 1 SMA Feed**	**Varactor Detuning**

Abbreviations: BS, beam scanning ability; F, frequency reconfigurable.

In comparison, this work presents a compact, single layer, single feed, very low profile (>0.01 λ_0), 2×2 planar miniaturized (reduced footprint area by 22%) MSA array operates at TM_{03} mode. The proposed design exhibits significantly large, measured gain of 17.1dBi. A complete 360 º beam scanning in azimuth plane and ±40º beam scanning (including HPBW) at elevation plane throughout 10% frequency tuning range around 2.45GHz band is realized. Contrarily the designed antenna encounters very low (2dBi) gain variation for entire frequency sweep and all scan angles. To the best of author's knowledge frequency and pattern agility in a miniaturized higher order (TM_{03}) MSA array is proposed for the first time in the literature. Design simplicity, ease of fabrication and optimal performance make the proposed antenna suitable for different advanced applications in present wireless domain.

9.6 Conclusion

RF frontend in the present communication era is playing a pivotal role to uphold the most advanced and critical applications based on the latest technologies. The deployment of numerous RF nodes catalyzed ISI (Inter System Interference/Inter Symbol Interference) and co-channel interference issues; hence multifunctional antennas specifically frequency and pattern reconfigurable antennas play an important role to mitigate these concerns. Most of the reconfigurable antennas in the open literature exhibit high profile, low gain and larger footprint with complex feeding structures. In this work a single layered 2×2 planar antenna array operating at TM03 mode is proposed; hence attain exceedingly high realized gain (17.1dBi). Subsequently the array elements are miniaturized by 22% which reduces the overall array footprint area. Varactor diode is used to attain 11% continuous frequency tuning around 2.45GHz band. Furthermore, continuous 360º beam scanning at azimuth plane and ±40º (including 3dB beam width) at elevation plane is achieved. The scalability of the proposed antenna can be used to design antennas for diverse applications in the impending heterogeneous 5G network. Along with the conventional multifunctional application, this study shows an antenna perspective approach that would provide an additional degree of freedom to the system designer along with signal processing and communication front to mitigate co-channel interference, SINR, and low Bit Rate issues by alleviating the severe multipath effects in the Ultra- Dense Network (UDN)

environment. Having a simple and single feeding structure the proposed antenna can easily be integrated with other trans-receiver systems. The gain can be increased further using larger array configuration along with elements operating at TM_{0n} modes such as TM_{05}, TM_{07} and so on. The proposed reconfigurable array is also compared with recently published works in the open literature. The design is found to be advantageous in all aspects as depicted in Table 9.2. Hence the design simplicity, compactness, ease of fabrication, scalability and optimal performance make the proposed antenna very suitable for diversified applications in present wireless ecosystem.

Reference

[1] L. H. Trinh, F. Ferrero, L. Lizzi, R. Staraj and J. -M. Ribero, "Reconfigurable Antenna for Future Spectrum Reallocations in 5G Communications," in IEEE Antennas and Wireless Propagation Letters, vol. 15, pp. 1297-1300, 2016, doi: 10.1109/LAWP.2015.2505669.

[2] Zhang Jiajie, Wang Anguo and Wang Peng, "A Survey on reconfigurable antennas," 2008 International Conference on Microwave and Millimeter Wave Technology, 2008, pp. 1156-1159, doi: 10.1109/ICMMT.2008.4540632.

[3] The Investigation of PIN diode switch on reconfigurable antenna

[4] Rappaport, Theodore S. 2002. Wireless communications: principles and practice. Upper Saddle River, N.J.: Prentice Hall PTR.

[5] J. -M. Hannula, T. Saarinen, J. Holopainen and V. Viikari, "Frequency Reconfigurable Multiband Handset Antenna Based on a Multichannel Transceiver," in IEEE Transactions on Antennas and Propagation, vol. 65, no. 9, pp. 4452-4460, Sept. 2017, doi: 10.1109/TAP.2017.2725384.

[6] T. Koch and A. Lapidoth, "On Multipath Fading Channels at High SNR," in IEEE Transactions on Information Theory, vol. 56, no. 12, pp. 5945-5957, Dec. 2010, doi: 10.1109/TIT.2010.2080995.

[7] S. Maddio, A. Cidronali, M. Passafiume, G. Collodi, M. Lucarelli and S. Maurri, "Multipath Robust Azimuthal Direction of Arrival Estimation in Dual-Band 2.45–5.2 GHz Networks,"

in IEEE Transactions on Microwave Theory and Techniques, vol. 65, no. 11, pp. 4438-4449, Nov. 2017, doi: 10.1109/TMTT.2017.2698459.

[8] J. X. Yun and R. G. Vaughan, "Open slot antenna in a small groundplane at the second resonance," 2010 IEEE Antennas and Propagation Society International Symposium, 2010, pp. 1-4, doi: 10.1109/APS.2010.5561824.

[9] A. Bhattacharyya, J. Pal, K. Patra and B. Gupta, "Bandwidth-Enhanced Miniaturized Patch Antenna Operating at Higher Order Dual-Mode Resonance Using Modal Analysis," in IEEE Antennas and Wireless Propagation Letters, vol. 20, no. 2, pp. 274-278, Feb. 2021, doi: 10.1109/LAWP.2020.3048444. [10] https://www.skyworksinc.com/en/Products/Diodes/SMV1231-Series

[11] Garg, Ramesh., Bhartia, Prakash., Bahl, Inder. and Ittipihoon, Apisak.: “Circularly polarized microstrip antenna and techniques in microstrip antenna design handbook,” Norwood (MA): Artech House; 2001.

[12] J. Zhang et al., "Dual-Port Phase Antenna and Its Application in 1-D Arrays to 2-D Scanning," in IEEE Transactions on Antennas and Propagation, vol. 69, no. 11, pp. 7508-7520, Nov. 2021, doi: 10.1109/TAP.2021.3076558.

[13] X. G. Zhang, W. X. Jiang, H. W. Tian, Z. X. Wang, Q. Wang and T. J. Cui, "Pattern-Reconfigurable Planar Array Antenna Characterized by Digital Coding Method," in IEEE Transactions on Antennas and Propagation, vol. 68, no. 2, pp. 1170-1175, Feb. 2020, doi: 10.1109/TAP.2019.2938678.

[14] S. N. M. Zainarry, N. Nguyen-Trong and C. Fumeaux, "A Frequency- and Pattern-Reconfigurable Two-Element Array Antenna," in IEEE Antennas and Wireless Propagation Letters, vol. 17, no. 4, pp. 617-620, April 2018, doi: 10.1109/LAWP.2018.2806355.

[15] Y. -F. Cheng, X. Ding, W. Shao, M. -X. Yu and B. -Z. Wang, "2-D Planar Wide-Angle Scanning-Phased Array Based on Wide-Beam Elements," in IEEE Antennas and Wireless Propagation Letters, vol. 16, pp. 876-879, 2017, doi: 10.1109/LAWP.2016.2613130.

[16] G. Yang, J. Li, R. Xu, Y. Ma and Y. Qi, "Improving the Performance of Wide-Angle Scanning Array Antenna With a High-Impedance Periodic Structure," in IEEE Antennas and Wireless Propagation Letters, vol. 15, pp. 1819-1822, 2016, doi: 10.1109/LAWP.2016.2537850.

[17] M. S. Alam and A. Abbosh, "A Compact Reconfigurable Antenna With Wide Tunable

Frequency and 360° Beam Scanning," in IEEE Antennas and Wireless Propagation Letters, vol. 18, no. 1, pp. 4-8, Jan. 2019, doi: 10.1109/LAWP.2018.2869753.

[18] K. Chen, Y. H. Zhang, S. Y. He, H. T. Chen and G. Q. Zhu, "An Electronically Controlled Leaky-Wave Antenna Based on Corrugated SIW Structure With Fixed-Frequency Beam Scanning," in IEEE Antennas and Wireless Propagation Letters, vol. 18, no. 3, pp. 551-555, March 2019, doi: 10.1109/LAWP.2019.2896354.

[19] J. Hu, X. Yang, L. Ge, Z. Guo, Z. -C. Hao and H. Wong, "A Reconfigurable 1 × 4 Circularly Polarized Patch Array Antenna With Frequency, Radiation Pattern, and Polarization Agility," in IEEE Transactions on Antennas and Propagation, vol. 69, no. 8, pp. 5124-5129, Aug. 2021, doi: 10.1109/TAP.2020.3048526.

[20] A. Pal, A. Mehta, D. Mirshekar-Syahkal and H. Nakano, "A Twelve-Beam Steering Low-Profile Patch Antenna With Shorting Vias for Vehicular Applications," in IEEE Transactions on Antennas and Propagation, vol. 65, no. 8, pp. 3905-3912, Aug. 2017, doi: 10.1109/TAP.2017.2715367.

Chapter 10
Conclusions and Future Scopes

10.1 Introduction

In this dissertation the challenges in the upcoming Ultra-Dense-Network environment in 5G scenarios are pointed out. One of them is severe signal interference due to massive deployment of wireless nodes in the constrained spectrum. Thus, insufficiency of usable spectrum is another crucial issue generating co-channel interference. SINR is reduced due to multipath fading in the ever changing static and dynamic environments resulting in low data throughput and bandwidth. In ultra-dense environmental scenarios, these effects are even more chronic. Thus, in this dissertation the wireless channel in different environments is studied in higher wide band frequencies to characterize the channel behavior. Subsequently channel models are proposed based on the measurement data.

To be more precise, the author has characterized the wireless channel to know the channel State Information prior to design antennas for specific application in 5G ecosystem. In the next part of this dissertation the author has emphasized on designing reconfigurable antennas that would reduce the signal and channel adversities to cater to high speed and high bandwidth signals with least BER in the near future.

10.2 A Qualitative summery of the Achievements

RF domain in present communication era is playing a pivotal role to uphold the most advanced and latest technology-based applications. The gradual deployment of innumerous RF nodes in existing and upcoming 5G ecosystem catalyzed ISI and co-channel interference issues. This dissertation dealt with the co-channel, inter-system-interferences and spectrum insufficiencies from antenna perspective approach which would provide additional degree of freedom to the system designer along with signal processing and communication domains to mitigate these issues. These challenges in any P2P or P2MP RF link in coming 5G ecosystem can be nullified significantly by selecting a suitable operating state from the multiple distinct

available reconfigurable states of the antenna system based on predefined SINR and RSS threshold. Due to the constraint in the available wireless spectrum, there is significant overlapping of operating frequency bands which causes co-channel and Inter-system interference resulting in low SINR and high BER. Signal multipath in the wireless channel on the other hand creates random fluctuation in the RSS. In this dissertation few novel approaches from RF perspectives are analyzed and designed to mitigate the mentioned issues.

The terminal antennas used in the frequency and time domain channel measurement introduce additional time delays and reduce the coherence bandwidth of the channel. Researchers in the literature have mostly modeled the radio Channel (propagation channel including terminal equipment effect) instead of propagation channel, where the models were terminal dependent and valid for specific measurement setup. Subsequently, the frequency and time dispersive channel parameters derive from the measured CTFs were found to be erroneous and formulate inaccurate channel models. In few cases authors have calibrated the measurement setup in an anechoic chamber to deconvolute the effect of terminal antennas and other active devices.

A standalone channel response (frequency and time domain) excluding the antenna effects has been derived using a two-port network approach. Identical horn antennas operating in the C band have been used to measure the channel transfer function and impulse response. A comparative investigation of the measured results with and without antenna effects is presented.

It is observed that indoor propagation scenarios are changing rapidly resulting from the coexistence to larger numbers of electronic devices and the inclusion of advanced building materials. In static indoor scenarios, the presence of diverse scattering objects significantly increases the channel fading due to the vector addition of amplitude and phase varied multipath components (MPCs) at the receiving end. Because of the high dynamic range, frequency domain techniques based on a Vector Network Analyzer (VNA) efficiently assess an indoor static environment. A distance and frequency-dependent indoor wireless channel characterization and modeling using the frequency domain approach is presented in this thesis for C, X, and Ku bands in both Line of Sight (LOS) and non-Line of Sight (nLOS) scenarios.

The recently proposed reconfigurable antennas with advanced techniques suffer from several unavoidable complications. Firstly, most of the antennas are having multilayer high profile bulky structures which impose significant difficulties in antenna fabrication. Secondly, most of the antennas are having multiple feed ports which trouble system integration or

interfacing the antenna with other devices in the trans-receiver system. Thirdly, the electro-mechanical mechanism to control the liquid metal in reconfigurable liquid antennas is extremely cumbersome. Finally, the asymmetric structure with a complex feed network and large footprint area impose difficulties for practical realization. In this dissertation, the author has principally focused to address the above-mentioned issues. Compact reconfigurable MSA is introduced in the literature for the very first time with five reconfigurable polarizations states at each of three reconfigurable frequency bands. Dual CP, dual LP along with 45° LP reconfigurability is achieved using PIN diodes and a suitable bias network.

High gain beam steerable antennas can provide a proficient way to alleviate the multi-path fading and increase SINR by aligning the high-power beam toward the direction of intended receiver; hence shunting out the interference and noise sources which results in higher SINR, larger diversity gain and improved data throughput in the network.

Broadside radiating MSA is also studied extensively to design novel reconfigurable antennas to achieve larger realized gain. A planar 2D array with antenna elements operating in TM_{03} mode is proposed in K band with 17dBi measured gain. A compact, high gain, single-layer single feed penta-polarization reconfigurable MSA operating at higher-order mode is proposed possibly for the first time in the literature. A prototype antenna operating at TM_{03} mode and designed at 5.8GHz WLAN band is analyzed, fabricated, and measured to validate the proposed theory.

Frequency tuned pattern reconfigurable antennas reported so far have dealt with 1-D and 2-D beam scanning in fixed, multi and continuous tunable frequency bands with certain inherent flaws such as structural complexities, multilayer high-profile designs along with complex feeding and large footprint area. Also, these antennas exhibit severe gain instability in the beam-scanning and frequency tuning range. The complex multilayered structure and critical biasing network placed additional constraints on the practical realization of those proposed antennas. A single layered 2×2 planar antenna array is proposed operating at TM_{03} mode; hence attaining exceedingly high realized gain. Subsequently the array elements are miniaturized by 22% which reduces the overall array footprint. Varactor diode is used to attain 11% continuous frequency tuning around 2.45GHz band. Furthermore, a continuous 360º beam scanning at azimuth plane and ±40º (including 3dB beam width) at elevation plane is achieved. The proposed protype

antenna can be rescaled to design antennas operating at higher frequencies for diverse applications in the impending heterogeneous 5G network.

10.3 Future Scopes

We have witnessed the advancement of cellular technology from 1G to 4G and are on the verge of deploying 5G. These heterogenous architecture is ever expanding with growing customer demand and advanced used cases. This desire is the prime driving force behind the continuous technical advancement of this domain. Thus, the scope of future work particularly in this front is immense. Few specific directions of further research can be taken in continuation of this dissertation.

1. The multiple reconfigurable states of the antennas are altered to make the interfered link stable. The proposed tri-band and penta-polarization reconfigurable antenna is designed with fifteen reconfigurable states. But the important fact is that to change the state of the link a sophisticated feedback mechanism need to be incorporated in the antenna system. The feedback mechanism analyzes the link quality based on preconfigured SINR or RSS values and takes the decision to change the state. Thus, the feedback mechanism to initialize reconfigurability can be studied.
2. Advanced Artificial Intelligence (AI) and Machine Learning (ML) algorithms can be merged with the antenna feedback system to sense the user availability so that the beam can be steered accordingly for efficient power usage.
3. Lossy RF diodes and switches used in the antenna design pose significant adverse impact on antenna performances. Advance low loss MEMS based RF switches and varactors can be incorporated in the reconfigurable antennas and further research can be opted to improve total antenna efficiencies in different reconfigurable states.
4. With the advancement of technology, the overall footprint of the antennas along with other RF sub-systems are being miniaturized. On the other hand we have studied antennas operated in higher order broadside modes to attain comparatively larger gain compensating for large antenna size. Advanced miniaturization techniques can be opted for further research in this direction.

5. Terminal independent wireless channel characterization is studied in static environment using frequency domain approach. The derived closed form expressions can further be investigated in time domain approach and also in dynamic environment.
6. We have studied UWB channel characterization and modeling in indoor static environment. But for practical outdoor applications, dynamic channel properties need to be investigated in high frequency regime. Hence this domain needs to investigate further in near future.

List of Publications

Journal Publications:

[1] **J. Pal**, K. Patra and B. Gupta, "Antenna-Independent Frequency- and Time-Domain Representation of Wireless Channel," in *IEEE Antennas and Wireless Propagation Letters*, vol. 19, no. 8, pp. 1447-1451, Aug. 2020, doi: 10.1109/LAWP.2020.3005419.

[2] **Pal, Joydeep** & Patra, Kaushik & Gupta, Bhaskar. (2020). A TM 03 mode reduced side lobe high-gain printed antenna array in K band for UDN and IoT applications in 5G. *International Journal of RF and Microwave Computer-Aided Engineering.* 30. 10.1002/mmce.22414

[3] **Pal, Joydeep** & Patra, Kaushik & Gupta, Bhaskar. (2022). A low profile single feed compact dual-band penta-polarization agile Microstrip Antenna for interference mitigation in point to point link in Ultra-Dense environment. *AEU - International Journal of Electronics and Communications.* 150. 154191. 10.1016/j.aeue.2022.154191.

[4] **Pal, Joydeep** & Patra, Kaushik & Gupta, Bhaskar. A compact TM03 mode penta-polarization agile MSA for interference mitigation in 5G ultra-dense point to point environment. *International Journal of RF and Microwave Computer-Aided Engineering*. 2020; e23290. doi:10.1002/mmce.23290

[5] **Pal, Joydeep** & Gupta, Bhaskar. A High Gain Reduced Side-lobe Miniaturized Frequency and Pattern Reconfigurable planar array operating in Higher order mode. *International Journal of RF and Microwave Computer-Aided Engineering*. 2022; e23364. doi:10.1002/ mmce.23364.

[6] **Pal, Joydeep** & Gupta, Bhaskar. A Compact Tri-Band Penta-Polarization Reconfigurable Planar Antenna for Interference Management in 5G Ultra-Dense Network Environment. *International Journal of RF and Microwave Computer-Aided Engineering*. 2023; e23364. 10.1155/2023/2679182.

List of Papers under review:

[7] **Pal J** and Gupta B. Frequency domain UWB channel characterization and modeling in indoor static environment. *International Journal of RF and Microwave Computer-Aided Engineering*. 2022;